PRIMARY INDUSTRIES AND RESOURCES SA

CRCLEME
Cooperative Research Centre for Landscape Evolution & Mineral Exploration

REGOLITH STUDIES AT EDOLDEH TANK (ET) GOLD PROSPECT, GAWLER CRATON, SOUTH AUSTRALIA.

Volume 1: Text

M. J. Lintern, I. J. Tapley, M. J. Sheard, M. A. Craig, G. Gouthas and A. J. Cornelius

CRC LEME Open File Report 150 / CSIRO Exploration and Mining Report1081F /
PIRSA Office of Minerals and Energy Resources South Australia, Report Book RB 2003/4

April 2003

Compiled by M. J. Lintern and M. A. Craig

CRC LEME is an unincorporated joint venture between CSIRO-Exploration and Mining, and Land and Water, The Australian National University, Curtin University of Technology, University of Adelaide, University of Canberra, Geoscience Australia, Bureau of Rural Sciences, Primary Industries and Resources SA, NSW Department of Mineral Resources-Geological Survey and Minerals Council of Australia, established and supported under the Australian Government's Cooperative Research Centres Program.

Headquarters: CRC LEME c/o CSIRO Exploration and Mining, PO Box 1130, Bentley WA 6102, Australia

© CRC LEME

This report presents outcomes of a collaborative research project between Dominion Mining Ltd., CRC LEME and the Department of Primary Industries and Resources, South Australia (PIRSA) that commenced in mid 1999 and continued until mid 2002. It was agreed, between the parties, that this report could be released into the public domain.

Copies of this publication can be obtained from:
The Publication Officer, c/- CRC LEME, CSIRO Exploration and Mining, P.O. Box 1130, Bentley, WA 6102, Australia. Information on other publications in this series may be obtained from the above or from http://leme.anu.edu.au/
Cataloguing-in-Publication:
Lintern, M.J.
Regolith studies at Edoldeh Tank (ET) Gold Prospect, Gawler Craton, South Australia.
ISBN v1: 0643 068481
1. Regolith - South Australia. 2. Landforms - South Australia. 3. Geochemistry – South Australia. 4. Gold – South Australia.
I. Tapley, I. J. II. Sheard, M.J. III. Craig, M. A. IV. Gouthas, G. V. Cornelius, A. J. VI. Title.
CRC LEME Open File Report 150.

Addresses of authors

M. J. Lintern, I. J. Tapley and A. J. Cornelius
CRC LEME
c/- CSIRO Exploration and Mining
P.O. Box 1130
Bentley 6102
Western Australia

M. J. Sheard and G. Gouthas
Geological Survey Branch
Mineral Resources Group
PIRSA
GPO Box 1671
Adelaide 5001
South Australia

M. A. Craig
CRC LEME
c/-Geoscience Australia
PO Box 378
Canberra
ACT 2601

PREFACE AND EXECUTIVE SUMMARY

The Edoldeh Tank (ET) Regolith Project is part of the broader "South Australia Regolith Project" of CRC LEME, the principal aim of which is "to develop technically efficient procedures for mineral exploration in the major cratons of South Australia through a comprehensive understanding of the processes of regolith development and landscape evolution and their effects on the surface expression of concealed mineralisation".

This project is a follow-on to an initial study of regolith geology and geochemistry in the Gawler Craton, sponsored by CRC LEME, PIRSA and Gawler Joint Venture exploration tenement holders completed in 2002. It was developed after extensive consultation with industry geologists, and an excursion to various sites. The principal problems identified relate to verification of the thickness of transported overburden and to procedures for exploration in terrains where transported overburden is present.

The principal objective of the ET Regolith Project was to evaluate the use of components of transported overburden for detecting buried Au deposits in the western Gawler Craton. Five prospects (ET, Monsoon, South Hilga, Golf Bore and Jumbuck) were initially investigated. The objective was to determine the most suitable site for a detailed study. A single traverse, several hundred metres in length, was selected across each prospect that had mineralisation, transported overburden and adequate drill spoil. The regolith stratigraphy was described at each site and drill spoil collected for multi-element analysis. An existing company geochemical database for each prospect was also used. The results of the five prospect survey are reported in Lintern *et al*, 2002. The initial studies (Lintern *et al*, 2002) indicated that ET has the following properties:

1) two hundred drill holes spread over the prospect with cuttings in good condition;
2) a large Au in calcrete anomaly that had not been linked to a primary source, leaving potential for additional areas of investigation and possible drill targets;
3) indications that mineralisation might be expressed in the transported overburden;
4) a greater spread and thickness of transported overburden compared with other sites; and
5) sand dunes, typical of the western Gawler Craton, and a hindrance to exploration in this region so there are few, if any, previous studies in this type of terrain.

Regolith mapping at ET was based on the identification and detailed representation of the distribution of surficial material and the broader surface regolith units. The map was not only based on datasets commonly used in regolith map construction *e.g.,* Landsat TM, aerial photography and DEM, but also processed AIRSAR, and HyMap™ data sets played an important role in determining the final regolith-landform relationships. Regolith stratigraphy was determined using field observations, collection and analysis of drill cuttings from chip trays, and PIMA analysis. These data determined relationships between materials, weathering, landform history and the geochemical data. Drill cuttings, calcrete, soil and vegetation were collected to determine the distribution of Au and other elements, which was visualised in 3D and 2D.

The principal results indicate that:

1. In *in situ* regolith, Au was found to be concentrated in calcrete near the surface and above an interpreted leached zone of low Au concentration (leached zone?) that can extend down several tens of metres into the weathered regolith. The surficial Au anomaly extends from the ridge into transported regolith and, in places with thin (<5 m) sand cover, appears to be locally enhanced, possibly due to Au additions to the surface from underlying buried mineralisation in the transported overburden. Calcrete appears to be the best sample medium for Au exploration over soil, vegetation and silcrete. Gold appears to be the best target element although As may also provide information on the location of mineralisation.
2. Data sets obtained by remote sensing were particular useful in discriminating regolith units and in determining surface mineralogies. They were important in assisting in the construction of the regolith-landform map.
3. Landsat TM was most useful in mapping at the 1:5000 scale required for this study. A DEM was generated from aerial photographs and was useful in distinguishing landforms. Ground-truthing was important in delineating features, such as the extent and type of lag deposits, and in the final construction of the map.

4. The complimentary use of PIMA and visual logging of chip trays enabled determination of selected clay mineralogy, colour and lithology of the regolith including the boundary between transported and *in situ* regolith. 3D and 2D visualisations of the data assisted in determining the regolith stratigraphy and were able to integrate the information from PIMA, geochemistry and other data sets.

The study has led to a better understanding of Au dispersion in sand dunes, improved interpretation of calcrete-hosted Au anomalies, and indicated potential new drilling targets.

M. J. Lintern and I. J. Tapley
Project Leaders

April 2003

TABLE OF CONTENTS

1 INTRODUCTION (M. J. Sheard) 18
1.1 Background 18
1.2 General Geomorphology 18
2 REMOTELY SENSED DATASETS (I. J. Tapley and A. J. Cornelius) 23
2.1 Introduction 23
2.2 Project datasets 23
2.2.1 SPOT-Pan 23
2.2.2 Digital elevation data 23
2.2.3 Airborne gamma-ray spectrometry data 29
2.2.4 Landsat TM 31
2.2.5 HyMap^{TM} data 47
2.2.6 Polarimetric AIRSAR radar data 60
2.3 Summary and conclusions 63
3 REGOLITH MAPPING (M. A. Craig) 64
3.1 Introduction 64
3.1.1 Objective 64
3.1.2 Previous investigations 64
3.2 Methodology and datasets 64
3.2.1 Mapping approach 64
3.2.2 Map compilation and supplementary datasets 65
3.3 Regolith-landform maps and GIS 68
3.3.1 Digital data and GIS formats 68
3.3.2 Map face key 68
3.3.3 Regolith-landform mapping units 70
3.4 Summary and Conclusions 71
4 STRATIGRAPHY AND REGOLITH (M. J. Sheard) 73
4.1 Methods 73
4.2 Scope 73
4.3 Down Hole Sample Contamination 73
4.4 Regolith overview 74
4.5 Regolith Materials 75
4.5.1 In situ Components 75
4.5.2 Transported Components 81
4.6 Regolith transect 340200E – a representative example 84
4.6.1 Regolith materials on section 340200E 87
5 GEOCHEMISTRY (M.J. Lintern. A.J. Cornelius and G. Gouthas) 89
5.1 Introduction 89
5.2 Sample collection 89
5.3 Sample preparation and analysis 91
5.3.1 Mineral samples 91
5.3.2 Vegetation samples 91
5.3.3 X-ray diffraction analysis 91
5.3.4 PIMA 91
5.4 Gold geochemistry 92
5.4.1 Mineralisation 92
5.4.2 Calcrete 92
5.4.3 Lag 97
5.4.4 Overview of Au distribution in the sub-surface regolith 97
5.4.5 Gold distribution in drill cuttings, section by section 104
5.4.6 Soil and soil profiles 136
5.4.7 Vegetation 137
5.5 Silver geochemistry 138
5.6 Copper geochemistry 144
5.7 Arsenic geochemistry 150
5.8 Elements related to lithology – Co, Cr, (Cu), Ni, V and Fe 156

5.9 Elements related to phyllic alteration – K, Cs, Rb and Tl....158
5.10 Conclusions....160
6 IMPLICATIONS FOR EXPLORATION....161
6.1 Remote sensing technologies....161
6.2 Regolith landform mapping....161
6.3 Regolith Stratigraphy....161
6.4 Geochemistry....161
7 CONCLUSIONS....162
8 REFERENCES....164

LIST OF FIGURES

Figure 1-1 Interpreted subsurface geology of the Gawler Craton. Edoldeh Tank Gold Prospect lies approximately 60 km SSW of the Challenger Gold Deposit in the Christie Domain. Modified after Daly, 1998. 19
Figure 1-2 General locality plan for ET. See Figure 1-1 for location of plan. The red polygon shape (labeled ET) marks the extent of the regolith-landform map. 20
Figure 1-3 Drill sites and area of investigation plan at ET....21
Figure 1-4 The digital elevation model (DEM) for the ET Gold Prospect derived from aerial photographs. It displays the westerly high ground and associated ridge trending SW. Drillholes are marked by red dots. 22
Figure 1-5 Isopachs to transported cover materials (sediment) over ET. Comparison with the DEM (Figure 1-4) reveals that the sediments are infilling a palaeolandscape and that there is no significant topographic inversion apparent. Sediment thins over the palaeo-ridgeline and most drillholes are sited within the area enclosed by the 4.5 m overburden thickness contour. Data derived from field and laboratory studies. 22
Figure 2-1 SPOT-PAN image (10 m resolution) of the ET region showing the grid of drill-holes over the prospect. Terrains of low albedo are generally rich in silcrete lag with cover of low shrubs, and medium albedo terrains are sandplains with minor gravels of silcrete, calcrete and quartz with an overstorey of eucalyptus trees, shrubs and low grasses. Sandplains with reduced vegetative cover and an absence of gravels have a high albedo whilst clay-rich landforms contrast strongly with those landforms masked by massive silcrete. 24
Figure 2-2 AUSLIG GEODATA 9-second DEM image of the ET region with an extended position X-Y of the Regolith Line A-B, and the local relief along the line 25
Figure 2-3 Digital elevation model of ET region, generated from 1:50,000 scale stereo aerial photography, and local relief along the Regolith Line A-B. The data have a ground resolution of 20 m and ~1 m height accuracy. Drill holes are marked as crosses. 25
Figure 2-4 TOPSAR DEM of ET with the position of drill-holes, height contours and access tracks shown. Height profiles for transect X-Y along the Regolith Line indicate the precision of the data. A 30 m moving average filter has been applied to the top profiles to suppress the presence of trees along the transect....26
Figure 2-5 TOPSAR digital elevation data of ET region presented as a 2D relief model (Left) and shaded relief model with psuedo-illumination of 0° azimuth and 5° elevation (Right). Heights range from 119 to 250 m with a mean height of 153 m and standard deviation of 20 m. 27
Figure 2-6 3-D perspective image of TOPSAR DEM viewed from the south with high features as dark tones 27
Figure 2-7 Three-dimensional perspective images generated from TOPSAR elevation data, highlighting the topographic style of the terrain in vicinity of ET Gold Prospect. The greytone scene in the TOP image shows topographic highs as bright features whereas the BOTTOM scene is a pseudo-colour perspective with height contours. See text for details. 28
Figure 2-8 Three-dimensional perspective view, centred on ET, of the SPOT-PAN data in Figure 2-1 overlaid on the TOPSAR DEM. A 10x vertical exaggeration has emphasised topographic highs associated with basement rocks in an otherwise flat landscape dominated by sand sheets and occasional sand dunes. 29
Figure 2-9 Enhancements of three-band gamma-ray spectrometric data of ET displayed as a composite image with K-red:Th-green: U–blue (Left) and Total Counts (Right). Drill holes are red crosses in left image and green crosses in right image. The relatively strong Th (green) response in the composite image and high counts in the Total Counts image in vicinity of Silcrete Hill is probably related to the deposition of wind-blown clays that have originated from the weathering of the exposed basement rocks. 30
Figure 2-10 3D perspective view of a psuedo-coloured enhancement of the Total Counts data overlaid on a 20x exaggeration of the TOPSAR DEM(Top) and the between high total counts and the position of basement highs in the landscape (dark tones) in the 3D perspective of the TOPSAR DEM (Bottom). The locations of Cudyea Hill, ET and rises with high Total Counts are shown. 30
Figure 2-11 Position of Landsat TM bands 1-5 and 7, and their relationship to the reflectance spectra of the common minerals occurring at ET. 31

Figure 2-12 Greytone images of Landsat TM bands 1-5 and 7 of the ET region. The similarity in the six images is a result of the pervasive nature of aeolian sand and minimal rock outcrop resulting in a strong correlation between the TM bands. Maximum spectral contrast exists between locales of silcrete (low albedo) and sand plains (high albedo) where gravels and outcrop are absent. Areas of calcareous soils tend to have the highest albedo in all bands. 32
Figure 2-13 Landsat TM bands 2:4:7 colour composite image of a 15x15 km area centred on ET (1). Other features include Silcrete Hill (2), Cudyea Hill (3) and Edoldeh Tank (4)....33
Figure 2-14 An enlarged 6x7 km section of the Landsat TM image in Figure 2-12 showing the location of field sites described in the text, and field photographs of the principal regolith-landform units for the region at Sites H1, H01, H02 and H04. Photographs of numbered sites 1-8 are shown in Figure 2-15. 34
Figure 2-15 Field sites of regolith-landform units in vicinity of ET Gold Prospect. The location of each site is shown in Figure 2-14 35
Figure 2-16 Band ratio images of calibrated Landsat TM data provide information on the distribution of various landcover types and the mineralogy of surface regolith materials. Ratio 3/1 highlights occurrences of massive silcrete and abundant silcrete lag at ET (1), Silcrete Hill (2) and Edoldeh Tank (3) as dark tones; Ratio 5/4 shows locations of massive and gravel silcrete in bright tones; and Ratio 5/7, clay-rich locations in bright tones. An abundance of molecular water in regions of high green biomass results in intermediate tones in Ratio 5/7. The composite ratio image shows the distribution of endmember mineral groups derived from ratios 5/7 (clay, Red), 5/4 (silcrete, Green) and 1/3 (Fe, Blue). 37
Figure 2-17 6-band Landsat TM reflectance spectra and values for regolith materials classified using the Spectral Angle Mapper classification technique. 38
Figure 2-18 Classification of silcrete-rich lags using the Spectral Angle Mapping technique. These gravels occur principally within mapped units ISer1 and CHer1. The rule image (TOP) shows the classification result before assignment of the class to the SAM classification image shown in the BOTTOM image as an overlay on the Landsat TM 247 image. In the rule image, areas with more similar spectra to the reference spectrum for units ISer1 and CHer1 appear as bright regions. These are carried over into the Classification Image as a red hue. 39
Figure 2-19 Classification of clay-rich saprolite in vicinity of silcrete-capped breakaways using the Spectral Angle Mapping technique. Saprolite occurs within the mapped unit RLer. The rule image (TOP) shows the classification result before assignment of the class to the SAM classification image shown in the BOTTOM image as an overlay on the Landsat TM 247 image. In the rule image, areas with more similar spectra to the reference spectrum for unit RLer appear as bright regions. These are carried over into the Classification Image as a green hue. 40
Figure 2-20 Classification of massive silcrete unit RLer using the Spectral Angle Mapping technique. The rule image (TOP) shows the classification result before assignment of the class to the SAM classification image shown in the BOTTOM image as an overlay on the Landsat TM 247 image. In the rule image, areas with more similar spectra to the reference spectrum appear as bright regions. These are carried over into the Classification Image as a blue hue. 41
Figure 2-21 Classification of three principal regolith materials of interest, silcrete gravels (Red), saprolite (Green) and massive silcrete (Blue), in vicinity of ET using the Spectral Angle Mapping technique. 42
Figure 2-22 3D shaded perspective of regolith classes in Figure 2-21, registered to a shaded relief model and overlaid on the TOPSAR DEM - looking southwest across Silcrete Hill, in foreground, to ET (middle background). 42
Figure 2-23 Plot of canonical vectors 1 and 2 and Landsat TM data showing the distribution of the classes representing each regolith type....44
Figure 2-24 A composite image of canonical vectors 2:1:4, assigned as RGB respectively, derived from a canonical variate analysis of 6-band Landsat TM data provides excellent visual separation of silica/iron rich terrain units (pale green to white) where lags of abundant silcrete cobbles and gravels with minor calcrete gravels predominate. 45
Figure 2-25 Greytone images of canonical vector #1 (TOP) and canonical vector #2 (Bottom) developed from canonical vector analysis of six Landsat TM bands, density-sliced to highlight the occurrence of four principal regolith units in vicinity of ET. These include massive silcrete and silcrete lag (top image), and clay-rich regolith materials and clay-rich saprolite (bottom image). 46

Figure 2-27 A subset of the HyMap™ image in Figure 2-26 showing the location of field sites representing the principal regolith-landform units of ET, photographs of the surface materials, and HyMap™ reflectance spectra for each of these sites. A field photo of Site 6 is shown in Figure 2-15. 49
Figure 2-28 A comparison between HyMap™ reflectance spectra of the field site, regolith materials when the spectra have been offset for clarity along the Y axis. 50
Figure 2-29 Normalised reflectance spectra of composite regolith materials at field sites on ET highlighting the iron minerals (Left) and clay minerals (Right). 51
Figure 2-30 Reflectance spectral measurements recorded by the IRIS radiometer of ET field sites.....51
Figure 2-31 Spectral endmember signatures derived from HyMap™ data of the ET region. Wavelength subsets of the VNIR-SWIR region are used to highlight the iron minerals (Top) and clay minerals (Bottom). Note that endmembers #5 and #6 are not in numerical order. 52
Figure 2-32 Mixture-Tune Matched Filter abundance images EM #2, #3, #5 and #6 for ET. Highest abundances are white.....53
Figure 2-33 Geolocated, colour composite image of MTMF endmembers 6:5:4 displayed as RGB, respectively.....56
Figure 2-34 A 3-D perspective view of colour composite image of endmembers 6:5:4 in Figure 2-33, overlaid on the TOPSAR DEM and viewed from the east, looking west across ET. 57
Figure 2-35 Colour composite image of regolith endmembers 1:7:3 displayed as RGB, respectively, highlights the terrain units at ET. 58
Figure 2-36 3D perspective model of regolith endmembers 1:7:3 overlaid on TOPSAR DEM and viewed from the west with ET in the foreground. 58
Figure 2-37 Spectral Angle Mapper classification of HyMap™ regolith endmembers at ET. 59
Figure 2-38 Colour composite image of AIRSAR bands Lvv/Cvv/Pvv displayed as RGB, of the ET region with an overlay of access tracks and drill-hole transects over the ET Gold Prospect itself. Silcrete gravels and massive silcrete, roughly at the wavelength of C band, are prominent as green hues. C band provides clear discrimination between erosional and depositional terrains owing to the relative smoothness, relative to P-band and, to a lesser extent, L-band wavelength, of regolith-landform units. These contrast strongly with the blanket of aeolian sediments (dark green) and vegetative cover of chenopod-shrubland communities, which have medium to high backscatter in L and P bands (magenta). 61
Figure 2-39 3D perspective image of ET with 10x vertical exaggeration of AIRSAR bands Lvv/Cvv/Pvv overlaid on TOPSAR DEM demonstrates the relationship between sites of abundant silcrete lag in hues of bright green and topographic highs where bedrock is proximal to the ground surface. This enhancement also highlights the position of a broad southeast-trending valley draining from ET. This might have implications for Au transport in the regolith (Section 5.4.3). 62
Figure 3-1 K17 aerial photography provided the basis for construction of a regional digital elevation model. A byproduct of the DEM construction is the georeferenced orthophotomosaic of the broader area surrounding ET. The orthophotomosaic contains visible spectrum data useful in the regolith map generation processes. 65
Figure 3-2 A colour composite image of AIRSAR bands, using Spectral Angle Mapping, (overlying a Landsat TM 247 image) highlighting in reds the interpreted locations of silcrete exposures including silcrete gravels (sub set of Figure 2-18). 66
Figure 3-3 Landsat TM imagery demonstrating the combined aerial extent of silcrete and calcrete gravels (red), saprolite (green) and massive silcrete (blue). At ET, these regolith materials may be of significant value as potential sampling media and their distribution is a useful component of the regolith-landform s map of the area. The TM derived regolith patterns are not represented in the general regolith map as discrete endmember polygons. Subset of Figure 2-21. 67
Figure 3-4 This image results from the processing of Thematic Mapper (TM) bands 2, 4 and 7. The TM data highlight, in red, the combined distribution of silcrete and calcrete materials throughout ET region. 67
Figure 3-5 ET region showing thematically classified areas as relict, erosional and depositional. 68
Figure 3-6 False colour RGB digital elevation model generated from K17 (1949 vintage) black and white aerial photography with the ET study outline and the ET Gold Prospect included. High areas are shown in reds with lowest areas in blue. 69
Figure 3-7 The CRC LEME conventional style for representing Regolith-Landform Map symbols. The modifier suffix is used to indicate subclasses related to the main map units. An explanation of the

code options within this convention is contained within the RTMAP Field Handbook (Pain *et al*., 2001). 69
Figure 3-8 An extract of the ET Gold Prospect Regolith-Landforms Map showing the gross pattern of regolith polygons for the study area. Detailed map-unit codes and descriptions are available from the full scale map included with this report. 70
Figure 3-9 ET regolith map shows a range of 16 distinct regolith-landform mapping units. The first two letters represents the regolith type (CH=colluvial; IS =aeolian sand; RL=residual lag) and the second two letters represent the landform association (ep=erosional plain; er=erosional rise; pd= depositional plain; ps=sandplain). The number suffixes indicate sub-classes determined by additional attributes. See Figure 3-7 for the labelling convention. A fuller description of these mapping units and their attributes is available from the legend of the printed map or from within the GIS package. 72
Figure 4-1 Regolith terminology for an idealised weathered profile with minor modifications for South Australian conditions (after Robertson and Butt, 1997). 74
Figure 4-2 3D images of the ET Gold Prospect showing Munsell (1975) and Kelly and Judd (1976) colors of the drillhole data that have been converted to RGB colours for digital display using public domain software from Munsell Color Corp. Contrasting backgrounds highlight the darker and paler colours respectively. With ARCVIEW 3D analyst software and data on the Appendix DVD, these images can be rotated in any direction. There are over 390 distinct bulk colours used to describe regolith materials at ET. These displays amply demonstrate the deep weathering profiles, pallid zones plus occurrences of mafic lithotypes, and the strongly coloured transported cover materials. 76
Figure 4-3 and 78
Figure 4-4 Moist chiptray photos of section 337600E (holes 114-125) displaying a mixed character profile where felsic composition basement dominates. (left image = S end of transect, right image = N end of transect). 78
Figure 4-5 and 78
Figure 4-6 Moist chiptray photos of section 338600E (holes 31-43 and 92-96) displaying a mixed character profile. (left image = S end of transect, right image = N end of transect). 78
Figure 4-7 and 78
Figure 4-8 Moist chiptray photos of section 339600E (holes 163-177) displaying a predominantly basic-mafic profile. (left image = S end of transect, right image = N end of transect). 78
Figure 4-9 The distribution of lags around the main rises and breakaway feature in the central part of ET Gold Prospect. Small white squares represent drillholes. The connected green circles represent the GPS traverse points and resultant polygon boundaries of major lag units overlain on a selected part of the ET orthophotomosaic. 83
Figure 4-10 Soil profile (LHS) developed within the dune sands, where white calcrete forms a prominent B_{Ca} horizon (exposed in soil pit 1). Pipe karst has developed within the calcrete through soil water dissolution and perhaps tree root activity, the enlargement (RHS) displays this feature more clearly. Scale bar in both images is 10 cm long. The calcrete and soil were geochemically analysed (see Profile 1a and b, Section 5.4.6) 84
Figure 4-11 The upper regolith cross-section at ET detailing the transported cover and upper *in situ* units. The PIMA-derived kaolinite crystallinity index (KCI) (red line) denotes the unconformity. 85
Figure 4-12 The full regolith cross-section at ET. The PIMA derived KCI denoting provenance boundary (red line) indicates the unconformity. 86
Figure 5-1 Location of geochemical sampling points at ET. Most drill cuttings were sampled to 10 m or to 3 m below the unconformity whichever was deeper. Some deeper drill cuttings were sampled for mineralised material and for other regolith studies. Also shown are the three holes with the highest Au concentration recorded in drill cuttings. 90
Figure 5-2 Maximum Au (ppm) in RAB drill cuttings at ET (GJV data). 94
Figure 5-3 Depth to calcrete sample in metres (from GJV data) 94
Figure 5-4 Comparison between Au in calcrete (ppb) and maximum Au in drill cuttings (ppm), (from GJV data) 95
Figure 5-5 Au concentration of calcrete and drill holes overlaid on vertically-exaggerated DEM viewed looking west with tilt of 27 degrees (from GJV data). 95
Figure 5-6 Comparison of highly calcareous material with less/not calcareous material from drill cuttings on 340200E. Data labels indicate depth of sample. Grey rectangle size indicates position and tenor of mineralisation 96

Figure 5-7 Histograms of upper regolith samples from selected sections: a) log Au data with samples from transported regolith unit in black; b) log Ca data with samples containing top 10% Au in black.... 97
Figure 5-8 Gold concentrations at 1 m intervals to 10 m depth. Mineralisation (black dots) and transported overburden (hatching) are shown. See text for details of data treatment. Crossed hammers indicate positions of the three highest Au concentrations found in the drill cuttings. 98
Figure 5-9 Location of drill holes and raw, un-clipped Au data. Data range is from 1-700 ppb with concentrations related to colour and size of circle. View from SE. 99
Figure 5-10 (a-c) A series of diagrams showing the change in Au distribution at 10 m intervals from the surface to 50 m depth, overlaid on the DEM. Drill hole samples are coloured according to Au content. Gold data have been Box-Cox transformed before gridding by kriging and reconverting to ppb. Features are arrowed and discussed in text. 100
Figure 5-11 Diagrammatic representation of method for calculating Au concentration from slices defined for the upper surface and for the unconformity. The shaded area represents mineralisation, with depletion near the top of the *in situ* regolith (Sergeev and Gray, 2001).....102
Figure 5-12 Average concentration of Au with depth from the surface. The concentrations are calculated using a series of slices at 1m intervals from, and parallel to, the surface. Calculations were performed using MVS and drill cutting data. Grey and white symbols illustrate decreasing confidence with data due to incomplete slices (see text). 103
Figure 5-13 Average concentration of Au versus depth from the unconformity. The concentrations are calculated using a series of slices at 1m intervals below, and parallel to, the unconformity. Calculations were performed using MVS and drill cutting data. Grey and white symbols illustrate decreasing confidence with data due to insufficient drilling and therefore incomplete slices (see text). 103
Figure 5-14 Plan showing location of drill holes, the three most mineralised holes and section 337400E. 104
Figure 5-15 Gold distribution in 0-10 m drill hole samples on 337400E. Dashed line indicates approximate position of the unconformity. Shaded area indicates semi-quantitative estimate of carbonate concentration. Holes are displayed sequentially south (top left) to north (bottom right). .104
Figure 5-16 Drill section 337400E showing drill holes, Au concentration, regolith geology, chip tray photographs (0-38 m) and land surface. For detailed description of regolith-landform map symbols see text or map. All map units in metres. 105
Figure 5-17 Plan showing location of drill holes, the three most mineralised holes and section 337600E. 106
Figure 5-18 Gold distribution in 0-10 m drill hole samples on 337600E. Dashed line indicates approximate position of the unconformity. Shaded area indicates semi-quantitative estimate of carbonate concentration. Holes are displayed sequentially south (top left) to north (bottom right). .106
Figure 5-19 Drill section 337600E showing drill holes, Au concentration, regolith geology, chip tray photographs (0-38 m) and depth of overburden ("surface"). For detailed description of regolith-landform map symbols see text or map. All map units in metres. 107
Figure 5-20 Plan showing location of drill holes, the three most mineralised holes and Diagonal section. 108
Figure 5-21 Gold, Ca and Mg distributions in 0-13 m drill hole samples on Diagonal section. Dashed line indicates approximate position of the unconformity. Shaded area indicates semi-quantitative estimate of carbonate concentration. Holes are displayed sequentially NW to SE (top left to bottom right). 108
Figure 5-22 Diagonal drill section showing drill holes, Au concentration, regolith geology, chip tray photographs (0-38 m) and depth of overburden ("surface"). For detailed description of regolith-landform map symbols see text or map. All map units in metres. 109
Figure 5-23 Plan showing location of drill holes, the three most mineralised holes and section 337800E. 110
Figure 5-24 Gold distribution in 0-13 m drill hole samples on 337800E. Dashed line indicates approximate position of the unconformity. Shaded area indicates semi-quantitative estimate of carbonate concentration. Holes are displayed sequentially (left to right) with the southern most hole located left and northern most hole right.....110

Figure 5-25 Drill section 337800E showing drill holes, Au concentration, regolith geology, chip tray photographs (0-38 m) and depth of overburden ("surface"). For detailed description of regolith-landform map symbols see text or map. All map units in metres. 111
Figure 5-26 Plan showing location of drill holes, the three most mineralised holes and section 338000E. 112
Figure 5-27 Gold, Ca and Mg distributions in 0-10 m drill hole samples on 338000E. Dashed line indicates approximate position of the unconformity. Shaded area indicates semi-quantitative estimate of carbonate concentration. Holes are displayed sequentially (left to right) with the southern most hole located left and northern most hole right. 112
Figure 5-28 Drill section 338000E showing drill holes, Au concentration, regolith geology, chip tray photographs (0-38 m) and depth of overburden ("surface"). For detailed description of regolith-landform map symbols see text or map. All map units in metres. 113
Figure 5-29 Plan showing location of drill holes, the three most mineralised holes and section 338200E. 114
Figure 5-30 Gold, Ca and Mg distributions in 0-10 m drill hole samples on 338200E. Dashed line indicates approximate position of the unconformity. Shaded area indicates semi-quantitative estimate of carbonate concentration. Holes are displayed sequentially (left to right) with the southern most hole located left and northern most hole right. 114
Figure 5-31 Drill section 338200E showing drill holes, Au concentration, regolith geology, chip tray photographs (0-38 m) and depth of overburden ("surface"). For detailed description of regolith-landform map symbols see text or map. All map units in metres. 115
Figure 5-32 Plan showing location of drill holes, the three most mineralised holes and section 338400E. 116
Figure 5-33 Gold distribution in 0-10 m drill hole samples on 338400E. Dashed line indicates approximate position of the unconformity. Shaded area indicates semi-quantitative estimate of carbonate concentration. Holes are displayed sequentially (left to right) with the southern most hole located left and northern most hole right. 116
Figure 5-34 Drill section 338400E showing drill holes, Au concentration, regolith geology, chip tray photographs (0-38 m) and depth of overburden ("surface"). For detailed description of regolith-landform map symbols see text or map. All map units in metres. 117
Figure 5-35 Plan showing location of drill holes, the three most mineralised holes and section 338600E. 118
Figure 5-36 Gold distribution in 0-10 m drill hole samples on 338600E. Dashed line indicates approximate position of the unconformity. Shaded area indicates semi-quantitative estimate of carbonate concentration. Holes are displayed sequentially (left to right) with the southern most hole located left and northern most hole right. 118
Figure 5-37 Drill section 338600E showing drill holes, Au concentration, regolith geology, chip tray photographs (0-38 m) and depth of overburden ("surface"). For detailed description of regolith-landform map symbols see text or map. All map units in metres. 119
Figure 5-38 Plan showing location of drill holes, the three most mineralised holes and section 338800E. 120
Figure 5-39 Gold, Ca and Mg distributions in 0-10 m drill hole samples on regolith section 338800E southern part. Dashed line indicates approximate position of the unconformity. Shaded area indicates semi-quantitative estimate of calcrete concentration. Holes are displayed sequentially (left to right) with the southern most hole located left and northern most hole right. 120
Figure 5-40 Gold distribution in 0-10 m drill hole samples on regolith section 338800E northern part. Dashed line indicates approximate position of the transported-*in situ* boundary. Shaded area indicates semi-quantitative estimate of carbonate concentration. Holes are displayed sequentially (left to right) with the southern most hole located left and northern most hole right. 120
Figure 5-41 Drill section 338800E showing drill holes, Au concentration, regolith geology, chip tray photographs (0-38 m) and depth of overburden ("surface"). For detailed description of regolith-landform map symbols see text or map. All map units in metres. 121
Figure 5-42 Plan showing location of drill holes, the three most mineralised holes and section 339000E. 122
Figure 5-43 Gold, Ca and Mg distributions in 0-10 m drill hole samples on 339000E. Dashed line indicates approximate position of the unconformity. Shaded area indicates semi-quantitative estimate

of carbonate concentration. Holes are displayed sequentially (left to right) with the southern most hole located left and northern most hole right. 122
Figure 5-44 Drill section 339000E showing drill holes, Au concentration, regolith geology, chip tray photographs (0-38 m) and depth of overburden ("surface"). For detailed description of regolith-landform map symbols see text or map. All map units in metres. 123
Figure 5-45 Plan showing location of drill holes, the three most mineralised holes and section 339200E. 124
Figure 5-46 Gold distribution in 0-10 m drill hole samples on 339200E. Dashed line indicates approximate position of the unconformity. Shaded area indicates semi-quantitative estimate of carbonate concentration. Holes are displayed sequentially (left to right) with the southern most hole located left and northern most hole right. 124
Figure 5-47 Drill section 339200E showing drill holes, Au concentration, regolith geology, chip tray photographs (0-38 m) and depth of overburden ("surface"). For detailed description of regolith-landform map symbols see text or map. All map units in metres. 125
Figure 5-49 Gold, Ca and Mg distributions in 0-10 m drill hole samples on 339400E, southern part. Dashed line indicates approximate position of the unconformity. Shaded area indicates semi-quantitative estimate of calcrete concentration. Holes are displayed sequentially (left to right) with the southern most hole located left and northern most hole right. 126
Figure 5-50 Gold distribution in drill hole samples on 339400E, northern part. Dashed line indicates approximate position of the unconformity. Shaded area indicates semi-quantitative estimate of carbonate concentration. Holes are displayed sequentially (left to right) with the southern most hole located left and northern most hole right. 126
Figure 5-51 Drill section 339400E showing drill holes, Au concentration, regolith geology, chip tray photographs (0-38 m) and depth of overburden ("surface"). The indicated depth of overburden for holes ETAR316-ETAR322 is incorrect due to data limitations. For detailed description of regolith-landform map symbols see text or map. All map units in metres. 127
Figure 5-52 Plan showing location of drill holes, the three most mineralised holes and section 339600E. 128
Figure 5-53 Gold distribution in 0-10 m drill hole samples on 339600E. Dashed line indicates approximate position of the unconformity. Shaded area indicates semi-quantitative estimate of carbonate concentration. Holes are displayed sequentially (left to right) with the southern most hole located left and northern most hole right. 128
Figure 5-54 Drill section 339600E showing drill holes, Au concentration, regolith geology, chip tray photographs (0-38 m) and depth of overburden ("surface"). For detailed description of regolith-landform map symbols see text or map. All map units in metres. 129
Figure 5-55 Plan showing location of drill holes, the three most mineralised holes and section 339800E. 130
Figure 5-56 Gold distribution in 0-10 m drill hole samples on 339800E. Dashed line indicates approximate position of the unconformity. Shaded area indicates semi-quantitative estimate of carbonate concentration. Holes are displayed sequentially (left to right) with the southern most hole located left and northern most hole right. 130
Figure 5-57 Drill section 339800E showing drill holes, Au concentration, regolith geology, chip tray photographs (0-38 m) and depth of overburden ("surface"). For detailed description of regolith-landform map symbols see text or map. All map units in metres. 131
Figure 5-58 Plan showing location of drill holes, the three most mineralised holes and section 340200E. 132
Figure 5-59 Gold, Ca and Mg distributions in 0-12 m drill hole samples on 340200E. Dashed line indicates approximate position of the unconformity. Shaded area indicates semi-quantitative estimate of carbonate concentration. Holes are displayed sequentially (left to right) with the southern most hole located left and northern most hole right. 132
Figure 5-60 Drill section 340200E showing drill holes, Au concentration, regolith geology, chip tray photographs (0-38 m) and depth of overburden ("surface"). The indicated depth of overburden for holes ETAR191-ETAR197 is incorrect due to data limitations. For detailed description of regolith-landform map symbols see text or map. All map units in metres. 133
Figure 5-61 Plan showing location of drill holes, the three most mineralised holes and section 341200E. 134

Figure 5-62 Gold, Ca and Mg distributions in 0-10 m drill hole samples on 341200E. Dashed line indicates approximate position of the unconformity. Shaded area indicates semi-quantitative estimate of carbonate concentration. Holes are displayed sequentially (left to right) with the southern most hole located left and northern most hole right. 134
Figure 5-63 Drill section 341200E showing drill holes, Au concentration and chip tray photographs (0-38 m) and surface. For detailed description of regolith-landform map symbols see text or map. All map units in metres....135
Figure 5-64 Distribution of Au in soil (10-20 cm) at ET. Concentrations range from 0.1 to 8.9 ppb. Boxes indicate positions of soil profiles....136
Figure 5-65 Gold and Ca (calcrete) concentrations in soil profiles at ET. Note that certain axis scales are logarithmic to highlight the gradational increase in Au concentration from the surface to the calcrete horizon where concentrations usually sharply increase. Top axis is Au; base axis is Ca. 137
Figure 5-66 Gold in vegetation (mostly *Acacia* phyllodes and small branches) at ET. Concentration ranges from <0.02 to 1.43 ppb Au in dry weight or <0.5 to 26 ppb ash weight....138
Figure 5-67 Histogram data (ppm, logarithmic) for Ag by the cyanide digest (left) and mixed acid digest (right). Data are normally distributed but skewed (particularly Ag_{tot}) after the transformation. ... .138
Figure 5-68: Scatter plot of cyanide digest Ag vs triple added digest (total) Ag. 139
Figure 5-69 Distribution of Ag in the regolith at ET. Circles indicate sample location. Minimum and maximum Ag_{tot} (ppm) and Ag_{cn} (ppb) drill cutting concentrations are 0.05, 5.5, 0.025 and 236, respectively....141
Figure 5-70 Ag_{cn} concentrations at 1 m intervals to 10 m. Mineralisation (black dots and hammer-pick symbols) as maximum Au concentration per hole, and transported overburden (hatching) are shown. See text for details of data treatment. 142
Figure 5-71 A series of diagrams showing the change in Ag_{cn} distribution at intervals from the surface to 9.5 m depth, overlaid on the DEM. Drill hole samples are coloured according to Ag_{cn} content. ..143
Figure 5-72 Histograms of Cu distribution in upper regolith: a) Cu_{tot} (ppm); b) Cu_{cn}.(ppb). Transported regolith unit data shown in black. 144
Figure 5-73 Selected scatter plots for Cu_{tot} (ppm) and Cu_{cn}.(ppb). Other elements in ppm. Large and small symbols are for samples located in transported and *in situ* regolith, respectively. 145
Figure 5-74 Distribution of Cu in the regolith at ET. Circles indicate sample location. Minimum and maximum Cu_{tot} (ppm) and Cu_{cn} (ppb) drill cutting concentrations are 0.05, 340, 50 and 15000, respectively....147
Figure 5-75 Cu_{cn} concentrations at 1 m intervals to 10 m. Mineralisation (black dots and hammer-pick symbols) as maximum Au concentration per hole, and transported overburden (hatching) are shown. See text for details of data treatment. 148
Figure 5-76 A series of diagrams showing the change in Cu_{cn} distribution at intervals from the surface to 9 m depth, overlaid on the DEM. Drill hole samples are coloured according to Cu_{cn} content. 149
Figure 5-77 Copper concentrations in calcrete. Concentration range is from 4 ppm to 44 ppm. Also shown is maximum Au concentration in drill cuttings (ppm, black circles). (GJV data). 150
Figure 5-78 Selected scatter plots for As. 151
Figure 5-79 Distribution of As in the regolith at ET. Circles indicate sample location. Minimum and maximum As drill cutting concentrations are 0.025 and135 ppm, respectively. 152
Figure 5-80 Arsenic concentration in imaged kriged calcrete data. Greyed area is where data are not available. Concentration range is from <5 ppm to 39 ppm. Also shown are maximum Au in drill cuttings (ppm). (GJV data). 153
Figure 5-81 Arsenic concentration for raw data imaged in Figure 5-80. Circle diameter represents As from <5 ppm to 39 ppm. Note how the anomaly at centre-east is accentuated compared with the imaged plot. 153
Figure 5-82 A series of diagrams showing the change in As distribution at intervals from the surface to 40 m depth; the surface diagram is overlaid on the DEM. Drill hole samples are coloured according to As content....154
Figure 5-83 Upper regolith sections 338000E (a) and 339000E (b) showing As/Fe anomaly. Circle size is proportional to concentration. Black rectangle locates known mineralisation. 156
Figure 5-84 Nickel concentrations in calcrete compared with Ni distribution in the upper regolith drill cuttings on 339000E. Land surface height (AHD) has been calculated from the DEM. Note curiously low Ni concentrations in the calcareous drill cuttings downslope of 6637000N. 157

Figure 5-85 a) Upper regolith geology and Ni concentrations for 339400E south and showing location of profiles for b); b) selected element concentrations down hole for ETAR 319. Land surface height (AHD) has been calculated from the DEM. 157
Figure 5-86 Three-dimensional image of the distribution and type of micas in drill hole cuttings as determined by PIMA. Red is muscovite, blue is biotite, green is phlogopite. Viewed from above and south east. 158
Figure 5-87 Distribution of K at ET. Circles indicate sample location. Minimum and maximum K drill cutting concentrations are 490 and 25400 ppm, respectively. 159

LIST OF TABLES

Table 2-1 General spectral features and specific regolith spectral responses associated with Landsat TM bands 32
Table 2-2 Summary of canonical variate analysis including information about the sum of the canonical roots, the variation explained by each canonical root, and the standardised canonical vectors that describe the loading of each band on the CVA. 43
Table 3 The three categories of regolith may be divided into sub-categories. The percentages of each sub-category are shown with wind blown sandy sediments clearly dominating the landscape. 71
Table 5-1 Classification of geochemical anomalies. Characters S, s, M and m denote high and low (including below detection) concentrations in exploration sample and mineralisation respectively. A chance anomaly is when the exploration sample is spatially related to mineralisation but probably not derived from it. 89
Table 5-2 Peak concentration, hole name, depth to mineralisation, and depth of transported overburden of sample with the 3 highest Au concentrations (ppm, GJV data). 92
Table 5-3 Selected mean concentrations of elements in weathered mineralisation. The mean of 45 samples with >100 ppb Au from the Challenger Gold Deposit is included for comparative purposes.93
Table 5-4 Summary statistics of Au (ppb) for samples collected during this study. Calcrete[1] was specifically collected and analysed by GJV. 93
Table 5-5 Comparison of element concentrations in different calcrete size fractions taken from the base of soil profile 4. All concentrations in ppm. 96
Table 5-6 Summary statistics for Ag data. 139
Table 5-7 Summary statistics for Cu data. 145
Table 5-8 Summary statistics for As data. 150

ABSTRACT

Much of the Gawler Craton (South Australia) is covered with soil and other regolith materials that hide basement rocks and hinder mineral exploration. In the western parts of the Gawler Craton, for example, weathered basement rocks are covered by sediments such as sand dunes. The principal objective of this study was to evaluate the use of components of transported overburden, including sand and calcrete, for detecting buried Au deposits in the western Gawler Craton.

The paucity of Au prospects in the Gawler Craton, with or without transported overburden, presented a problem to finding a suitable study site. Edoldeh Tank (ET) was selected because of:

1) two hundred drill holes spread over the prospect with cuttings in good condition;
2) a large Au in calcrete anomaly that had not been linked to a primary source, leaving potential for additional areas of investigation and possible drill targets;
3) indications that mineralisation might be expressed in the transported overburden;
4) a greater spread and thickness of transported overburden compared with other sites; and
5) the presence of sand dunes, typical of the western Gawler Craton.

Mapping, regolith stratigraphy and geochemistry were used to characterise the ET Gold Prospect and determine best exploration methods.

There are few, if any, previous detailed geochemical, mapping and regolith stratigraphy studies where sand dunes cover a Au prospect. The study at ET provides new information on how to explore for Au deposits in this type of terrain.

The principal results indicate that:

1. In *in situ* regolith, Au was found to be concentrated in calcrete near the surface and above an interpreted leached zone of low Au concentration (leached zone?) that can extend down several tens of metres into the weathered regolith. The surficial Au anomaly extends from the ridge into transported regolith and, in places with thin (<5 m) sand cover, appears to be locally enhanced, possibly due to Au additions to the surface from underlying buried mineralisation in the transported overburden. Calcrete appears to be the best sample medium for Au exploration over soil, vegetation and silcrete. Gold appears to be the best target element although As may also provide information on the location of mineralisation.
2. Data sets obtained by remote sensing were particularly useful in discriminating regolith units and in determining surface mineralogies. They were important in assisting in the construction of the regolith-landform map.
3. Landsat TM was most useful in mapping at the 1:5000 scale required for this study. A DEM was generated from aerial photographs and was useful in distinguishing landforms. Ground truthing was important in delineating features, such as the extent and type of lag deposits, and in the final construction of the map.
4. The complimentary use of PIMA and visual logging of chip trays enabled determination of selected clay mineralogy, colour and lithology of the regolith, including the boundary between transported and *in situ* regolith. 3D and 2D visualisations of the data assisted in determining the regolith stratigraphy and were able to integrate the information from PIMA, geochemistry and other data sets.

ACKNOWLEDGEMENTS

The authors wish to acknowledge the assistance they received with this research: Dominion Mining Ltd with access to data; R. Klampt (Integraph Australia) for the production of the DEM; P. Kilgour for assistance with the final version of the regolith-landform map; A. Vartesi and T. Naughton for drafting some of the diagrams; H. Hink for assisting with document formatting; C. Pain, M. Schwarz and, particularly, M. Cornelius and C. R. M. Butt for providing valuable comment on earlier drafts of this report. All this was received with thanks.

REGOLITH STUDIES AT EDOLDEH TANK (ET) GOLD PROSPECT, GAWLER CRATON, SOUTH AUSTRALIA.

M. J. Lintern, I. J. Tapley, M. J. Sheard, M. A. Craig, G. Gouthas and A. J. Cornelius

1 INTRODUCTION (M. J. Sheard)

1.1 Background

The ET Gold Prospect is located in the Western Gawler Craton within the Christie Domain (Figure 1-1). ET's unusual two letter name is an acronym contraction of the nearby abandoned Edoldeh Tank. The area of interest encloses a surface geochemical Au anomaly approximately 16 km west of the Dog Fence and outside of designated pastoral lease coverage (centroid coordinates: Zone 53J, 6636500N, 339200E; Figure 1-2). Access is via the Tarcoola to Barton unsealed road and a northerly turn off just west of Wynbring Rocks. Alternatively, access can be made via the Stuart Highway approximately 100 km north of Glendambo then along the westerly trending unsealed road through Commonwealth Hill Pastoral Station and south from Jumbuck Outstation via several pastoral and exploration tracks (see Figure 1-1 and Figure 1-2).

A regional geochemical orientation study was carried out on five Au prospects within 100 km radius of and including ET Gold Prospect, prior to selecting it as the site for more detailed investigations. Details of the ET component to that work is included herein (Section 5) and involves a preliminary investigation on section 340200E. At ET an area was selected that encompasses all of the pre-existing drilling and the surface geochemical anomaly (3.3 x 4.2 km rectangle) trending west (Figure 1-3). The drilling pattern appears to be controlled more by surface geochemistry than other factors. Infill drilling was based on earlier work and has provided closer sampling opportunities. However, some isolated drilling clusters were difficult to link in with the main target area.

1.2 General Geomorphology

The selected study area extends across undulating terrain (<35 m elevation difference) comprising Archaean basement outcrop to subcrop, overlain by westerly-trending Pleistocene linear sand dunes (Figure 1-4) and associated sand spreads. An east-west trending ridge of silicified basement dominates the central part of the study area (Figure 1-4). An account of the regolith-landforms identified in the ET area is provided in Sections 2 and 3. All basement outcrop is deeply weathered (ranging from <35->70 m) and capped by 1-2 m of silcrete duricrust (Section 4). Orange to reddish coloured dunes overly the basement and form an easterly fringe to the Great Victoria Desert. They partly mantle the basement palaeotopography by infilling many low areas with quartz-rich sand (<15 m thick, Figure 1-5). Luminescent dating of dunes approximately 80 km to the west of this prospect established surface sand stability for at least the last 20,000 years (Huntley *et al*., 1999).

This region is arid with hot dry summers and cool winters, average annual precipitation is about 150 mm and annual evaporation exceeds 3500 mm,. Pleistocene climates appear to have been drier, windier and, possibly, cooler than present, leading to extensive desert dunefield development (Callen and Benbow, 1995).

Vegetative cover is substantially denser and of larger stature than to the east where pastoral lease holdings occur. The vegetation at ET is composed of a complex mosaic of different plant communities. Sand spreads and dunes commonly support open woodlands and mallee over shrublands. Dominant plants include large trees and woody shrubs of *Acacia, Eucalyptus, Cratystylis, Scleroleana, Casuarina* and *Senna* species. The areas with thinner cover consist of woodlands and open woodlands over open shrublands with woody shrubs and trees such as *Casuarina, Senna* and *Eremophila* species common. Appendix 7 has a full plant list for section 340200E across the ET Gold Prospect. Vegetation in this area forms a significant impediment to exploration and vehicular movement but stabilises the dunes.

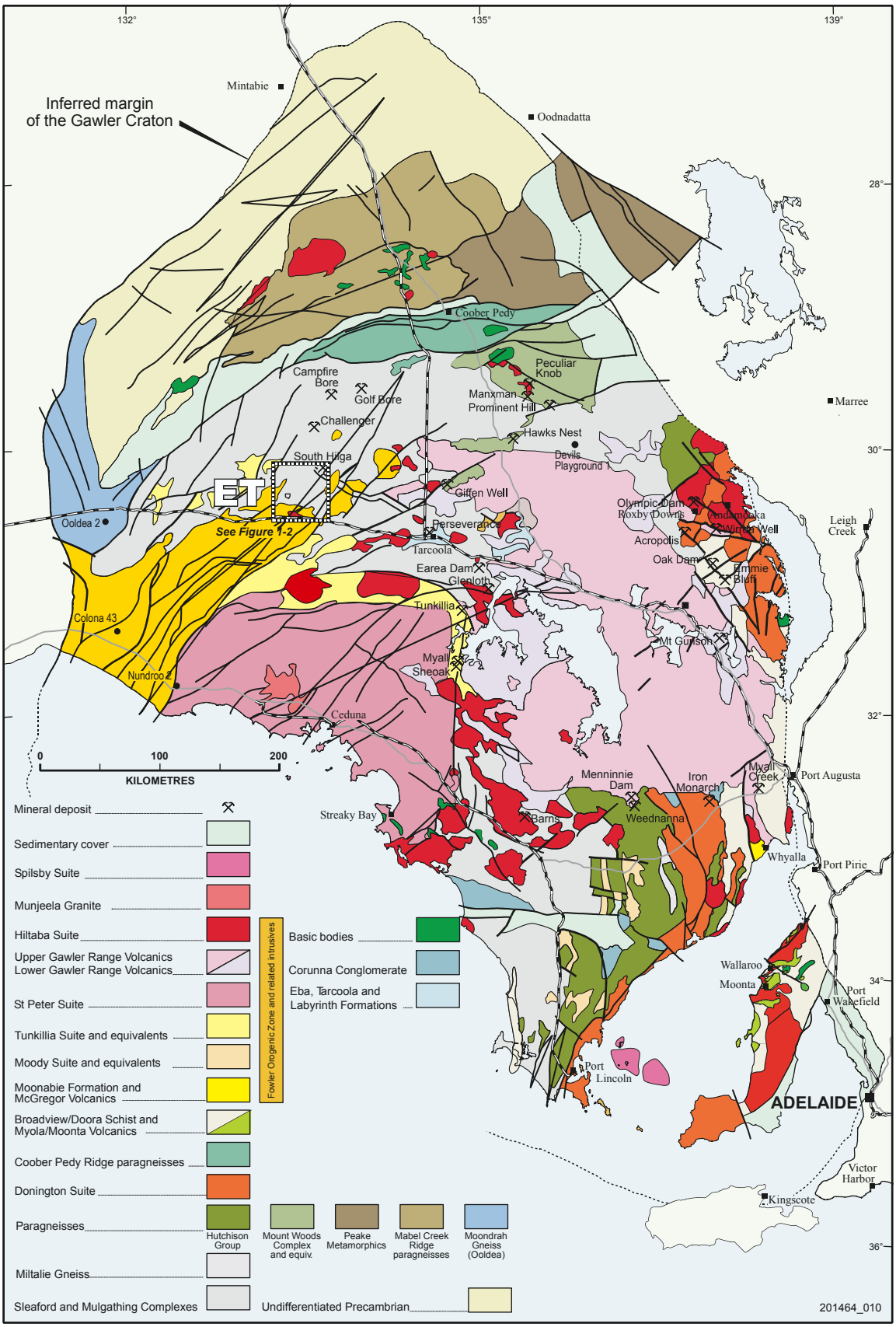

Figure 1-1 Interpreted subsurface geology of the Gawler Craton. Edoldeh Tank Gold Prospect lies approximately 60 km SSW of the Challenger Gold Deposit in the Christie Domain. Modified after Daly, 1998.

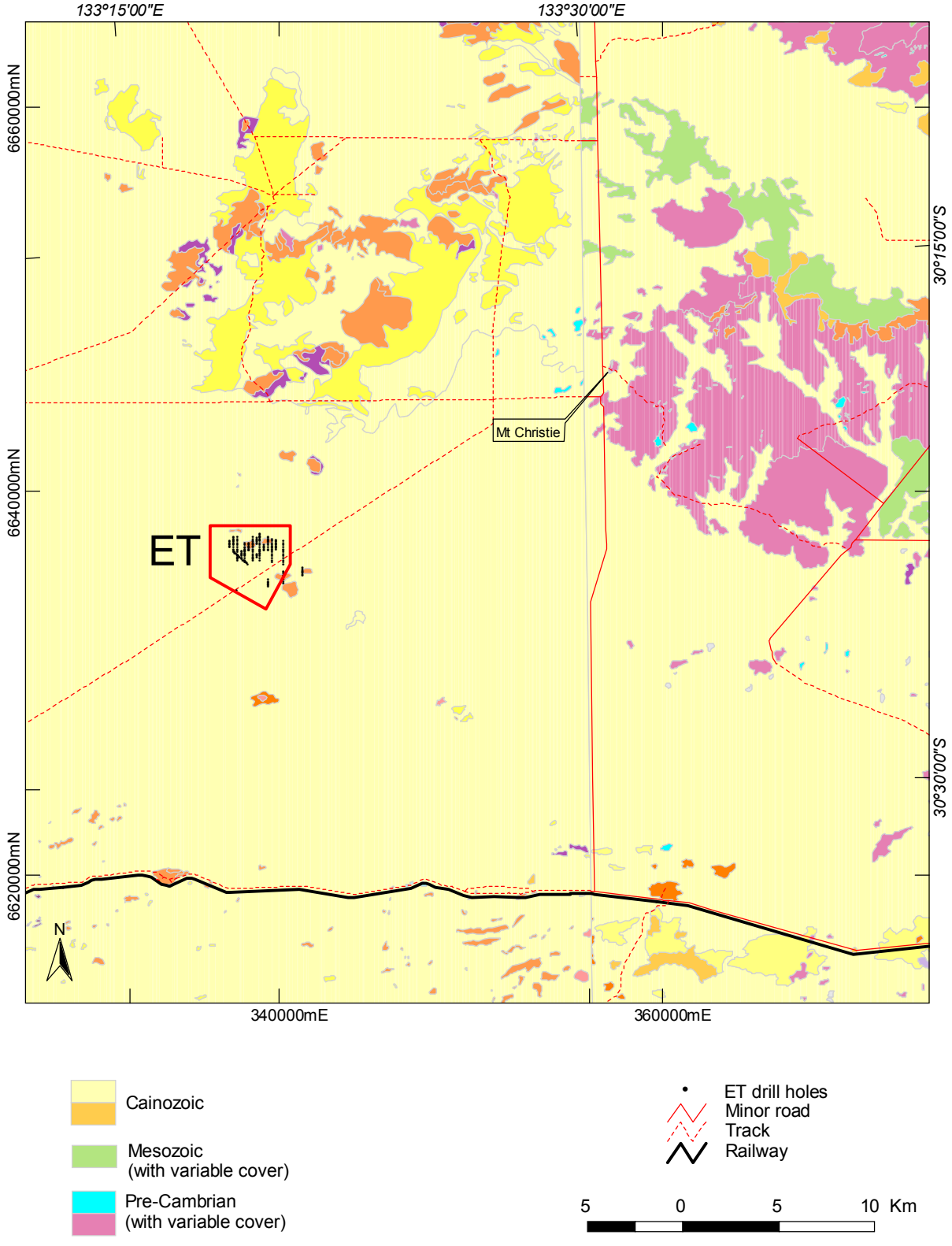

Figure 1-2 General locality plan for ET. See Figure 1-1 for location of plan. The red polygon shape (labeled ET) marks the extent of the regolith-landform map.

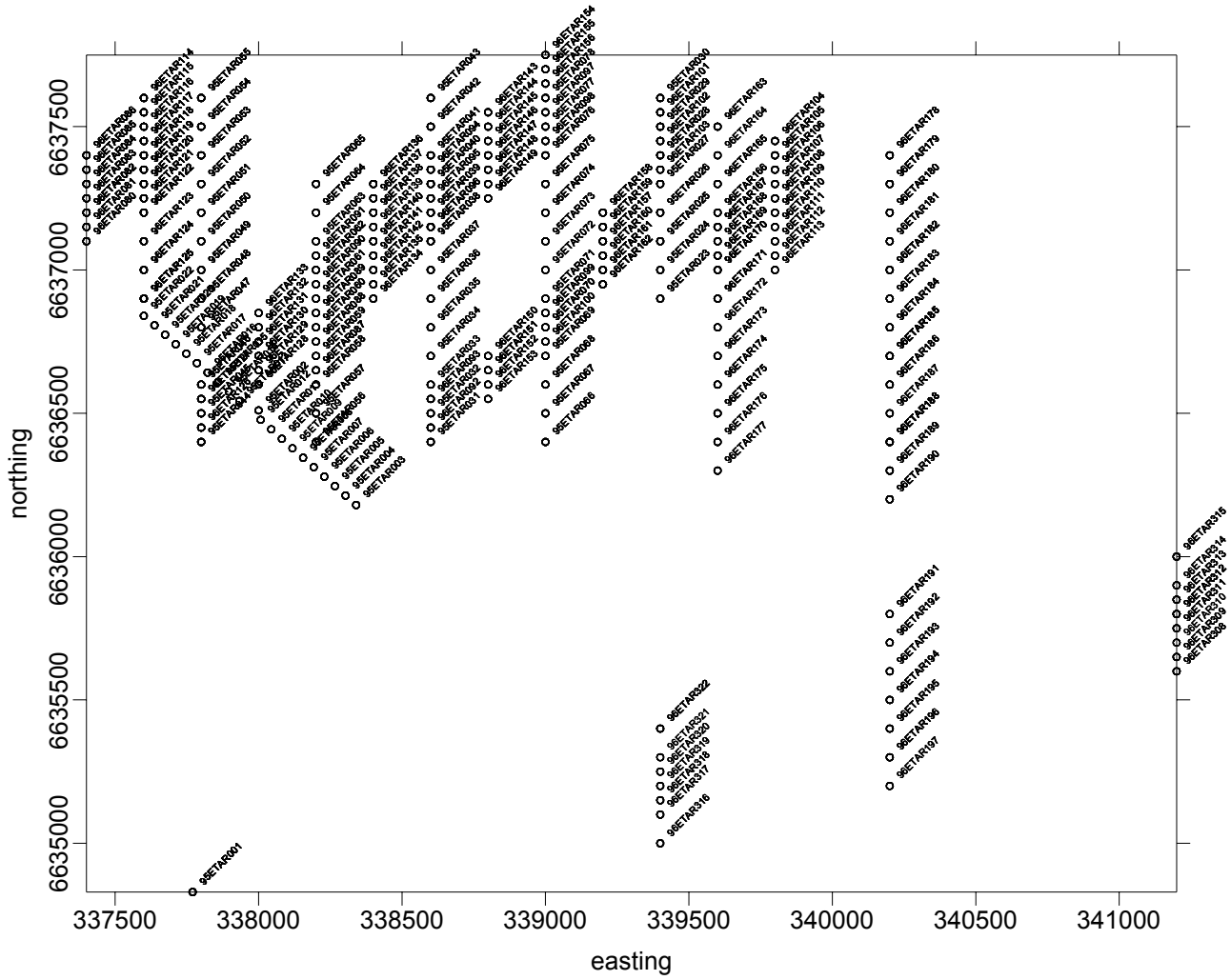

Figure 1-3 Drill sites and area of investigation plan at ET.

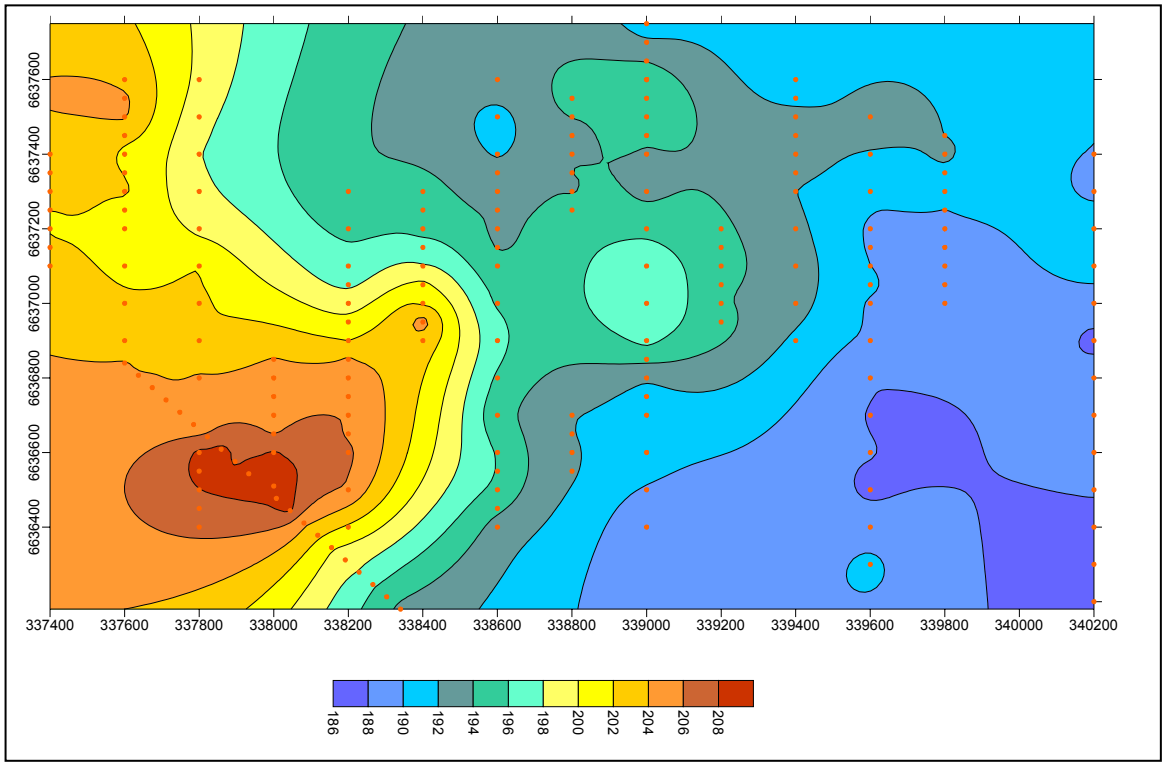

Figure 1-4 The digital elevation model (DEM) for the ET Gold Prospect derived from aerial photographs. It displays the westerly high ground and associated ridge trending SW. Drillholes are marked by red dots.

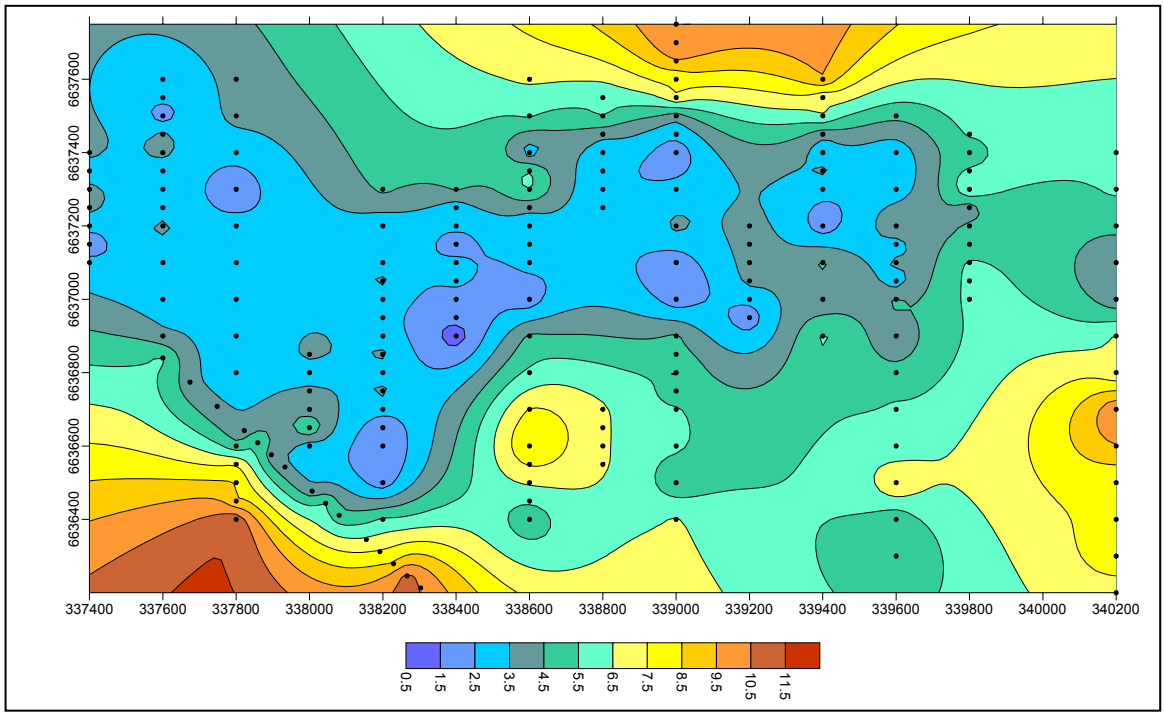

Figure 1-5 Isopachs to transported cover materials (sediment) over ET. Comparison with the DEM (Figure 1-4) reveals that the sediments are infilling a palaeolandscape and that there is no significant topographic inversion apparent. Sediment thins over the palaeo-ridgeline and most drillholes are sited within the area enclosed by the 4.5 m overburden thickness contour. Data derived from field and laboratory studies.

2 THE ROLE OF REMOTELY SENSED DATASETS IN MAPPING LANDFORMS AND REGOLITH (I. J. Tapley and A. J. Cornelius)

2.1 Introduction

The importance of the Gawler Craton has been recognised by the Au exploration industry, which faces the difficult task of exploration in a complex and deeply weathered terrain masked by a discontinuous blanket of calcrete, colluvium and aeolian sands. It is a region where the mapping of landforms and an understanding of the nature and distribution of regolith materials are critical to a range of geological and geochemical exploration methods. The regolith can generally hinder mineral exploration by concealing the bedrock and preventing easy sampling, mapping and photo-interpretation of structure. Exploration in the Gawler Craton must, therefore, rely on regolith geochemistry, geophysics and remote sensing.

The landforms, surficial regolith and vegetative cover that characterise ET are considered representative of a much larger region of the western Gawler Craton that is masked by the dunefields and sandplains of the Great Victoria Desert. Therefore, techniques developed to identify terrain parameters over the ET region can be considered as appropriate to assist explorers of the larger region.

This chapter reports on the use and relevance of remotely sensed datasets for interpreting the landforms and surficial regolith materials in vicinity of ET. Data processing, image enhancement and display techniques considered appropriate to regolith and landform mapping in this region are examined. Five types of data were used: (1) SPOT-PAN; (2) Landsat Thematic Mapper; (3) polarimetric airborne radar; (4) digital elevation datasets of various resolutions and precision; and (5) HyMap^{TM} hyperspectral data. Landsat TM and elevation datasets represent the level of operational datasets that are available for routine mapping whereas limited radar data are available from space-borne systems. Radar data and one of the elevation datasets examined over ET in this study were acquired in November 1996 during the PacRim1 NASA deployment to Australia of the JPL-built AIRSAR system.

2.2 Project datasets

2.2.1 SPOT-Pan

A high quality SPOT-PAN dataset, acquired in February 1997, aided the geocoding process of project spatial datasets including Landsat TM and radar data. It also acted as a baseline image for interpreting the landform and regolith units, and was used as a navigation tool during fieldwork. The image in Figure 2-1 shows the locations of the exploratory drill-holes over ET and the original section (Regolith Line 340200E) along which the initial study was performed (Lintern *et al*., 2002). Other landmarks include Silcrete Hill, a topographically prominent, circular-shaped, remnant of Archaean basement rock, capped with a lag of silcrete gravels; Cudyea Hill, a prominent hill masked by aeolian sand and sand-dunes, and the highest feature in the region; and Edoldeh Tank itself, the abandoned watering point located on a silcreted hill at the intersection of access tracks after which the prospect was named.

2.2.2 Digital elevation data

Elevation datasets were enhanced to provide shaded relief images, and combined with other datasets to provide three-dimensional (3-D) views of the mapping areas (Figure 2-13, Figure 2-14 and Figure 2-15). Perspective modelling of the relationships between rock units and topography presents the geology and landforms in a more informative way, assists their interpretability and helps to understand the relationships between landforms, geomorphic processes and terrain relief. In addition, perspective modelling facilitates the visualisation of complex relationships between the landscape attributes and thematic data such as geochemistry, Landsat TM and radar. For example, in very low relief terrain in vicinity of the Challenger Gold Deposit in South Australia, Wilford *et al*., (1998) demonstrated a strong relationship between topographic highs (generally less than 10 m), *in situ* landforms and higher Au concentrations.

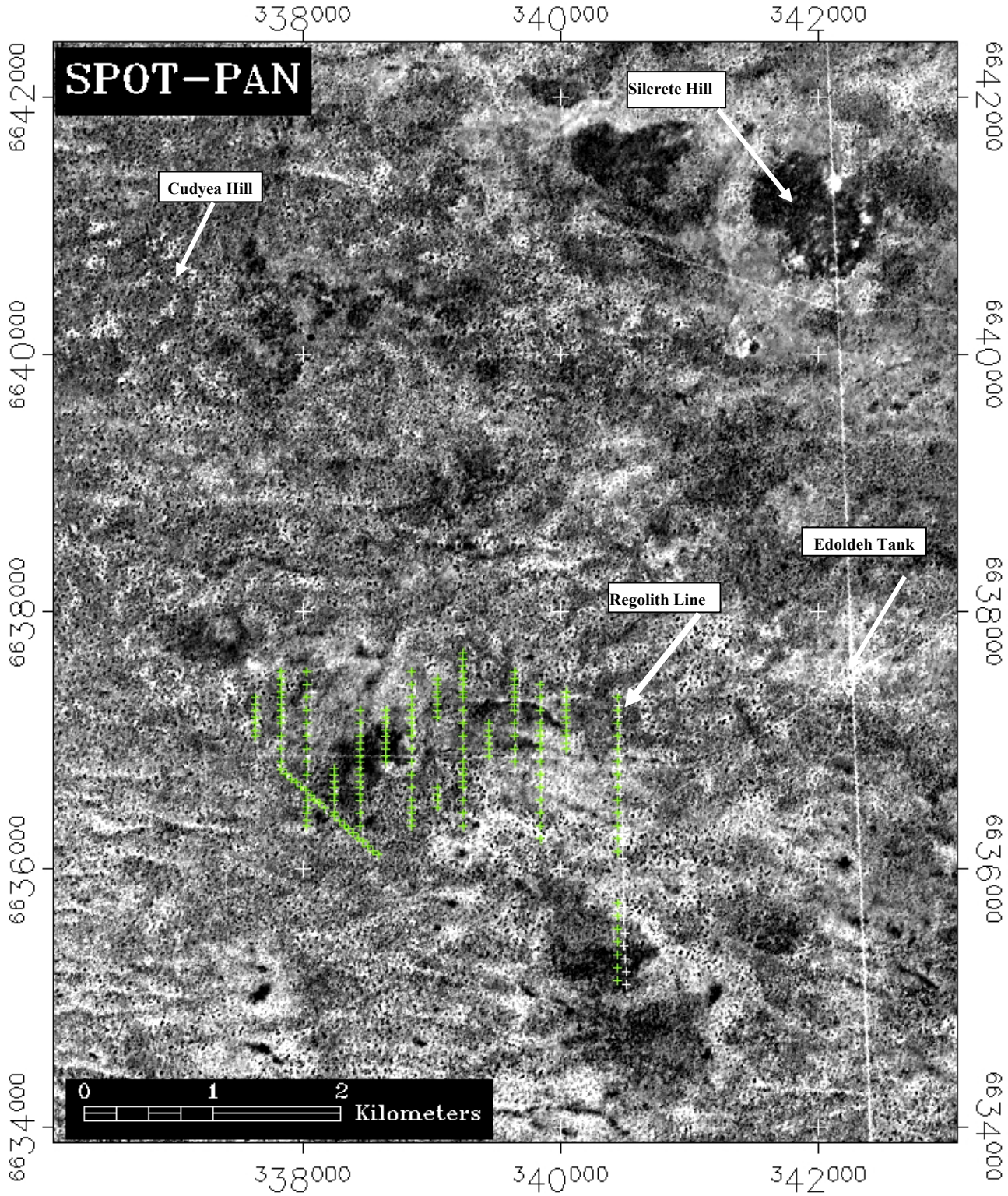

Figure 2-1 SPOT-PAN image (10 m resolution) of the ET region showing the grid of drill-holes over the prospect. Terrains of low albedo are generally rich in silcrete lag with cover of low shrubs, and medium albedo terrains are sandplains with minor gravels of silcrete, calcrete and quartz with an overstorey of eucalyptus trees, shrubs and low grasses. Sandplains with reduced vegetative cover and an absence of gravels have a high albedo whilst clay-rich landforms contrast strongly with those landforms masked by massive silcrete.

Three elevation datasets were available to this project.

1. The AUSLIG GEODATA 9-second DEM. These data have a spatial resolution of 250 m and a height accuracy of ~30 m and, as demonstrated in the shaded relief image in Figure 2-2, are unsuitable to resolve local variations in the height and shape of subtle landforms, particularly in this low relief, sandplain terrain that covers much of the western Gawler Craton. However, at a regional scale of between 1:250 000 and 1:5 000 000, enhancements of the AUSLIG DEM can be very useful for mapping regional landforms and topographically expressed, linear structures that are near-continuous in their alignment - for example, palaeochannels in sandridge terrains and strandlines in the vicinity of palaeocoastlines (Tapley, 2000).

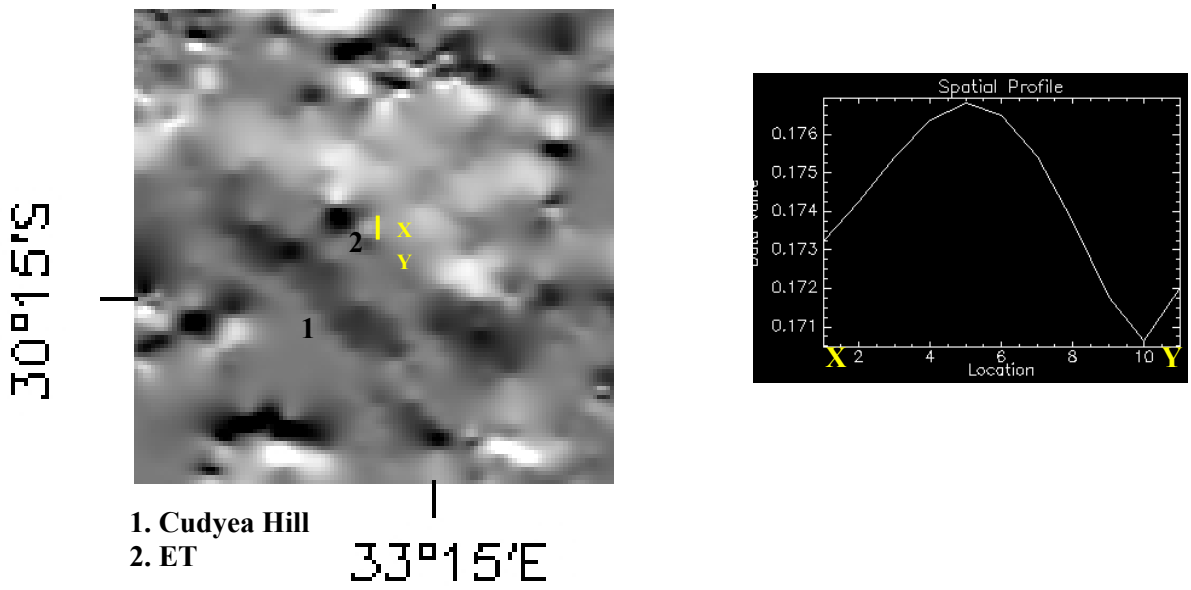

Figure 2-2 AUSLIG GEODATA 9-second DEM image of the ET region with an extended position X-Y of the Regolith Line A-B, and the local relief along the line

2. A custom-built DEM constructed on an Intergraph Soft photogrammetric digital workstation from 1:50,000 scale, stereo aerial photography collected in 1942 using a K7 camera system (Figure 2-3). Positional accuracy is calculated to be in the order of X-Y = +/- 20 m and Z = +/- 1 m. The 2D relief image and profile information in Figure 2-3 indicate that the increased grey levels have resulted in the improved relief definition of local landform along the Regolith Line, and that these data are appropriate for detailing the height and shape of the ET landscape at both local and regional scales.

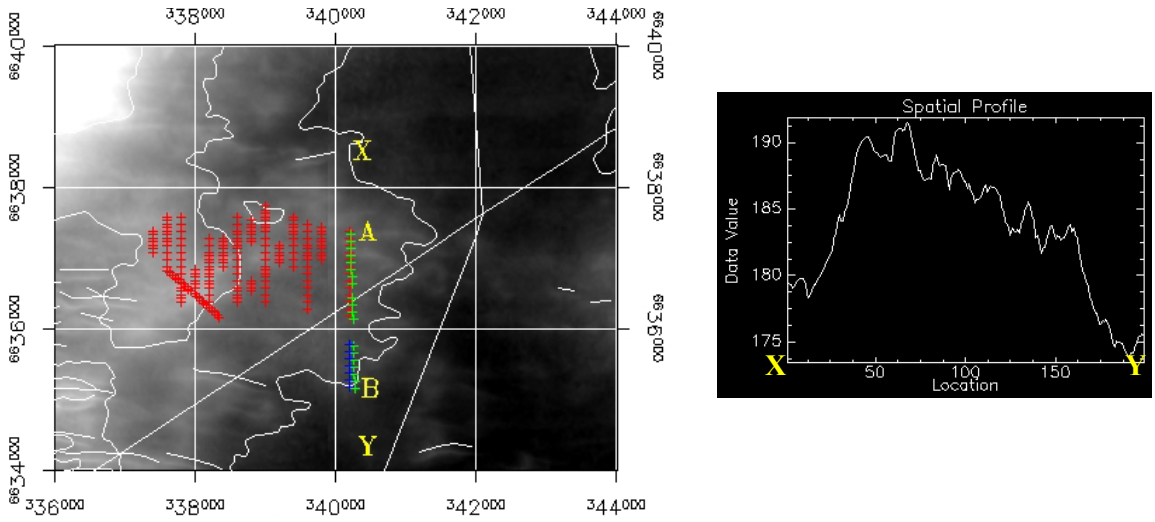

Figure 2-3 Digital elevation model of ET region, generated from 1:50,000 scale stereo aerial photography, and local relief along the Regolith Line A-B. The data have a ground resolution of 20 m and ~1 m height accuracy. Drill holes are marked as crosses.

3. A TOPSAR (TOPographic Synthetic Aperture Radar) DEM captured by the NASA-JPL AIRSAR instrument in 1996 (Figure 2-4). The TOPSAR system is a 5 cm wavelength, C-band interferometer

that captures precision height data for every 10 x 10 m pixel across a 10 km wide swath. Results from the examination of TOPSAR elevation datasets indicate that in low relief terrains, sub-metre accuracy can be achieved whereas in high relief areas, height differences of 2-5 m are resolved. Because the height data are generated from every 5x5 m pixel and not from more widely spaced postings as in the case of DEMs generated by photogrammetric means, TOPSAR DEM data are distorted by the presence of trees, some several metres tall, which occupy part of ET. Essentially the C-band phase difference information used to construct the DEM is a measure of the average height for all scatterers in each 5 m pixel. The signal is backscattered by the upper-most surface of the terrain objects including ground surface and tree canopy. As shown in the transect height profiles accompanying the 2D relief image in Figure 2-4, the height readings are locally distorted by trees that cause "spikes" in the topographic profiles. A three-pixel (30 m) averaging filter has been applied to suppress this effect.

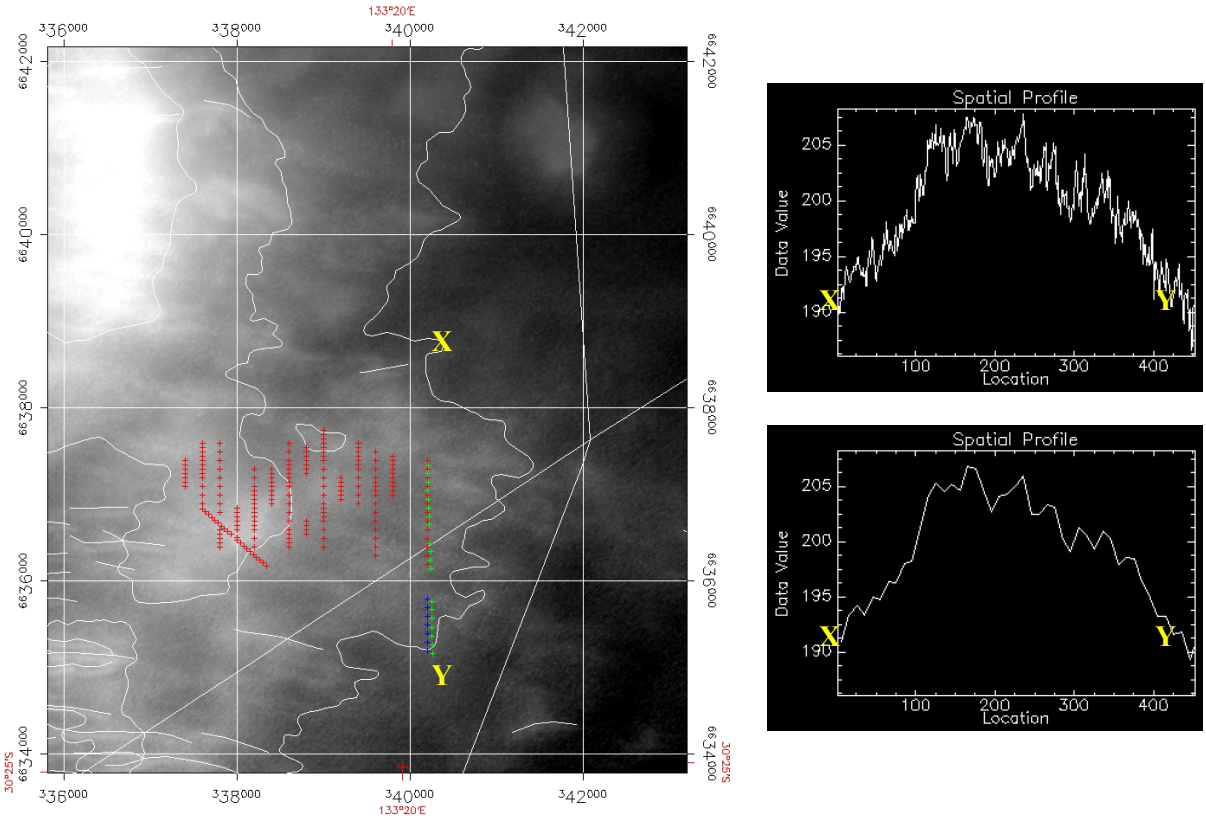

Figure 2-4 TOPSAR DEM of ET with the position of drill-holes, height contours and access tracks shown. Height profiles for transect X-Y along the Regolith Line indicate the precision of the data. A 30 m moving average filter has been applied to the top profiles to suppress the presence of trees along the transect.

The real value of the TOPSAR DEM is the information it provides when processed and enhanced to highlight terrain morphology of a landscape where low sand dunes provide the highest local relief. Subtle basement highs, commonly not perceptible from ground observations, can be highlighted by the high resolution of the data. For example, in Figure 2-5 (left), a 2D relief image where bright areas correspond to elevation highs, the position and extent of basement rocks at or near the surface are readily observed. In addition, the pattern and symmetry of the dune fields that occupy this section of the eastern Great Victoria Desert can be recognised. In the right-side image of Figure 2-5 a shaded relief model provides an illusion of relief in three dimensions and accentuates the arrangement of the dunes in relation to the changing relief and position of topographic highs. While many dunes have developed over basement highs including Cudyea Hill, the highest densities of dunes are positioned in topographic lows.

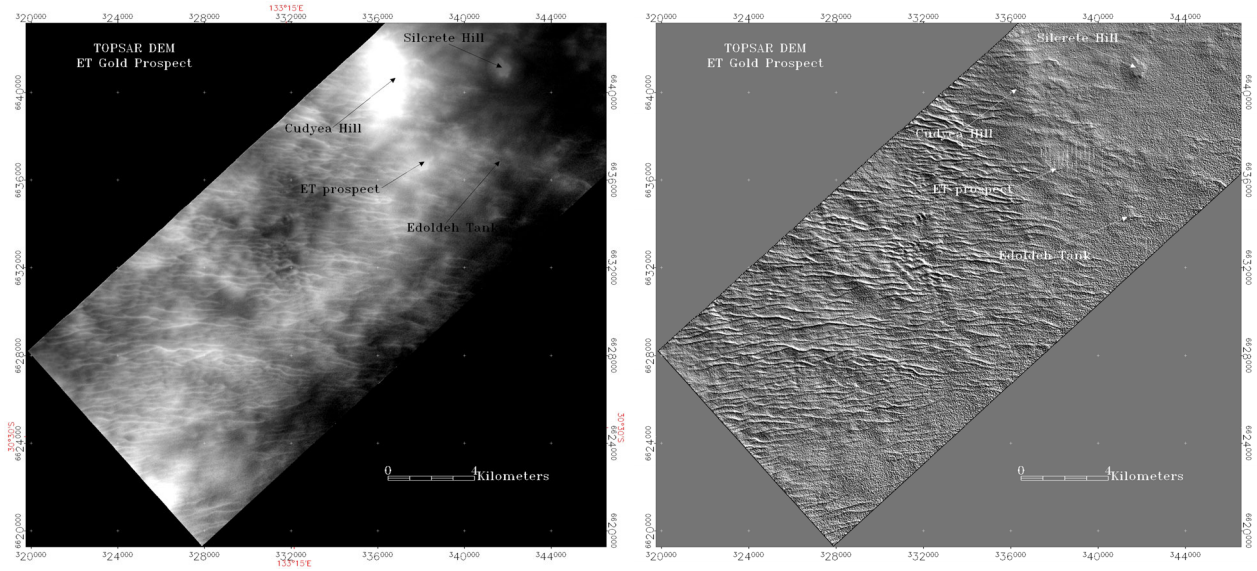

Figure 2-5 TOPSAR digital elevation data of ET region presented as a 2D relief model (Left) and shaded relief model with psuedo-illumination of 0° azimuth and 5° elevation (Right). Heights range from 119 to 250 m with a mean height of 153 m and standard deviation of 20 m.

A 3D perspective image in Figure 2-6 highlights, as dark greytones, the near-continuous position of a northwest-trending ridge that includes Cudyea Hill and ET. Isolated basement highs can also be observed within the dunefields.

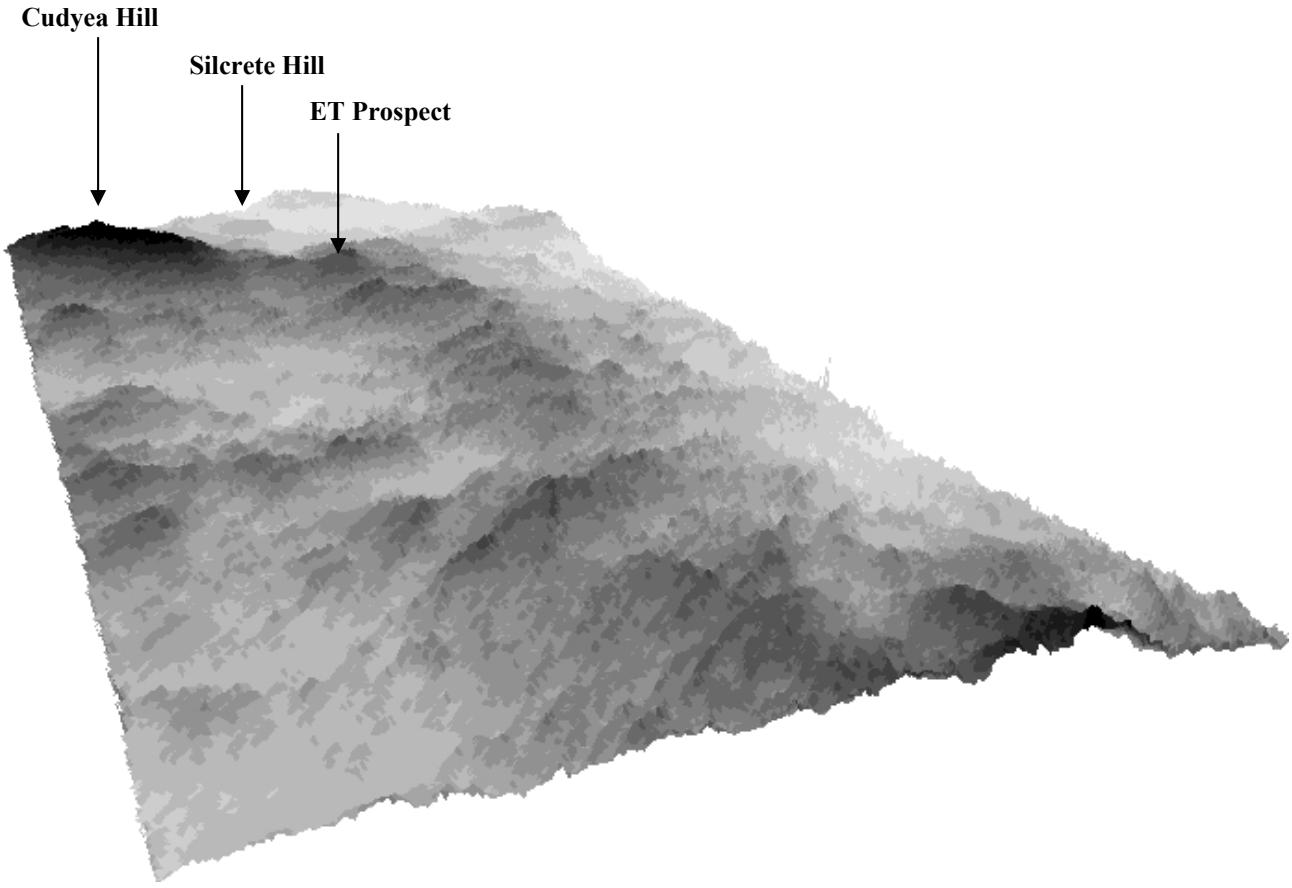

Figure 2-6 3-D perspective image of TOPSAR DEM viewed from the south with high features as dark tones

The importance of precise elevation data in low relief terrains is readily shown in the 3D perspective images in Figure 2-7 where a section of the TOPSAR DEM, centred on ET (1), has been rotated with north

direction now to the page bottom. The emphasis of both images is on exaggerating the topographic style of this relatively flat landscape. In the upper image, a 15x magnification of the height values depicts basement highs as prominent topographic highs. A height-coded 3-D perspective of the site in the lower image offers an insight into the morphology of the terrain prior to the formation of sand dunes approximately 200 000 years BP (Huntley *et al*., 1999). It is perhaps fortuitous that the triangulation process to create the 3-D model has been coarse enough to suppress the effect of the sand dunes. Although masked by a veneer of sand and vegetation, and a regular pattern of seif dunes, the position and extent of a topographically-high remnant landscape, comprising silicified Archaean gneiss, is clearly visible in these enhancements.

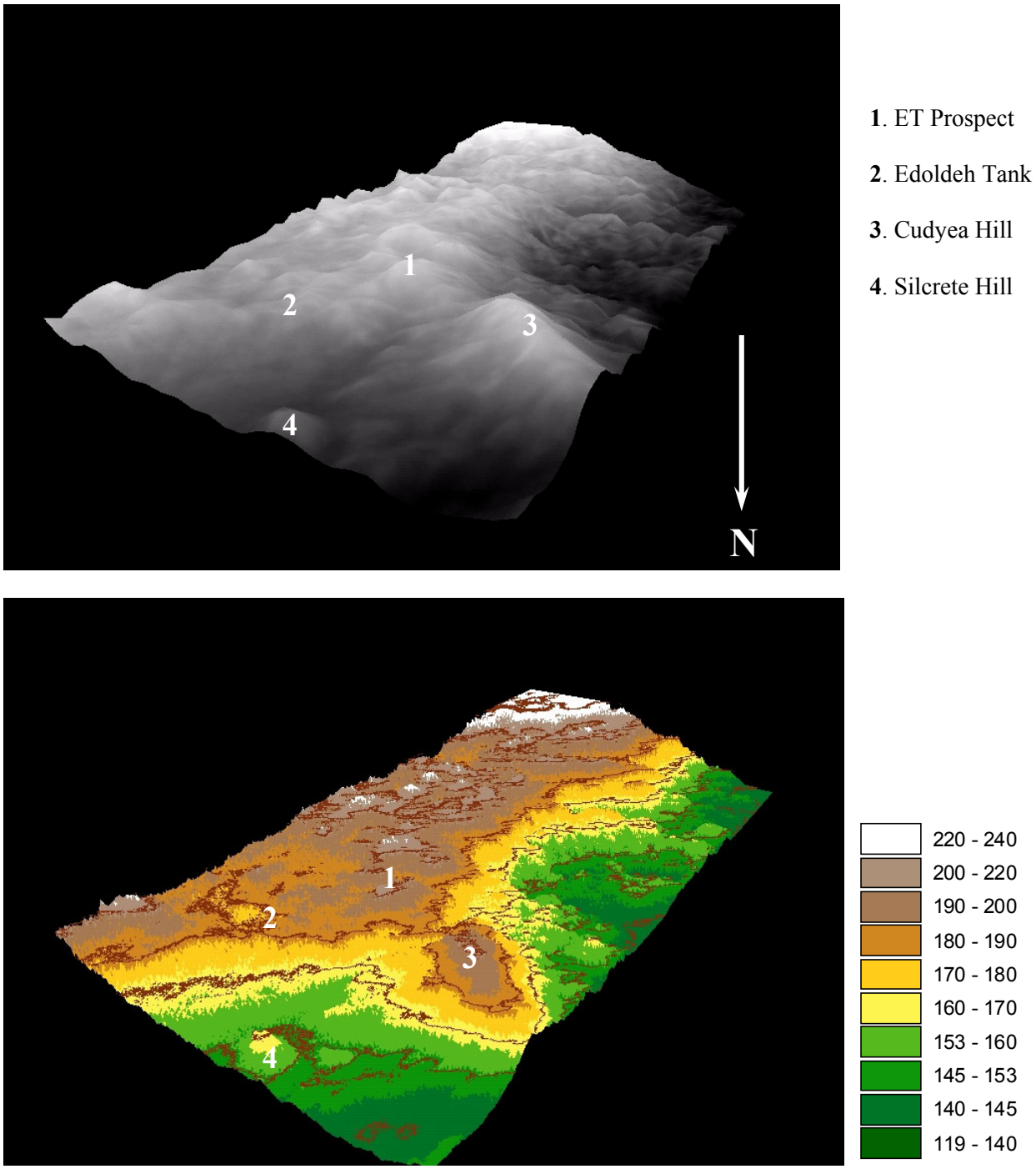

Figure 2-7 Three-dimensional perspective images generated from TOPSAR elevation data, highlighting the topographic style of the terrain in vicinity of ET Gold Prospect. The greytone scene in the TOP image shows topographic highs as bright features whereas the BOTTOM scene is a pseudo-colour perspective with height contours. See text for details.

Similarly, when overlain by the SPOT scene in Figure 2-1 and viewed in 3D, the landform characteristics of ET and its surrounds are presented in a realistic manner that assists their interpretation (Figure 2-8).

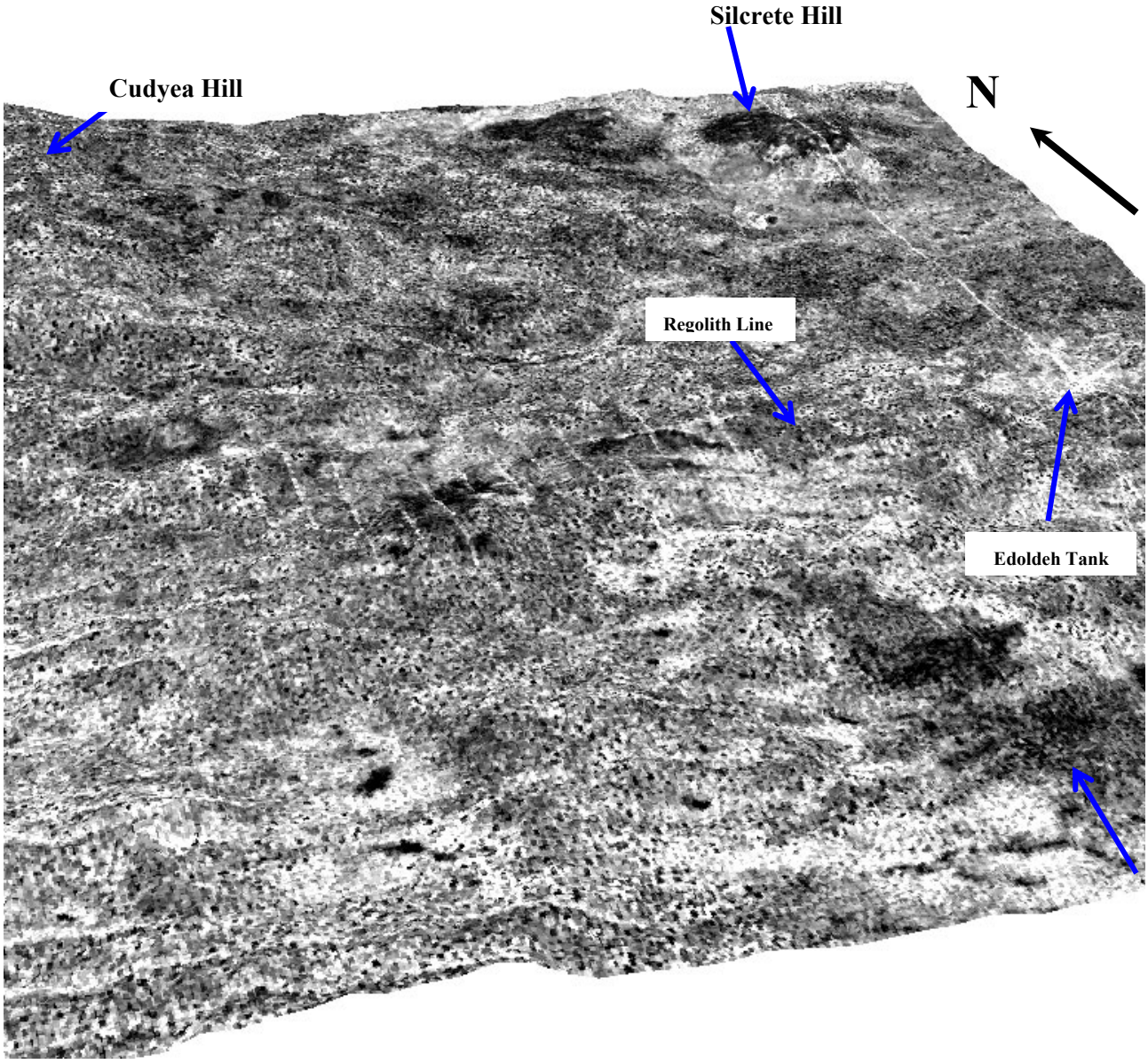

Figure 2-8 Three-dimensional perspective view, centred on ET, of the SPOT-PAN data in Figure 2-1 overlaid on the TOPSAR DEM. A 10x vertical exaggeration has emphasised topographic highs associated with basement rocks in an otherwise flat landscape dominated by sand sheets and occasional sand dunes.

2.2.3 Airborne gamma-ray spectrometry data

Unfortunately, the poor quality of the 3-channel radiometric data of ET limited its use for discriminating between *in situ* and transported materials and mapping the regolith of the region. The Maximum Noise Fraction (MNF) method was used as a noise reduction technique on the original data, however, as shown in the RGB image of K, Th and U (KTU) in Figure 2-9, minimal information can be resolved from the data. This differs from a study by Wilford *et al*., (1998) of RGB colour composites of K, Th and U emissions recorded over the Half Moon Lake region in South Australia where the data were most useful in developing a regolith and landform map. A greytone image in Figure 2-9 of Total Counts does allow the identification of an elongated NW-trending area with elevated surface radioelement concentrations in vicinity of ET. Its spatial relationship with a topographic ridge, as shown in 3D perspectives in Figure 2-10, points to separation of different regolith-landform units, specifically *in situ* weathered products, and down-slope mobilisation of these weathered products, from a background of deep aeolian soils. Bright targets such as that over ET (Location 2) reflect an increased response from exposures of abundant silcrete and calcrete gravels and minor saprolite over areas of shallow bedrock where erosion is most active.

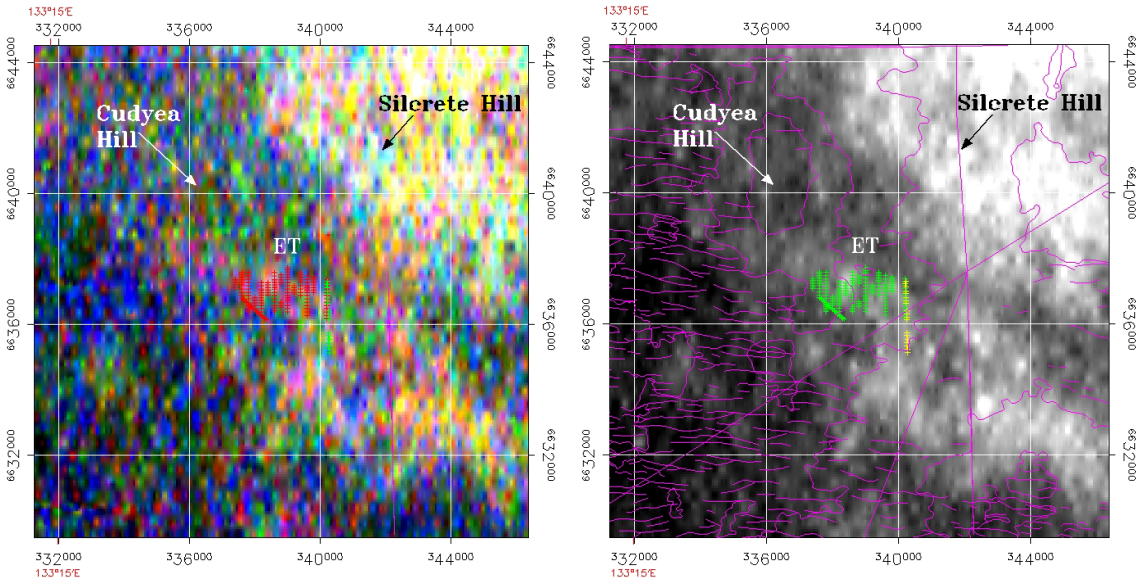

Figure 2-9 Enhancements of three-band gamma-ray spectrometric data of ET displayed as a composite image with K-red:Th-green: U–blue (Left) and Total Counts (Right). Drill holes are red crosses in left image and green crosses in right image. The relatively strong Th (green) response in the composite image and high counts in the Total Counts image in vicinity of Silcrete Hill is probably related to the deposition of wind-blown clays that have originated from the weathering of the exposed basement rocks.

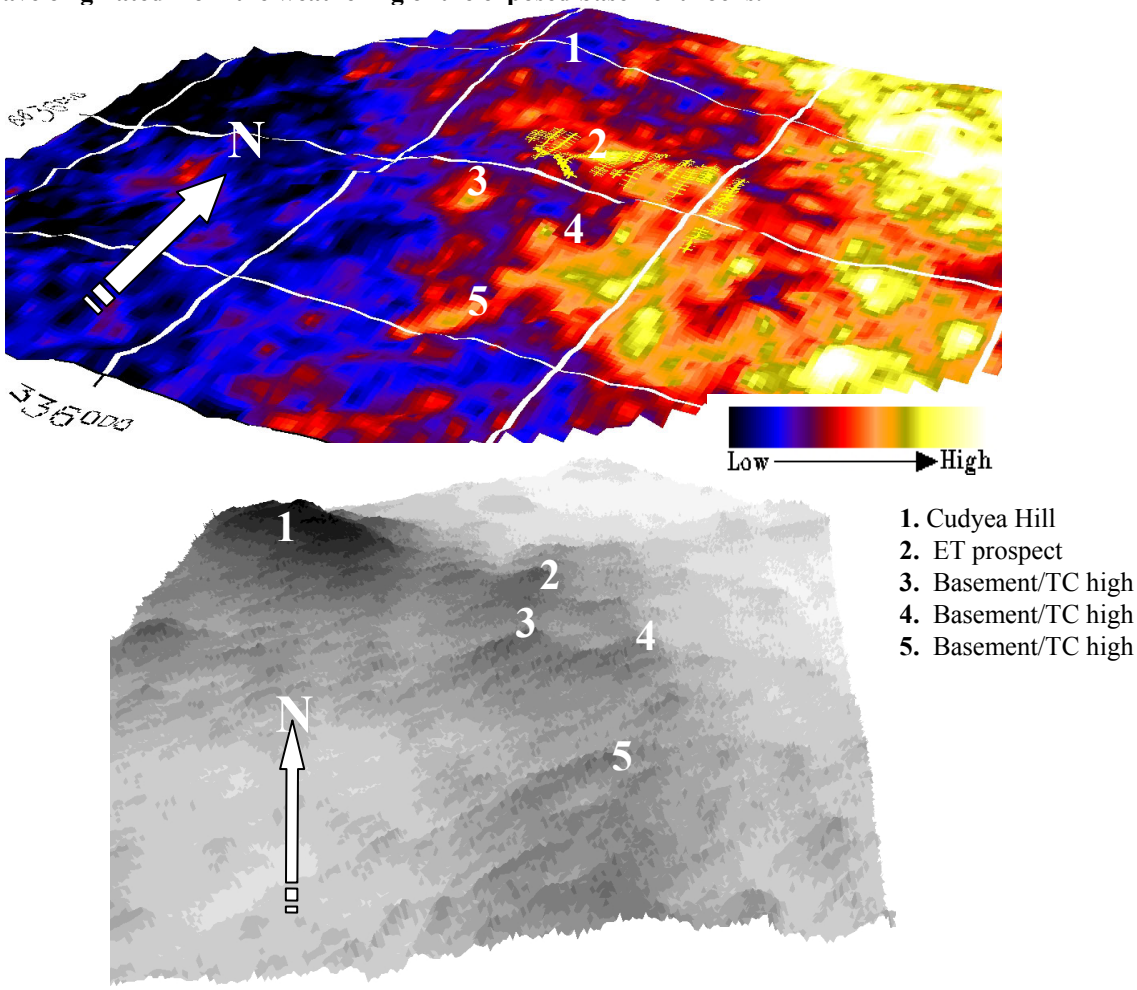

Figure 2-10 3D perspective view of a psuedo-coloured enhancement of the Total Counts data overlaid on a 20x exaggeration of the TOPSAR DEM(Top) and the between high total counts and the position of basement highs in the landscape (dark tones) in the 3D perspective of the TOPSAR DEM (Bottom). The locations of Cudyea Hill, ET and rises with high Total Counts are shown.

2.2.4 Landsat TM

2.2.4.1 Data description

A cloud-free scene of Landsat Thematic Mapper data covering ET was recorded on 12th November 1999. Analysis of the data indicated that ground conditions were dry with green biomass limited to local areas within the dunefields. Owing to the subdued topography of the study area, data masking from hill shading was negligible.

Spectral characteristics of common surface features including vegetation, bedrock and regolith materials that can be resolved in the visible and near infrared part of the electromagnetic spectrum when using Landsat ETM data are shown in Figure 2-11 and Table 2-1. TM bands 1 to 4 are primarily related to the spectral response of vegetation and Fe minerals including hematite and goethite. TM1 (0.45–0.52 μm) and TM3 (0.63–0 69 μm) correspond to the position of absorption bands of chlorophyll pigments and TM2 (0.52–0.60 μm) lies in the "green peak" caused by reflection by chlorophyll. TM4 (0.76–0.90 μm) senses part of the spectrum in which reflectance is dominated by the photosynthetic activity of leaves. The positions of TM1 to 4 also coincide with several diagnostic Fe oxide features including the charge-transfer absorption feature in TM1, a reflectance ramp in TM2, a crystal-field absorption feature in TM3, and a strong crystal-field absorption feature in TM4. Because green biomass produces a reflection peak in TM4, the responses from green vegetation and Fe oxide can be uncoupled by either least squares analysis or band ratio techniques. TM5, centred at 1.65 μm, is located where most soils and rocks have their maximum reflectance. TM7, centred at 2.22 μm, covers the absorption region of Al-OH- and Mg-OH-bearing minerals. These minerals include chlorite, clay, mica, and the amphibole and carbonate groups. However, research by Cudahy (1992) and Cudahy *et al.* (1992) have shown that carbonate-rich materials are mostly very difficult to detect spectrally in Australia's weathered landscapes owing to the dominating presence of kaolinite.

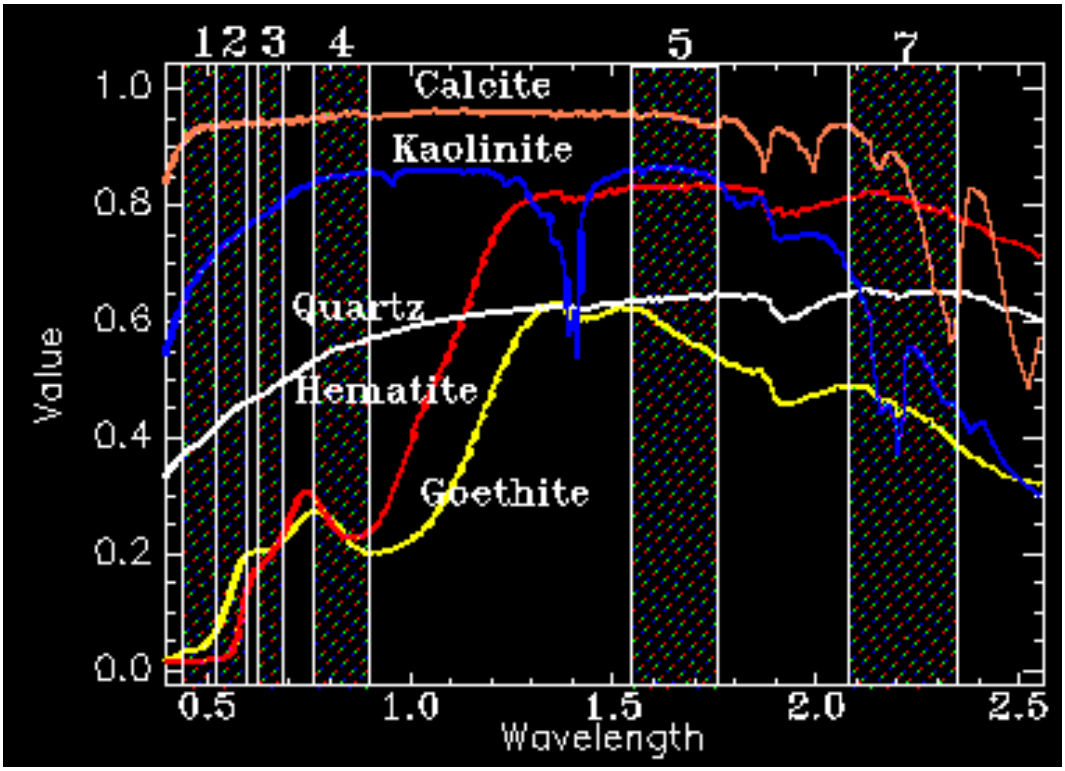

Figure 2-11 Position of Landsat TM bands 1-5 and 7, and their relationship to the reflectance spectra of the common minerals occurring at ET.

Table 2-1 General spectral features and specific regolith spectral responses associated with Landsat TM bands

TM bands	General spectral features*	Regolith spectral responses
Band 1	Ferric and ferrous charge transfer Fe absorption.	Fe and Si duricrusts, ferruginous saprolite low. Hematitic Fe very low. Kaolinite high.
Band 2	Ferric Fe absorption and ferrous Fe reflection. Chlorophyll reflection peak	Fe and Si duricrusts, ferruginous saprolite low. Kaolinite high.
Band 3	Short-wavelength shoulder of ferric Fe reflection. Ferrous Fe absorption. Chlorophyll absorption	Moderate reflection for goethitic and hematitic Fe. Kaolinite high.
Band 4	Short-wavelength shoulder of ferric Fe and ferrous Fe absorption. Vegetation reflection peak.	Moderate reflection for goethitic and hematitic Fe. Kaolinite high.
Band 5	Highest reflection for most rock types. Vegetation absorption.	Highly reflective for haematitic Fe duricrusts and ferruginous saprolite and clays
Band 7	Absorption band for Al-OH, Mg-O-H and $C0_3$ (clays, micas, carbonates, sulphates. Vegetation water absorption. Dry grass has high reflectance.	Absorption associated with hydroxyl bearing minerals and carbonates (Bleached or pallid zone, secondary carbonate-calcrete and travertine). Highly reflective for hematitic Fe duricrusts and ferruginous saprolite.

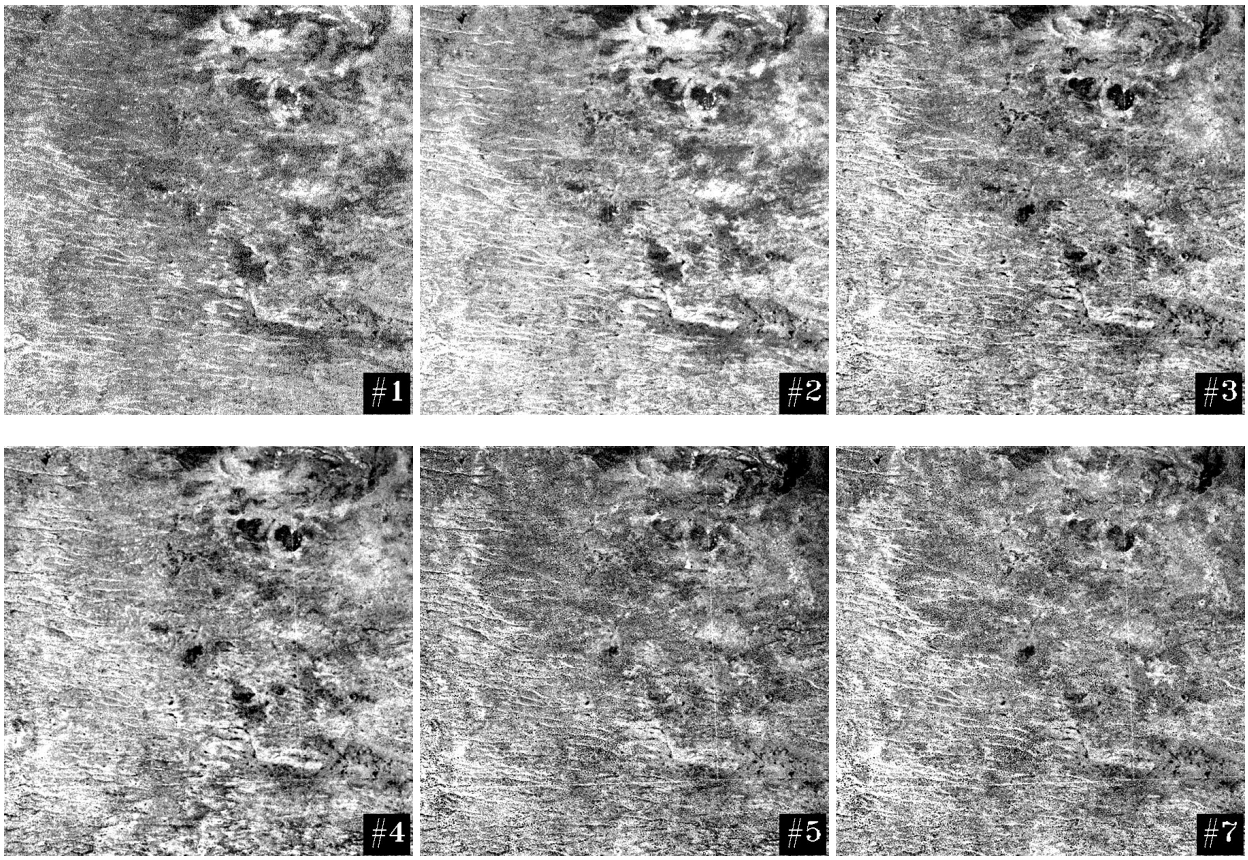

Figure 2-12 Greytone images of Landsat TM bands 1-5 and 7 of the ET region. The similarity in the six images is a result of the pervasive nature of aeolian sand and minimal rock outcrop resulting in a strong correlation between the TM bands. Maximum spectral contrast exists between locales of silcrete (low albedo) and sand plains (high albedo) where gravels and outcrop are absent. Areas of calcareous soils tend to have the highest albedo in all bands.

The rationale for the use of Landsat TM data is that the radiance measured by the sensor is a measure of the integration of soil, rock and vegetation characteristics. A processed Landsat TM image should, therefore, display a high degree of correspondence to a regolith-landform map and show that spectrally homogeneous units can be equated with terrain units and therefore named and described.

A sequence of three processing steps using simple physical models has been developed by CSIRO Mathematics and Information Sciences to convert the Landsat TM radiance-at-sensor data to that approaching ground surface reflectance. These are:

- application of LUT (Look Up Table) linear transforms (from file header information) to create TOA (Top Of Atmosphere) radiance in energy units;
- application of a solar distance and angle correction to adjust for incoming solar radiation so that "reflectance" can be calculated; and
- application of a BRDF (Bi-directional Reflectance Distribution Function) model to "remove" the effects of spatial scene brightness.

There are some assumptions at each stage; for example, the solar angle correction has no input for changing atmospheric effects of absorption or scattering. However, the "BDRF" image can be considered as a close approximation of ground reflectance and is appropriate for enhancement and feature interpretation. A composite image of bands 2:4:7 displayed as RGB, respectively, is shown in Figure 2-13.

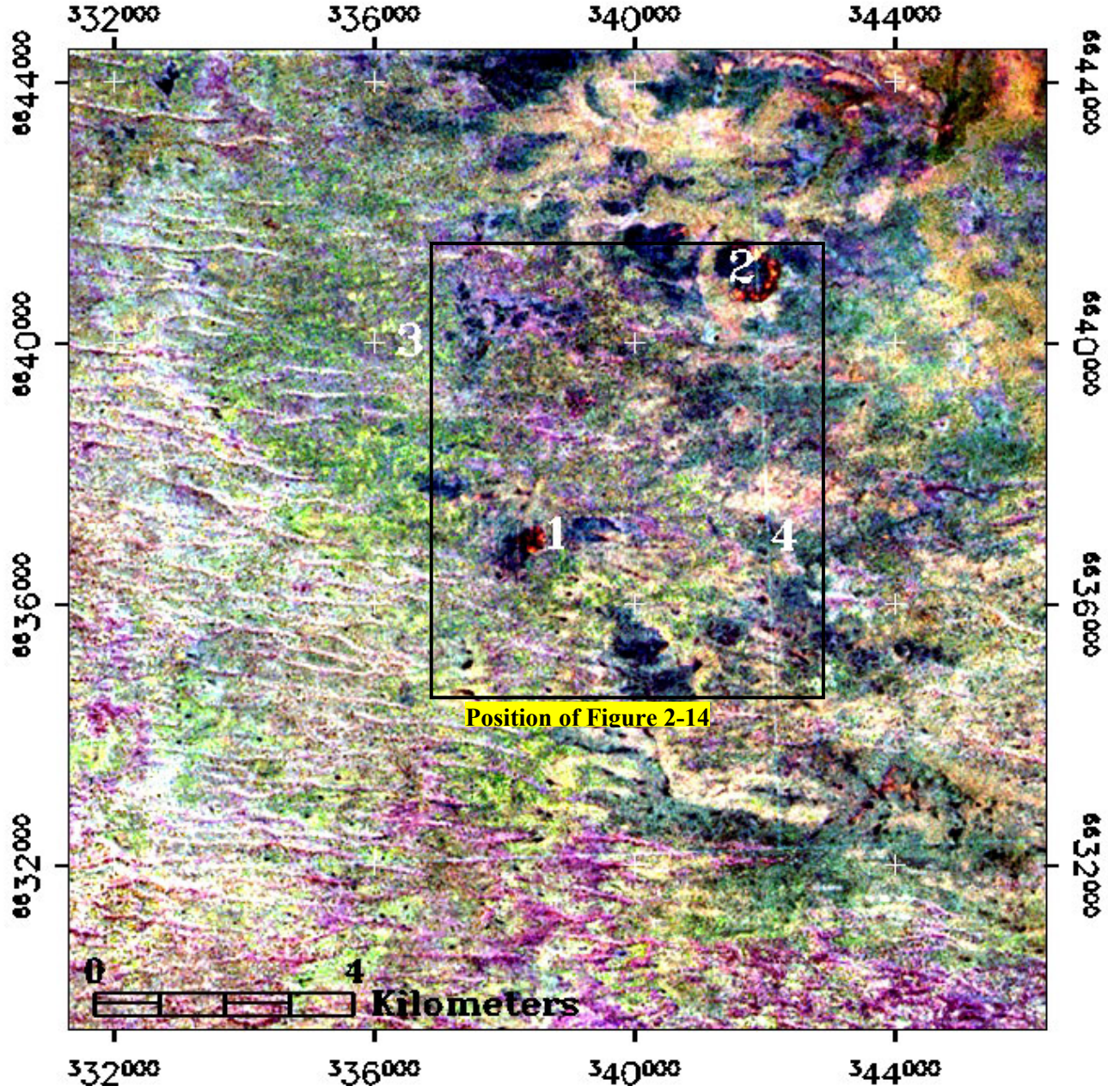

Figure 2-13 Landsat TM bands 2:4:7 colour composite image of a 15x15 km area centred on ET (1). Other features include Silcrete Hill (2), Cudyea Hill (3) and Edoldeh Tank (4).

Clay-rich terrain units in vicinity of ET and Silcrete Hill have red-orange hues, units with minor amounts of silcrete and Fe-rich lags have magenta hues, and units with abundant silcrete lag, often co-occurring with massive silcrete, are dark blue to black. Their identities have been established from advanced processing of the data and confirmed by field checking. Highly calcareous soils containing calcrete lags and granules appear as light yellow to white hues in response to an overall increase in albedo. Sand dunes are apparent from their linear shape, principally in the western-southwestern sectors where sand cover is deepest. In the vicinity of topographic highs, as depicted in images of elevation datasets in Figure 2-5 and Figure 2-6, and where gravel lags occur and outcrop is present at or near the surface, sandplains predominate. Areas of prolific green biomass within the dune fields have light green hues.

The locations of field sites 1-8 over ET are shown on an enlargement of the TM scene in Figure 2-14. Information collected at these sites included observations on the site characteristics, and recordings of visible-near infrared reflectance spectra of surface materials using the IRIS spectroradiometer. Descriptions of these field sites are included in Figure 2-15.

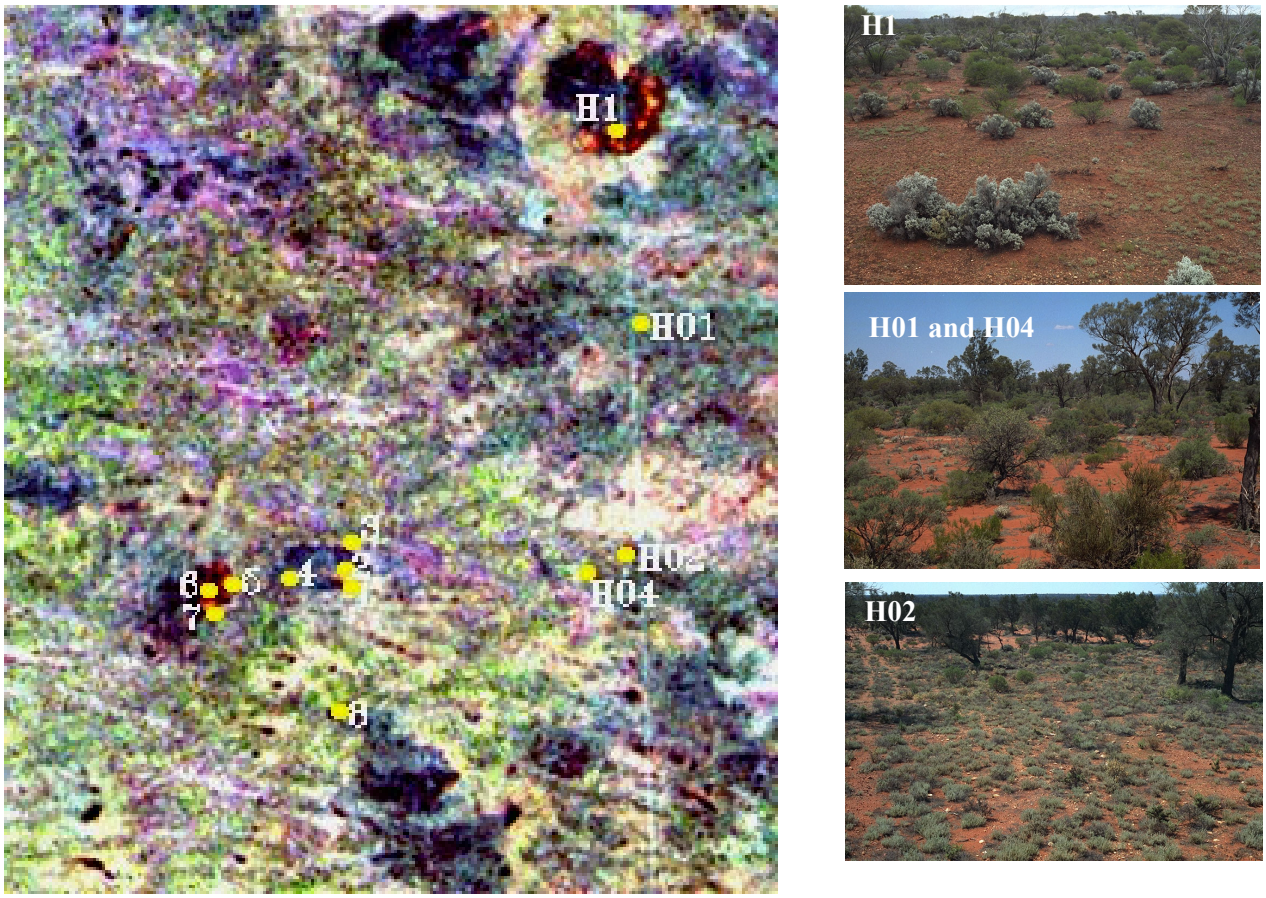

Figure 2-14 An enlarged 6x7 km section of the Landsat TM image in Figure 2-12 showing the location of field sites described in the text, and field photographs of the principal regolith-landform units for the region at Sites H1, H01, H02 and H04. Photographs of numbered sites 1-8 are shown in Figure 2-15.

Silcrete Hill (H1): Erosional landform - low hill of highly-weathered, silicified basement rock with locally developed soils. Medium- to coarse-grained gravels of silcrete with occasional cobbles, overlying fine- to medium-textured soils, partially lichen-covered, with an overstorey of bluebush (*Maireana sedifolia*) and *Eremophila* spp. shrubs.

Aeolian sandplain (H01 and H04): Flat to very gently sloping with low micro-relief-medium-textured, an absence of gravels, sandy-clay soil with cover of low *Acacia* spp. shrubs and minor grasses.

Edoldeh Tank (H02): Erosional surface – low hill of sub-cropping silcrete with a veneer of undifferentiated sand. Moderate cover of fine- to medium-grained gravels of silcrete fragments, rare cobbles with occasional patches of fine- to coarse-grained gravels of calcrete.

Site 1: Low rise – abundant lag of medium-coarse silcrete and quartz gravels, minor fine-grained Fe-silcrete over lichen-covered soil.

Site 2: Occasional massive calcrete, abundant calcrete fragments with some Fe silcrete gravels over yellowish calcareous soil.

Site 3: Dune sand, slightly calcareous, flank of low rise, minor development of lichen on soil– no gravels.

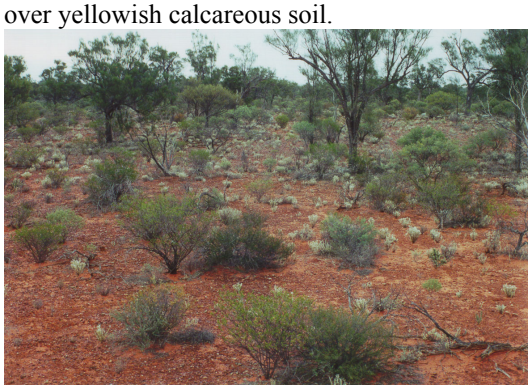

Site 4: Flank of low rise with abundant medium-coarse lag of silcrete gravels with minor fine-grained gravels of quartz over shallow soil – calcrete at <1 m.

Site 5: Flank of prominent hill capped by massive silcrete. Lichen-covered soil with abundant medium-coarse grained gravels of silcrete and lenses of fine-grained calcrete.

Site 6: Erosional rise capped with massive outcrop and lag of Fe-silcrete boulders, cobbles and gravels with minor quartz gravels.

Site 7: Escarpment, abundant gravels and minor cobbles of saprolite, some with calcareous coating, vein quartz, minor cobbles and fine gravels of silcrete, minor Fe- silcrete.

Site 8: Lichen-covered soil with abundant lag of coarse- medium grained gravels of silcrete and calcrete.

Figure 2-15 Field sites of regolith-landform units in vicinity of ET Gold Prospect. The location of each site is shown in Figure 2-14

2.2.4.2 Image processing methods for mapping regolith-landform units using Landsat TM data

Introduction

The following discussion briefly outlines and demonstrates three techniques for selectively highlighting nominated regolith and landform units within the Landsat TM dataset of ET. Each examines the contribution of the 6 original bands of TM data. The first technique, *Band Ratios*, employs prior knowledge of the spectral characteristics of the primary minerals present in the landscape. The second, *Supervised Classification*, employs 6-band end-member spectra of selected regolith units to classify an image. The third, *Canonical Variate Analysis*, assumes some knowledge of the existence of regolith-landform units to discriminate between units and classify them.

Band ratios

The use of band ratios is a simple and useful image processing method to emphasise spectral differences between chosen bands. If the bands used correspond to the positions of reflectance peaks, absorption troughs and changes in the curve of the slope, then ratioing will maximise the spectral and absorption contrasts thereby enhancing subtle variations between materials that otherwise may not be apparent in a three-band composite image. Based on spectral knowledge of the commonly occurring minerals at ET (as displayed in Figure 2-11), Landsat TM ratios 3/1, 5/4 and 5/7 were examined (Figure 2-16). This combination is most effective for highlighting the occurrence and relative surficial concentrations of the Fe oxide minerals (Fe-stained silcrete gravels), quartz (silcrete) and clay minerals (kaolinite) respectively, within the lags and rock outcrops that are infrequent in the ET landscape. Initial calibration of the data to surface reflectance or psuedo-reflectance is highly desirable for optimal feature separation if concurrent spectral measurements of ground targets with the acquisition of the Landsat TM data are not available.

TM Ratio 3/1 is commonly used to map the distribution of Fe oxides in arid and semi-arid environments because, as the reflectance plots in Figure 2-16 show, they generally have a high reflectance level in TM3 (particularly goethite) and a strong absorption level in TM1. Neither band coincides with the diagnostic absorption features of clay minerals, and green biomass has a primary chlorophyll absorption feature in TM3 and a secondary one in TM1. Thus, areas of relatively high Fe content should appear as bright areas on a greytone image. Conversely, regions that are either low in Fe, rich in clay or have a green vegetative overstorey should manifest themselves on the image by dark and dark to medium tones respectively.

Examination of Figure 2-16 suggests that areas of highest Fe concentration occur in the western sector where aeolian sand is deepest and sand dunes predominate. The most obvious features in this ratio image are the Fe-poor regions of silica-rich gravels at ET and Silcrete Hill. Although dominated by a heavy lag of silcrete gravels and cobbles, some of which are Fe-rich, they have relatively lower 3/1 ratio values than the sand plains.

The primary information revealed by examination of the ratio 5/4 enhancement in Figure 2-16 is the location and distribution of gravel and cobble lags of silcrete as high albedo features. Areas rich in massive silcrete with an abundant lag of boulders, cobbles and gravels of silcrete have the brightest tones (Figure 2-15, Site 6) whereas those sites with a lag of minor gravels of silcrete and calcrete such as Site 8 (Figure 2-15), have medium tones. Their relative distribution is best observed in the composite ratio image where silcrete-rich sites are bright green and less extensive lags are dark green. TM5 is centred on 1650 nm where most minerals have similar high reflectance values, while TM4 provides a measure of Fe-oxide (low reflectance) and vegetation (high reflectance). Terrain units characterised by silcrete lags units have relatively lower TM4 values resulting from the presence of ferruginous materials, and will have darker tones on the same image.

Ratio 5/7 is used to enhance areas rich in clays and other hydroxyl (-OH)- bearing minerals such as mica. Clay minerals have a strong absorption band(s) in TM7 around 2200 nm and high reflectance values around 1650 nm in TM5. Clay-rich areas will manifest themselves as bright tones (high TM5, low TM7) and clay-poor areas as dark tones (high TM5, high TM7). However, the 5/7 ratio can also ambiguously enhance areas of intense green biomass owing to the abundance of molecular water causing a low reflectance value in TM7 relative to the TM5 value. Thus, areas rich in clay and green vegetation may be "doubly enhanced" by the ratio.

Examination of the 5/7 ratio image and composite ratio image in Figure 2-16 shows the distribution of the clay-rich areas in the brightest tones. In particular, exposed saprolite within the pediment slopes of an erosional rise at ET, and kaolinisation within the flanks of deeply weathered basement at Silcrete Hill are well discriminated. A threshold of the 5/7 ratio response has been applied to the values in the composite ratio image to suppress the effects of local green biomass.

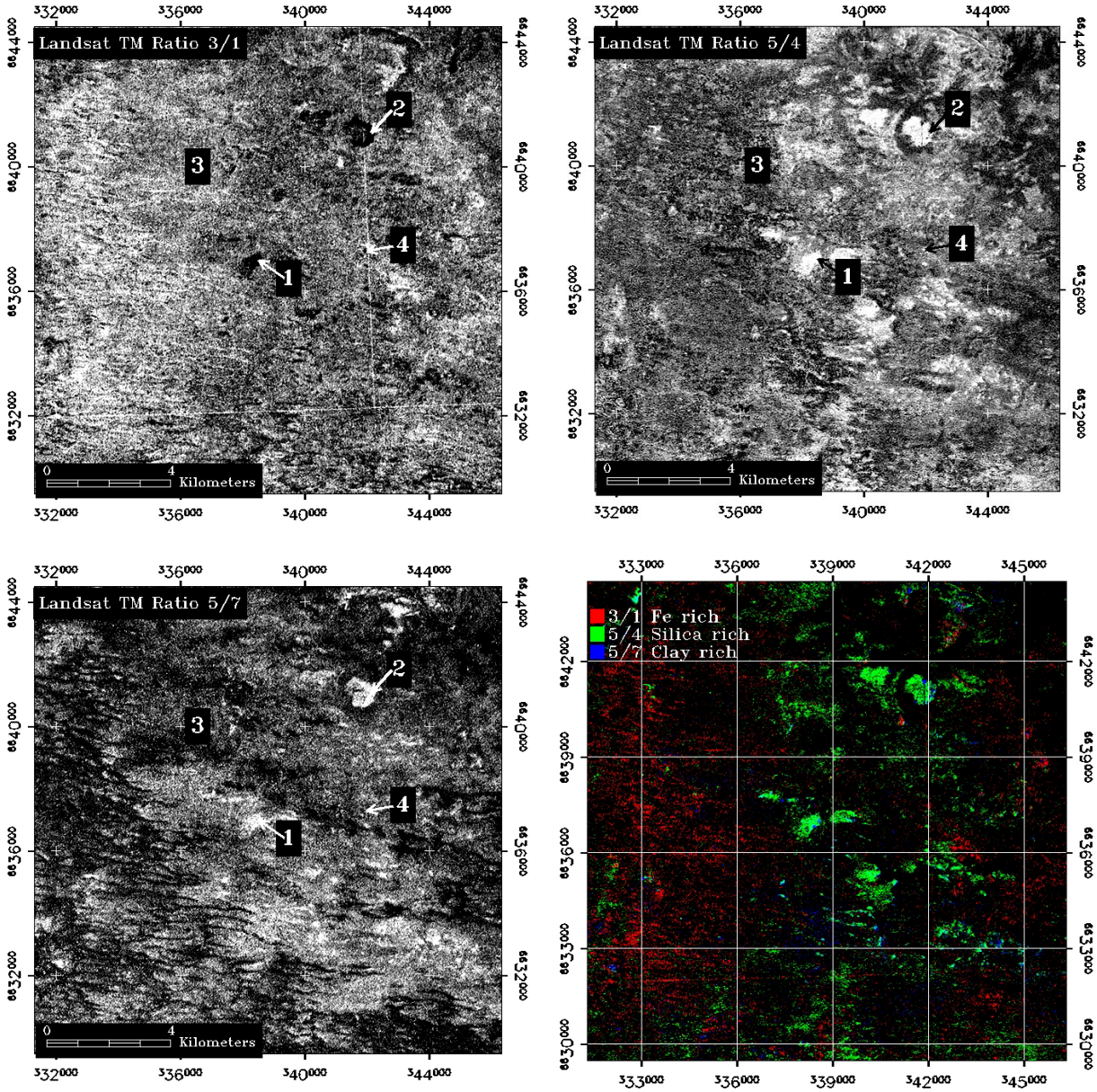

Figure 2-16 Band ratio images of calibrated Landsat TM data provide information on the distribution of various landcover types and the mineralogy of surface regolith materials. Ratio 3/1 highlights occurrences of massive silcrete and abundant silcrete lag at ET (1), Silcrete Hill (2) and Edoldeh Tank (3) as dark tones; Ratio 5/4 shows locations of massive and gravel silcrete in bright tones; and Ratio 5/7, clay-rich locations in bright tones. An abundance of molecular water in regions of high green biomass results in intermediate tones in Ratio 5/7. The composite ratio image shows the distribution of endmember mineral groups derived from ratios 5/7 (clay, Red), 5/4 (silcrete, Green) and 3/1 (Fe, Blue).

Supervised classification

Following the modelling of the TM data to reflectance, a supervised classification has highlighted three regolith classes based on the relatively coarse spectral definition provided by the TM sensor (Figure 2-17). The Spectral Angle Mapper (SAM) technique is a method of determining the spectral similarity of selected end-member spectra, to spectra in the scene (Kruse *et al*., 1993). It essentially uses the *n*-dimensional Spectral Angle Mapper to match image spectra to reference spectra that in this study are the average

spectra of surface materials from selected landforms. The algorithm determines the spectral similarity between two spectra by calculating the angle between them, treating them as vectors in space with dimensionality equal to the number of bands (6). Smaller angles represent closer matches to the reference spectrum. Areas that satisfy the criterion are carried over from the *rule image*, where classification results are shown before final assignment of classes, to the *classified image*. Pixels further away than the specified threshold are not classified. Although SAM does no spectral unmixing, it is a simple and rapid classification tool.

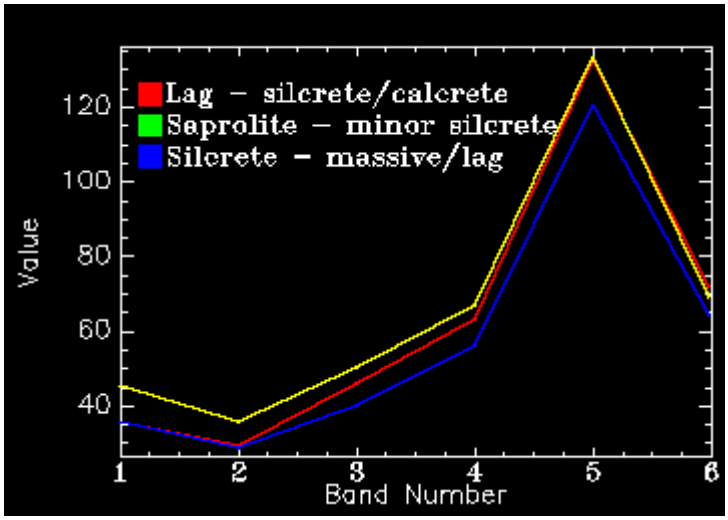

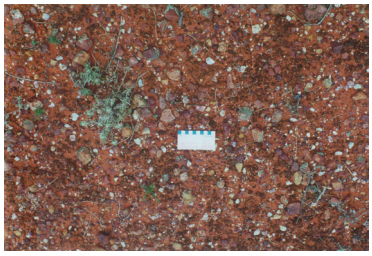

	Lags- silcrete and calcrete		Saprolite – minor silcrete		Silcrete – massive and lag	
Band	**Min**	**Max**	**Min**	**Max**	**Min**	**Max**
1	34	41	42	51	33	40
2	28	32	33	40	27	31
3	42	51	45	55	37	45
4	59	68	63	73	53	60
5	124	142	127	143	113	130
7	67	79	66	71	59	69

Figure 2-17 6-band Landsat TM reflectance spectra and values for regolith materials classified using the Spectral Angle Mapper classification technique.

Three examples of this process (Figure 2-18, Figure 2-19 and Figure 2-20) isolate and map the distribution of three principal regolith-landform units where the surface materials may be significant for geochemical sampling (Lintern *et al.*, 2000). They include, respectively: lag of silcrete and calcrete gravels (Figure 2-15, Sites 1 and 2); saprolite with minor silcrete and calcrete gravels (Figure 2-15, Site 7); and massive silcrete with abundant lag of cobbles and gravels of silcrete (Figure 2-15, Site 6). Six-band Landsat TM spectral reflectance signatures and values of these units, as presented in Figure 2-17, illustrate minimum spectral variability between these materials. Predictably, the saprolite has the highest albedo in bands 1-5 and deepest absorption in band 7, relative to band 5, due to the increased clay content. This contrasts with the overall reduction in reflectance from the silcrete units owing to the increased presence of Fe oxides. In the presence of calcrete, band 5 reflectance is increased. Classification techniques such as Spectral Angle Mapper are designed to maximise these 6-dimensional variations between cover types and develop unique classes for mapping their distribution.

The grey-scale rule image of silcrete lags and gravels units is presented in Figure 2-21 together with the classification image where the cover class is superimposed on a composite image of TM bands 247. A

high value (bright) in the rule image means that the spectra of these pixels are similar to the reference spectrum sampled from Sites 1 and 2 and shown in Figure 2-15. These are mapped as red pixels in the classification image. Because of the inherent presence of shrub vegetation over units and the spectral similarity between units, misclassification has occurred with vegetation of similar structure to that covering the lag gravels. These have been suppressed by the use of a 3 x 3 low-pass filter. Although not all areas have been field checked, the residual concentrations of red pixels most likely represent the spatial occurrences of lag units.

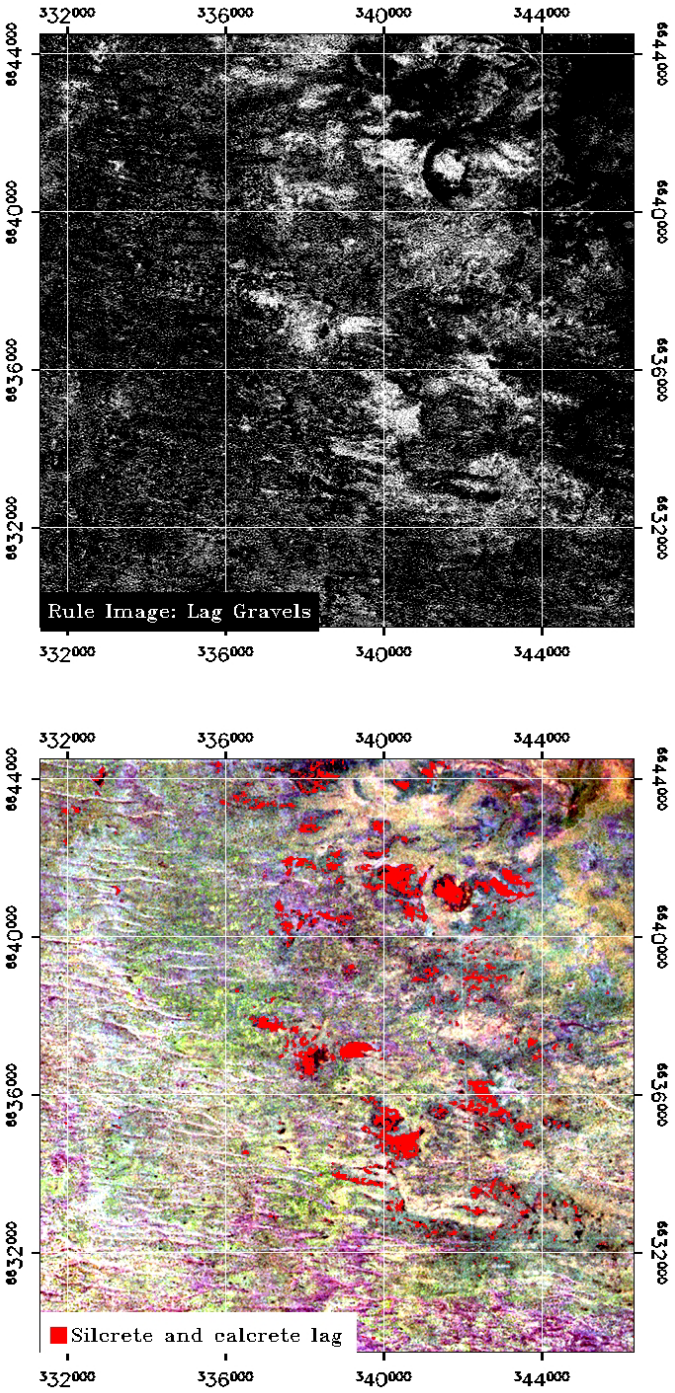

Figure 2-18 Classification of silcrete-rich lags using the Spectral Angle Mapping technique. These gravels occur principally within mapped units ISer1 and CHer1. The rule image (TOP) shows the classification result before assignment of the class to the SAM classification image shown in the BOTTOM image as an overlay on the Landsat TM 247 image. In the rule image, areas with more similar spectra to the reference spectrum for units ISer1 and CHer1 appear as bright regions. These are carried over into the Classification Image as a red hue.

Similarly, the classification of regolith-landform units characterised by saprolite and minor gravels, and massive silcrete (green and blue spectra, respectively, in Figure 2-17) required filtering to suppress spuriously classified pixels. However, misclassifications for these two units were minimal owing to the extraction of very specific reference spectra for each from sites of known homogeneous cover. Rule images and classification image maps are displayed in Figure 2-19 and Figure 2-20 for these two units.

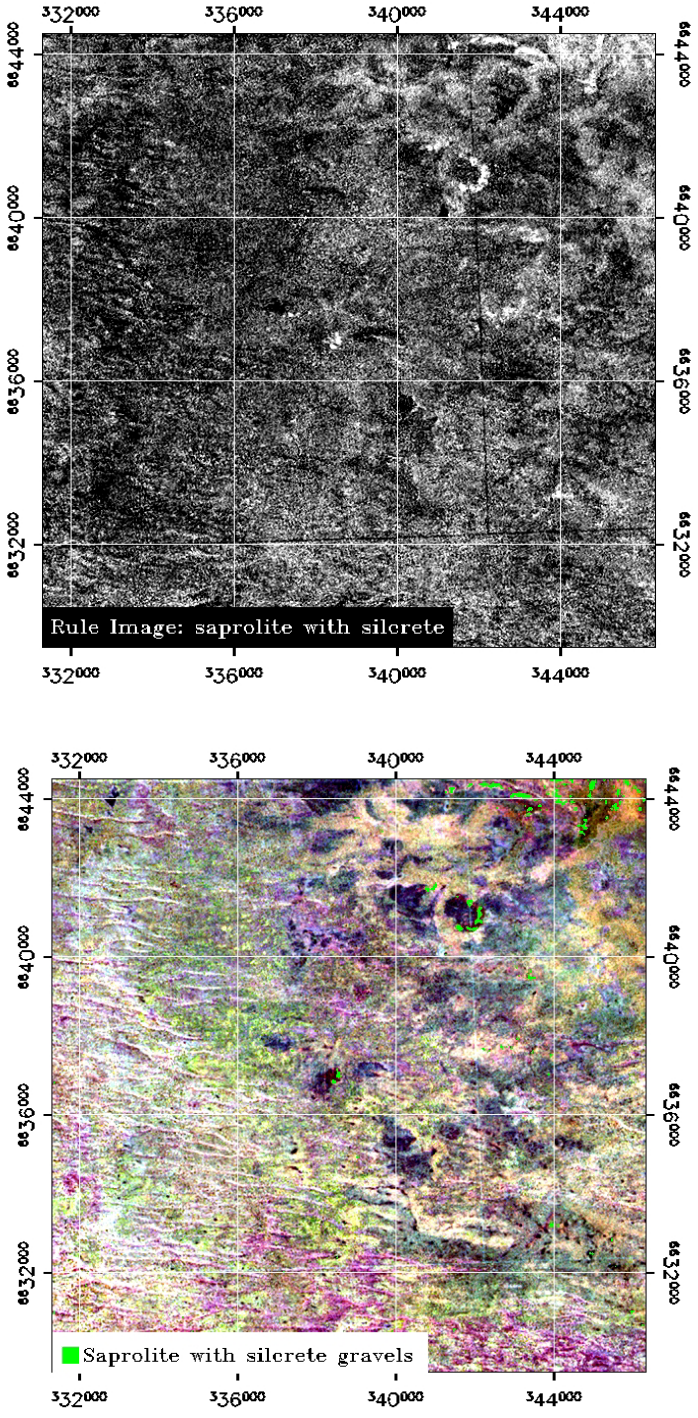

Figure 2-19 Classification of clay-rich saprolite in vicinity of silcrete-capped breakaways using the Spectral Angle Mapping technique. Saprolite occurs within the mapped unit RLer. The rule image (TOP) shows the classification result before assignment of the class to the SAM classification image shown in the BOTTOM image as an overlay on the Landsat TM 247 image. In the rule image, areas with more similar spectra to the reference spectrum for unit RLer appear as bright regions. These are carried over into the Classification Image as a green hue.

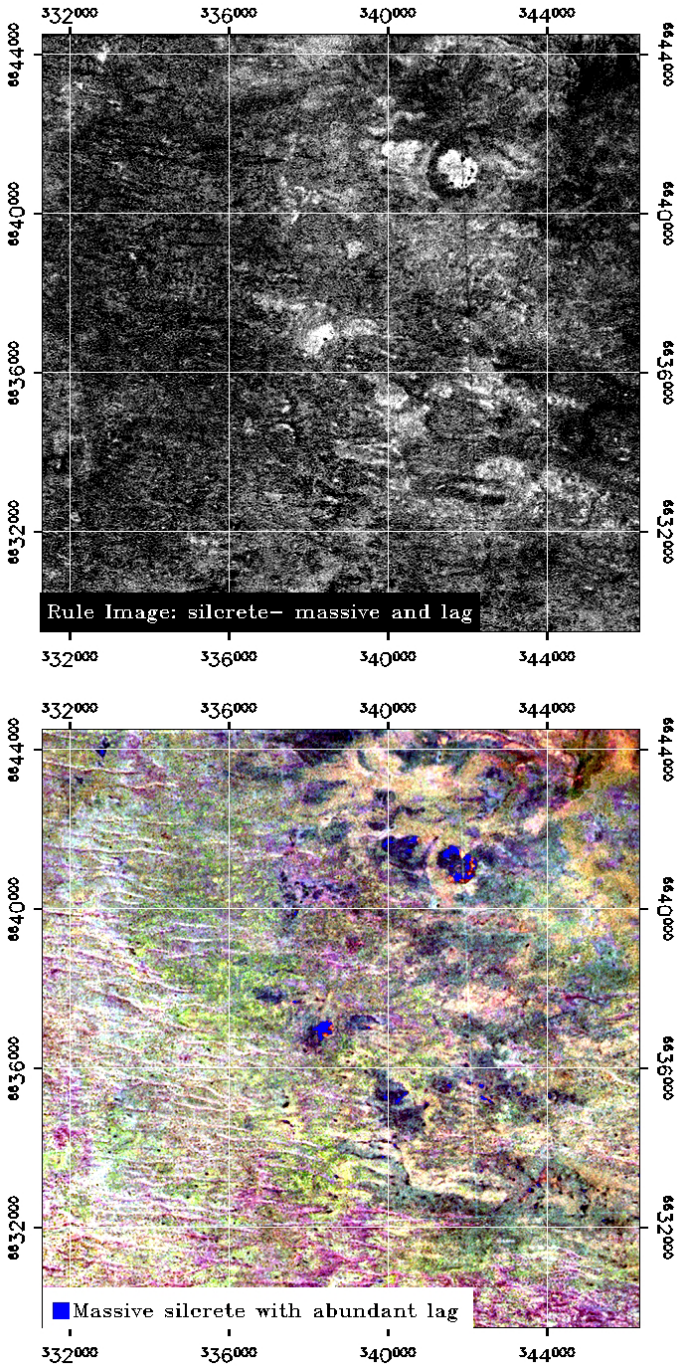

Figure 2-20 Classification of massive silcrete unit RLer using the Spectral Angle Mapping technique. The rule image (TOP) shows the classification result before assignment of the class to the SAM classification image shown in the BOTTOM image as an overlay on the Landsat TM 247 image. In the rule image, areas with more similar spectra to the reference spectrum appear as bright regions. These are carried over into the Classification Image as a blue hue.

The combined results of the SAM process are displayed in Figure 2-21, and in Figure 2-22 as an overlay to the TOPSAR DEM.

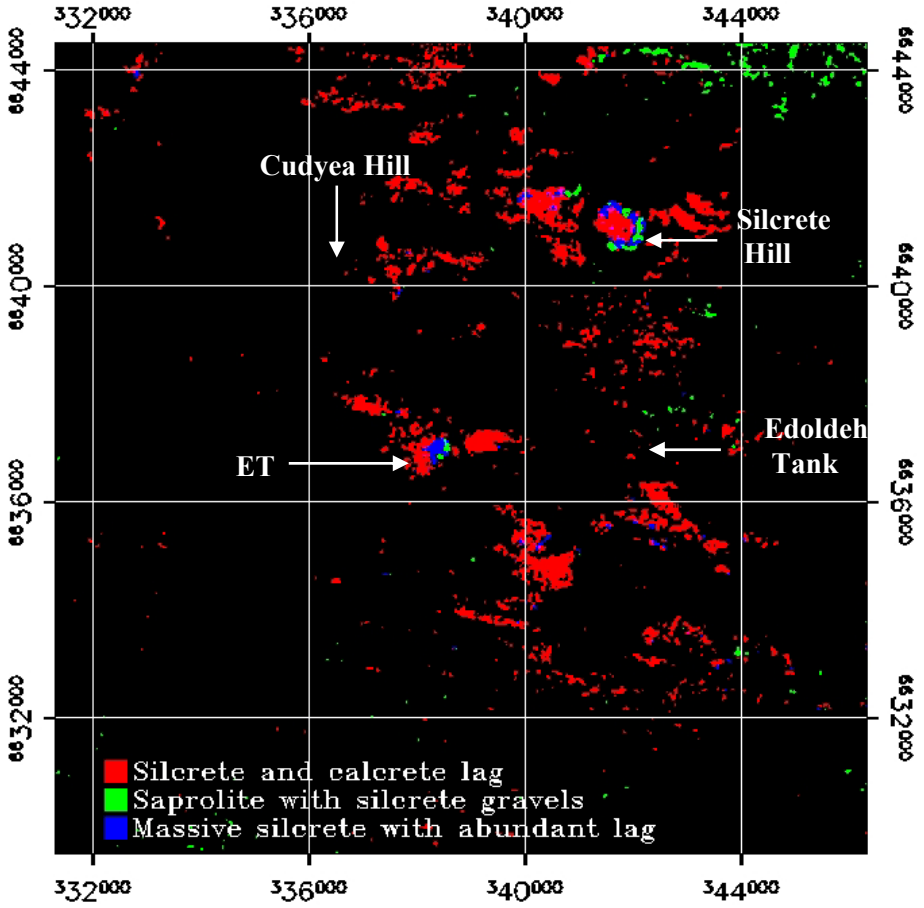

Figure 2-21 Classification of three principal regolith materials of interest, silcrete gravels (Red), saprolite (Green) and massive silcrete (Blue), in vicinity of ET using the Spectral Angle Mapping technique.

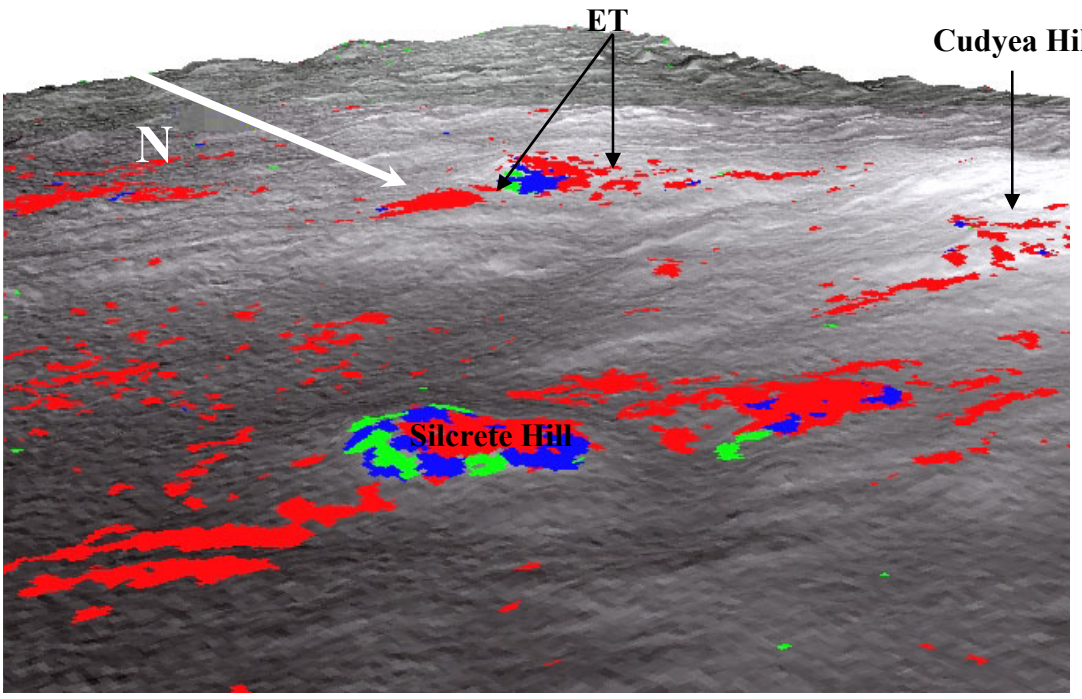

Figure 2-22 3D shaded perspective of regolith classes in Figure 2-21, registered to a shaded relief model and overlaid on the TOPSAR DEM - looking southwest across Silcrete Hill, in foreground, to ET (middle background).

Although the accuracy of the SAM process is limited by the spectral resolution of the Landsat TM data, the technique is very useful for delineating broad mineral assemblages associated with specific regolith-landform units - for example, the saprolite unit. However, where the regolith materials that characterise a unit are more diverse in terms of abundance, type and distribution, such as a lag of mixed gravels over aeolian and colluvial soils, the technique is not as sound. Then, it must be constrained by developing threshold values and filters to isolate those sites most spectrally similar to the reference site and enable them to be classified correctly. This may result in borderline occurrences being omitted from the final classification.

Canonical variate analysis

Canonical variate analysis (CVA) is a very powerful and robust technique used to process the six Landsat TM bands and enhance the subtle spectral variability between the terrain units examined previously using the Spectral Angle Mapper but with two additional classes. Based on field knowledge, the saprolite unit has been sub-divided into: 1. Abundant clay (saprolite) regolith; and 2. Clay-rich regolith. The latter class includes units where clay is not as exposed and dominant as in the former class, in which kaolinite is abundant. An aeolian sand cover class has also been included.

CVA statistically determines the degree of spectral separation between training sites representing each regolith-landform unit. The process produces a data transformation, based on the spectral responses of the units, to maximise the separability of the types defined within the data while minimising the variance within each type (Merembeck *et al*., 1977). Geometrically, a set of mutually orthogonal (independent) axes are fitted to the data such that the first new axis, Canonical Vector I (CV1), accounts for the greatest amount of variance with succeeding axes containing lesser amounts. That is, the degree of separation provided by the canonical variates decreases with each new canonical vector. Each vector is made up of linear functions or combinations of the original six Landsat TM bands. The sizes and strengths of the canonical weights displayed in the canonical factor structure matrix indicate the relative contribution of the TM bands to the correlation between each pair of canonical vectors. CVA is similar to Principal Components Analysis (PCA) in that a linear transformation is computed from the data. However, the advantage of CVA is the increased discrimination of classes with small spectral differences because the transformation is determined from the unique spectral properties of training areas selected to characterise the classes.

A CVA of homogeneous training classes representing each regolith-landform unit revealed a satisfactory degree of spectral division between each unit. A good indicator of this is the relatively large sum of the canonical roots (38.9). The six canonical variates explain approximately 60%, 30%, 6%, 3%, 1% and <1%, respectively, of the between-sites to within-sites separation. Note that training classes do not necessarily coincide with the same reference sites used in the SAM analysis, and for each unit, several classes have been selected. The results of the CVA are summarised below in Table 2-2.

Table 2-2 Summary of canonical variate analysis including information about the sum of the canonical roots, the variation explained by each canonical root, and the standardised canonical vectors that describe the loading of each band on the CVA.

TM bands used in calculation: 1 2 3 4 5 7			Sum of canonical roots:		38.9		
Canonical roots:	1	2	3	4	5		
value	23.2	11.7	2.4	1.3	0.3		
% variation	59.6	29.9	6.3	3.5	0.7		
Significant standardised canonical vectors:							
	B1	B2	B3	B4	B5	B7	Abbreviated vectors
canonical variate I	0.0331	-0.0686	0.0695	-0.7512	0.1139	-0.0981	(-7B4+B5)
canonical variate II	0.3525	0.6755	0.0393	-0.3459	0.2155	-0.4753	(2B2-1.5B7+B1)
canonical variate III	0.0060	0.3945	-0.0822	0.2652	-0.5342	0.2528	(-2B5+B2+B4+B7)
canonical variate IV	-0.1517	-0.0338	-0.8374	0.7518	0.2727	-0.4712	(B4 – B3)
canonical variate V	-0.1975	-0.5723	0.8529	-0.1206	0.1735	-0.7426	(B3-B7-B2)

The results of the CVA are plotted in the space defined by two canonical variates to show the spectral (dis-) similarities between the training classes. These are referred to as C-V plots (Figure 2-23). The

visual degree of separation between the terrain classes on the plot reflects the degree of separation - the criteria for one class being reasonably distinct from another is a minimum distance of 2 standard deviations, the unit of measurement along each axis (N. Campbell, CSIRO Mathematics and Statistics, personal communication).

Figure 2-23 is a C-V plot of canonical variates I and II. Of the total dispersion, 90% is explained by these two variables. Separation along CVI is mainly a function of band 4 and, to a much lesser extent, band 5 suggesting that an increasing Fe content drives increases along this axis. Sites with a low response, such as quartzose sand (Figure 2-14, Site H01), have minimal hematite content whereas sites of massive silcrete and lags of silcrete gravels are generally more Fe- enriched and have reduced albedo *e.g.*, Figure 2-15, Site 6.

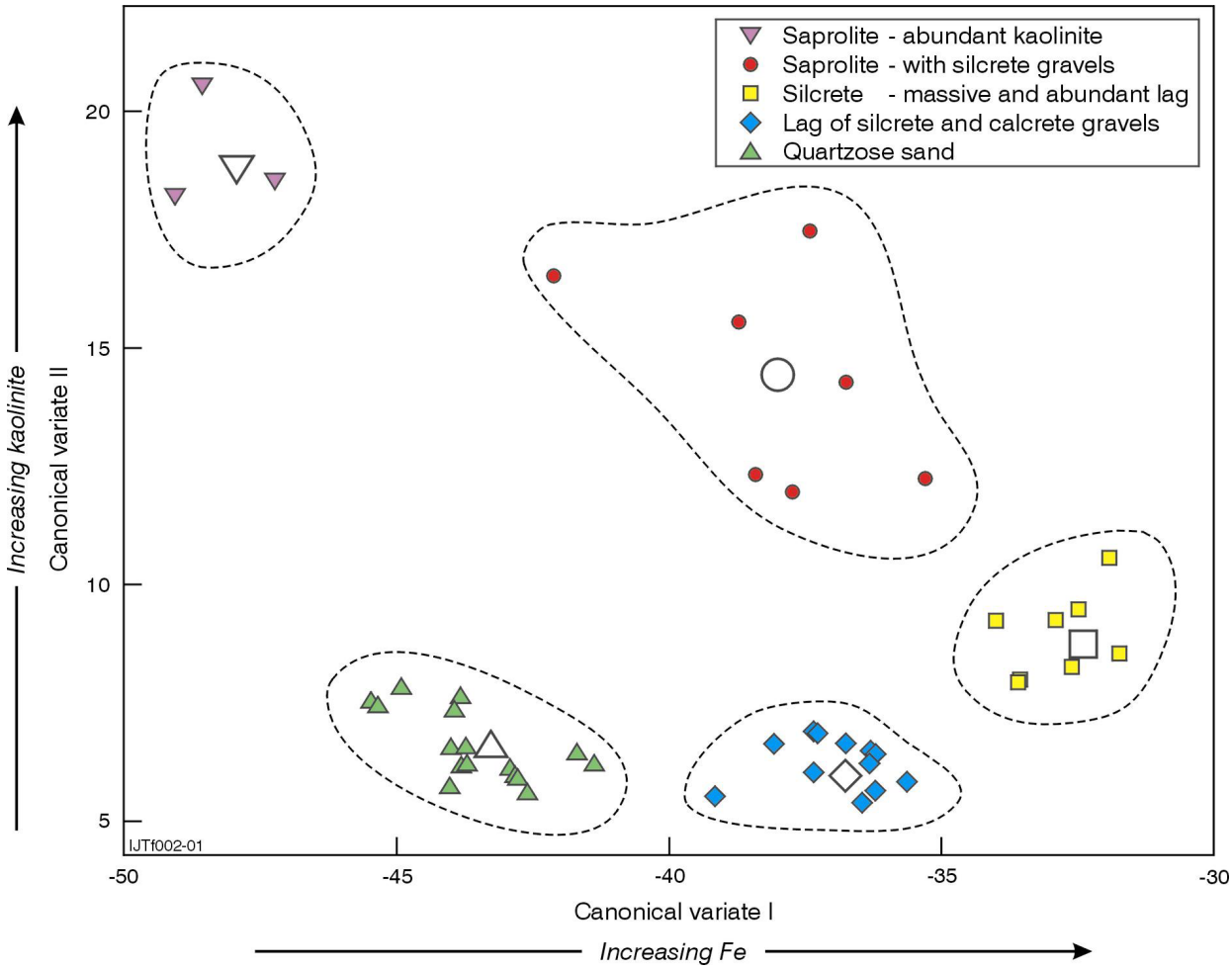

Figure 2-23 Plot of canonical vectors 1 and 2 and Landsat TM data showing the distribution of the classes representing each regolith type

The second axis of the C-V plot is primarily a function of increasing clay content (6 and 7) and possibly other hydroxyl (-OH)-bearing minerals with the breakaway slopes flanking the silcrete-capped basement rocks of Silcrete Hill having the highest values. Sites characterised by saprolite, silcrete and calcrete gravels have reduced clay and increased Fe values – for example Figure 2-15, Site 7.

An examination of the plot CVI v CVII shows that all classes are significantly separate from each other. Classes quartzose sand, lag gravels and massive silcrete are spectrally separate along CVI while the saprolite-lag gravels class is distinct from the others along CVII. Apart from the saprolite-lag gravels class, each class forms a single cluster with no outlying points demonstrating the spectral uniformity of this unit across ET. The variable presence of lag gravels of silcrete and calcrete over the saprolite causes within-class spectral variation of the saprolite-lag gravels.

These results show that canonical variate analysis of Landsat TM data is a viable method for demonstrating the spectral uniqueness of regolith-landform classes. Most importantly, it demonstrates in a statistical manner that regolith units of different compositions can be mapped and discriminated between based on their distinct spectral properties according to their lithology, weathering and erosional characteristics.

The canonical transformation image in Figure 2-24 of CVs 2:1:4 displayed as R:G:B respectively, is a brightly-coloured, linear contrast-stretched image that provides excellent visual separation of the various terrain units. Vegetation-rich areas are blue in colour and contrast strongly with the distribution of silcrete-rich units. Silcrete-rich units are essentially white to pale yellow green features and provide a picture of the distribution of erosional landforms and areas where minimal overburden exists over shallow bedrock. Areas of bright green hues mark the extent of calcareous soils and calcrete nodules developed over shallow calcrete, which in the location of drainage lines has been exposed – for example, in the top-right corner of the image.

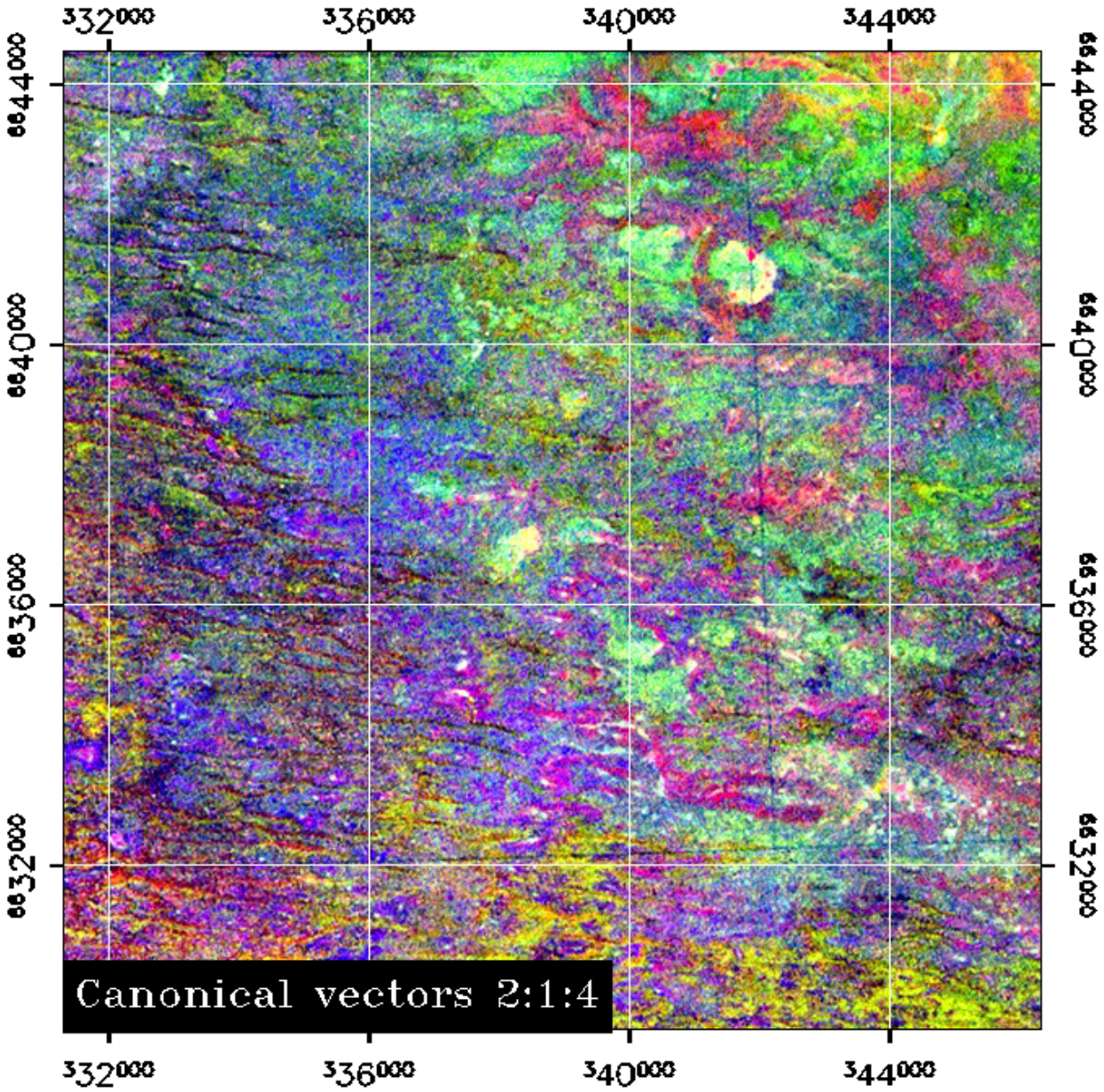

Figure 2-24 A composite image of canonical vectors 2:1:4, assigned as RGB respectively, derived from a canonical variate analysis of 6-band Landsat TM data provides excellent visual separation of silica/iron rich terrain units (pale green to white) where lags of abundant silcrete cobbles and gravels with minor calcrete gravels predominate.

The spectral separation provided by the CVA process has been further exploited by density slicing the aggregate spectral response of four of the classes and displaying them as images in Figure 2-25. The top image shows the distribution of abundant gravels (yellow) and massive silcrete (blue). The lower image highlights the presence of the clay saprolite (blue) and clay-rich regolith units (yellow).

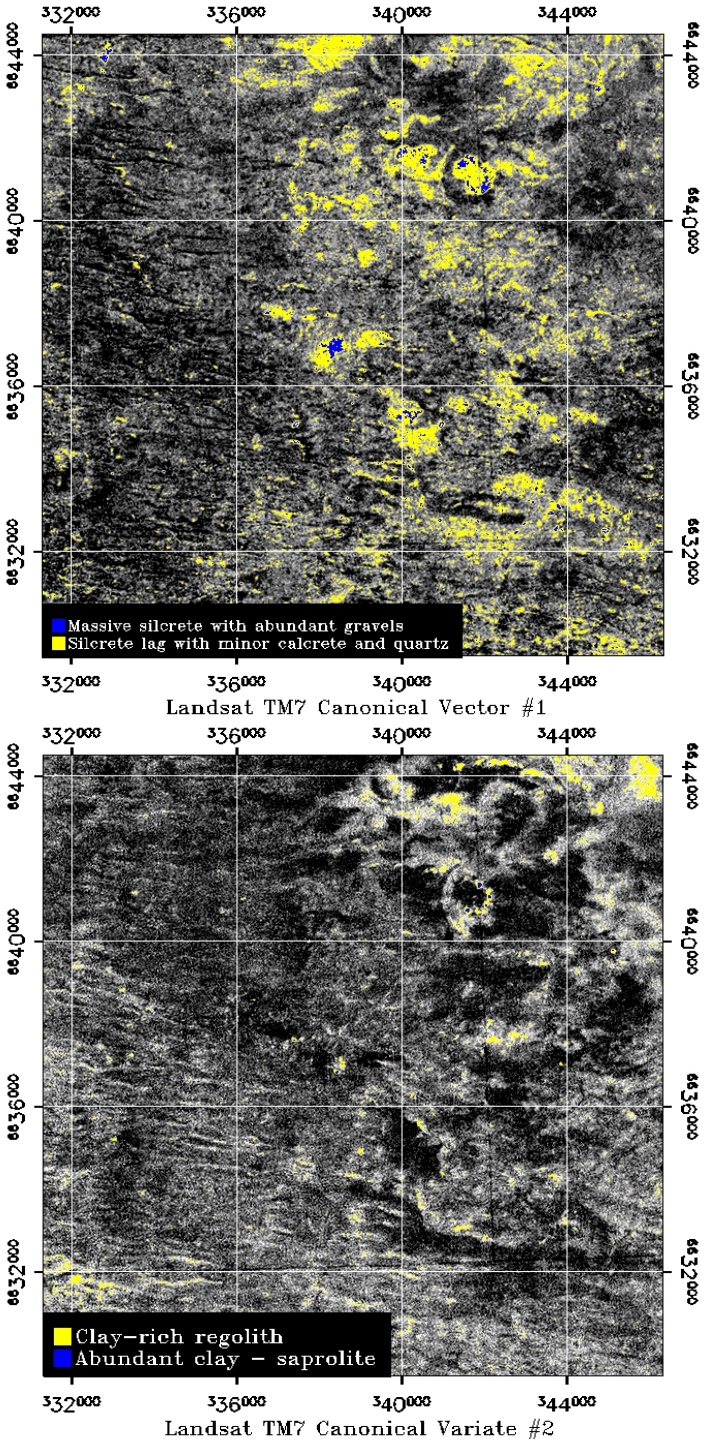

Figure 2-25 Greytone images of canonical vector #1 (TOP) and canonical vector #2 (Bottom) developed from canonical vector analysis of six Landsat TM bands, density-sliced to highlight the occurrence of four principal regolith units in vicinity of ET. These include massive silcrete and silcrete lag (top image), and clay-rich regolith materials and clay-rich saprolite (bottom image).

2.2.5 HyMap™ data

2.2.5.1 Data description

HyMap™ data are highly regarded by researchers and users as the state-of-the-art hyperspectral data available for airborne mapping with an ability to identify mineral species including Fe oxides, phyllosilicates, hydroxylated silicates, sulphates and rare earths in the visible, near infrared and short wavelength infrared regions of the electromagnetic spectrum. The purpose of examining HyMap™ data over ET was to determine if the hyperspectral resolution could resolve minerals and/or mineral combinations present within the surficial regolith of the *in situ* regolith-landform units not visible in enhancements of Landsat TM data. A single flightline of data 2.3 km wide and 70 km long, extending from southwest of ET, northeast to the Monsoon prospect, was collected in November 1998. Unfortunately, high accuracy position information was not available for the HyMap™ instrument at this time. In addition, segments of lines were offset as a result of problems with the instrument mounting system. Fortunately, the data in vicinity of ET was not compromised by this problem. Figure 2-26 shows a non-geocorrected false colour-infrared composite image of the flightline and its position in relation to the SPOT-PAN scene.

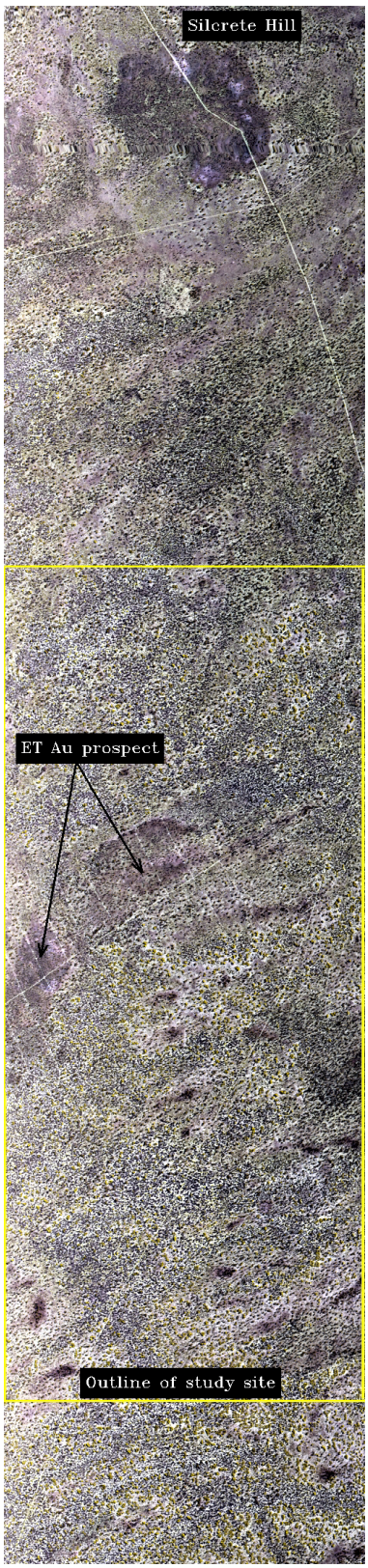

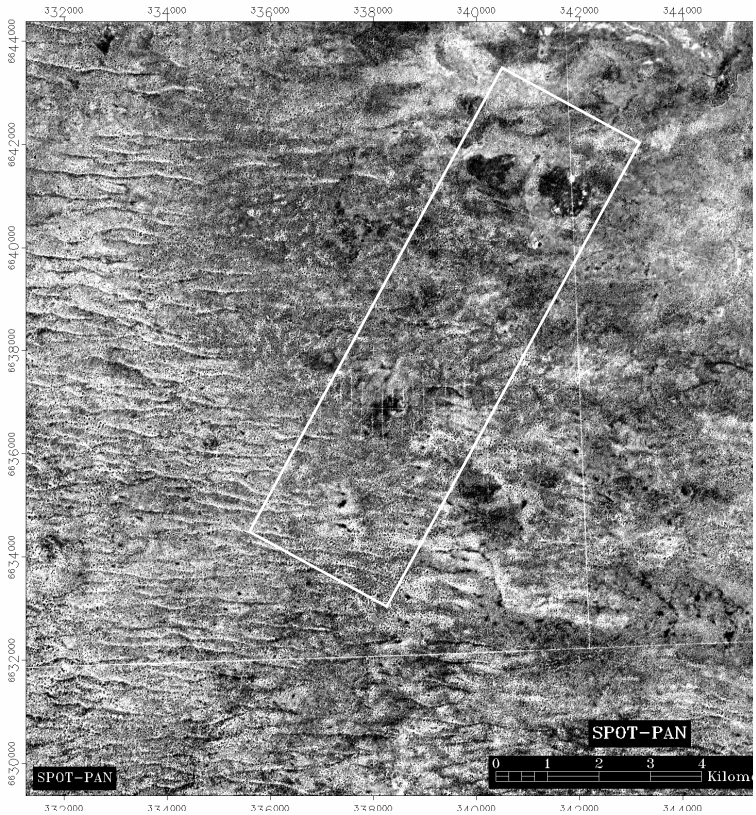

Figure 2-26 SPOT-PAN image of the ET region showing the position of the HyMap™ flightline extending from Silcrete Hill to beyond ET prospect (Above), and non-geocorrected composite image of HyMap™ bands 32 (0.904 µm), 23 (0.792 µm) and 13 (0.6408 µm) (Left) with an outline of the main study area. An offset of a group of scan lines can be observed across Silcrete Hill at the top of the image. The presence and distribution of eucalyptus trees (green clumps), low shrubs (dark irregular shaped features), lags of silcrete gravels (dark grey to black hues) and calcareous soils and nodules (light grey hues) are readily apparent in this enhancement of HyMap™ data.

2.2.5.2 Spectral analysis

HyMap™ data, comprising 128 bands covering the 0.45-2.5 µm range, with a spatial resolution of 5x5 m were supplied as radiance at the sensor. These were corrected to apparent surface reflectance using the ATREM atmospheric model-based calibration routine (CSES, 1999) and EFFORT correction in the HYCORR software, a CSIRO program. No ground measurements of calibration targets were used in the correction process. The corrected data were then processed to extract spectral end-members using the spectral analyst routines implemented in the ENVI image analysis software.

The effectiveness of the calibration steps is demonstrated below (Figure 2-27) in the reflectance spectra of the surficial materials comprising the regolith cover at eight sites over the ET prospect. Except for several bands of bad data at the spectral boundary of the visible and near-infrared detector modules (~0.89 µm), and the omission of bands in vicinity of the water absorption features at 1.4 and 1.9 µm, the data exhibit pronounced spectral information describing the presence and identification of Fe (0.5-0.85 µm) and clay minerals (2.1-2.4 µm).

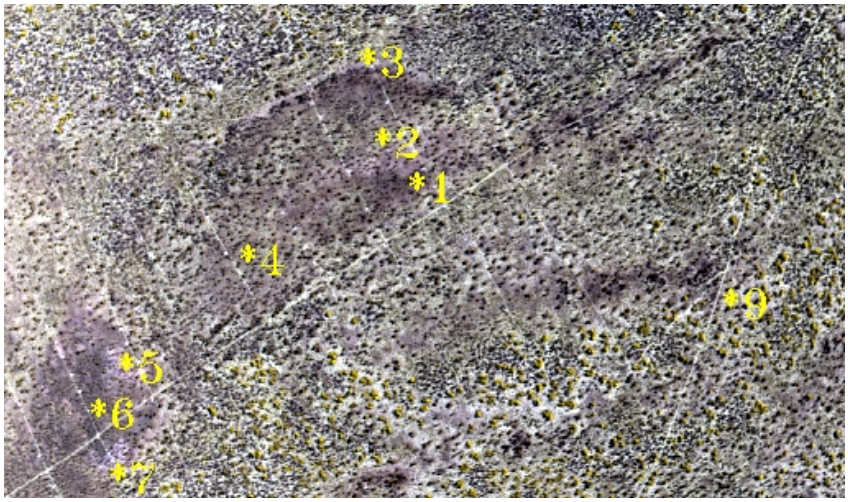

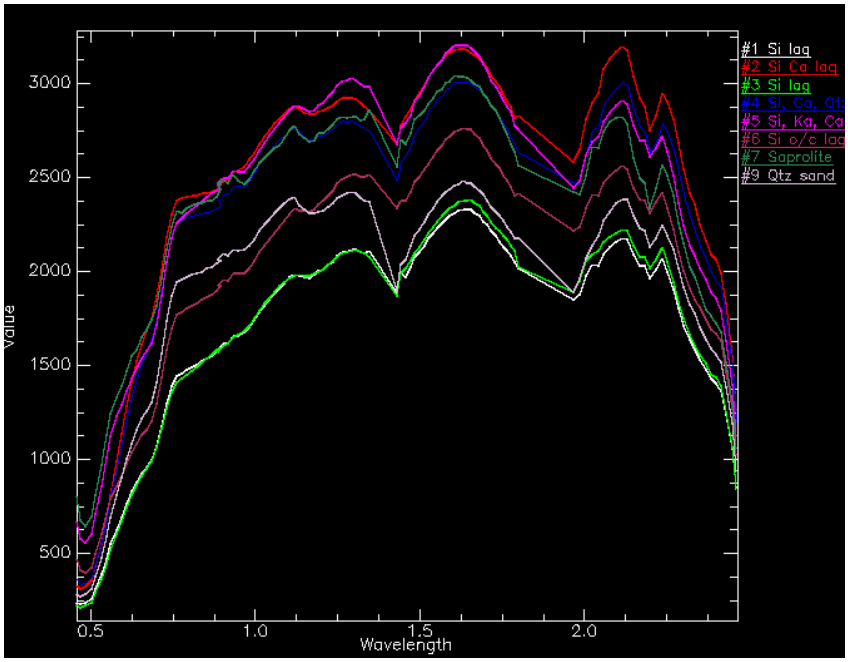

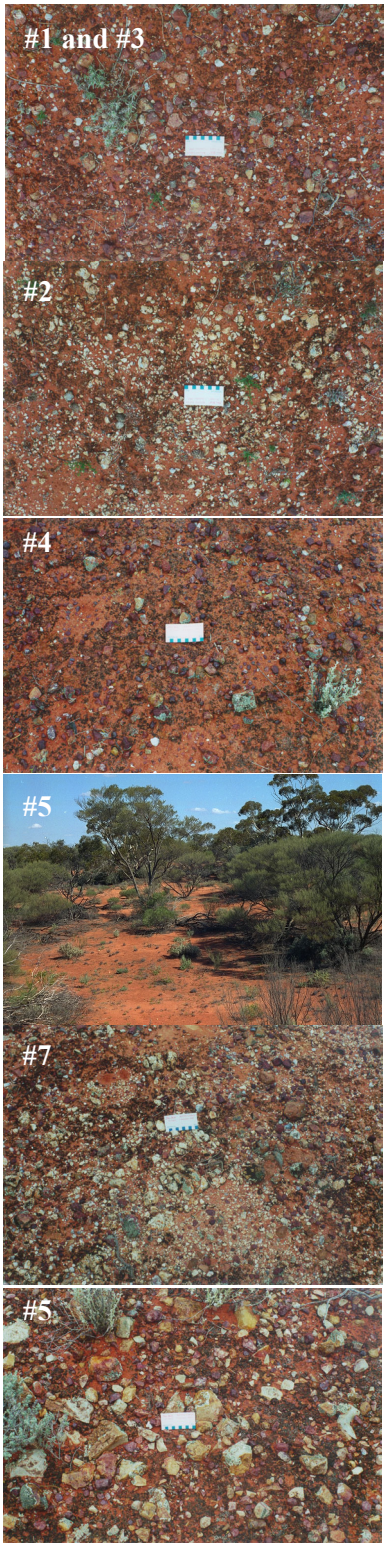

Figure 2-27 A subset of the HyMap™ image in Figure 2-26 showing the location of field sites representing the principal regolith-landform units of ET, photographs of the surface materials, and HyMap™ reflectance spectra for each of these sites. A field photo of Site 6 is shown in Figure 2-15.

Each spectrum represents the average reflectance from the composite of materials present in a 2x2 pixel (10x10 m) sample area. Sites characterised by lags of silcrete gravels, some relatively Fe-rich (#1 and #3), have the lowest overall reflectance compared with those sites with calcareous soils, calcrete nodules, saprolite and quartz fragments (#2, #4, #5 and #7). However, the overall high reflectance of each spectrum indicates the relatively high content of silica and relatively low content of Fe minerals present in the surface regolith.

The similarity between the spectra including mineralogy, shape and symmetry is apparent when the spectra are offset for clarity and are displayed in site numerical order as in Figure 2-28. Each has a reflectance peak around 1.6 m, exhibits clay doublets at 2.2 µm and minor doublets at 1.4 µm, are relatively symmetric and, apart from steep slopes between 0.5 and 0.7 µm for calcrete-rich Sites 2 and 4, have very similar shapes. The consistent symmetry of the spectra is further evidence of their low abundances of Fe oxides. Research by Gozzard and Tapley (1992) in the Yilgarn Craton of Western Australia demonstrated a strong and consistent relationship between symmetry and Fe oxide mineralogy of weathered regolith materials. Hematitic materials are normally brighter and right-asymmetric in shape while goethitic materials have reduced albedo and their shape is left-asymmetric. The spectra in Figure 2-29 and Figure 2-30 indicate the presence of both goethite and hematite by the changing position of the charge-transfer reflectance shoulder at 0.6 µm, but the symmetric shape of the spectra suggest relatively low contents of Fe oxides.

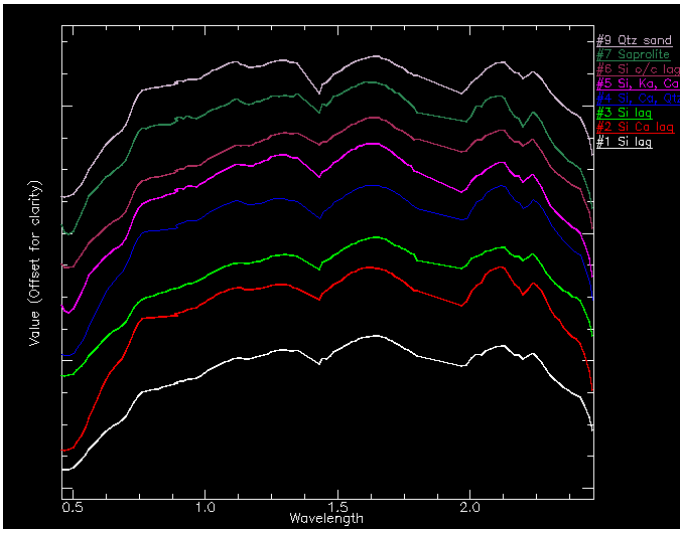

Figure 2-28 A comparison between HyMap™ reflectance spectra of the field site, regolith materials when the spectra have been offset for clarity along the Y axis.

The identity of the minerals is best observed in wavelength subsets of HyMap™ spectra. In Figure 2-29, field site spectra have been normalised to allow improved recognition and comparison of individual absorption features. Spectra are shown for the wavelength regions 0.5-1.0 µm (Left) and 2.1-2.4 µm (Right) to enable the identification of Fe oxides and clay minerals, respectively. The dominant occurrence of the minerals goethite, hematite and kaolinite is readily apparent. In fact, no other minerals are recognisable which has been a major disappointment.

Diagnostic spectral reflectance features for Fe oxides, hematite and goethite, include a steep charge-transfer absorption feature centred at 0.5 µm, a small reflectance shoulder at 0.6 µm and a crystal-field absorption trough that, depending on the Fe oxide species, occurs between 0.80 and 1.0 µm. As shown by the reference spectra in Figure 2-11 the wavelength of maximum absorption for this crystal field feature varies from 0.85 µm for hematite to 0.92 µm for goethite. Cudahy and Ramanaidou (1992) demonstrated a unique relationship between the depth of this feature and Fe oxide content. The same authors also reported a diagnostic relationship between the hematite-goethite ratio and the wavelength of the reflectance shoulder at 0.6 µm. The shoulder for goethitic-rich materials typically occurs at wavelengths between 0.58 and 0.6 µm while hematite materials peak at around 0.6 µm. Based on these findings, the Fe oxide species of the ET sites can be described in terms of their identity and relative abundance. Firstly, regolith-landform units comprising weathered *in situ* materials, including saprolite, are goethitic whereas units with lags and

veneers of remobilised soils over calcrete and, probably, bedrock are hematitic. This is evidenced by the relative position of the reflectance shoulder at 0.6 µm in Figure 2-29. Secondly, the shallow crystal field absorption in vicinity of 0.9 µm is further evidence of the minor amounts of Fe oxides present in the regolith.

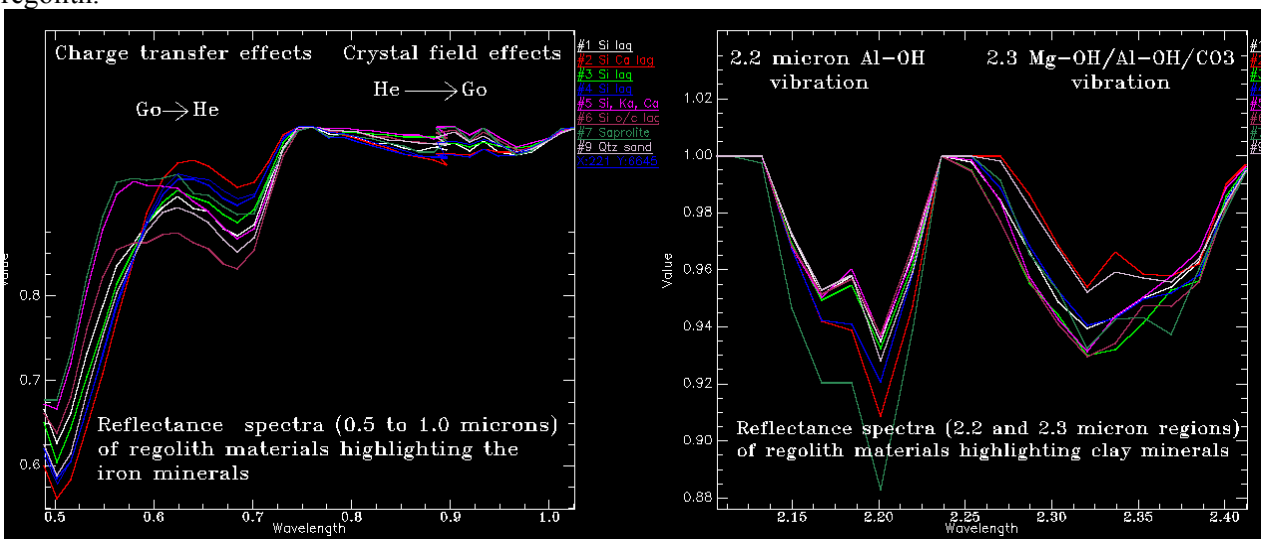

Figure 2-29 Normalised reflectance spectra of composite regolith materials at field sites on ET highlighting the iron minerals (Left) and clay minerals (Right).

The reflectance spectra in the 2.1-2.4 µm region of Figure 2-29 show diagnostic absorption features for kaolinite. All have prominent doublet absorptions at 2.16 µm and 2.2 µm with complementary features at 2.32, 2.36 and 2.38 µm. The depth and geometry of the 2.2 µm feature has been reported by Cudahy (1998) to relate to the abundance and crystalline nature of kaolinite. It can be inferred that the saprolite-rich Site 7 has the greater abundance of kaolinite (maximum depth of 2.2 µm feature) followed by Sites 2 and 4, whereas Site 5, which is primarily calcrete with a skin of kaolinite, plus silcrete gravels, and Site 6, both *in situ* terrains, have well crystalline kaolinite as indicated by the sharper and shorter wavelength to the absorption at 2.16 µm. Comparison of these normalised spectra with their original form in Figure 2-27 confirms that Site 7 and Site 2 have the most narrow and distinct absorption troughs, confirming the abundance of kaolinite.

Measurements of field spectra with the IRIS spectra-radiometer Mk5 were not very successful owing to rain showers and subsequently dampened soils. Spectral measurements were restricted to Sites 1, 2, 5, 6 and 7. In addition, the visible and near-infrared module was not functioning correctly as shown by the noise in the spectra (Figure 2-30). Each spectrum is of a composite of materials in a 12 x 12 cm area.

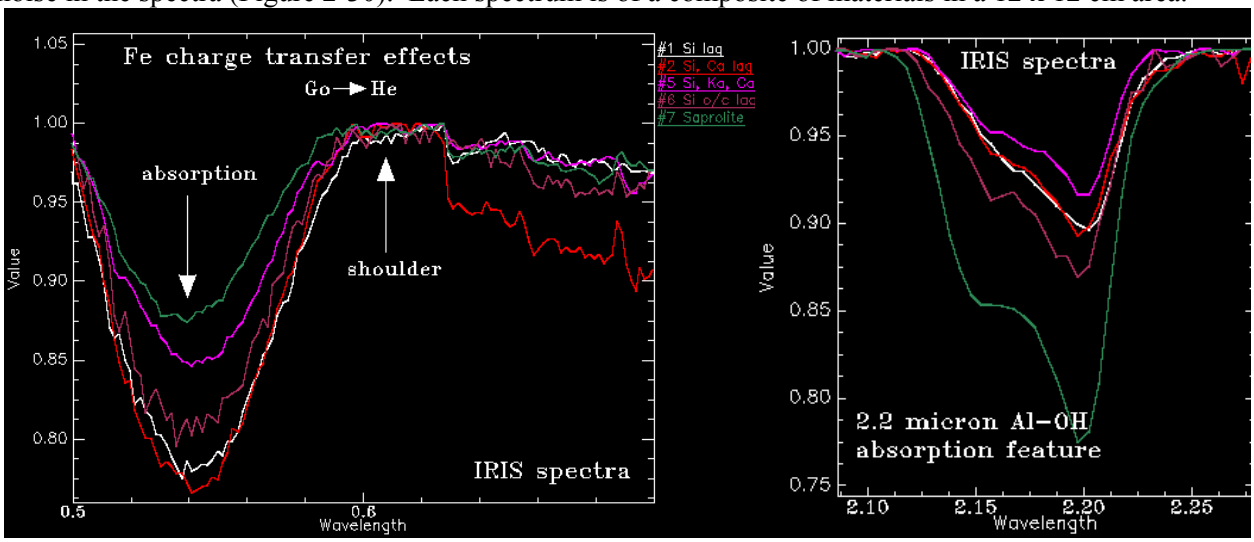

Figure 2-30 Reflectance spectral measurements recorded by the IRIS radiometer of ET field sites

Importantly, the presence of hematite, goethite and kaolinite can be identified in the IRIS spectra for the same sites as observed in the HyMap™ spectra. In situ materials at Sites 5, 6 and 7 retain their goethite and kaolinite identity, whereas the lag gravels and background soils over Sites 1 and 2 have hematitic signatures with reduced and poorly crystalline kaolinite.

2.2.5.3 Endmember selection and mineral mapping

The selection of spectral endmembers was implemented using the ENVI image processing software. Firstly, the spectral and spatial dimensionalities of the calibrated HyMap™ data were reduced with the Minimum Noise Fraction (MNF) transformation and Pixel Purity Index (PPI), respectively. Secondly, image endmembers were determined from the n-Dimensional Visualizer and their identities established by a combination of visual inspection and comparison with library reflectance spectra in Spectral Analyst. Nine key endmembers were identified from the data. Normalised spectra and their interpreted identities are shown in Figure 2-31. As spectral subsetting was not used in the above processes, each endmember spectrum combines information describing Fe (hematite and goethite) and clay (kaolinite with a suggestion of smectite) minerals and minor quartz. Variations in the crystalline form and abundance of kaolinite together with spectral shifts between goethite and hematite are readily observed in the spectra.

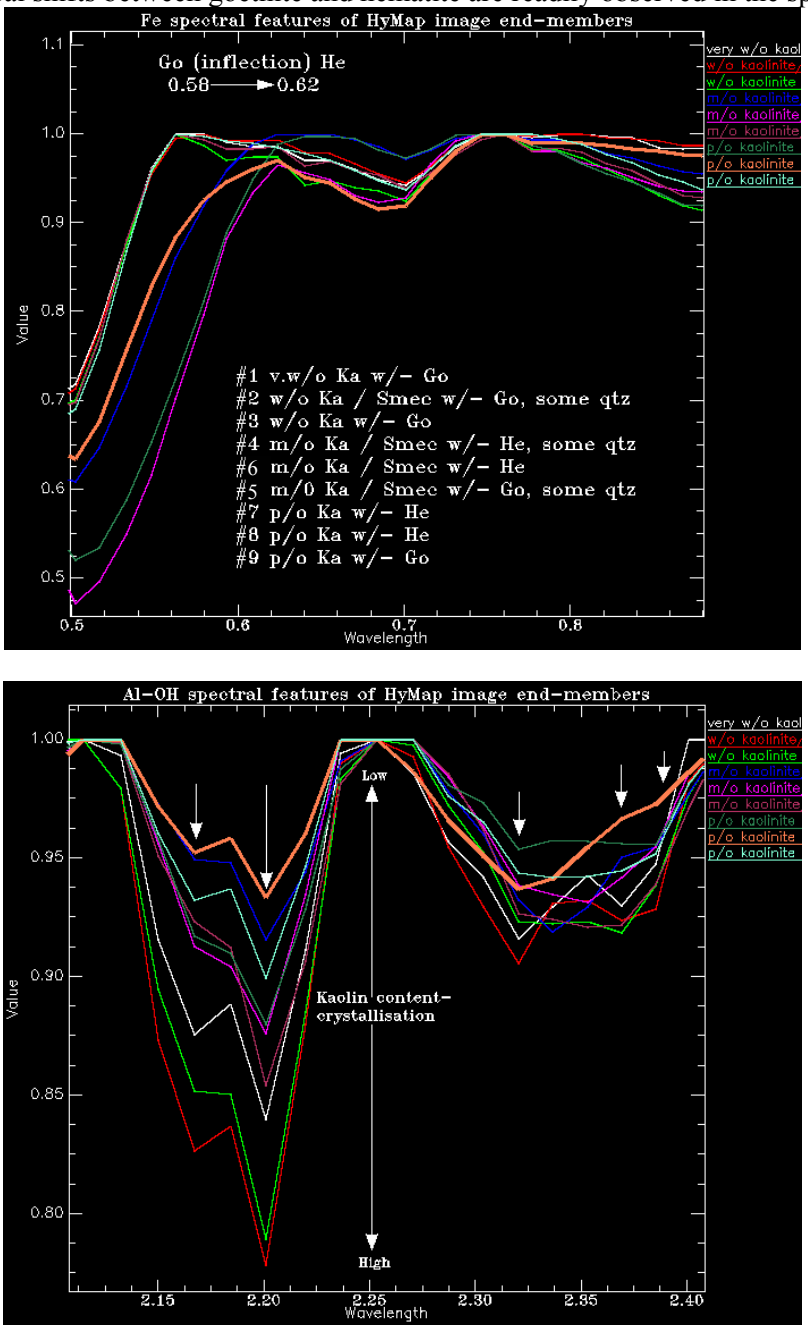

Figure 2-31 Spectral endmember signatures derived from HyMap™ data of the ET region. Wavelength subsets of the VNIR-SWIR region are used to highlight the iron minerals (Top) and clay minerals (Bottom). Note that endmembers #5 and #6 are not in numerical order.

The Mixture-Tune Matched Filtering (MTMF) option was used to produce mineral maps from the endmember (EM) spectra. The results are presented in Figure 2-32 as grey-scale images with values from 0 to 1.0, which provides a means of estimating mineral abundance. Brighter pixels in the images represent higher mineral abundances and are a mixture of Fe and clay mineralogies. .

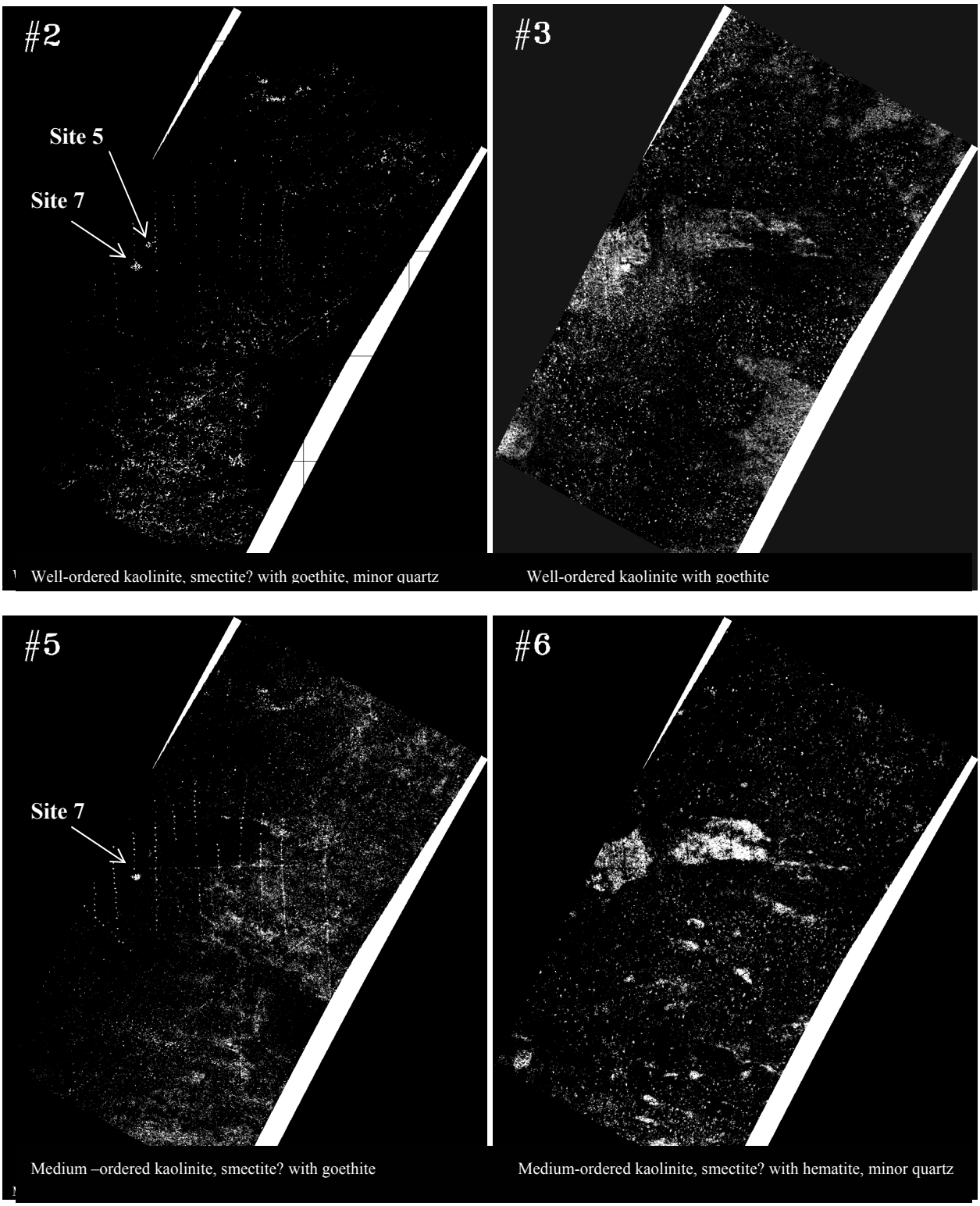

Figure 2-32 Mixture-Tune Matched Filter abundance images EM #2, #3, #5 and #6 for ET. Highest abundances are white.

It is apparent in Figure 2-32 that several endmembers (EM) can co-exist within the same regolith-landform unit and within the drill spoil, including:

i) EM#2 (*well-ordered kaolinite, possibly smectite, with goethite and quartz*) highlights the saprolite along the breakaway at Site 7, kaolinite and calcrete association at Site 5, and has subdued signatures from sites of drill spoil over ET. The identity of a prominent signature from a narrow, elongated feature north of ET requires field checking.
ii) EM#3 (*well-ordered kaolinite with goethite*) occupies the low, prominent rise at the western end of ET and other sites where lags of silcrete gravels occur in abundance. Examination of the spectra in Figure 2-31 indicates that the 0.9 μm crystal field absorption trough for this endmember is the deepest for all endmembers. This suggests that EM#3 is highlighting Fe-rich regolith materials, specifically goethite, in the region.
iii) EM#5 (*medium-ordered kaolinite, possibly some smectite, and goethite*), co-occurring with EM#2 and mapping the location of the drill spoil and clay- and goethite-rich saprolite at Site 7.
iv) EM#6 (*medium-ordered kaolinite, possibly some smectite, with hematite and minor quartz*) is interpreted from the deep charge-transfer absorption feature at 0.5 μm in Figure 2-31 as the most hematite-rich of all the endmembers, and maps the spatial distribution of lag gravels, silcrete and calcrete, over ET and within the sand dunes to the south. The response matches closely that observed in the supervised classification of the Landsat TM data, and the textural mapping from the AIRSAR data.
v) EM#7 (*poorly-ordered kaolinite with hematite*) is the most abundant and is associated with the distribution of aeolian quartzose sands. Areas of no association (dark tones) match those where calcareous sands occur.
vi) EM#9 (*poorly-ordered kaolinite with goethite*) co-occurs with EM#3 and EM#6 over ET.

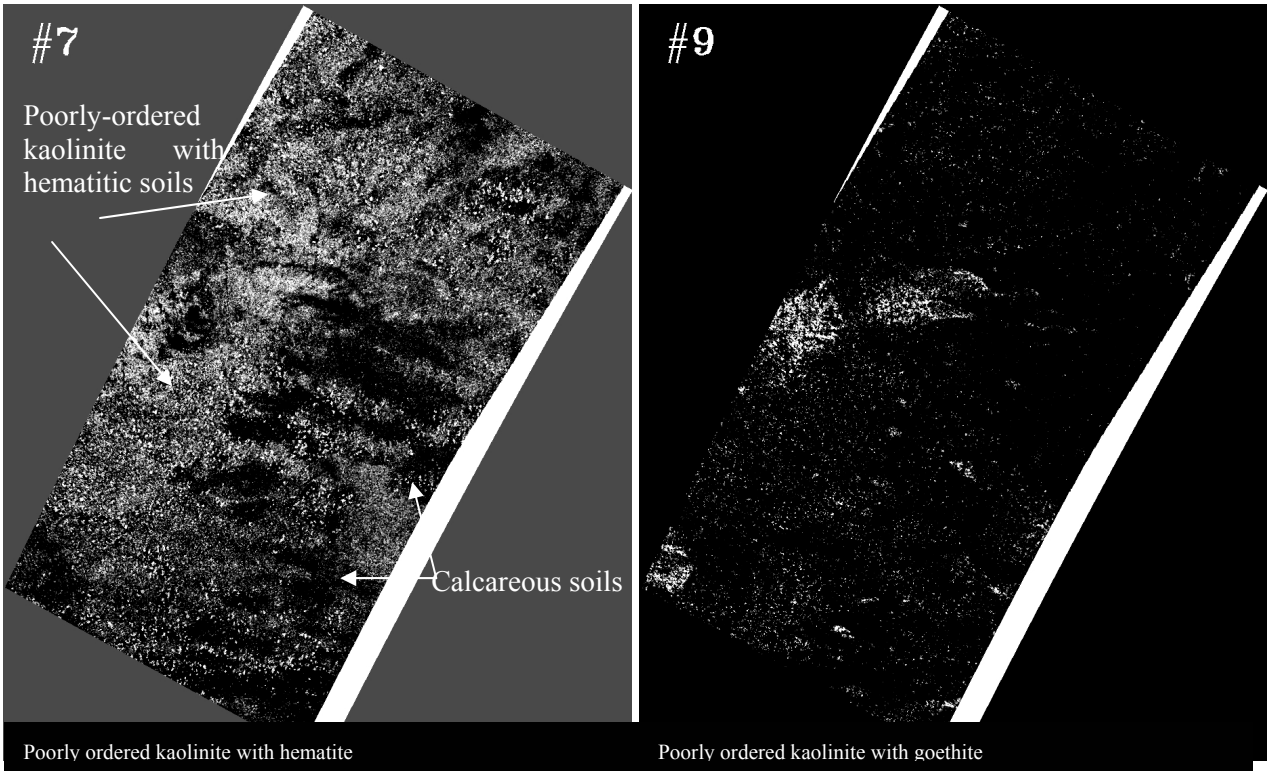

Figure 2-33 (cont): MTMF abundance images #7 and #9 for ET. Highest abundances are white.

Several of the mineral abundance maps generated using the MTMF process show a high level of agreement with the image products generated from the Landsat TM and AIRSAR datasets, particularly the location of regolith-landform units rich in either lag gravels or saprolite. Importantly, each makes spectral sense by their association with the regolith-landforms that they highlight. It is well documented by Cudahy (1992) and Gozzard and Tapley (1992) that exposures of ferruginous saprolite within erosional landforms have well-expressed goethite and kaolinite in their reflectance spectra. An interesting observation is the delineation in EM#3 of kaolinite-rich regolith over *in situ* landforms at Position A whereas it is not mapped in other endmembers of similar definition. Inspection of the endmember spectra in Figure 2-31 shows a

similar goethite response to EM#6 but a much deeper and well-defined kaolinite doublet. With reference to EM#7, regions with a veneer or cover of aeolian quartzose sand, stained with hematite, are mapped as bright areas whereas calcareous soils have the lowest response, and appear in dark tones.

Composite images of MTMF endmembers displayed as RGB, respectively, are valuable for viewing the locations and spatial distribution of the principal regolith-landform units that can be separated based on their relative abundances of Fe and clay minerals. Careful selection of the combination of endmembers and their allocation to RGB is required to gain optimum separation. In Figure 2-33, an RGB composite of EMs 6:5:4 identifies sites of gravels and thin cover over bedrock (red hues), calcareous soils with a mixture of silcrete gravels and calcrete nodules (bluish hues), saprolite and clay-rich drill spoil (green) and quartzose sands (green-red combinations). Prominent trees are identified in the image as dark dots.

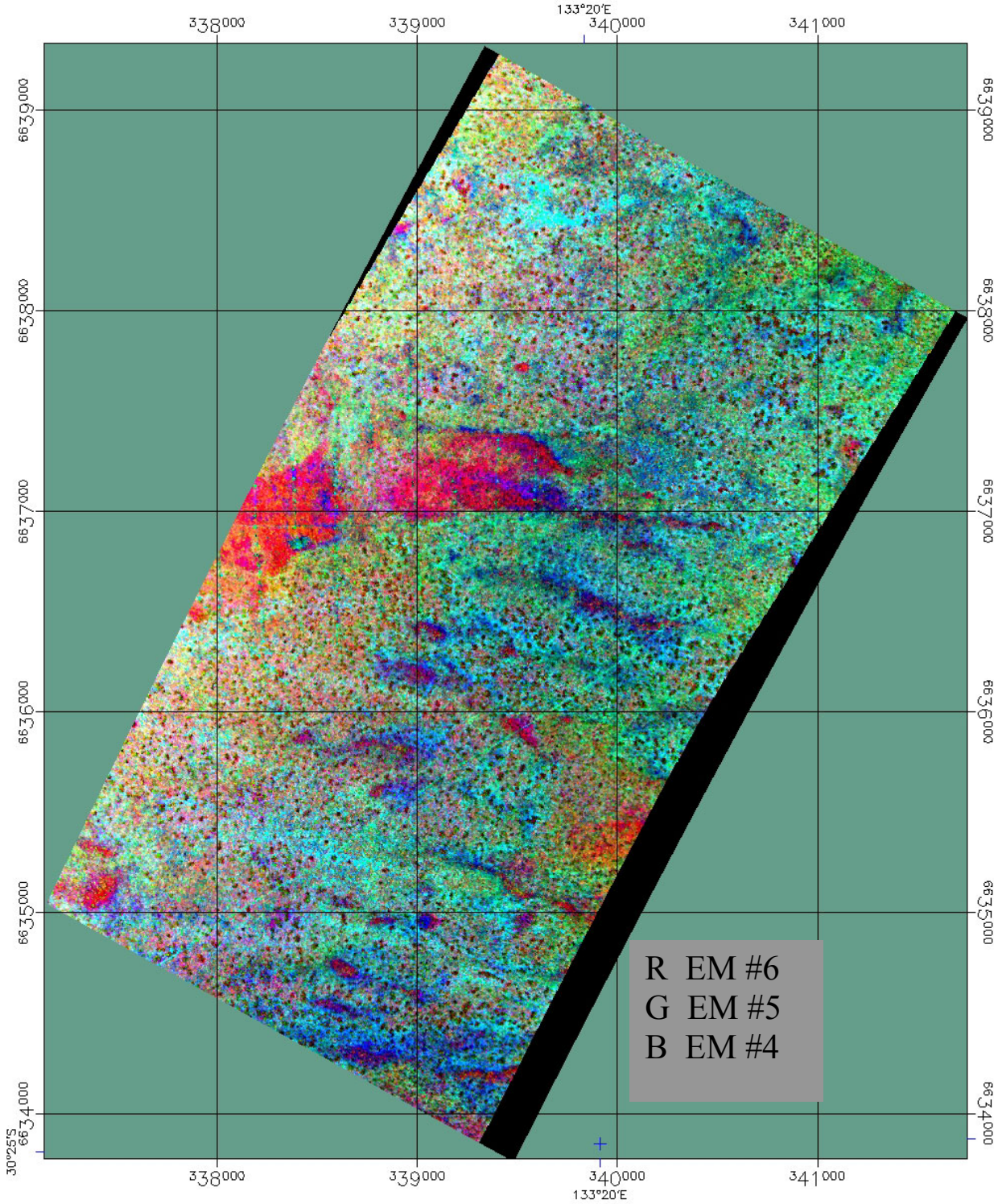

Figure 2-33 Geolocated, colour composite image of MTMF endmembers 6:5:4 displayed as RGB, respectively. The relationships between the landforms in vicinity of ET, mineral composition of the surficial regolith and local relief are well seen in 3D perspective view (Figure 2-34). This illustrates that ET is positioned essentially on a north-facing backslope above a south- and southeast-facing breakaway that is most apparent in the western sector in vicinity of Site 7. Calcareous soils (bluish hues) occur primarily in low-lying areas including between sand dunes where isolated patches of silcrete gravels (red hues) can also be observed.

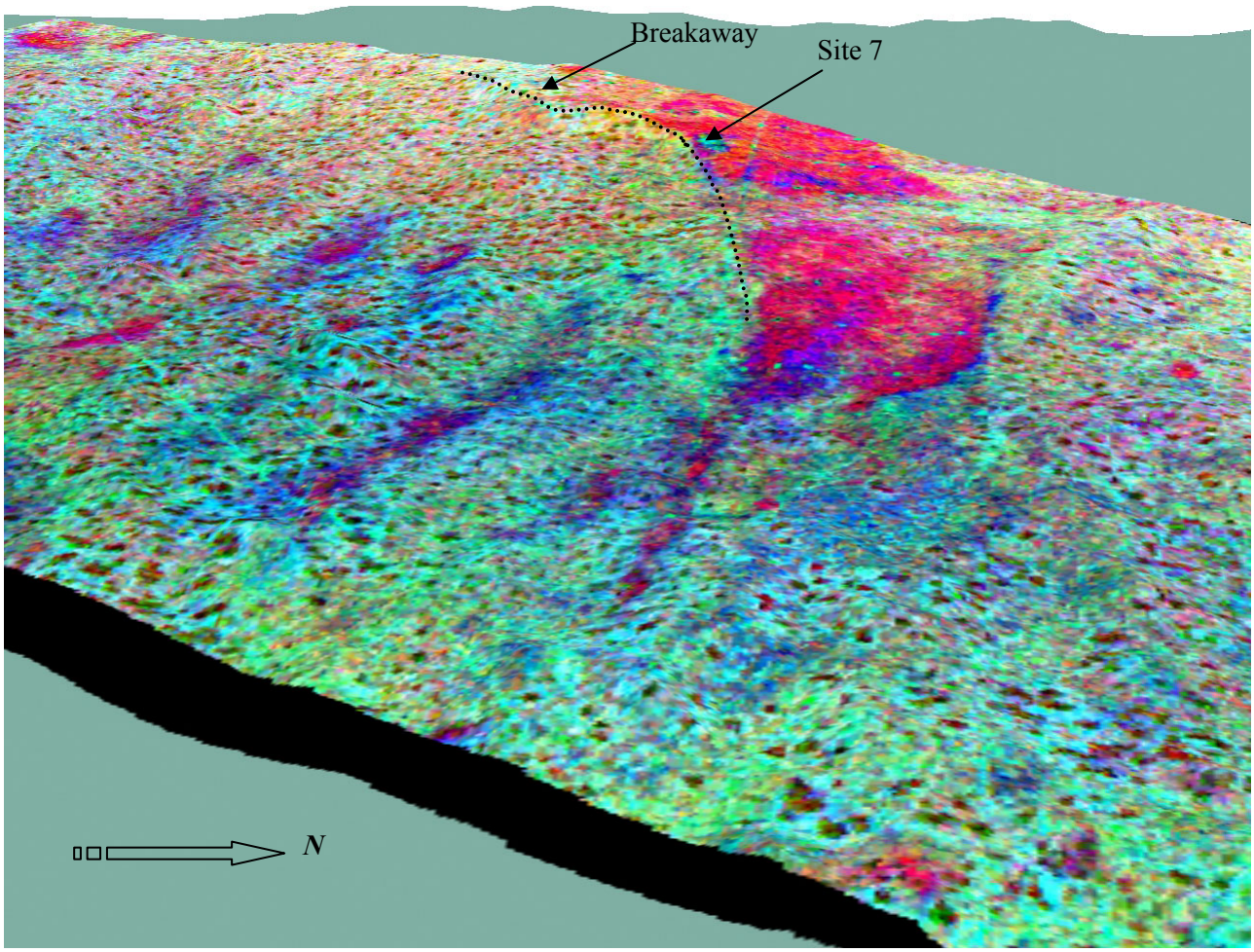

Figure 2-34 A 3-D perspective view of colour composite image of endmembers 6:5:4 in Figure 2-33, overlaid on the TOPSAR DEM and viewed from the east, looking west across ET.

Figure 2-35 and Figure 2-36 display the information from combining EMs 1:7:3 as an RGB image and as a 3D perspective, respectively. Clay-rich units including those where calcrete has a coating of kaolinite, for example Site 5, are vivid yellow. These contrast with units of massive silcrete and abundant silcrete gravels, depicted in orange at, for example, Site 6. Units of silcrete gravels and aeolian and colluvial soils over shallow bedrock are predominantly dark green, calcareous soils are pale yellow while hematitic aeolian sands have bluish hues. As composite images, the endmember combinations of 1:7:3 and 6:5:4 display the most information describing the identity and distribution of the regolith-landform units in vicinity of ET.

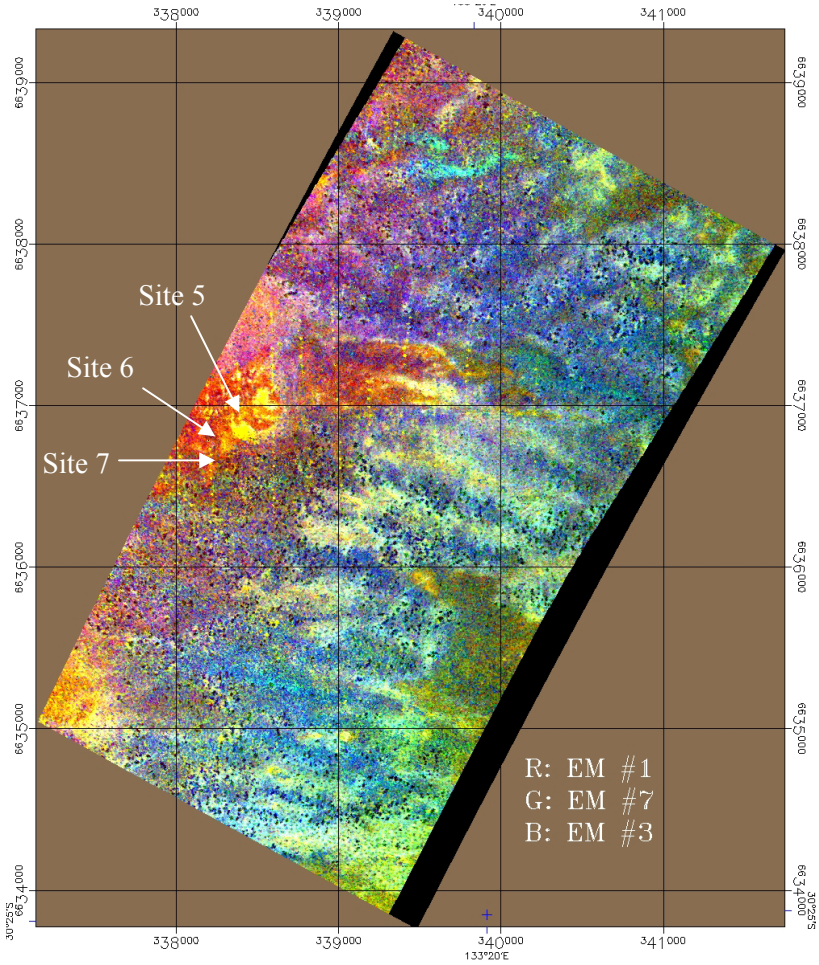

Figure 2-35 Colour composite image of regolith endmembers 1:7:3 displayed as RGB, respectively, highlights the terrain units at ET.

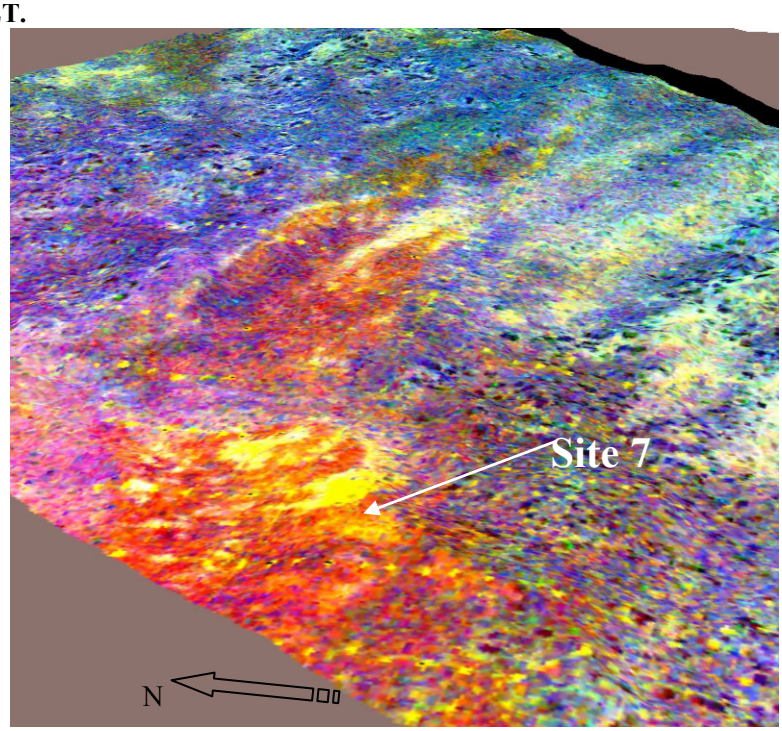

Figure 2-36 3D perspective model of regolith endmembers 1:7:3 overlaid on TOPSAR DEM and viewed from the west with ET in the foreground.

Supervised classification using the Spectral Angle Mapper (SAM) technique was attempted using reference spectra of four classes generated from the calibrated dataset and using all available spectral bands. Thresholds were selected to prevent commission resulting in rather patchy classes and the probable omission of small-localised (one or two pixels) occurrences having very narrow spectral shifts from the reference spectrum. The image in Figure 2-37 displays the location of relatively pure regolith endmembers calculated from the regions-of-interest used to generate the spectra displayed in Figures 2-29 and 2-30. Because the spectra in the wavelength region 1.0 to 2.0 μm contain minimal spectral information (Figure 2-29), the accuracy of the SAM classification may have been improved if the bands in this wavelength region had been omitted from the classification.

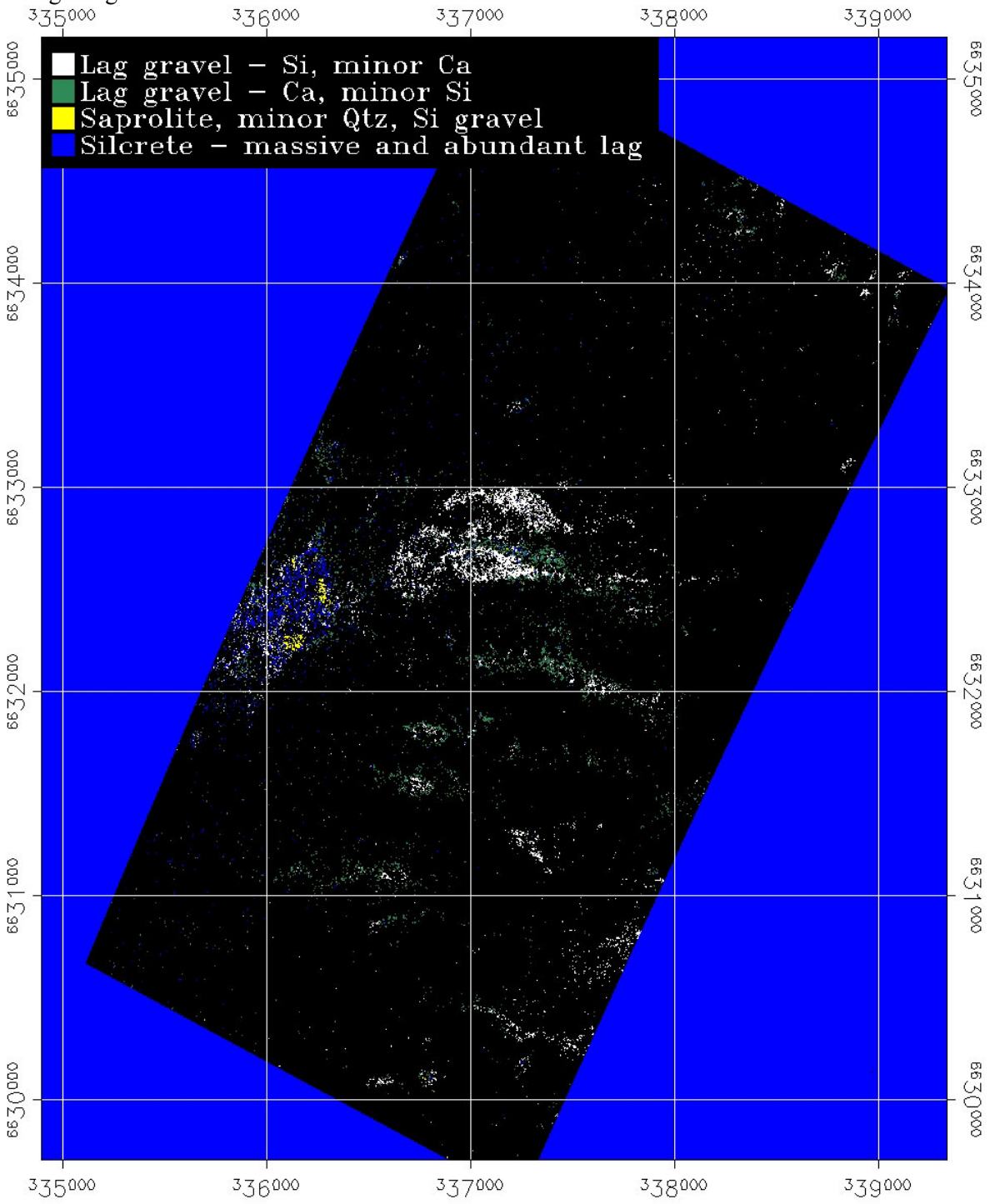

Figure 2-37 Spectral Angle Mapper classification of HyMap™ regolith endmembers at ET.

2.2.6 Polarimetric AIRSAR radar data

Radar remote sensing provides imagery that characterises the physical properties (morphology, roughness, dielectric properties and geometric shapes) of the terrain surface, its cover and near-surface volume. Image enhancements are particularly suited to landform analysis from which geomorphological and geological inferences can be made. In radar imagery, surface roughness is the dominant factor in determining the amplitude of the return signal. Surface roughness is a measure of the irregularity of the terrain surface (both vertical and horizontal) compared with the radar wavelength. On radar images, surfaces can be classified as smooth, slightly rough, moderately rough or very rough, relative to the radar wavelength and angle of incidence. A consequence is that a surface that appears smooth at a long radar wavelength may appear rough at a short wavelength. The level of radar backscatter indicates the tone of an image - rough targets appear bright and smooth targets dark. The mean intensity of the radar backscatter from an area of interest is usually expressed in decibels (dB). Typical values (of σ°) for natural surfaces range from +5 dB for very rough surfaces to -40 db for very smooth surfaces.

The radar dataset covering ET was collected in 1996 by the NASA-JPL AIRSAR (AIRborne Synthetic Aperture Radar) system. AIRSAR is an imaging radar polarimeter and measures the complete polarisation response of every pixel in an image in three frequencies. Radar polarimetry is a valuable tool for identifying the dominant scattering mechanisms present in a scene and for resolving minor differences in the physical and electrical properties between surface features.

Over ET, AIRSAR operated in TOPSAR (TOPographic Synthetic Aperture Radar) mode to collect precision elevation data via the process of radar interferometry, and radar amplitude data in three frequencies referred to as C-band (5 cm wavelength), L-band (24 cm wavelength), and P-band (68 cm wavelength). The shorter wavelength C and L bands are recognised as being more sensitive to small-scale variations in surface roughness that can be related to the extent of soil erosion, size of surface lag gravels and the extent of landscape truncation (Tapley, 1998). Under dry conditions and low soil moisture levels, L and P bands have a greater potential for penetrating sand cover and mapping subsurface structures.

The benefits of radar for mapping landforms and discriminating between regolith materials in deeply weathered terrains are well described by reference to studies in the Northeastern Goldfields, Western Australia (Tapley, 1998), and the Gawler Craton, South Australia (Tapley, 1999). Importantly, fundamental attributes of a deeply weathered terrain, namely erosional and depositional regimes, can be recognised in enhancements of AIRSAR data. In the Great Sandy Desert, near the Telfer Gold Mine, Landsat TM data were severely limited owing to the minimal spectral variability of the terrain. However, AIRSAR's sensitivity to the micromorphology of sparse exposures of subcrop and lag gravels provided a new insight into the region's geological framework, its landforms and their evolution (Tapley and Craig, 1995).

Inspection of the 8x7 km composite image of L, C and P bands, assigned to RGB, respectively, in Figure 2-38 highlights the value of the high quality AIRSAR data in the ET region. Regolith-landform units of the erosional regime can be delineated from those in other regimes by the increased surface roughness resulting from the accumulation of coarser lag gravels and exposure of bedrock during active erosion of the landscape. Units comprising massive silcrete and lags of abundant silcrete and calcrete gravels are "radar rough" at the C-band wavelength and produce the strongest returns, appearing as bright green to yellow in the composite image. Because the C-band signal responds strictly to the physical characteristics of the surface elements, a small change in surface texture, caused by the presence of gravels or subcrop, results in single- and double-bounce interactions of the incoming radar signals. The resulting increase in C-band backscatter allows an improved synthesis of the regional distribution of erosional and depositional landforms.

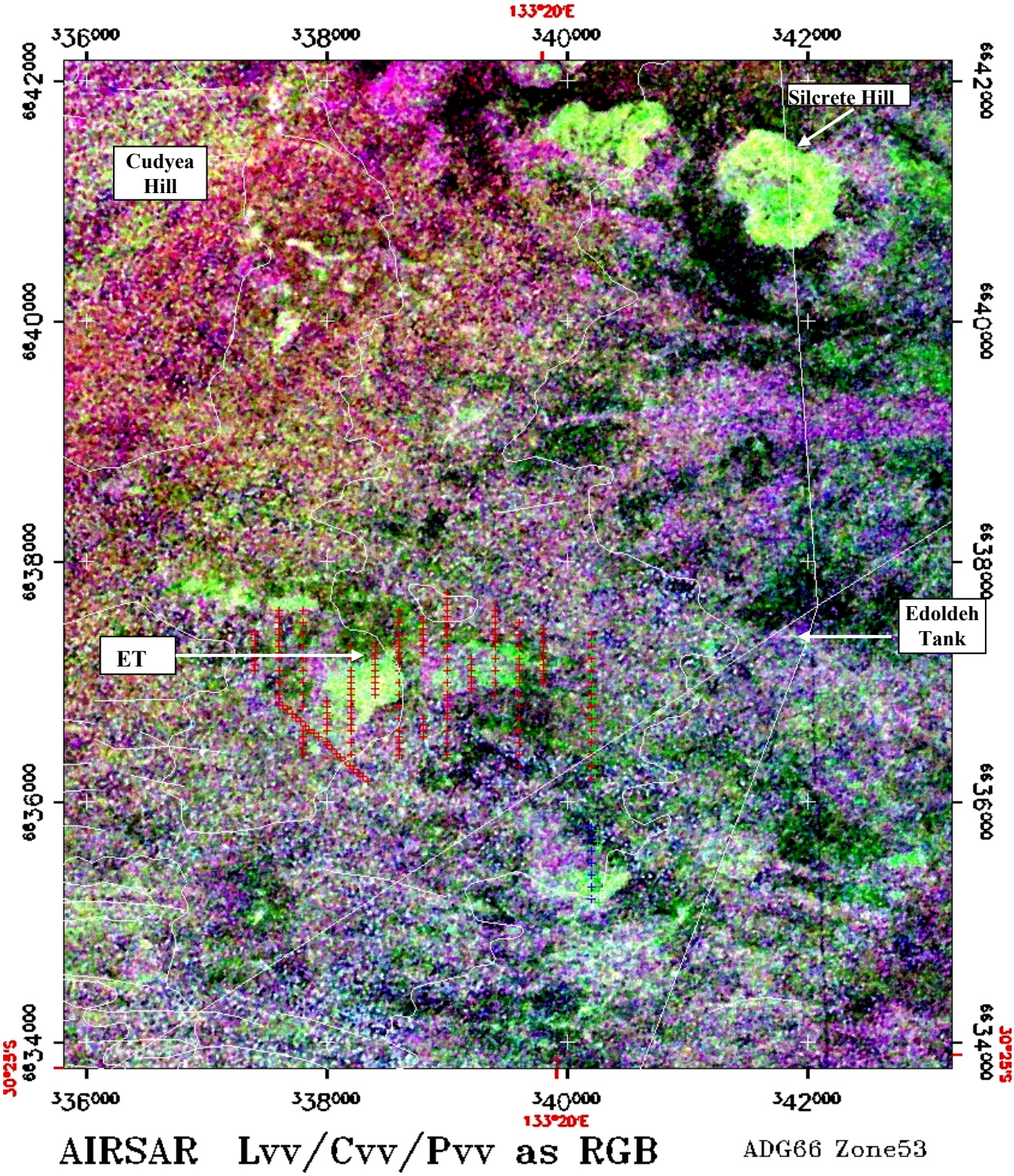

Figure 2-38 Colour composite image of AIRSAR bands Lvv/Cvv/Pvv displayed as RGB, of the ET region with an overlay of access tracks and drill-hole transects over the ET Gold Prospect itself. Silcrete gravels and massive silcrete, roughly at the wavelength of C band, are prominent as green hues. C band provides clear discrimination between erosional and depositional terrains owing to the relative smoothness, relative to P-band and, to a lesser extent, L-band wavelength, of regolith-landform units. These contrast strongly with the blanket of aeolian sediments (dark green) and vegetative cover of chenopod-shrubland communities, which have medium to high backscatter in L and P bands (magenta).

The spatial distribution of lag gravels is very apparent in vicinity of ET and northwards towards Cudyea Hill. Small, localised scatterings of gravels can be observed together with larger units on the eastern pediment slopes of Cudyea Hill. Comparison of the image in Figure 2-38 with those of Landsat TM data in Figure 2-18 and Figure 2-25 show a strong correspondence at locations where there are large

occurrences of gravels and outcrop, such as ET and Silcrete Hill. However, the Landsat images are unable to resolve the small and isolated patches. This is partly due to the reduced spatial resolution of Landsat TM compared with AIRSAR, and the fact that Landsat signals are in response to the chemical or mineralogical properties of the surface materials whereas radar responds to changes in surface texture. Where scattered gravels occur over sand, the spectral response from the gravels is often disguised by that of the background sand, thereby reducing the ability to determine their presence. Radar's sensitivity to textural changes often results in a superior ability to map surface materials present in low amounts, even in the presence of grassland vegetation.

A 3D perspective image in Figure 2-39 of the radar bands superimposed on the TOPSAR elevation data and viewed from the southeast provides an excellent view of the relationship between local topography and landscape elements (particularly the erosional units where outcrop and lag gravels occur).

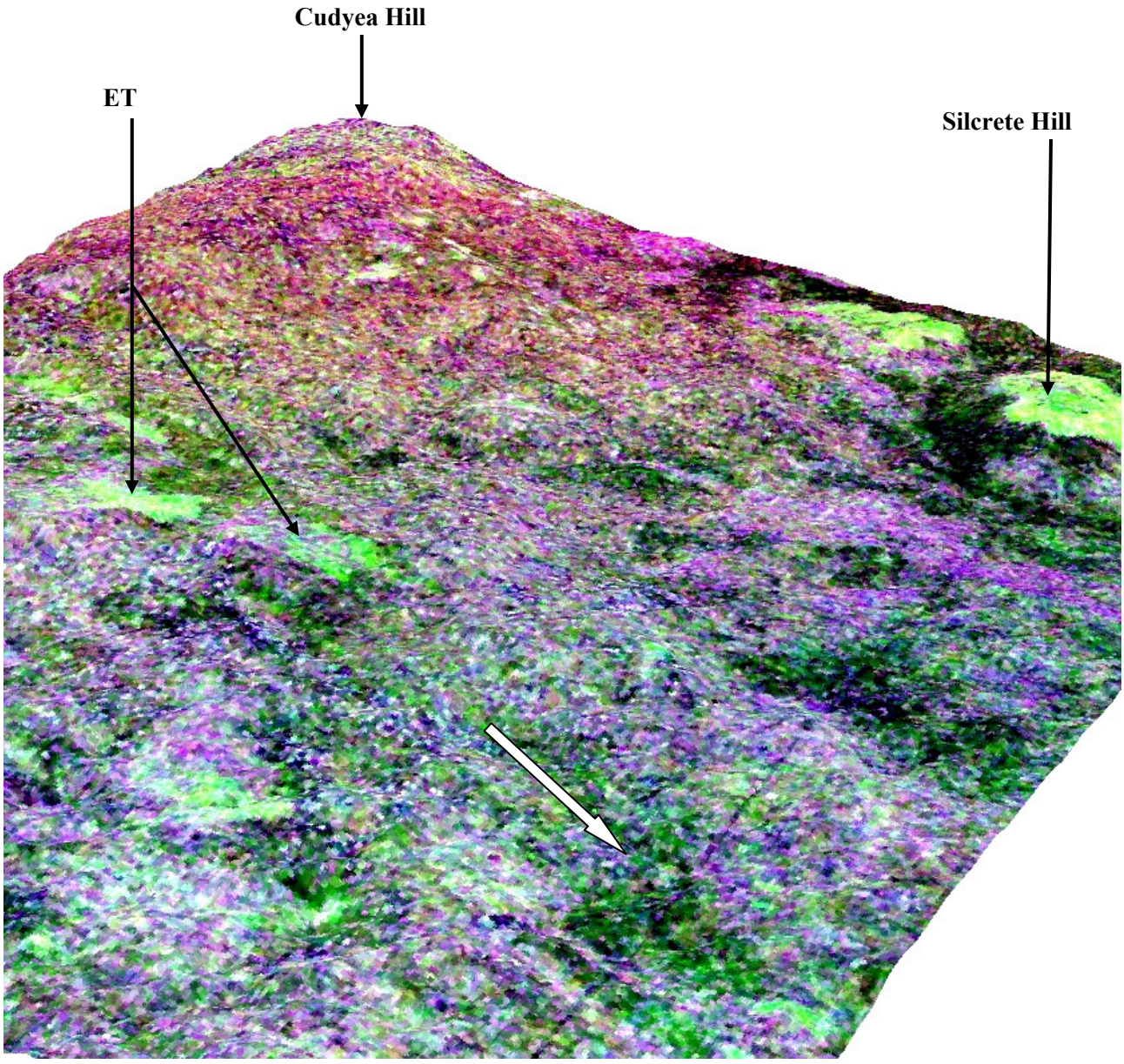

Figure 2-39 3D perspective image of ET with 10x vertical exaggeration of AIRSAR bands Lvv/Cvv/Pvv overlaid on TOPSAR DEM demonstrates the relationship between sites of abundant silcrete lag in hues of bright green and topographic highs where bedrock is proximal to the ground surface. This enhancement also highlights the position of a broad southeast-trending valley draining from ET. This might have implications for Au transport in the regolith (Section 5.4.3).

2.3 Summary and conclusions

Various datasets have been examined to investigate their potential to provide information useful for regolith-landform mapping in the ET area where, apart from minor outcrop, localised colluvium and lag gravels in vicinity of shallow bedrock, the basement rocks are masked by sand plains and dune fields of the Great Victoria Desert. The mapping of regolith-landforms and their representation in map form is considered essential to develop an understanding of the presence and distribution of regolith regimes (Figure 3-5) and regolith units (Figure 3-9), and a pre-requisite for geochemical sampling (Section 5) to be employed. Once a map has been compiled, simplified map sheets of thematic information, such as geomorphic regimes (erosional *vs* depositional) with present-day drainage, can be compiled.

It is difficult to interpret or postulate subsurface details of regolith stratigraphy, geological structures or palaeodrainage with any confidence from SPOT-PAN, Landsat TM and HyMap^{TM} datasets. Image enhancements of these datasets present very informative 2D views of the landforms and surface properties that can be further enhanced by overlaying on a DEM and viewing the surface as a 3D perspective model. Near-surface (0-25 cm depth) descriptions of radioelement concentrations of K, Th and U are available from airborne gamma-ray spectrometry signals but the usefulness of these data for mapping the regolith is controlled by the line spacing, gridding and calibration of the data. This is particularly important in areas of minimal definition such as ET where the majority of bedrock and indurated materials are masked by aeolian sands.

Precision DEMs are invaluable for mapping and understanding the attributes of a landscape, and should always be regarded as a critical baseline dataset. DEMs are especially useful in low-relief sandridge terrains where sand dunes will often disguise local undulations in basement topography and the presence of basement highs. In deeply weathered and eroded landscapes such as at Challenger Gold Deposit, the majority of erosional landforms are disguised by a thin cover of sands that can result in their misinterpretation as depositional landforms. A high resolution DEM will normally allow the very subtle topographic imprint of these landforms to be recognised. In general, shaded relief images and derivative images of height including slope, aspect and curvature will provide an informative insight into the topography, geological structures and drainage systems of a landscape. In addition, elevation datasets should always be a pre-requisite for improved understanding of enhancements of geophysical, optical and radar datasets.

Landsat TM data is the only operational multispectral dataset of adequate spatial resolution available for routine regolith-landform mapping. Nevertheless, it has been demonstrated in this and other projects including Tapley and Gozzard (1992), Gozzard and Tapley (1992), Wilford *et al*., (1998) that many terrain classes are spectrally unique using Landsat TM data. For example, in this project, canonical variate analysis and the Spectral Angle Mapper classification technique have demonstrated that regolith units of different compositions can be mapped and discriminated based on their distinct 6-band spectral properties according to lithology, weathering and erosional characteristics. The costs of generating enhancements from Landsat TM data are relatively small. A full scene is equivalent in area to a 1:250,000 scale map and the geolocated data are available from the Australian archive for around $2,000. The data can be quickly reduced to apparent reflectance using a radiative transfer program such as HYCORR and a draft image-map, unsupported by field verification, produced using appropriate processing techniques.

The limited numbers of minerals present in the surficial regolith at ET indicate that the use of hyperspectral data is most likely unwarranted. Although these data have been shown to provide quantitative information about the mineralogy of the regolith and, in effect, map regolith endmembers, and may have an untested potential for geobotanical studies (including possible indication of sub-surface structures), the considerable expense of the data probably precludes use for routine regolith-landform mapping in regions dominated by dune fields and aeolian sand cover.

As shown in this study, radar data of appropriate frequency and polarisation are very effective at discriminating between erosional and depositional regimes, based on differences in their surface texture, providing the speckle and electronic noise content of the data is minimal. Datasets from future satellite radar systems including the European ENVISAT and Japanese ALOS-PALSAR should be considered. Each system is considered appropriate for mapping landforms and surficial regolith in semi-arid and arid regions of Australia.

3 REGOLITH MAPPING (M. A. Craig)

3.1 Introduction

3.1.1 Objective

The purpose of constructing the ET Regolith-Landforms Map is to provide a detailed regolith framework for further geochemical investigations of anomalous Au concentrations found as a result of an earlier regional geochemical survey conducted over the ET Gold Prospect area. This regolith map, its associated databases and GIS data, should provide essential information about the detailed distribution of regolith materials and landform associations where it is not currently available from other sources.

3.1.2 Previous investigations

The ET Regolith-Landform Map is at a scale of 1:10k and covers an area of approximately 5 km by 5 km. The location details are provided in Section 1.1. Regolith polygons for this new map are generated largely from information derived from local fieldwork, interpretations of enhanced Landsat TM imagery, AIRSAR processed imagery, HyMap™ data and a custom local digital elevation model. All spatially located datasets including regolith polygons, field-site descriptions, and field-site photography are provided in an ArcView® Geographic Information System (GIS) of the study area (Appendix DVD). A plot-file, suitable for creating hard copies of the map, has also been included with the digital data.

Existing information about regolith and landscape evolution of the area is sparse or may only be extracted from information contained in much broader studies. Geological mapping in the region includes aspects of the geomorphology of much larger areas (*e.g.*, Benbow, 1982 (Coober Pedy 1:250k map sheet) and Rankin and Benbow, 1996 (Barton 1:250k map sheet). There are more recent regolith-landform maps, supplementary databases, GIS packages, and reports produced for areas near to the study area or that includes the study area. One map, the 1:100k scale Half-Moon Lake Regolith-Landform Map (Wilford and Craig, 1998a) covers an area of 64 km by 81 km, and includes the study area. The map is based largely on reconnaissance fieldwork, interpretations from enhanced Landsat-5 TM imagery, gamma-ray spectrometry and regional scale digital elevation models. Although it includes the ET Gold Prospect study area in its SW extremity, it is not at a scale that is suitable to support the more detailed investigations described in this study. The other map, the Jumbuck Regolith-Landform Map (Wilford and Craig, 1998b), describes areas beyond ET and so is not directly relevant to the scale of this present study. Supplementing these recent, regolith-landform maps, and derived from their parent data, is a series of thematic regolith-landform maps. These thematic maps are either not at suitable scales or they do not include the present study area. A new and much more detailed regolith map, at 1:10k scale, was therefore required to support the ET study.

3.2 Methodology and datasets

3.2.1 Mapping approach

The ET study required a regolith map of at least 1:10k scale to establish a regolith framework to assist detailed geochemical investigations at the site (Section 5). This scale requirement presented some early difficulties, because for example, aerial photographs (which are often the initial datasets used), were only available at either 1:25k or 1:82k scale. In the case of the 1:25k, photos were acquired by a K17 camera in 1949 (Figure 3-1), and in the case of the 1:82k, they were acquired by an RC9 camera in 1970. Neither dataset was entirely suitable because their scales were not optimal for determining the detailed regolith-polygon boundary positions needed to produce the regolith map at 1:10k scale. Even when diapositives were scanned at a very high resolution enabling good quality enlargements to be made, regolith characteristics were still too difficult to recognise and therefore boundary positions could not be determined with sufficient confidence. Greater reliance on other datasets was therefore required to construct suitable regolith-landform mapping units for the area.

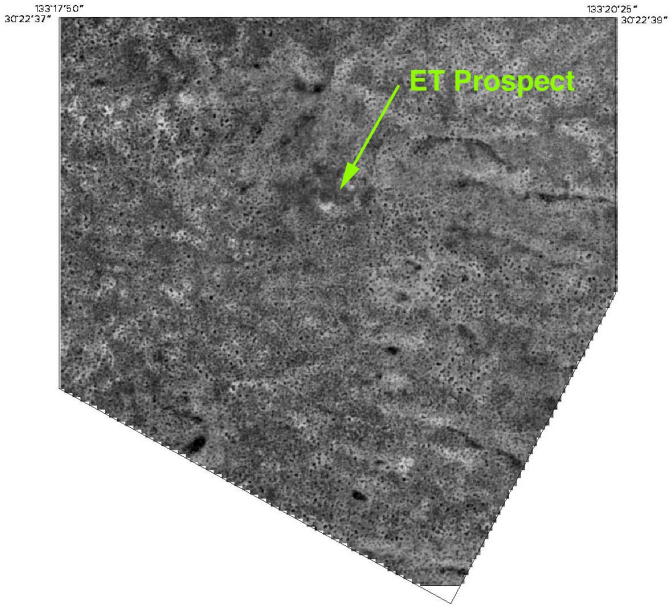

Figure 3-1 K17 aerial photography provided the basis for construction of a regional digital elevation model. A byproduct of the DEM construction is the georeferenced orthophotomosaic of the broader area surrounding ET. The orthophotomosaic contains visible spectrum data useful in the regolith map generation processes.

Subtle variations in regolith attributes were recorded by field observation to help determine regolith-landform unit boundaries and to improve final boundary positioning when using other datasets. Minor regolith material and landform variations, determined from the field, were then compared with the more general landform boundaries and regolith material clues extracted from aerial photography, remote sensing (Section 2) and the custom-built digital elevation model (DEM). The field patterns were then adjusted by a combination of regolith patterns derived from processed Landsat TM and HyMap™ and AIRSAR datasets and, to a lesser extent, by the digital elevation-model data. Fixing the final regolith-landform polygon boundaries in their map positions was a difficult process because there was no clearly identifiable recurring factor common through each dataset layer used that would allow a single simple boundary to be drawn. The final regolith-landform unit boundaries may still require experience and judgement from the regolith mapper for their optimal placement on a map, as was the case in constructing the ET map.

Processed remotely-sensed imagery played an important, but not a dominant, contributing role in determining the final regolith-landform relationships shown on the map. Detailed local field calibration is still an essential step when assessing the gross character of any patterns presented by processed remote-sensed imagery. Construction of the ET map is no exception. Field observations are essential in providing the clues to the subtle variability contained within local regolith frameworks especially for those determined at ET. Field observations of, for example, the location of diffuse lag boundaries or dispersed lag occurrences, still reveal that some helpful data are not observable in the remotely sensed imagery.

3.2.2 Map compilation and supplementary datasets

A number of datasets were used in the course of interpreting the regolith materials classes and the regolith-landform boundaries for the construction of the ET map. The false colour composite image shown in Figure 3-2 is from an AIRSAR dataset acquired over the study area and was one of the additional datasets examined as part of the process of the regolith-landform map construction. Field observations were required to help establish correlations between image signatures and materials at the surface. The dataset was processed to highlight (in red) locations interpreted to represent silcrete gravels. Comparisons of the red and blue responses in the image with detailed field observations show that the image is able to highlight areas where silcrete gravel concentrations and silcreted saprolite exposures occur, respectively. The image does not show areas on the ground where these are relatively small or scattered (*i.e.,* less than about 40% surface cover) but ground inspection does. Some polygons on the regolith map made use of

this extra ground information. Some silcrete can be seen on the ground in areas smaller than the 30 m pixel-size of the final processed image. This helps explain why some regolith-landform polygons shown in the regolith map have a strong correlation with the AIRSAR image patterns and others do not but still indicate that some silcrete is present. The regolith map is not meant to be a faithful mirror of the AIRSAR image patterns. Instead, the map draws upon the strong correlations between field observations and the AIRSAR image patterns. Elements of each of these datasets may be reflected in the regolith-landform unit boundaries. The map does not replicate all of the patterns present in each image used.

The images shown in Figure 3-2, Figure 3-3 and Figure 3-4 were used to assist with the construction of the regolith-landform map. The images were not used to generate specific TM-derived endmember polygons but to assist generally in regolith-landform unit construction and description. The imagery and its endmember units are available for examination within the study area GIS (Appendix DVD).

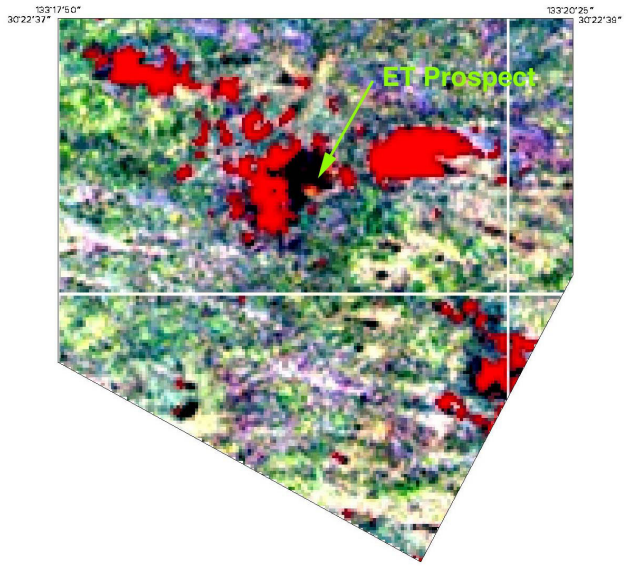

Figure 3-2 A colour composite image of AIRSAR bands, using Spectral Angle Mapping, (overlying a Landsat TM 247 image) highlighting in reds the interpreted locations of silcrete exposures including silcrete gravels (sub set of Figure 2-18).

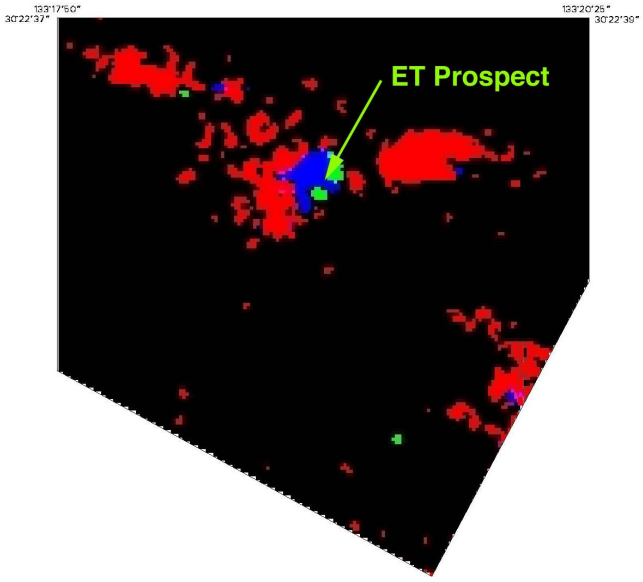

Figure 3-3 Landsat TM imagery demonstrating the combined aerial extent of silcrete and calcrete gravels (red), saprolite (green) and massive silcrete (blue). At ET, these regolith materials may be of significant value as potential sampling media and their distribution is a useful component of the regolith-landform s map of the area. The TM derived regolith patterns are not represented in the general regolith map as discrete endmember polygons. Subset of Figure 2-21.

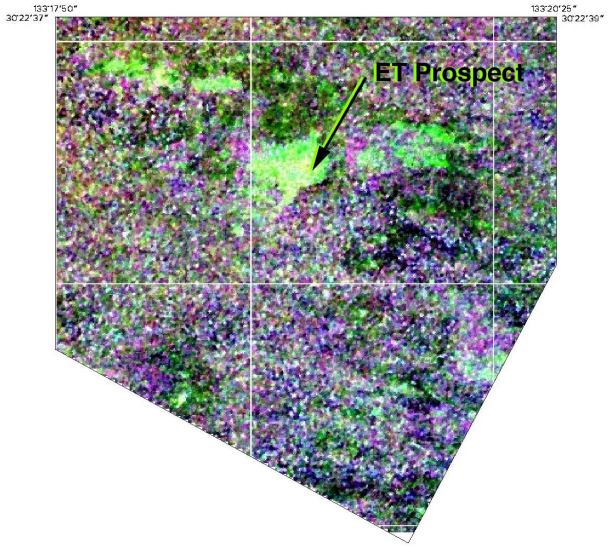

Figure 3-4 This image results from the processing of Thematic Mapper (TM) bands 2, 4 and 7. The TM data highlight, in red, the combined distribution of silcrete and calcrete materials throughout ET region.

Aerial photography provided the large scale 3D perspective and, as an orthophotomosaic, provided the small scale contextual framework for the construction of the map. The orthophotomosaic was a by-product of the construction of a detailed DEM by Intergraph Australia.

3.3 Regolith-landform maps and GIS

3.3.1 Digital data and GIS formats

Field data were collected in a digital notepad system using FieldworkerPro software and was connected to a Garmin 12XL GPS unit. During the field data collection phase, highly accurate GPS position data were not available because of restrictions by the satellite operators. Positional accuracy is reliable to within approximately 50-80 m. Field sites were selected for description where their contribution to map unit generation could be maximised. Most sites were photographed with a digital camera. The images assisted in generating accurate legend descriptions for the map and formed the basis of regolith-landform unit descriptions for later entry into RTMAP. RTMAP is the national regolith-landform attribute database, the custodian of which is Geoscience Australia, Canberra. The digital images were also used to assist with the calibration of various forms of remotely sensed imagery used in the study. At intermediate, and final stages, data were transferred into ESRI's ArcView® software for examination and analysis.

The final regolith map was generated in ESRI's ArcInfo™ because it allows greater compositional flexibility and also allows easier compliance with established national regolith map standards already operational at Geoscience Australia. A final version hard copy map has been produced. This map is a general regolith map and does not purport to follow any one the many possible themes that can be produced from the digital mapping data collected for the study area. Options for the construction of custom thematic map are probably better explored within the ArcView® digital environment. Hard copies may be generated from those data assessments.

3.3.2 Map face key

Eight supplementary images were included in the standard map-face layout of the regolith-landform map. One image included is the RED tile Figure 3-5. This classification theme is now well understood by the exploration industry and seen as a simple lead to understanding the often-complex data contained within the regolith map. The RED scheme (Anand *et al.*, 1989; Craig, *et al.*, 1992) is a geomorphic processed-based theme (Craig, 2001) dividing the mapped area into "Relict" (*i.e.* elements of "old landscapes" including silcrete duricrust), Erosional and Depositional.

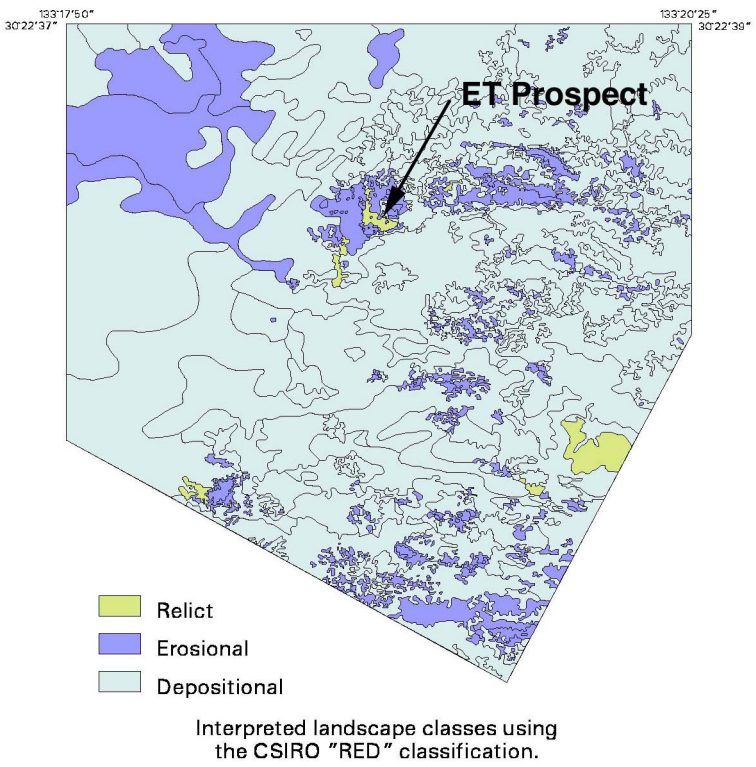

Figure 3-5 ET region showing thematically classified areas as relict, erosional and depositional.

A DEM showing the location of the study area and the position of the ET Gold Prospect is also included on the map Figure 3-6 (see also Figure 1-4). This style of image is not yet routinely added to regolith-landform maps but is an available option whenever a DEM has been constructed. The DEM was a useful reference image used during the generation of map unit polygons. It also assisted when visualising spatial distribution patterns within datasets, including geochemistry (Section 5).

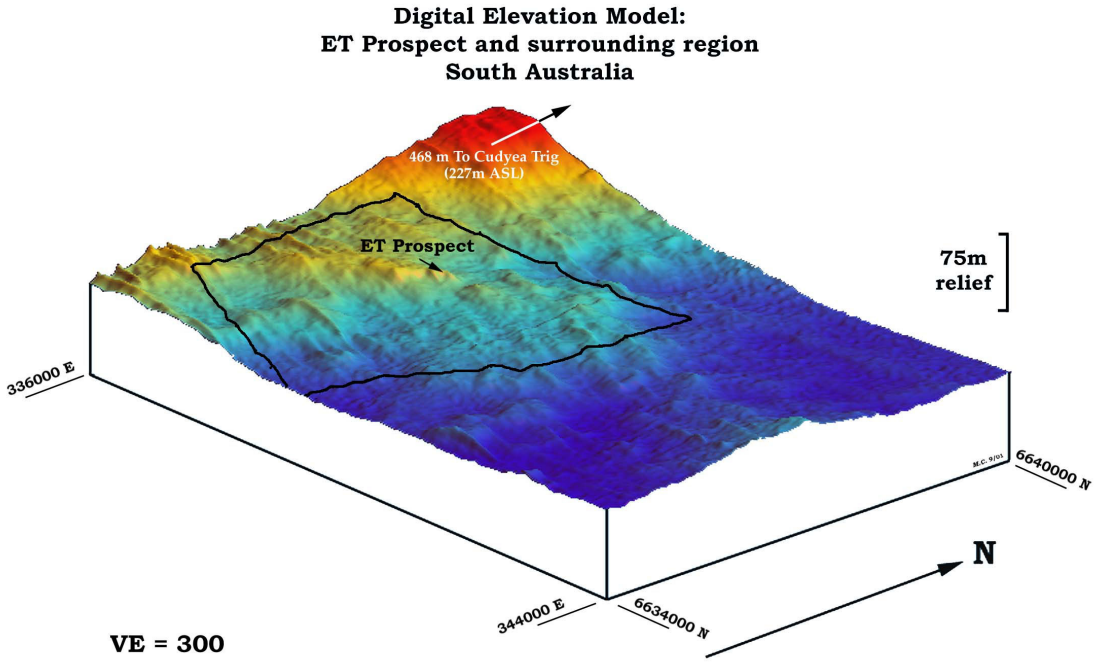

Figure 3-6 False colour RGB digital elevation model generated from K17 (1949 vintage) black and white aerial photography with the ET study outline and the ET Gold Prospect included. High areas are shown in reds with lowest areas in blue.

The RTMAP (Pain *et al.*, 2001) recommended style of map unit labelling is a well-accepted standard within CRC LEME regolith-landform mapping practices. The format for depicting regolith-landform units is shown in Figure 3-7. This convention has been used in the construction of the ET Gold Prospect regolith-landform map shown in Figure 3-8.

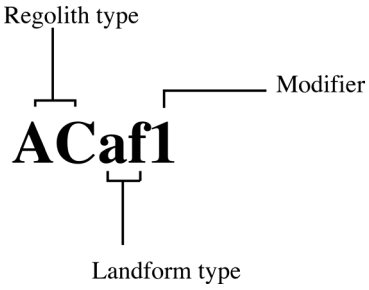

Figure 3-7 The CRC LEME conventional style for representing Regolith-Landform Map symbols. The modifier suffix is used to indicate subclasses related to the main map units. An explanation of the code options within this convention is contained within the RTMAP Field Handbook (Pain *et al.*, 2001).

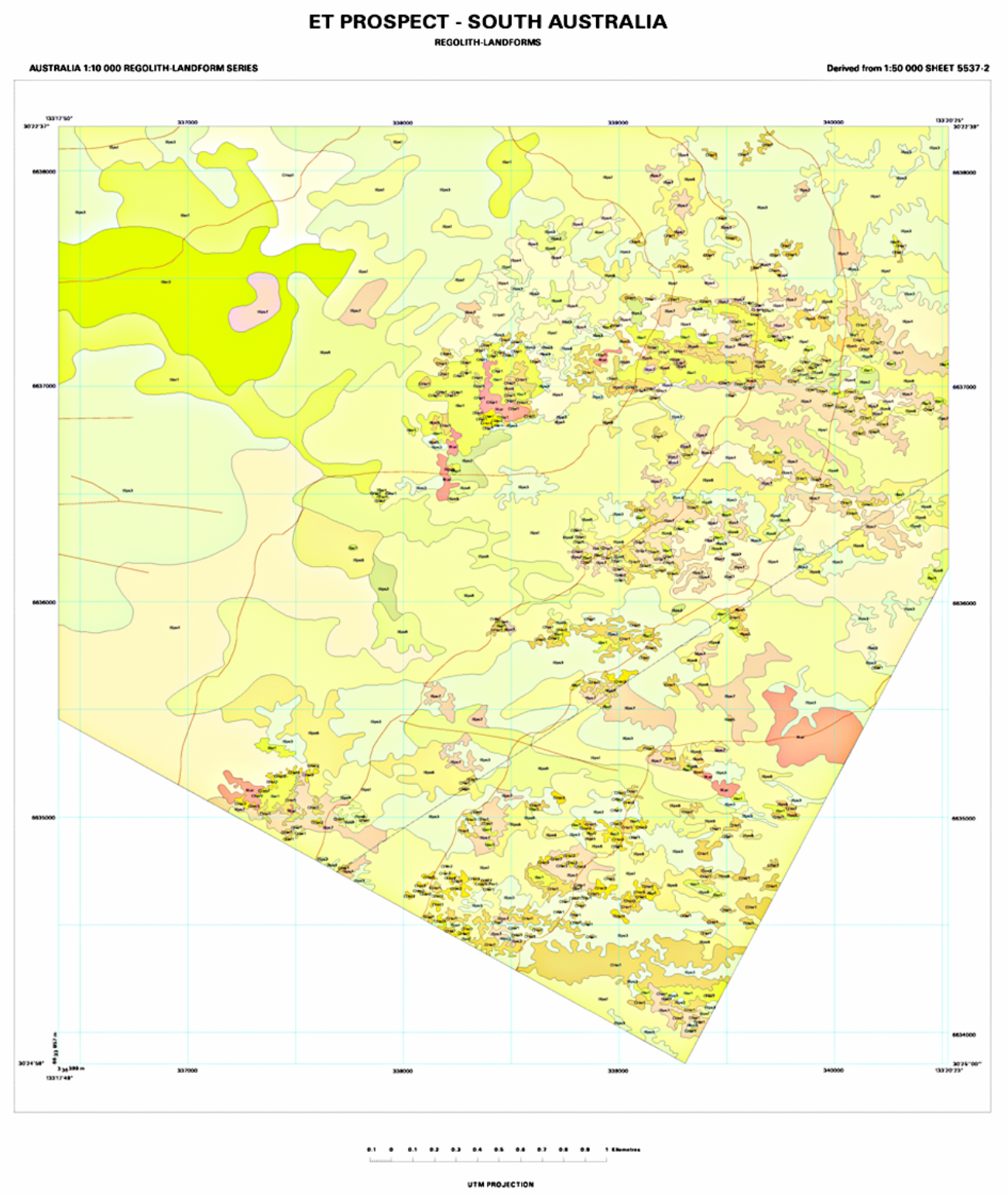

Figure 3-8 An extract of the ET Gold Prospect Regolith-Landforms Map showing the gross pattern of regolith polygons for the study area. Detailed map-unit codes and descriptions are available from the full scale map included with this report.

3.3.3 Regolith-landform mapping units

The ET regolith-landform map depicts a monotonous landscape consisting principally of sandplains, including stabilised dunes, with relatively minor windows through to weathered bedrock (Figure 3-8). It is a landscape with low to moderate overall relief (<50 m). Saprolite is rarely exposed at the surface. Instead, large areas are covered with sediments, predominantly aeolian but showing some colluvial influence.

3.4 Summary and Conclusions

Because previous maps were at inappropriate scales, a new map at 1:10k scale was required to provide the necessary regolith framework at ET. The use of multiple datasets and detailed field observation were required to achieve a suitable quality regolith-landform map in relatively featureless sandplain dominated terrain of the study area.

The ET study area consists of undulating sandplains (landform map symbol - ps) with distinct linear stabilised dunes. This sandplain landform category represents 82 percent of the area mapped. In the broader context, this landform class forms a portion of a much larger sandplain-dunefield complex at the eastern edge of the Great Victoria Desert. Minor landform features classified as depositional plains (pd) are windows within the sandplains that represent about 1 percent of the mapped area. Erosional landforms are also identified as are relict areas of silcrete duricrust Rises (er) represent about 16 percent of the landscape and a minor erosional plain representing about 1 percent of the area has been mapped.

Overall, in terms of process, the ET Gold Prospect study area consists dominantly of transported regolith (99% of map area) with a much smaller amount of *in situ* regolith (1% of map area) occurring as saprolite. The pie chart in Table 3 shows, as a "rolled-up" or simplest classification, the proportions of process-based, broad regolith classes for the entire study area. In contrast, the pie chart in Table 3 shows the expanded regolith material class-types that are independent of process.

The three regolith material types identified are shown as a percentage of the map area they occupy (Table 3). Subtle variations can be identified within each principal regolith type and these are shown in the complete map-symbol pie chart in Figure 3-9. The RTMAP (Figure 3-7) convention of subscripted suffixes is used to show subdivisions of the principal mapping classes. The ET regolith map shows a range of 16 distinct regolith-landform mapping units. The three most extensive regolith-landform units are variants of sandplains *i.e.,* $ISps_1$ (~29%), $ISps_3$ (~24%) and then $ISps_4$ (~12%). The remaining units represent smaller percentages of the total map area. Mapping units with aeolian sand as the regolith material still accounts for 92% of the map area.

Table 3 The three categories of regolith may be divided into sub-categories. The percentages of each sub-category are shown with wind blown sandy sediments clearly dominating the landscape.

Category	Sub category	Percentage
Regolith class	*In situ*	1
	Transported	99
Regolith group	Aeolian sediment (IS)	92
	Colluvial sediment (CH)	7
	Residual materials (RL)	1
Regolith material type	Aeolian sand (IS)	92
	Sheetflow (CH)	7
	Lags (RL)	1

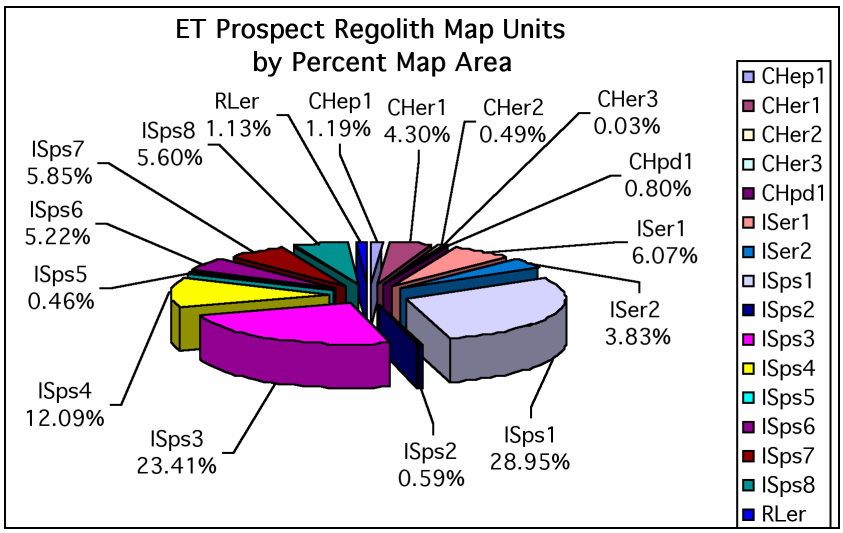

Figure 3-9 ET regolith map shows a range of 16 distinct regolith-landform mapping units. The first two letters represents the regolith type (CH=colluvial; IS =aeolian sand; RL=residual lag) and the second two letters represent the landform association (ep=erosional plain; er=erosional rise; pd= depositional plain; ps=sandplain). The number suffixes indicate sub-classes determined by additional attributes. See Figure 3-7 for the labelling convention. A fuller description of these mapping units and their attributes is available from the legend of the printed map or from within the GIS package.

The regolith-landform map provides constraints for the interpretation of the geochemical signatures (Section 5), and for the interpretation of regolith information extracted from detailed investigation of regolith stratigraphy (Section 4). The regolith-landform boundaries, especially on the printed map, provide a two dimensional representation of regolith exposed at the surface. A printed paper map can not easily depict the third dimension because it represents the intersection of regolith with the landsurface. Other digital data alternatives are available to better represent regolith in the third dimension. Some limited information for regolith in the third dimension is provided by the DEM image, and through extra information provided in the legend descriptions. Information about the third dimension is best provided within a database and additional visual layers forming part of a broader GIS package for the area (Appendix DVD). A comprehensive database was constructed from fieldsite observations, including information derived from the logging and analysis off drillspoil at the surface.

4 STRATIGRAPHY AND REGOLITH (M. J. Sheard)

4.1 Methods

All RAB drill cuttings were field logged and sampled for later detailed logging and sub-sampling at the PIRSA Core Store Facility in Adelaide where they have been permanently lodged for future reference. Small reference samples from all drilled intervals were collected in the field (chiptrays, 200 drillholes). Each was photographed dry and moist, the dry phase photographs are incorporated in the GIS (Appendix DVD) and the moist set form a separate file to provide a colour enhanced view of materials that commonly present subtle colours or colour variants when dry. Logging was based on visual examinations and grain-clast characterisation, microscope examination, plus input from: PIMA spectral analysis (see 5.3.4), XRD (section 5.3.3) and SEM mineral identifications on unusual features, and geochemistry (section 5). The logs in the Appendix DVD are in an Excel spread sheet with four levels of description for each 2 m interval between 0-38 m plus an end-of-hole sample. The logging levels are as follows.

- 1st, provenance: transported *vs in situ*.
- 2nd, standard colours and brief textures.
- 3rd, broad regolith zones and bulk average colour.
- 4th, detailed materials descriptions.

The regolith terminology is based on the *Atlas of Weathered Rocks* (Robertson and Butt, 1997) and *Glossary of Regolith and Related Terms* (Eggleton, 1999). Refer to Figure 4-1 for an idealised regolith column and associated terminology (after Robertson and Butt, 1997). Standard colour notations follow those of Munsell Color (1975) and the associated descriptive word colours follow Kelly and Judd (1976). Where space was limited, codes were abbreviated following Sheard and Bowman (1996, table A2.1).

4.2 Scope

There are important limitations to the information that can be gained from RAB or RC drill cuttings at the macro- and megascopic scale. Regolith zonation, boundaries, colour or mineral partitioning (mottles, banding, cementation, staining, *etc.*), mineral species weathering variance with depth, and true thicknesses of important but narrow marker or mineral bands, are all difficult to establish. Understanding regolith profiles is crucial to properly interpreting any surface geochemical anomaly, or for inter-hole stratigraphic correlations where eroded or markedly thinned zones may occur. For instance, pedolith often retains some key residual chemical characteristics from the deeper underlying basement, whereas much of the leached saprolite may be depleted. Therefore, determining whether or not pedolith is present (partially or fully) should be a crucial part of any logging process. However, RAB cuttings are a poor medium for this type of work.

4.3 Down Hole Sample Contamination

Down hole sample contamination was found to occur at many of the 200 drill sites sampled during this investigation. In many cases, this contamination was visually obvious, *e.g.*, near-surface derived calcrete nodules, silcrete fragments and red-brown hardpan fragments at 30 m below their original source horizon. However, there were also less obvious contaminants found at similar depths including well-rounded quartz pebbles (3-30 mm diam.) within quartz-rich or clay-rich materials. These pebbles were initially interpreted to indicate the presence of thick transported materials but later laboratory microscope examination revealed otherwise. Although these rounded clasts superficially appeared to have derived from the kaolinite-rich saprolite, each one retained residual ferruginous coatings plus cavity and/or fracture infill more consistent with their derivation from higher in the profile. To resolve any confusing sample provenances in a few difficult cases, bulk cuttings were washed of fines and examined by microscope for the presence of *in situ* material indicators (relict resistate minerals with angular or delicate shapes, *e.g.*, graphite, multi-grained lithic fragments, quartz micro-vein fragments or minerals not likely to have been transported by fluvial or aeolian processes). Once visual logging was complete, additional checks on the *in situ vs* transported material boundary were made using PIMA spectroscopy.

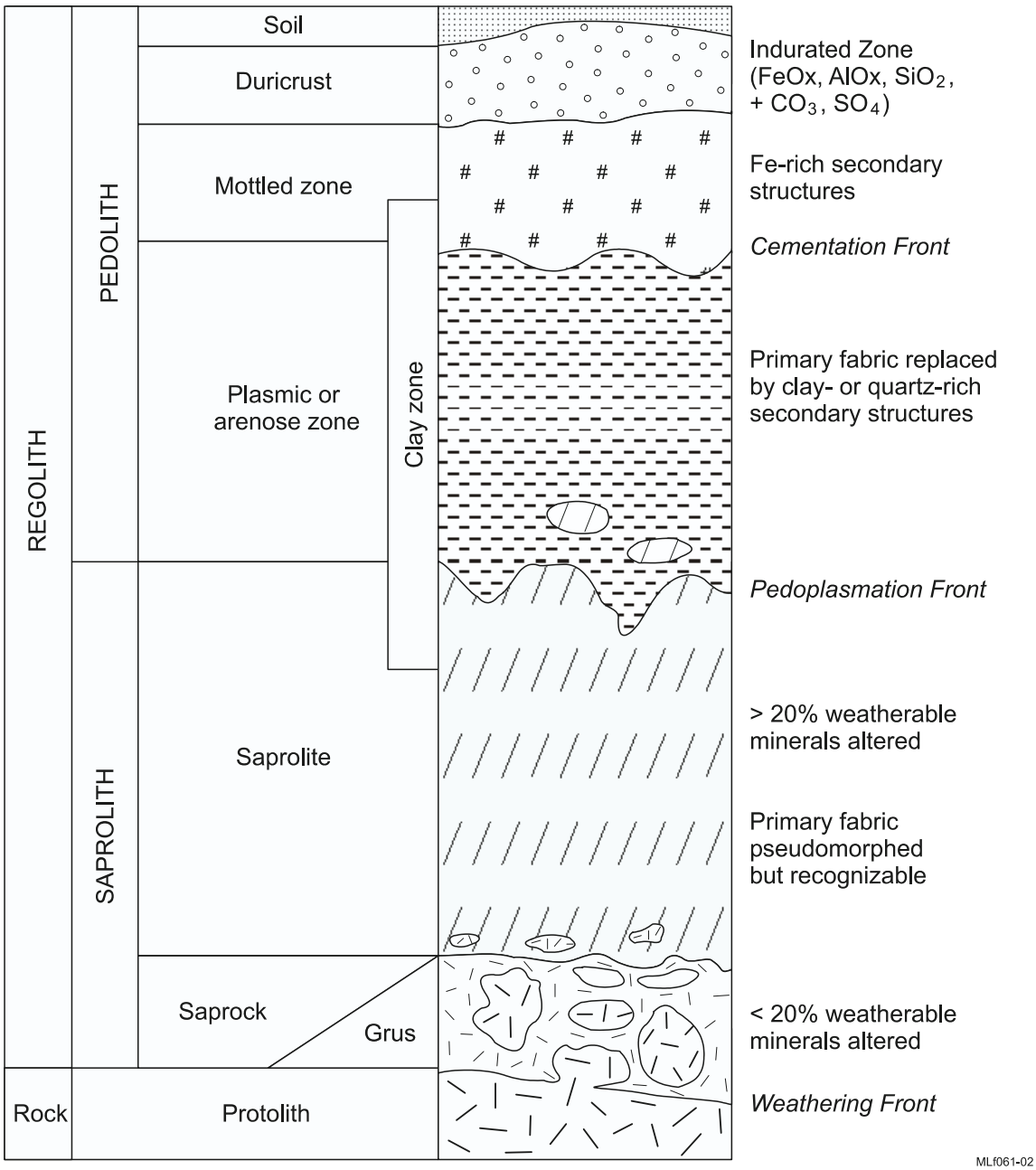

Figure 4-1 Regolith terminology for an idealised weathered profile with minor modifications for South Australian conditions (after Robertson and Butt, 1997).

Stacked PIMA spectra and kaolinite crystallinity indices (KCI) as vertical bar charts indicate the most likely boundary position. PIMA spectra and other related data can be found incorporated in the GIS Appendix DVD. Allowances were made for down hole contamination, sampling intervals and ambiguity where kaolinite content was too low for an accurate determination. Further allowances were made for silcrete and some pedolith or where smectite interference was high. Despite these, the visually logged *vs* the KCI boundary are highly correlated.

This finding leads us to recommend broad-scale use of PIMA with KCI's in the field, for inexperienced personnel to determine sample provenance more reliably and therefore to improve sampling, analysis and data interpretation.

4.4 Regolith overview

Archaean bedrock is extensively weathered to depths exceeding 70 m, commonly well below the normal maximum depth of RAB drilling; true protolith (unweathered basement) is thus rarely encountered. Saprock, with some altered feldspars and micas, appears to thicken on finer grained rocks. A more

complex saprolite zone overlies the saprock and is variably coloured, partly Fe-stained or mottled (red, brown or yellow) with distinct weathered minerals partitioning. Much of the upper saprolite is pale coloured to near white where the original rock was felsic in bulk composition, but where a more basic-mafic lithotype occurs, saprolite is usually strongly or brightly coloured. A pedolith <4 m to >18 m thick caps the saprolite. It can exhibit micro-mottles, Fe and Mn staining, and secondary cementation, but usually all primary rock textures have been obliterated by pedogenesis. The pedolith is intensely silicified within its upper part (silcrete horizon), whereas deeper partial silicification has yielded porcellanite and indurated or incipiently indurated pedolith. Transported materials up to ~11 m thick (holes 044 and 185) overly the deeply weathered basement (Figure 1-5). These sediments include: a colluvial-alluvial part of the silcrete horizon, a hardpan unit, a younger colluvium-alluvium, aeolian sand and calcrete. Dune sand dominates the transported materials in volume and lateral coverage. Those materials above the silcrete are essentially un-cemented, apart from the calcrete horizons. An impression of the overall extent and thickness of the transported cover is provided by an isopach plan (Figure 1-5) that should be compared with the local DEM (Figure 1-4).

Field inspections of silcrete outcrop indicated a dual provenance for its host lithotype (*i.e.*, saprolith plus sediment). The boundary between these two distinct regolith provenance components is within the silcrete duricrust horizon. PIMA KCI data confirmed the *in situ*-transported boundary to usually occur within the silcrete or just below it (Appendix 6).

A 3 D overview from the regolith drillhole information (Figure 4-2) shows the standard colours, plotted after conversion to digital RGB format for display (see also Appendix DVD and GIS). Where, weathering depth, pallid-leached zones, occurrences of basic-mafic lithotypes, lithotype and regolith zone facies variations between holes or across the prospect and the transported materials are easily examined. The use of 3 D visualisation for regolith analysis is strongly recommended.

4.5 Regolith Materials

4.5.1 In situ *Components*

4.5.1.1 Crystalline Basement – Protolith

Christie Gneiss, a compositionally layered Archaean metasediment, forms the crystalline basement at ET. This has undergone multiple deformation and peak metamorphism to granulite facies. Later intrusions and hydrothermal mineral deposition have led to a complex foliated crystalline rock with pro-grade and retrograde textural fabrics. In the nearby Mt Christie outcrop area (~20 km ENE) this paragneiss is described in bulk as being a cordierite-garnet gneiss with plagioclase-K-feldspar-quartz-cordierite-garnet-biotite mineralogy. However, its more basic variant bands contain quartz-plagioclase-diopside ± hypersthene ± garnet ± K-feldspar (Whitten, 1965: Daly *et al*., 1978; Daly and Fanning, 1993; Benbow *et al*., 1995; Rankin *et al.*, 1996). BIF lenses and bands, as seen at Mt Christie, previously described by the same authors, were not observed at ET. Local deformation has led to strongly schistose variants within the otherwise gneissic fabric. Some of these variants may be true tectonic mylonites whilst others represent genuine meta-pelitic bands. Unweathered-unaltered basement fragments in drill cuttings appear in less than 7% of all holes, and most basement fragments are transitional to saprock.

Medium- to course-grained rocks in a near unweathered state are rare and have a mineral assemblage comprising quartz-feldspar-mica-garnet ± opaques, where the mica is commonly muscovite but biotite was also observed. Garnets are 1-2 mm in size and reddish to brown coloured, comprising up to 20% of some rock chips. Graphite, a trace accessory mineral, forms sub-millimetre sized irregular grains to plates, or slightly longer rods and these persist within the profile even where the rock has been altered or strongly weathered. Medium-grained basic rocks are not common but their mineral assemblages comprise quartz-feldspar-biotite-muscovite- ±?amphibole or ?pyroxene. Because the end-of-hole samples are generally very altered and/or weathered, more broad scale comments must derive from materials and relict textures retained within the saprolite. Where the saprolite is pale and thick, the mineralogy and fabric suggest a felsic-intermediate rather than basic-mafic composition. Section 337600E (holes 114-125) is predominantly of felsic composition (except hole 123) and indicates how deeply weathered these rocks generally are (Figure 4-3 and Figure 4-4).

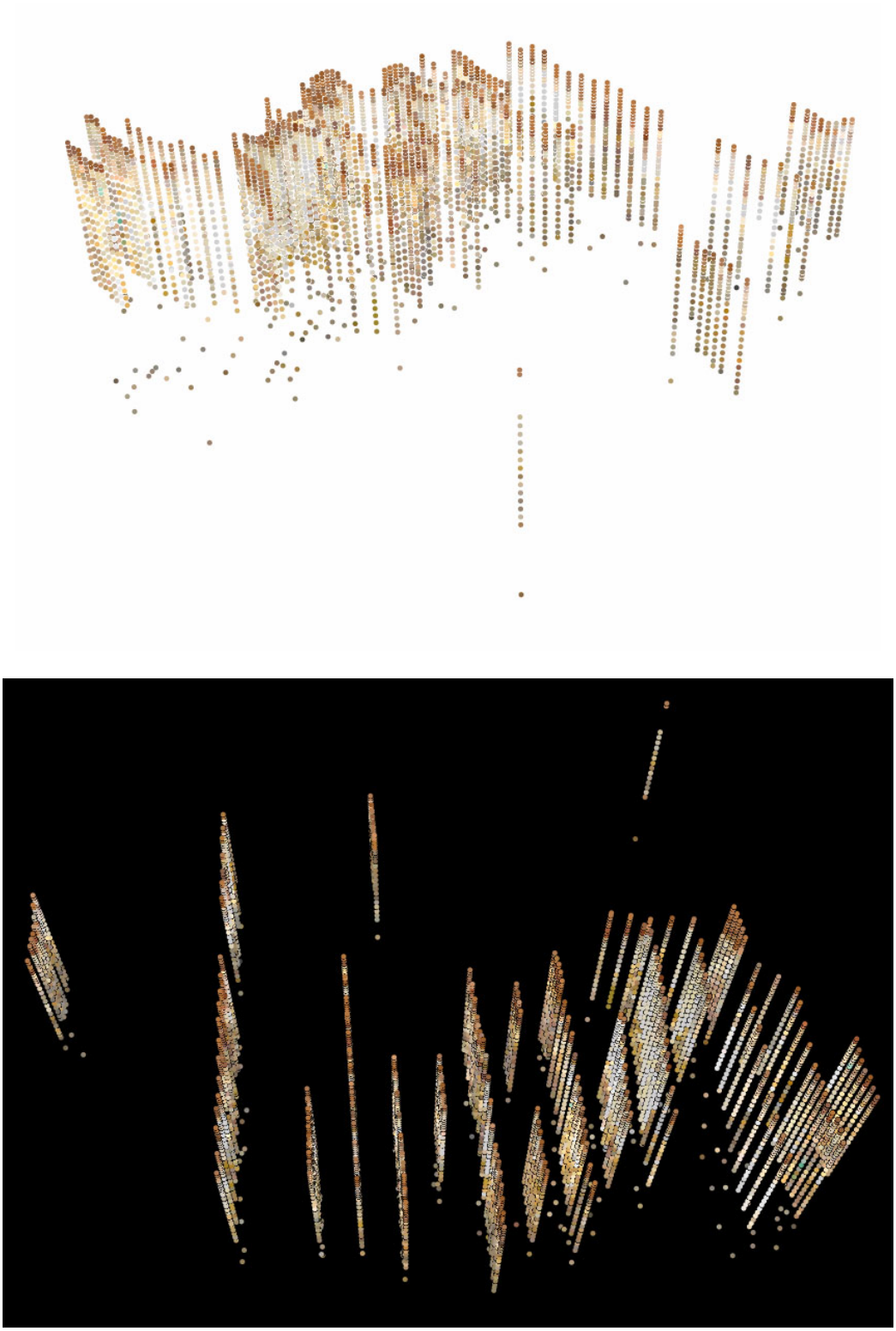

Figure 4-2 3D images of the ET Gold Prospect showing Munsell (1975) and Kelly and Judd (1976) colors of the drillhole data that have been converted to RGB colours for digital display using public domain software from Munsell Color Corp. Contrasting backgrounds highlight the darker and paler colours respectively. With ARCVIEW 3D analyst software and data on the Appendix DVD, these images can be rotated in any direction. There are over 390 distinct bulk colours used to describe regolith materials at ET. These displays amply demonstrate the deep weathering profiles, pallid zones plus occurrences of mafic lithotypes, and the strongly coloured transported cover materials.

Basement with a more basic-mafic to possibly ultramafic composition was intersected in 106 holes. In another nine holes the weathering front has extended far below drilling depth, leaving some ambiguity regarding classification. Basic-mafic lithofacies are generally fine-grained with a schistose rather than gneissic fabric. Many are weakly to strongly chloritic and contain abundant biotite and sericite with variable amounts of feldspar and quartz. This assemblage indicates a low temperature-pressure hydrothermal alteration regime has affected the rocks at ET prior to deep chemical weathering. Section 338600E (holes 031-043 and 092-096) demonstrates the mixed character (layered or banded) basement of this area (Figure 4-5 and Figure 4-6). Darker saprolith zones (basic-mafic composition) are interspersed with lighter more felsic lithofacies. In comparison, 339600E (holes 163-177) consists entirely of basic-mafic composition lithofacies (Figure 4-7 and Figure 4-8). In general, the more basic or mafic and fine-grained the basement, the less affected by deep weathering it appears to be. Nevertheless, most of these rocks were altered by earlier hydrothermal processes.

4.5.1.2 Saprock

Saprock (<20% weatherable minerals altered) is the common end-of-hole regolith zone available for analysis. From the 200 holes examined, 31 terminated in saprock (sometimes with protolith as well) and another 62 holes had mixed character saprock and saprolite. In general, felsic saprock has a medium grey colour, the basic-mafic rock colours range over very dark grey to dark olive grey or dark olive. Staining and weathering colours tend to be dark brown or occasionally red and yellow. Saprock thickness varies markedly from approximately 2 to >10 m which may reflect the pre-existing degree of fracturing and alteration. Weathering consists of fracture alteration on scales of millimetres to centimetres, ferruginous spotting and/or staining, black Mn mineral dendritic growths on fracture surfaces, some partial feldspar alteration to sericitic kaolinite plus random pseudomorphs thereof. Partial mica alteration to clays, and thin clay seams are recognised. At a few sites, chlorite may also have altered to nontronite (see Section 4.5.1.5). Smectite minerals are also prominent as a weathering product in the more mafic rocks. Saprock usually carries most of the relict mica although some muscovite flakes were also observed well into the saprolite zone.

Samples exhibiting different degrees of weathering reflect the often gradational or irregular weathering front and these were observed in several drillholes, *i.e*., protolith blocks remaining above the weathering front or saprock corestones remaining within clayey saprolite, as less altered relict enclaves within more weathered surrounds. Changes in the degree of weathering are shown on the Drillhole Logs (Appendix DVD). A further complication in determining whether a sample is protolith, saprock or saprolite relates to the degree of hydrothermal alteration at each site and how much this may influence classification at the visual logging stage.

4.5.1.3 Saprolite

Saprolite (>20% weatherable minerals altered but with rock textures-fabric generally preserved) is the dominant weathering zone material in drill spoil at ET. Its overall thickness ranges from approximately 25 m to more than 60 m and, like the protolith, consists of two broad types: felsic derived and basic-mafic derived.

Locating an accurate saprolite upper boundary position in drill cuttings is problematic. This boundary, the pedoplasmation front, normally marks a change from weathered material where primary rock fabric is pseudomorphed but still recognisable, to one where that fabric is totally replaced by secondary clay- or quartz-rich structures. Establishing an upper boundary is often difficult or requires an arbitrary decision in cases where the lithofacies is fine-grained, mica or platy mineral poor, or otherwise lacking in fabric indicators. Sites within a 100 km radius of ET indicate that the Christie Gneiss often exhibits primary fabric persisting throughout thick saprolite to within <3 m of the surface (Lintern and Sheard, 1999a; Lintern *et al*., 2000; Mason and Mason, 1998). Similarly, observations of the Mt Christie diamond drill cores CD01-CD03 demonstrated the presence of relict fabric within <5 m of the current land surface (Whitten, 1965: Daly *et al*., 1978; M.J. Sheard, 1999 unpublished data).

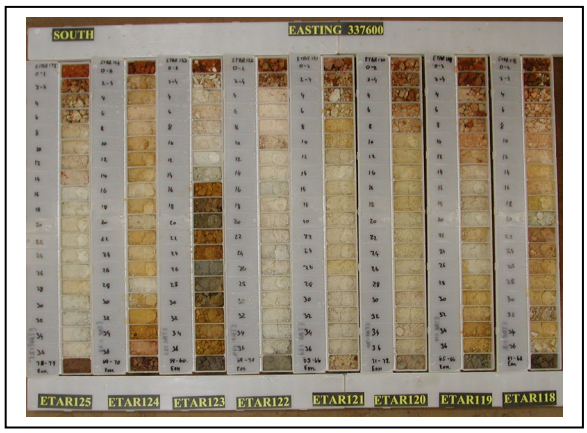

Figure 4-3 and

Figure 4-4 Moist chiptray photos of section 337600E (holes 114-125) displaying a mixed character profile where felsic composition basement dominates. (left image = S end of transect, right image = N end of transect).

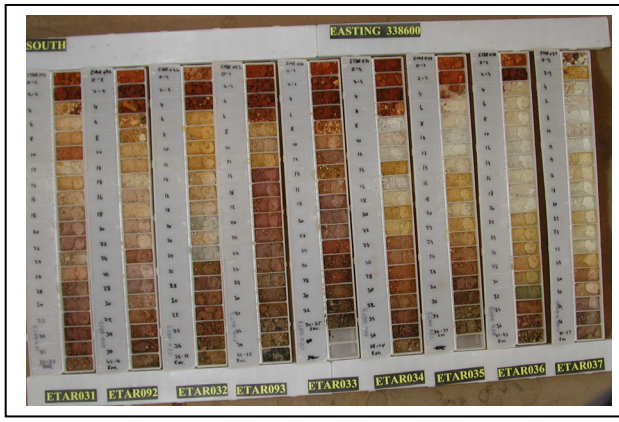

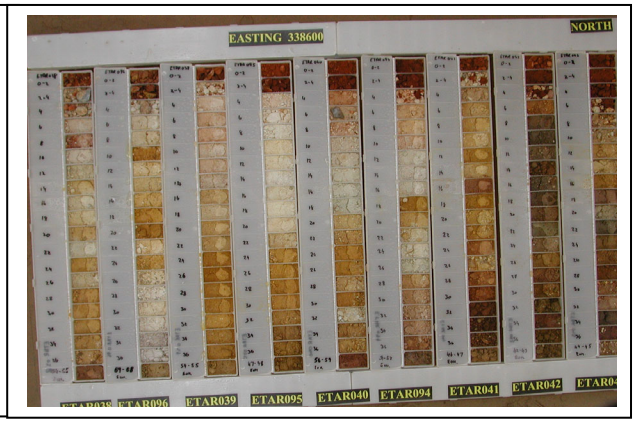

Figure 4-5 and

Figure 4-6 Moist chiptray photos of section 338600E (holes 31-43 and 92-96) displaying a mixed character profile. (left image = S end of transect, right image = N end of transect).

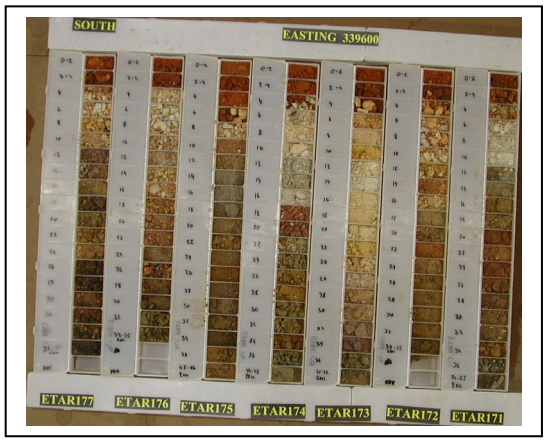

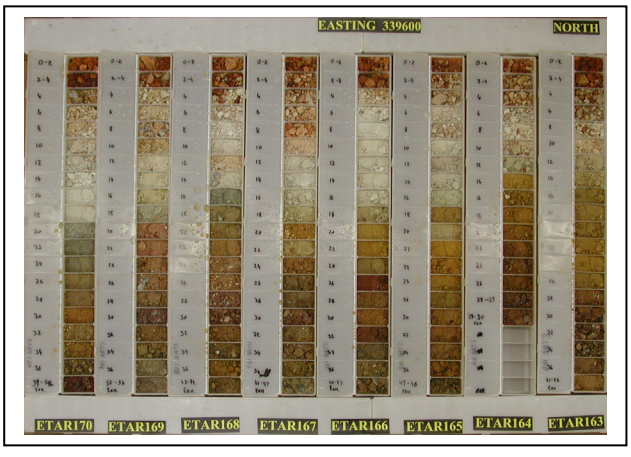

Figure 4-7 and

Figure 4-8 Moist chiptray photos of section 339600E (holes 163-177) displaying a predominantly basic-mafic profile. (left image = S end of transect, right image = N end of transect).

Where there was doubt during logging, the upper boundary has been shown as a gradational interval or has been placed where the last evidence of fabric was observed. In the latter cases, it may well be too low in the profile.

Felsic-derived saprolite generally consists of two main parts – a lower colour-rich zone and an upper colour depleted zone (referred to herein as a pallid or a leached zone). Colours in the lower zone range from medium neutrals with dark to medium grey tinting to strong and dark browns, reds, oranges and yellows. Upper felsic-derived saprolite has more subdued colours and where it is pallid, colours are subtle tints within an otherwise near neutral light grey to white quartz-kaolinite-rich material. Pallid saprolite (Munsell Value/Chroma: Neutrals >7/- or for all Hues 7/1-2 or >8/1-10) was intersected in ~75% of all drillholes. In the main, this material is dominated by kaolinite and quartz with minor illite, smectite, sericite, relict quartz veins and only weak mineral staining (if at all). In numerous holes, pallid saprolite has a thickness of >20 m but is more commonly <10 m. Observing any relict structures or fabric within this zone is difficult from cuttings but samples may occasionally exhibit mineral lineation and/or colour banding plus textural facies variants.

Small mottles (<15 mm) occur within both zones of the felsic-derived saprolite. They represent localised Fe oxide and hydroxide accumulations but do not appear related to the pedogenic mottles of near-surface soil horizons or to the mega-mottles in places encountered in pedolith. Mottles are coloured red, orange or yellow where the oxidation state reflects weathering and/or groundwater conditions during their formation. Sampling methods have prevented any determination of mottle morphology, separation or internal structures (such as fabric or zoning). Staining, different to mottling, was also present but its true nature is not fully definable. Some appears to be of a Liesegang type, some affects fracture surfaces only and some may form bands related to palaeogroundwater redox still-stands. Most of this staining is weaker in colour strength than the mottles mentioned above except where abundant Fe is present, as in the more basic-mafic lithotypes.

The **basic-mafic derived saprolite** consists of dark and strongly coloured materials in its lower zone while the upper more leached zone is much less obvious due to similar strong brown, red or orange colours being present. In this area, mottling can be present within either or both of the saprolite zones, but the true character of these coloured mineral partitions in a strongly coloured host is often difficult to determine. Colours in the lower zone tend to range from dark neutrals with colour tinting (dark to medium grey) to strong and dark hues (olives, rare greens, and browns). Chlorite is a ubiquitous mineral in the lower zone and usually determines overall coloration but commonly persists well into the upper zone. Smectite minerals are a common weathering product, especially in the upper zone. Black Mn oxide staining seems restricted to these more mafic rocks. It is unclear why in many intersections of this more ferruginous saprolite a pale to pallid top developed whereas at other, adjoining sites, little or no pallid zone occurs (*c.f.* holes 183 with 186, or several holes along section 339600E, or Figure 4-7 and Figure 4-8).

Resistate mineral preservation throughout both broad saprolite types is highly variable and somewhat unpredictable between holes or drill transects. Opaque accessory minerals such as graphite and, perhaps, ilmenite persist throughout the weathering profile. Whereas white micas, most biotite and chlorite usually disappear before the upper zone is encountered, some muscovite and rare biotite flakes were observed next to the pedoplasmation front. Garnet, amphibole and feldspar do not survive far into the lower saprolite. How far cordierite survives into this zone is not known but, at the Challenger Gold Deposit to the north, parallel lineation ghosts of this mineral were observed (from pit excavations) surviving well into the lower pedolith (Lintern and Sheard, 1999a; Mason and Mason, 1998). Unusual green and yellow-green minerals were encountered within the lower saprolite and less commonly into the upper saprolite. These occurrences are described below (Section 4.5.1.5).

4.5.1.4 Pedolith

Pedolith is the zone that has been affected by pedogenesis or soil forming processes. Its lower boundary, the pedoplasmation front, marks a change from persisting relict rock fabric to no original fabric preservation. It also indicates where newly formed weathering mineral fabrics and textures appear. In this area, an upper boundary is generally located within the siliceous duricrust, although elsewhere it might include the entire duricrust (see below). Due to the problems in recognising pedolith from saprolite already alluded to, its true thickness range is hard to establish but probably covers <4 m to approximately 20 m. There are two broad types of pedolith, felsic-derived and mafic-derived, but the distinction is blurred and not a reliable designation in isolation. Colours are similar to those of the underlying upper saprolite but often include pronounced reddish to brownish micro-mottles, lamellae, Liesegang haloes or

rings, bands and variable colouration horizons. Ferruginous staining along fractures, or of broad bands and irregular patches is common, especially above mafic rocks. The pedolith zone parallels the palaeotopography where the upper portion often presents as a waste mantle capping in which fines have been lost or much reduced through leaching, mechanical deflation or silicification processes. This upper portion has been, in-part, intensely silicified to silcrete but below there is often variably intense to incipient silicification. At sites where clay-rich hosts have been silicified, the end product is usually porcellanite. Some of that material preserves delicate 3D black Mn oxide dendritic structures on sub-millimetre to millimetre scales.

None of the drilled materials could be described as thick arenose or thick purely clay zones but some intersections approach those pedolith end members, being either quartz grit-rich or clay-rich. Mega-mottle zones (mottles >100 mm) were not observed either but that may just reflect the sampling method. Unusual green minerals were observed in this zone and are described below.

4.5.1.5 Unusual weathering products

Fourteen drill sites and 21 sample intersections revealed unusual yellow green (5GY 5.5/1, 5.5/4, 6/5, 7/4, 7/5, 8/4, 8/6) to bright green (5G 5/2, 5/5, 5/6, 6/3, 6/5, 6/6, 7/2, 7/4, 8/2 8/4, 8/6) mineral matter within the saprolith. These colours are unlike those of chlorite or fuchsite in being much brighter and paler. In two cases there were two distinct green colours present, suggesting banding or some other colour partitioning (holes 110 and 117). PIMA analysis suggested nontronite as the source for these colourations. Nontronite is a smectite with interlayer ferric iron. Occurrences were intersected within saprolith at depths of 14-26 and >32 m (holes 038, 104, 105, 107, 110, 117, 138, 178) or within the pedolith zone associated with or just below the silicification horizon at depths from 6 m to approximately 10 m (holes 077, 081, 092, 140, 151, 317). Most of these horizons are of ~2 m or less thick but four were up to ~4 m (holes 105, 107, 117, 138). Multiple intersections of these bright green horizons occurred in holes 105, 107 and 117, where horizon separation ranged from 4-27 m. Some clustering of occurrences is obvious (holes 138 and 140 and 038; 104 and 105 and 107 and 110) but otherwise the pattern is more random. However, in a broad context there may be an ENE trend to three of the possible linear parallel patterns. As most of the deeper occurrences are within weathered basement with a mafic bulk mineralogy, it is possible these are weathering products of Fe-rich materials (?dykes or bands). Alternatively they may indicate unusual weathering conditions involving Fe-rich groundwaters circulating at those locations sometime in the past.

SEM analyses indicate that Si, Al and O are the most abundant elements present in the greenish material with some Fe, K and Mn. Analyses suggest that some of the green colour may be due to Ni or Cr (Appendix 12). No quantitative analyses were performed but concentrations of Cr were estimated to be about 2-5% (M. Verall, CSIRO, pers. comm. 2001). Monazite grains were present in some samples as indicated by high concentrations of REE.

4.5.1.6 Duricrust – silcrete (silicified pedolith)

Within the silcrete duricrust horizon are two derived components, a lower silicified pedolith containing angular quartz grit and relict quartz veins, and an upper part containing silicified colluvium and/or alluvium (see below). All silcrete encountered at ET is pedogenic and silicifies existing regolith. This duricrust commonly contains partitioned wisps of titania minerals (*e.g.*, anatase and rutile) and relict resistate minerals such as graphite, zircon, magnetite and ?ilmenite. Sometimes pedolith micro-mottling and other colour segregations have been preserved within this siliceous horizon. Over most of the investigated area, silcrete averages from about 1 m to approximately 2 m in thickness but silicification fronts extending below the massive duricrust may increase total thickness to >6 m. Outcrop is limited, but a significant exposed pavement occurs near hole 134, where a breakaway escarpment has developed, exposing the duricrust profile down to partially silicified pedolith. The lower portion is generally pale grey to cream and sometimes yellowish coloured but can be stained a strong yellow to reddish along fractures. Colours due to the presence of subsurface brown or red ferruginous pedolith-saprolite are highly variable, commonly inconsistent and not predictable from bedrock. For instance, in an area of strongly coloured pedolith (S end of section 339400E) at holes 321 and 322, the silcrete is pale grey to yellowish. Nearby, between holes 317 to 320, the silcrete horizon ranges from pink to dark red-brown. Moreover, some of the brown to red-brown forms are porous, as if the silicification has captured an original ferruginous framework structure. Only at two locations (holes 039 and 141) did the silcrete appear to be exclusively silicified pedolith, without any transported components. Regionally the silcrete probably represents an

overprinting by at least two silicification cycles during the Tertiary (Lintern and Sheard, 1998: Lintern and Sheard, 1999a, b; Mason and Mason, 1998).

General duricrust thickness, being similar to the RAB drilling sample interval, in conjunction with downhole contamination, have made it difficult to comment in a meaningful way on silcrete thickness patterns, landscape position and palaeo-landscape preservation factors. Reference to the DEM (Figure 1-4) and sediment isopach (Figure 1-5) indicate there to be no significant landscape inversion, and silcrete along the NE-SW trending ridge, on the whole, is no thicker than elsewhere. These factors imply that the duricrust has preserved a palaeolandscape where subsequent erosion has been minimal rather than preferentially preserving more thickly armoured landscape elements.

4.5.1.7 Veining

Hydrothermal quartz veins occur randomly throughout the basement, these are usually semi-translucent and have colours from white to grey to bluish to dark bluish and zoned variants thereof. Vein mineralogy is unaffected by the weathering process, but the veins may have undergone physical disruption where the host rock has undergone a volumetric change during weathering. Vein fragments can exhibit entrapped wall rock lithotypes and minerals derived from there (*e.g.*, feldspar and muscovite). Vein thickness ranges from sub-millimetre to possibly tens of centimetres, yielding drilled fragments of 10-30 mm.

4.5.2 Transported Components

4.5.2.1 Duricrust – Silcrete (silicified colluvium-alluvium)

The siliceous duricrust horizon has two separately-derived components; an upper silicified colluvium to alluvium part, containing subangular to rounded quartz-rich gravel plus alluvial well-rounded quartz-rich clasts from fine gravel to large pebbles. Silcrete cement in this part is pale grey to cream and yellowish coloured, but can be stained a strong yellow to reddish along fractures (similar to the lower portion). It is a pedogenic overprinting and can contain partitioned wisps of titania minerals such as anatase. Whereas the total silcrete horizon is generally ~1-2 m thick, the *in situ vs* transported boundary may be anywhere within that horizon. Only at two locations, holes 039 and 141, did the silcrete appear to have no transported component, and these may represent places where erosion has removed part of the silcrete. This upper part probably represents an overprinting by at least two silicification cycles during the Tertiary (Lintern and Sheard, 1998: Lintern and Sheard, 1999a, b; Mason and Mason, 1998).

4.5.2.2 Alluvium

Fluvial alluvium, as distinct deposits (>0.5 m thick) of sand or gravel or cobbles, were not identified within any of the drill intersections. However, such materials do make up parts of other units described herein (upper silcrete and red-brown hardpan). It is likely that coarse-grained creek to sheet alluvium does occur in this area but limited outcrop, drilling methods and chosen sample intervals all preclude confirmation of this. Some of the silcrete outcrop exhibits well-rounded quartz clasts in sizes from fine gravel to pebbles and rare cobbles. Many of these indicate a long transport history in high energy fluvial regimes but distinct channel deposits of these were not observed.

4.5.2.3 Colluvium

Various colluvial horizons have been identified. The lowest is at the upper surface of the pedolith, where erosion by limited water sheet flow and wind deflation of fines or mechanical exhumation has left behind quartz vein fragments and resistate grains to form a palaeo-lag. Much of this material is highly angular to subangular, where little or no lateral transportation has occurred. On palaeoslopes, some down hill movement by gravity may have taken place. All of this colluvium was later massively cemented by one or more silicification phases to form silcrete. Subsequent partial erosion of the silcrete has yielded more colluvial horizons. The oldest of these directly underlies the red-brown hardpan and another younger one rests on top of it. These contain silcrete clasts, as well as vein quartz clasts. Again, most clasts are angular to subangular. A complication arises when no red-brown hardpan is present, in that colluvium is known to underlie both the dune sand and also sit on the current silcrete outcrop. Obviously these two units display a diachronous overlap from pre-hardpan deposition to modern day and they will partly equate to others separated by defined sediments like the hardpan. Cements in the post-silcrete colluvium include some Fe sesquioxides and calcrete, some are also weakly bound by illuviated fines.

4.5.2.4 Red-brown hardpan

Hardpan is used herein to describe a distinct red-brown to strong brown clay-rich colluvium to alluvium, partly or wholly silicified, that ranges from <1 m to <4 m thick. It sporadically underlies the dune sand and overlies the silcrete horizon but was not observed to outcrop. Hardpan contains dense or heavy textured clay, but some facies have appreciable quantities of silt to fine sand. Lenses, stringers and beds of well-rounded gravel also occur, both near the top and at the base; these are mostly clast supported but some may approach a matrix supported character. These data support this unit being dominantly of fluvial origin, as an overbank facies deposit, with minor channel facies and some colluvial facies contribution. Dark brown to black Fe and Mn sesquioxide and hydroxide cementing and/or segregations occur randomly. In places, this clay-rich material is partially coated near its top by a later input of powdery carbonate. Strong red-brown colours (2.5YR 3/7 to 3/8, 4/5 to 4/8 and 5/6) to brown colours (5YR 4/6 to 5/8) and overall clay-rich texture make this unit easily identified from all the others. An irregular upper surface to the hardpan indicates it has been partly incised by later erosive fluvial activity (*c.f.* between holes 185 and 195).

4.5.2.5 Dune sand

Aeolian dune sand blankets a large portion of this prospect and forms a significant dunefield fringe to the Great Victoria Desert system. Dating of these sands 80 km west of ET, exposed in a cutting ~3 km east of Immarna Siding on the Transcontinental Railway, places them into the early latter quarter of the Quaternary (dune crest near-surface sand >20 ka and dune core sand ~200 ka; Huntley *et al.*, 1999). Sand colours ranged through moderate orange (5YR 6/7) to brownish orange (5YR 5/7) to light brown (5YR 5/6) to strong brown (5YR 4/6 and 4/8) and less commonly moderate reddish brown (2.5YR 4/5). In some instances, illuviated fines have established more clay-rich dune cores that are darker or richer in colour than the sandier materials above them but the colour shift is never more than one hue interval. These colours are caused by thin ferruginous coatings on the sand grains. Grain sorting is generally uniform, of medium sand size and typical of aeolian-derived material but textures increase where illuviated silt-clay components form the denser dune cores. Over the investigated area these sands range in thickness from almost 0 m to approximately 11 m, where the overall average sand spreads are ~1-3 m thick and dunes average 4-7 m in height. Section 340200E has the consistently thickest dunes, peaking at >10 m in hole 185 but along section 337800E the thickest intersection occurs at hole 044 (~11 m). The sands are dominantly quartz, but may contain up to 20% feldspar. The sands host calcrete as nodules to massive bands to earthy-powdery or low density weakly cemented forms, sometimes in more than one horizon. The sand is generally loose or free running unless cemented by calcrete or clays (dune cores) but is mostly stabilised from reactivation erosion through the presence of vegetation. Palaeosols were evident in holes 185 and 182 (340200E) here the sand exhibited colour changes and possible mottling due to pedogenesis (Figure 4-11 and Figure 4-12).

4.5.2.6 Calcrete

Calcrete occurs throughout the upper regolith within dune sand, exposed silcrete and the soil profile. In the sands there is often more than one calcrete horizon. Forms include mostly nodules within dunes, earthy powders or coatings in some of the hardpan upper portions and significant laminated coatings plus joint infill on silcrete outcrop and subcrop. More indurated massive calcrete forms (some exhibiting karst features, Figure 4-10) occur in the thicker sediment wedges at the base of slopes or in depocentres. These depocentres may have developed in response to ephemeral down slope migration of soil-borne carbonate during times of intense meteoric water influx. Most indurated calcretes are mildly coloured, pale pink to pale orange. According to company (GJV) sample logging, there appears to be a trend towards massive calcrete in areas of thin to no cover and nodular calcrete adjacent to them in areas of shallow cover. However, many calcrete types were not specified in the database.

4.5.2.7 Lags

Surface residual lags are a minor component of this landscape (Figure 3-2). The lags are restricted to silcrete outcrop and generally consist of silcrete clasts, vein quartz clasts (both rounded and angular) and more rarely, calcrete fragments. At seven sites from the soil survey (see section 5.2), ferruginous silcrete clasts were sampled (R435950 to R435956). Four of the ferruginous silcrete lag sites are widely scattered but three are clustered between 338200E-338400E and 6636300N-6636600N. They comprise gravel to small pebble sized silcrete clasts with dark brown to dark yellow-brown colours, commonly containing

white to grey quartz sand grains. Despite their dark colouration, the total Fe content of these lags is <4%. Titanium concentration (<1.5%) is lower than expected for pedogenic silcrete and may reflect the general paucity of this element within the overall regolith profile. Gold concentrations do not exceed 2 ppb. Materials similar to these have also been reported from several other localities in the Western Gawler Craton (Lintern and Sheard, 1998, 1999a, b; Lintern *et al*., 2000; Povey, 2000). The lag component was further considered during the collection of site data for construction of the Regolith Landform Map (Figure 3-8). To represent better the distribution of lags (mostly undifferentiated) detailed boundary traversing was done using a GPS connected to a hand-held computer (see Section 3.3.1). Although the GPS accuracy was <50 m, a fair representation of the major lag polygons from the rises and associated backslopes was obtained. These are available within the GIS and a simple image of them is provided in Figure 4-9.

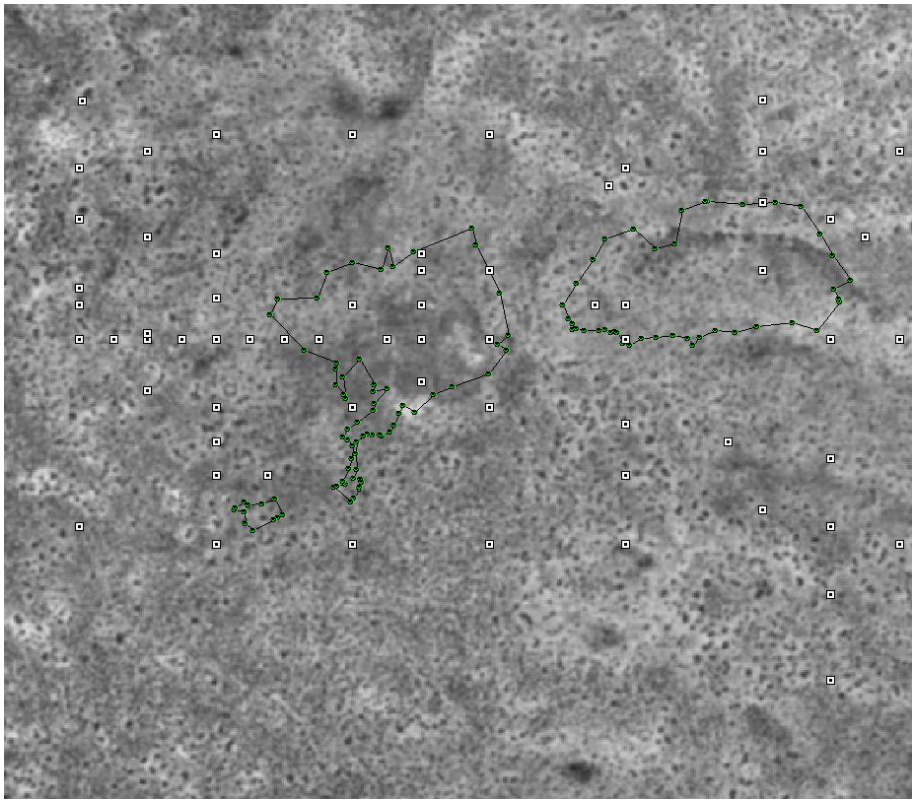

Figure 4-9 The distribution of lags around the main rises and breakaway feature in the central part of ET Gold Prospect. Small white squares represent drillholes. The connected green circles represent the GPS traverse points and resultant polygon boundaries of major lag units overlain on a selected part of the ET orthophotomosaic.

4.5.2.8 Soils

Soils over the investigated area are in the main limited to those with weakly developed horizons and very little organic content. A_0 horizons (leaf litter and related organic mulch) were restricted to small areas directly below substantive trees or large shrubs. Genuine coloured A-horizons were also restricted and consisted of humic staining or slight texture contrast with the underlying B-horizon. Texture contrasting B-horizons were not encountered, but occasional colour strengthening was observed in some dune profiles. Prominent B_{Ca} horizons coincide with the calcretes and are generally paler in colour than the host material above or below (Figure 4-10). Mostly, soils ranged from uniform sandy (Uc) to poorly structured lithosols around silcrete outcrop. All have a strong alkaline reaction trend and the fines-rich types near outcrop or within dune core materials are probably sodic and therefore highly dispersive (sodic type AS2; Northcote and Skene, 1972; Northcote, 1979).

Figure 4-10 Soil profile (LHS) developed within the dune sands, where white calcrete forms a prominent B_{Ca} horizon (exposed in soil pit 1). Pipe karst has developed within the calcrete through soil water dissolution and perhaps tree root activity, the enlargement (RHS) displays this feature more clearly. Scale bar in both images is 10 cm long. The calcrete and soil were geochemically analysed (see Profile 1a and b, Section 5.4.6)

4.6 Regolith transect 340200E – a representative example

A detailed study of a representative cross-section (340200 E) of the ET Gold Prospect was undertaken to investigate the effect of thin to moderate sedimentary cover on the regolith Au signature. This is reported in full in Lintern *et al*., 2002.

A broad lens of transported material up to ~11 m thick, centred on hole 185, overlies weathered Christie Gneiss (Figure 4-11 and Figure 4-12). The boundary between these two distinct regolith components is within the silcrete duricrust horizon. The PIMA-derived KCI boundaries are indicated by a red line on each profile.

The depth of weathering is 35 to >60 m and commonly extends well below the drilling limit. Protolith was only encountered in hole 192, with relicts (probably corestones within saprock) in holes 186 and 193. The saprock (greyish to brownish) thickens over fine-grained rocks. The saprock is variably coloured, in-part ferruginous mottled (reddish or yellow) and has distinct weathered mineral partitioning. The pedolith varies in thickness from <3 to approximately 16 m and is not always recognisable from cuttings. However, it can exhibit micro-mottles, Fe and Mn staining, but primary rock textures are usually obliterated. Along this transect, all pedolith is intensely silicified within its upper 1-2 m, forming a silcrete horizon; deeper partial silicification has formed porcellanite and an indurated zone. Aeolian sand, colluvium-alluvium and red-brown hardpan make up the overlying transported materials. Those above the silcrete and hardpan are essentially un-cemented apart from the calcrete horizons within.

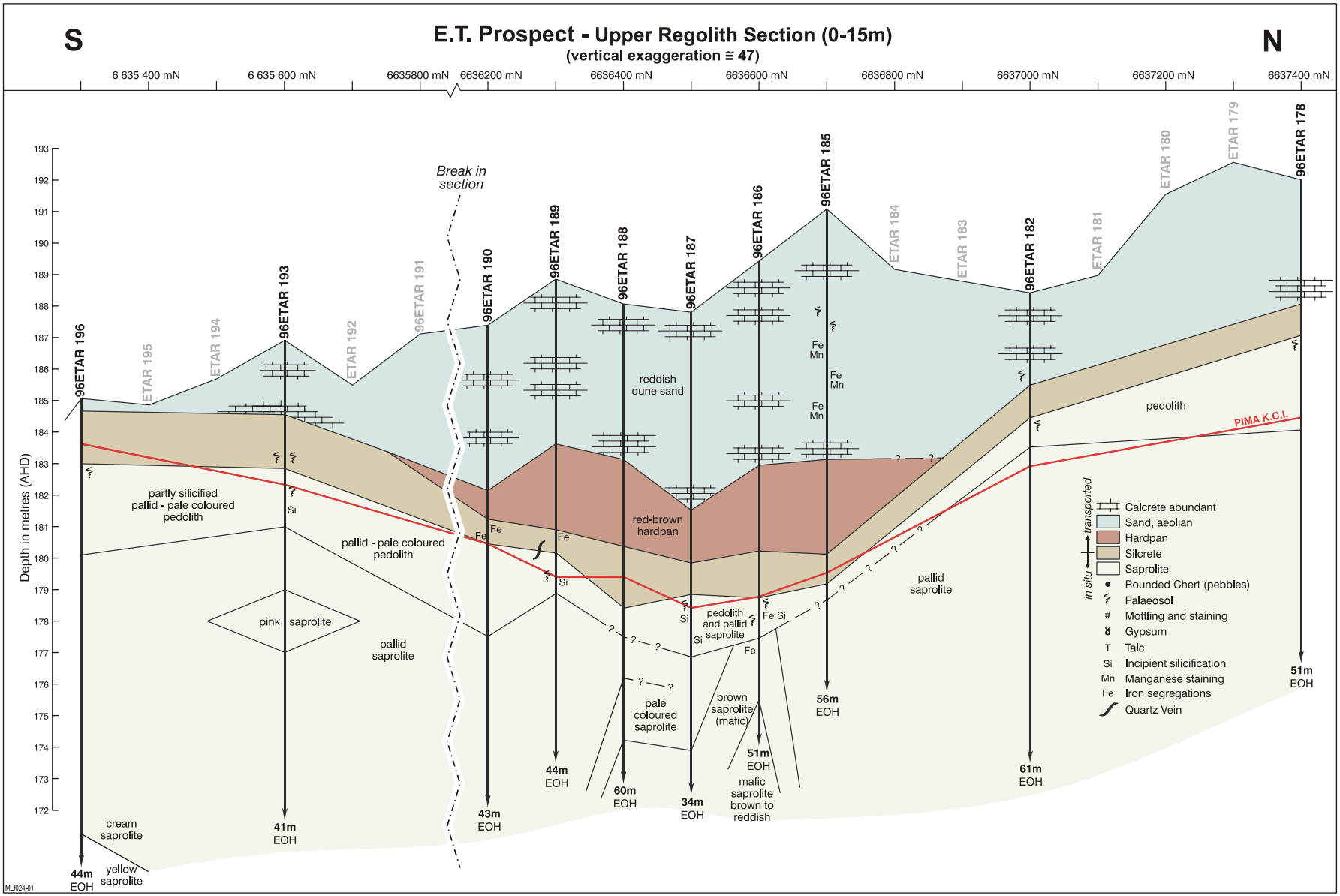

Figure 4-11 The upper regolith cross-section at ET detailing the transported cover and upper *in situ* units. The PIMA-derived kaolinite crystallinity index (KCI) (red line) denotes the unconformity.

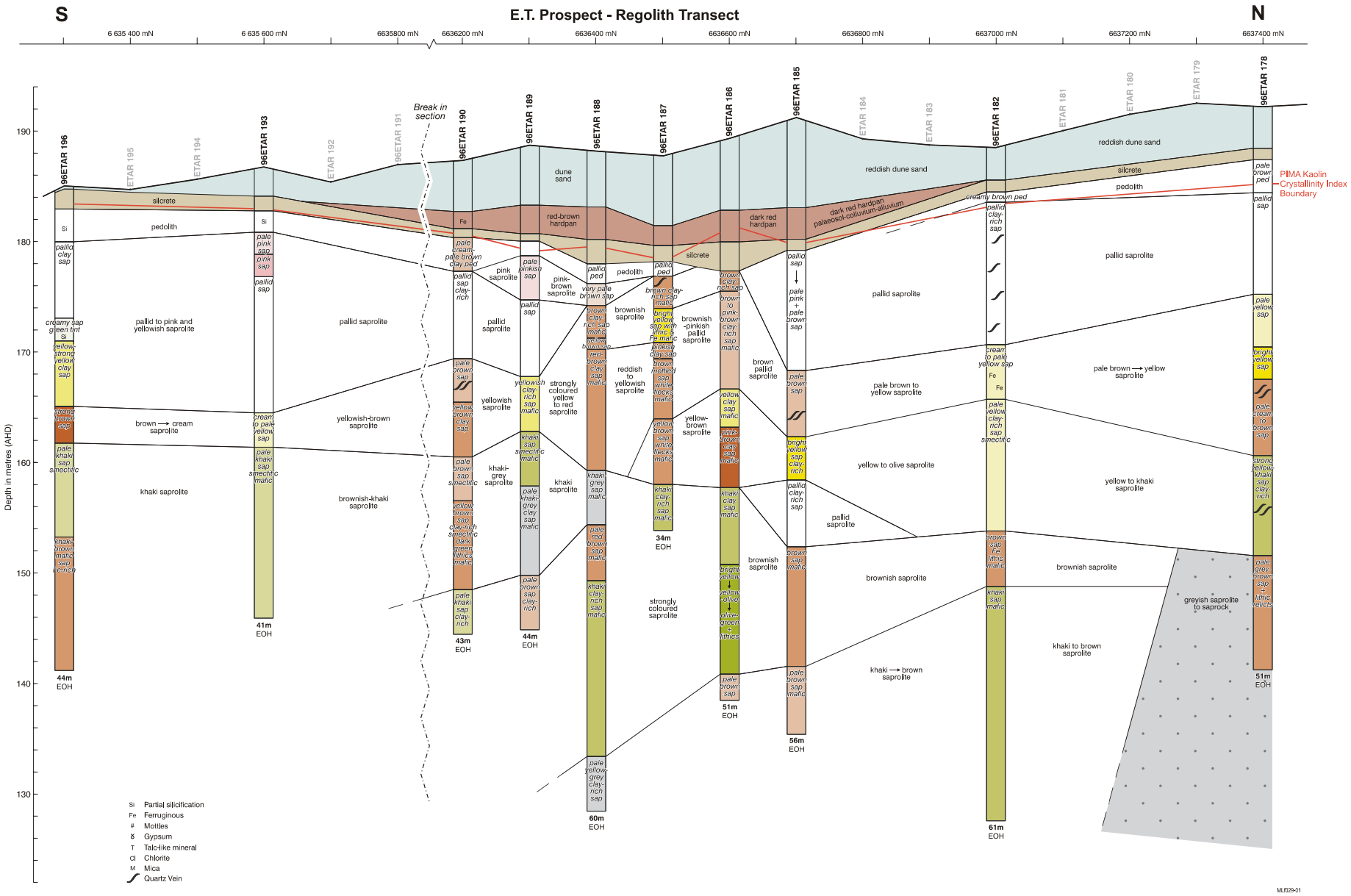

Figure 4-12 The full regolith cross-section at ET. The PIMA derived KCI denoting provenance boundary (red line) indicates the unconformity.

4.6.1 Regolith materials on section 340200E

4.6.1.1 Basement (in situ)

Christie Gneiss along this transect is deeply weathered and fresh rock was encountered in only three of the 20 holes (186, 192 – intermediate composition gneissic granulite, 193 – medium- to coarse-grained felsic granulite). Therefore, a major portion of the basement description derives from saprolith relics. Much of the saprock to lower saprolite is variably chloritic, indicating the basement is of an intermediate to basic general bulk composition. Thicker, pallid saprolite at the northern and southern ends of the transect suggest a more felsic form of the Christie Gneiss there. However, more mafic versions were intersected in holes 186-188. Course-grained basic-mafic varieties were not encountered in this transect but do occur elsewhere on the prospect. Quartz veins occur randomly throughout the basement and have variable colours including white, grey and blue.

4.6.1.2 Saprock

In general, the felsic-derived saprock is a medium grey colour, whereas over more basic or mafic rocks, colours may be very dark grey to dark olive grey or dark olive. Staining and weathering colours tend to be dark brown or occasionally red and yellow. Saprock thickness varies markedly from <2 m to approximately 10 m, which may reflect the pre-existing degree of fracturing and alteration. Weathering in this zone consists of fracture alteration on scales of millimetres to centimetres. It also consists of Fe oxide or hydroxide spotting and/or staining, black Mn mineral dendritic growths on fracture surfaces, some partial feldspar alteration to sericitic kaolinite and random pseudomorphs thereof, some partial mica alteration to clays, and thin clay seams. Saprock usually carries most of the relict mica although ubiquitous muscovite flakes were observed well into the saprolite zone in some profiles (*c.f.* hole 186).

Samples showing mixed weathering character reflect the commonly gradational weathering front developed into pre-altered basement. The presence of sizeable protolith corestones remaining above the weathering front or saprock corestones remaining within clayey saprolite, as less altered relict enclaves within more weathered surrounds, also demonstrates the nature of the weathering front. Holes 179-181 exhibit this apparent irregular or multi-weathering front pattern.

4.6.1.3 Saprolite

Saprolite intersections along this transect range from ~32 to >50 m, and may be felsic- or mafic-derived.

Felsic-derived saprolite is colour-rich at the base, becoming colour depleted (pallid) upwards. Colours in the lower range from medium neutrals with colour tinting (medium grey) to moderate and strong colours (browns, reds, oranges and yellows). Upper felsic derived saprolite colours are more subdued, and where this portion is pallid, colours are subtle tints within an otherwise near neutral light grey to white quartz-kaolinite-rich material. Minor illite, smectite and sericite, relict quartz veins, are present. In hole 195, pallid saprolite achieves a thickness of ~18 m but is more commonly <5 m along this transect. Mottles are rare in this transect but all appear to be small and coloured yellow or brown.

The **mafic-derived saprolite** consists of dark and strongly coloured materials throughout. Hues in the lower saprolite tend to range from dark neutrals with colour tinting (dark to medium grey) to strong and dark colours (olives and browns). The presence of chlorite appears to determine colour through to the upper saprolite. Black Mn mineral staining was also noted. It is unclear why some intersections of this more ferruginous saprolite have developed a pallid top while at holes 186-188 little or no pallid material occurs but may be due to a shear. Opaque accessory minerals like graphite and perhaps ilmenite, persist throughout the weathering profile. White micas, biotite and chlorite are commonly present in the upper saprolite.

4.6.1.4 Pedolith

Pedolith along this transect covers a thickness range of between <6 m to 16 m where the thickest zones are intersected in holes 181-185. Colours are similar to those of the upper saprolite but where the pedolith derives from felsic rocks it commonly includes pronounced reddish to brownish micro-mottles, lamellae, Liesegang haloes or rings and bands. Ferruginous staining can occur along fractures, or as broader bands and irregular patches. Alternatively, where pedolith has developed above basic-mafic protolith (holes 186 and 187) the colours are strong browns, reddish browns and oranges. Mottling and other colour

partitioning is harder to visually detect in these darker profiles. Intense silicification has indurated the upper pedolith but below this there is often a variable incipient silicification zone.

4.6.1.5 Silcrete (in situ and *transported)*

Silcrete is thickest at the southern end (~1.5 m) of the section and thinnest (<1 m) below the sediment infilled palaeo-low area (channel), possibly due to erosion. This duricrust probably represents an overprinting by at least two silicification cycles during the Tertiary (Lintern and Sheard, 1998: Lintern and Sheard, 1999a, b). There are two separately sourced components: a lower silicified pedolith containing angular quartz grit and relict quartz veins and an upper silicified colluvium containing subangular to rounded quartz-rich gravel and alluvial well-rounded quartz-rich fine gravel to large pebbles. Silcrete is pale grey to cream (2.5Y 7/2) and yellowish coloured (2.5Y 8/2) but can be stained strong yellow to reddish along fractures. However, some silcrete developed within more mafic pedolith may display bright orange-yellow colours (hole 186, 8-10 m, 7.5YR 8/7). All silcrete here is pedogenic, contains partitioned wisps of titania minerals (such as anatase and rutile) and within the silicified pedolith, contains relict or weathering resistant minerals such as graphite. Porcellanite is sometimes observed within that part and occasionally it has preserved delicate 3D black Mn dendritic structures on sub-millimetre to millimetre scales,

4.6.1.6 Red-brown hardpan (transported)

The hardpan unit forms a distinctive strong brown (2.5YR 4/6, 4/8) clay-rich colluvium to alluvium that may display evidence of pedogenesis. It is <1-~3 m thick, underlies the dune sand and overlies the silcrete horizon. Red-brown hardpan can contain dark brown to black Fe sesquioxide and hydroxide cements and/or segregations, the clay component may also be partly silicified and is often noticeably silty. In places this unit is partially coated near its top by earthy carbonate, probably illuviating from the overlying dune sand. Its stratigraphic position, strong colour and clay-rich texture make this unit easily identified from all the others. An irregular upper surface to the red-brown hardpan along this transect indicates it has been partly incised by later small scale fluvial activity (*c.f.* holes 190 and 187).

4.6.1.7 Dune sand (transported)

Aeolian dune sand blankets this transect and forms a significant dune between holes 182-191, it ranges in thickness from <1 m to ~8 m. Colours' spanning hues from brownish orange (5YR 5/6, 6/6) to brown (5YR 5/8) are caused by thin ferruginous coatings on quartz-rich sand grains. These sands are uniformly sorted and textured with some illuviated silt-clay components forming a denser, more strongly coloured dune core (5YR 4/6, 4/8). The sand is often loose and free running, unless cemented by calcrete or clays (dune core). Mostly it is stabilised from reactivation erosion through the presence of substantial deep rooted vegetation. Palaeosols were evident in holes 185 and 182, where the sands exhibited colour changes and possible mottling due to pedogenesis.

4.6.1.8 Calcrete

Calcrete occurs across the upper regolith within dune sand, exposed silcrete and the soil profile. In the dunes there is often more than one calcrete horizon, especially at the transect centre. Forms include nodules to hard bars in dunes, earthy powders or coatings in the hardpan upper portions, and significant laminated coatings to joint infill on silcrete outcrop or subcrop. Most indurated calcretes were mildly coloured pale pink to pale orange.

4.6.1.9 Soils

Soils range from uniform sandy (Uc) to poorly structured lithosols, especially surrounding silcrete outcrop. They all have weakly developed horizons with very little organic component in the A-horizon. All soils have a strong alkaline reaction trend due to the presence of calcrete in the B_{Ca}-horizon. The fines-rich types near outcrop or within the more clayey dune cores are probably sodic (type AS2; Northcote and Skene, 1972; Northcote, 1979).

5 GEOCHEMISTRY (M.J. Lintern. A.J. Cornelius and G. Gouthas)

5.1 Introduction

The geochemical exploration problem at ET Gold Prospect is typical of many prospects in the Gawler Craton: a spatially large and intense gold-in-calcrete anomaly has been identified but follow-up drilling fails to find significant mineralisation. At ET, there is the added complication of determining to what extent recent transported material, in the form of aeolian sand dunes, masks potential mineralisation. Both problems were investigated using the existing database of the Gawler Joint Venture (GJV) together with additional sampling and analyses undertaken during the course of this project.

Results are discussed in terms of anomalies and background. Any geochemical data may be classified into anomaly or background, and further classified as being true, false or by chance/coincidence (Table 5-1). Background is considered as the normal range of data values. An anomaly is a deviation (usually an increased concentration) from this normal range and can be defined quantitatively as being a value greater than the upper limit of normal background fluctuation (threshold). A true anomaly is where elevated element concentrations exist in the vicinity of mineralisation. A "false" or displaced anomaly is where elevated element concentrations exist with no apparent mineralisation. True and false backgrounds are where low surface geochemical concentrations occur with no mineralisation and mineralisation, respectively. Many false (displaced) anomalies are due to (i) mobilisation of elements during weathering which become concentrated at another site, (ii) isolation (disconnection) due to landform change *e.g.*, the formation of a creek or (iii) inadequate concentration and/or depth of drilling. The term "false" used here can be misleading since concentrations of elements without an immediate explanation as to their origin still have an initial source. True anomalies are easily explained as residual accumulation of elements close to source due to mechanical and/or chemical processes. False backgrounds may be due to, for example, mechanical removal of an existing anomaly *e.g.,* stripping of a lateritic residuum to expose a target-element-depleted upper saprolite, or the mineralisation never reaching the current land surface during its formation (e.g. due to the geometry of an ore body). In regolith-dominated terrain, verification of anomaly type usually can be only achieved after extensive drilling. In the sections that follow, anomalies are described in the above terms. Limitations of this classification are due to the extent of drilling since the drill fences are 200 m or more apart. One of the main problems in the classification system is that it does not readily allow for the apparent true anomaly that appears by non-causal processes *i.e.,* a chance anomaly. This situation is most readily identified in transported overburden where a surficial anomaly is drilled and mineralisation is found beneath. Often the depth to mineralisation can be tens or hundreds of metres and so the likelihood of the surficial anomaly being produced by the deeply-buried mineralisation is suspect, given the absence of a plausible and verifiable mechanism of formation. As transported overburden at ET is relatively thin (mostly <5 m), the proof of whether an anomaly is by "chance" is less of an issue, since the source of an anomaly may be readily explained (rightly or wrongly) by bioturbation and/or capillarity mechanisms. Thus, distinguishing chance anomalies from true anomalies may be especially difficult in areas of shallow transported overburden.

Table 5-1 Classification of geochemical anomalies. Characters S, s, M and m denote high and low (including below detection) concentrations in exploration sample and mineralisation respectively. A chance anomaly is when the exploration sample is spatially related to mineralisation but probably not derived from it.

	ANOMALY	BACKGROUND
TRUE	S M	s m
FALSE	S m	s M
Chance	S M	

5.2 Sample collection

Samples were collected on two field trips. The first reconnaissance trip (November 1999) was restricted principally to sampling drill cuttings from a series of holes along traverse 340200E (described in Section 4.6). Some calcrete samples were hand-picked from the drill cuttings. The second trip involved

sampling a variety of media across the entire prospect. Most of the cuttings were sampled (~200 holes) at 2 m composite intervals to 38 m or end-of-hole and collected in chip trays for future regolith descriptions, photography and mineralogical study (see Section 4 and Appendix DVD). Several hundred larger samples (up to 500 g) were collected from the first 10 to 13 m of drill hole cuttings for geochemical analyses. Care was taken with sampling but the problem of down hole contamination was unavoidable (Section 4.3). Soil (10-20 cm) and about 50 vegetation samples (mostly *Acacia* phyllodes) were collected on an approximately linear 500 m x 500 m grid with supplementary samples (including silcrete lag) collected in particular areas. Vegetation was taken at shoulder height from healthy bushes with trunk diameter and shrub height recorded. Four soil pits were excavated to variable depth (maximum of 1.3 m) and 6 profiles sampled therein at 10 to 20 cm intervals (Figure 5-1).

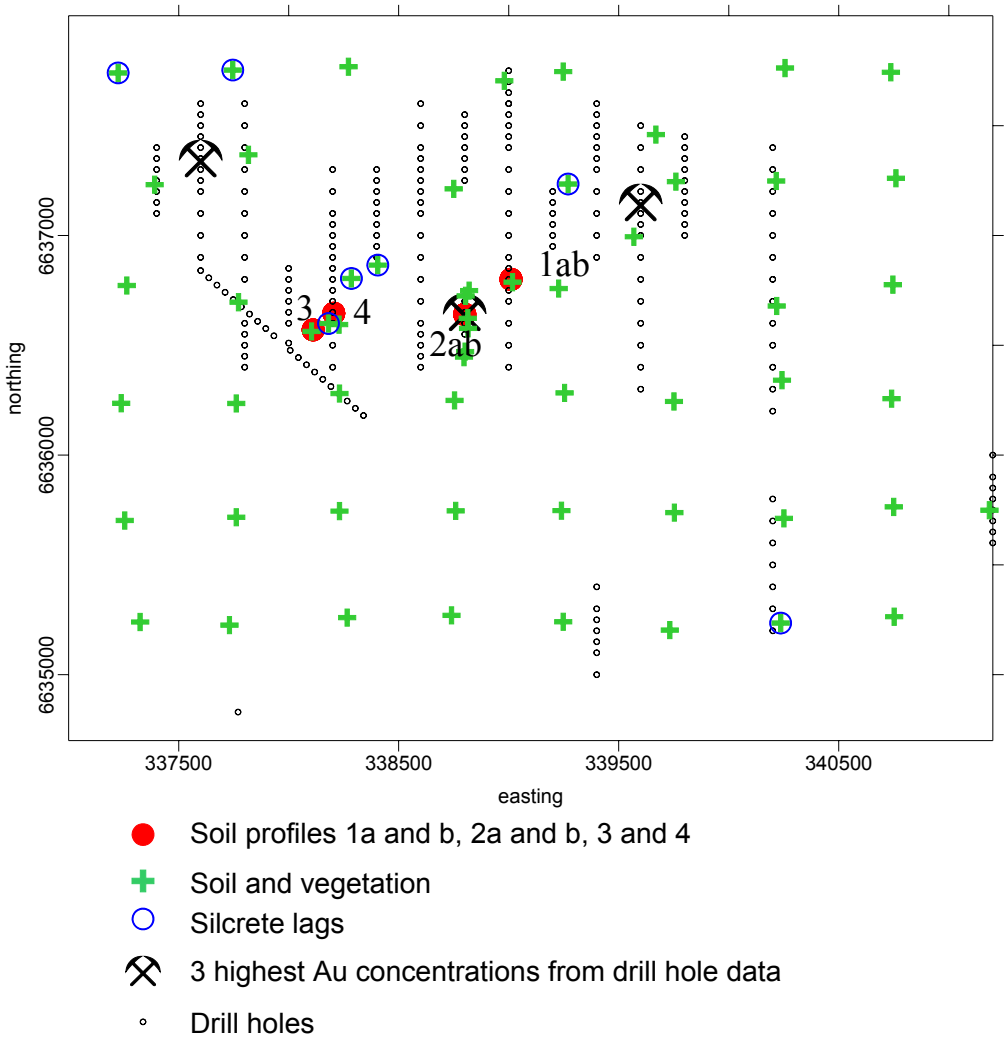

Figure 5-1 Location of geochemical sampling points at ET. Most drill cuttings were sampled to 10 m or to 3 m below the unconformity whichever was deeper. Some deeper drill cuttings were sampled for mineralised material and for other regolith studies. Also shown are the three holes with the highest Au concentration recorded in drill cuttings.

5.3 Sample preparation and analysis

5.3.1 Mineral samples

Soil, calcrete and 0-10 m samples were prepared in the CSIRO laboratory by weighing, mixing the sample on a plastic sheet, then incrementally extracting approximately 200 g of material (or ~50%, whichever was the smaller) to be sent to AMDEL Laboratories Ltd. Samples were also tested for their carbonate content using dilute acid.

Geochemical standards were submitted "blind" with each analytical sample set sent at the rate of approximately 1 per 30 samples to check for analytical precision and accuracy. All samples and standards were analysed by AMDEL Laboratories Ltd as follows (detection limits in ppm):

(i) approximately 0.25 g of sample was analysed by ICP-OES after mixed acid digest (HF-HCl-HNO_3) for Ba (10), Ca (10), Cr (2), Fe (100), K (10), Mg (10), Mn (5), Na (10), Ni (2), P (5), S (500), Ti (10), V (2), and Zn (2);

(ii) approximately 0.25g of sample was analysed by ICP-MS after mixed acid digest (HF, HCl and HNO_3) for Ag (0.1), As (0.5), Bi (0.1), Cd (0.1), Cs (0.1), Ce (0.2), Cu (0.5), Ga (0.1), In (0.05), Mo (0.1), Nb (0.5), Pb (0.5), Rb (0.1), Sb (0.5), Se (0.5), Sr (0.1), Te (0.2), Th (0.02), Tl (0.1), U (0.02), W (0.1), Y (0.05), Zn (0.5) and the REEs Ce (0.05), La (0.05), Dy (0.02), Er (0.05), Eu (0.02), Gd (0.05), Ho (0.02), Lu (0.02), Nd (0.02), Pr (0.05), Sm (0.02), Tb (0.02), Tm (0.05) and Yb (0.05);

(iii) 25 g of sample was analysed by graphite furnace AAS after aqua regia digest for Au (0.001) or by cyanide digest followed by ICP-MS for Au (0.00005), Ag (0.0005) and Cu (0.1).

5.3.2 Vegetation samples

Vegetation samples were sent to the laboratory within a few days of collection to prevent mould growth. Samples were considered relatively free of dust and, therefore, not washed. Samples were weighed then dried at approximately 80^{o}C for at least 24 hours to prevent smearing during grinding, then re-weighed. Samples were ground using a blender. The samples were step-wise ashed using the following programme: 4 hours at 200^{o}C, 4 hours at 400^{o}C and then 15 hours at 550^{o}C before being re-weighed and sent for analysis as for the mineral samples. Concentrations were reported in the ash and then converted to dry weight.

5.3.3 X-ray diffraction analysis

X-Ray diffraction of selected samples was performed by CSIRO (Floreat Park, WA) using a Philips PW1050 diffractometer, fitted with a graphite crystal diffracted beam monochromator. CuKα radiation was used. Each sample was scanned over the range 2–65º 2θ at a speed of 1º 2θ a per minute and data were collected at 0.02º2θ intervals. Mineralogical compositions were determined by comparison with JCPDS files and XPLOT software spectra.

5.3.4 PIMA

Short Wave Infra Red (SWIR) spectra of selected RAB and RC cuttings were collected using an Integrated Spectronics PIMA II spectrometer. PIMA Acquisition Software (version 1.1B) using Petri Dish Calibration mode was used to acquire the data. A new calibration was performed approximately every hour unless prompted earlier by the software. Each sample was deposited in a Petri dish and placed on the PIMA scanning window and scanned with the default integration setting set to 1. An integration setting of 2 was used where the sample was too dark to give relatively noise-free spectra. Mineralogical compositions were determined using Spectral Geologist v2.0 software (Ausspec International Pty Ltd) to compare sample spectra with the reference library of spectra within the software package, and by comparisons on a limited number of samples with XRD data. PIMA was used to identify kaolinite crystallinity (see Section 4).

5.4 Gold geochemistry

5.4.1 Mineralisation

Geochemical analyses of drill cutting and calcrete samples had already been performed by GJV prior to CRC LEME investigations. The GJV database for Au at ET is comprised of 1862 individual drill cutting analyses (from 212 RAB holes) and 896 calcrete analyses. The maximum Au concentration obtained from the drill cuttings database was 0.685 ppm (GJV data) (Table 5-2); one sample collected by CRC LEME recorded 0.755 ppm. The three holes with the highest Au concentrations in saprolite are marked with "hammer and pick" symbols in Figure 5-2 and subsequent figures.

Table 5-2 Peak concentration, hole name, depth to mineralisation, and depth of transported overburden of sample with the 3 highest Au concentrations (ppm, GJV data).

Hole	Maximum Au	Depth to mineralisation	Depth of overburden
ETAR119	0.67	50-51	2.5 m
ETAR151	0.69	40-41	6 m
ETAR167	0.68	40-44	2 m

Drilling at ET was restricted to RAB with only 14 holes reaching the protolith or fresh rock. Most drill cuttings samples were weathered to some degree and element determinations of fresh rock were, therefore, not possible. The drill cuttings from the top 10 m of each drill hole were analysed for Au, and selected major and trace elements including those commonly associated with Au. Mean concentrations of elements in weathered mineralisation are listed in Table 5-3. Concentrations of potential pathfinder elements are generally low although they are not markedly different from anomalous concentrations found at the Challenger Gold Deposit, located 60 km to the NNE of ET Gold Prospect (Table 5-3). At Challenger Gold Deposit, where the regional geology is similar to ET (Christie Gneiss), elements associated with Au mineralisation fall into two groups: sulphide-related (Ag, As, Bi, Cd, Cr, Cu, Fe, Mo, S, Se, ?W and Zn) and potassic alteration-related (Ba, Cs, K, Rb and Tl) (Lintern and Sheard, 1999). Challenger has significantly more As, K and W associated with mineralisation than at ET, whereas the latter is richer in Cr, Cu, Fe, Mg, Ni, Se and Zn, possibly reflecting a more mafic style to the mineralisation.

5.4.2 Calcrete

The Au in calcrete and depth-to-calcrete sample distributions (GJV data) are shown in Figure 5-3 to Figure 5-5. Samples of calcrete were obtained from different depths and were of different types. Interpretation of GJV sample logging indicates a trend towards "massive" calcrete type being collected from areas of thin or no cover (Section 4.5.2.6) and nodular calcrete collected adjacent to these in areas of shallow cover. However, many calcrete types were not specified in the database. The spatially largest Au anomaly (maximum of 115 ppb) is located W of centre of the prospect on the exposed silcreted and lag-strewn ridge that runs through the centre of the prospect; this area was determined as "erosional" and signifies little transported cover (Section 3.3.2). Drilling of this anomaly failed to find any corresponding mineralised saprolite i.e the anomaly is false. Moreover, there is a generally a poor correlation between Au in calcrete and mineralisation (Figure 5-5). This may be due to several reasons including inadequate drilling (depth and density), "hit and miss" style of mineralisation i.e. Au associated with narrow quartz veins, and/or displaced anomalies due to active hydromorphic dispersion in the calcrete (Figure 5-5). From Figure 5-5, even the holes with the three highest maximum Au concentrations found in drill holes do not have a significant Au in calcrete anomaly associated with them, although there is an offset, lower-order anomaly associated with mineralisation on 338800E.

Geochemical data were processed from the GJV database and from samples collected by the authors. Summary statistics for Au in calcrete and samples collected by CRC LEME are shown in Table 5-4.

Table 5-3 Selected mean concentrations of elements in weathered mineralisation. The mean of 45 samples with >100 ppb Au from the Challenger Gold Deposit is included for comparative purposes.

DrillHole	Sample ID	E	N	depth	Ag	As	Au	Bi	Ce	Co	Cr	Cu	Fe	K
96ETAR170	R436527	339600	6637000	50.5	0.2	16	84	0.1	100	29	260	115	67400	26800
96ETAR187	R391846	340237	6636441	33.5	0.2	10	101	0.1	67	38	300	40	40800	19500
96ETAR125	R436526	337600	6636900	61.5	1.4	105	140	0.2	240	140	220	300	28000	6250
96ETAR167	R436522	339600	6637150	43.5	0.2	110	150	0.7	74	56	1500	70	52200	17000
96ETAR151	R436524	338800	6636650	39.5	0.3	85	170	0.1	110	77	550	78	48400	18000
96ETAR119	R436520	337600	6637350	51.5	1.1	21	215	0.1	95	43	440	125	45200	15000
96ETAR125	R436528	337600	6636900	63.5	0.4	63	260	0.1	140	43	210	160	41300	7150
96ETAR119	R436521	337600	6637350	50.5	4.9	54	290	0.2	75	46	950	300	60100	3450
96ETAR070	R436519	339000	6636800	25.5	0.3	23	330	0.1	150	38	370	96	67300	22600
96ETAR185	R436523	340227	6636654	47.5	0.2	105	390	0.1	77	200	900	180	127000	5850
96ETAR151	R436525	338800	6636650	40.5	1.2	350	475	0.1	69	98	1300	115	70500	26200
96ETAR189	R391789	340239	6636246	7.5	5.5	3	755	0.1	13	3	18	10	11700	2700
mean	**ET**				**1.3**	**79**	**280**	**0.1**	**101**	**67**	**584**	**132**	**54992**	**14208**
mean	**Challenger**				**0.7**	**202**	**1192**	**0.3**	**108**	**-**	**187**	**48**	**26751**	**20665**
DrillHole	**Sample ID**	**E**	**N**	**depth**	**Mg**	**Mn**	**Mo**	**Ni**	**Pb**	**S**	**Sb**	**Se**	**W**	**Zn**
96ETAR170	R436527	339600	6637000	50.5	10200	400	8.5	165	30	750	0.3	3.5	0.7	155
96ETAR187	R391846	340237	6636441	33.5	17200	700	1.3	78	16	800	0.3	0.5	1.3	95
96ETAR125	R436526	337600	6636900	61.5	3250	370	7.0	390	36	400	0.3	2.5	0.6	210
96ETAR167	R436522	339600	6637150	43.5	26700	1000	2.8	230	10	650	4.5	0.3	0.3	110
96ETAR151	R436524	338800	6636650	39.5	40600	700	1.9	260	23	1100	0.3	0.3	0.7	230
96ETAR119	R436520	337600	6637350	51.5	13300	250	3.4	135	74	9600	0.3	1.0	1.7	145
96ETAR125	R436528	337600	6636900	63.5	3000	170	4.1	200	51	350	0.3	6.0	1.7	160
96ETAR119	R436521	337600	6637350	50.5	9600	60	2.0	230	155	12000	0.3	5.5	1.2	150
96ETAR070	R436519	339000	6636800	25.5	10000	280	6.5	140	40	400	0.3	0.3	0.5	155
96ETAR185	R436523	340227	6636654	47.5	38900	950	2.2	700	21	700	1.0	1.5	0.8	380
96ETAR151	R436525	338800	6636650	40.5	85700	1000	2.0	390	5	1950	1.5	0.3	0.1	390
96ETAR189	R391789	340239	6636246	7.5	1350	50	0.9	10	5	650	0.3	0.5	1.0	14
mean	**ET**				**21650**	**494**	**3.6**	**244**	**39**	**2446**	**0.8**	**1.8**	**0.9**	**183**
mean	**Challenger**				**7147**	**381**	**4.7**	**56**	**28**	**997**	**0.3**	**0.4**	**4.3**	**93**

Table 5-4 Summary statistics of Au (ppb) for samples collected during this study. Calcrete[1] was specifically collected and analysed by GJV.

Sample medium	Detection limit	Range	Mean	Standard deviation	Number of samples
0-~10 m	**0.05**	**<0.05-755**	**2.4**	**7.4**	**2079**
Calcrete[1]	**1**	**<1-115**	**8**	**11**	**895**
Soil (10-20 cm)	**0.05**	**0.1-8.9**	**0.9**	**1.35**	**57**
Soil pit samples	**0.05**	**0.45-75**	**11**	**19**	**55**
Vegetation (dry)	**~0.02**	**<0.02-1.43**	**0.21**	**0.26**	**58**

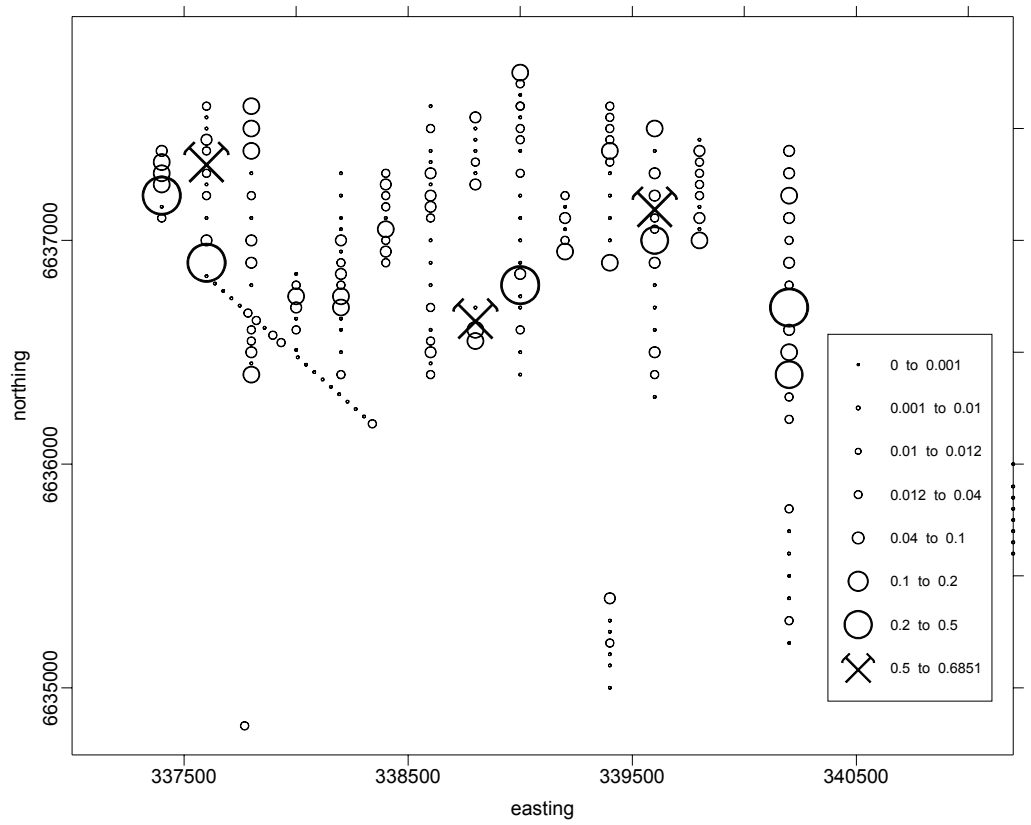

Figure 5-2 Maximum Au (ppm) in RAB drill cuttings at ET (GJV data).

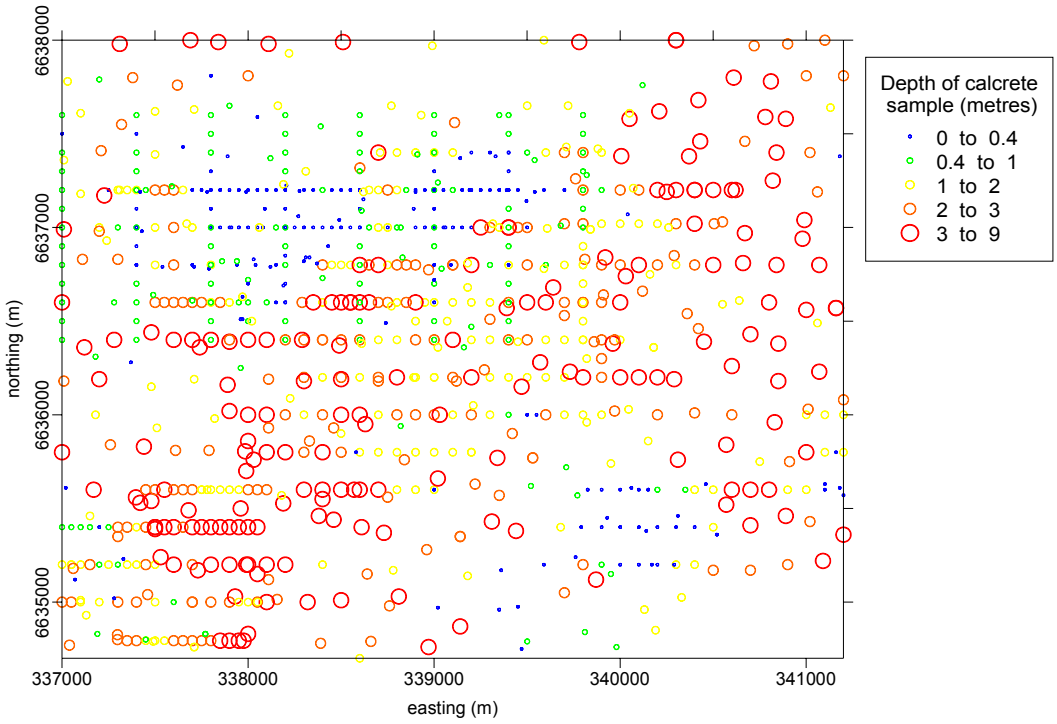

Figure 5-3 Depth to calcrete sample in metres (from GJV data).

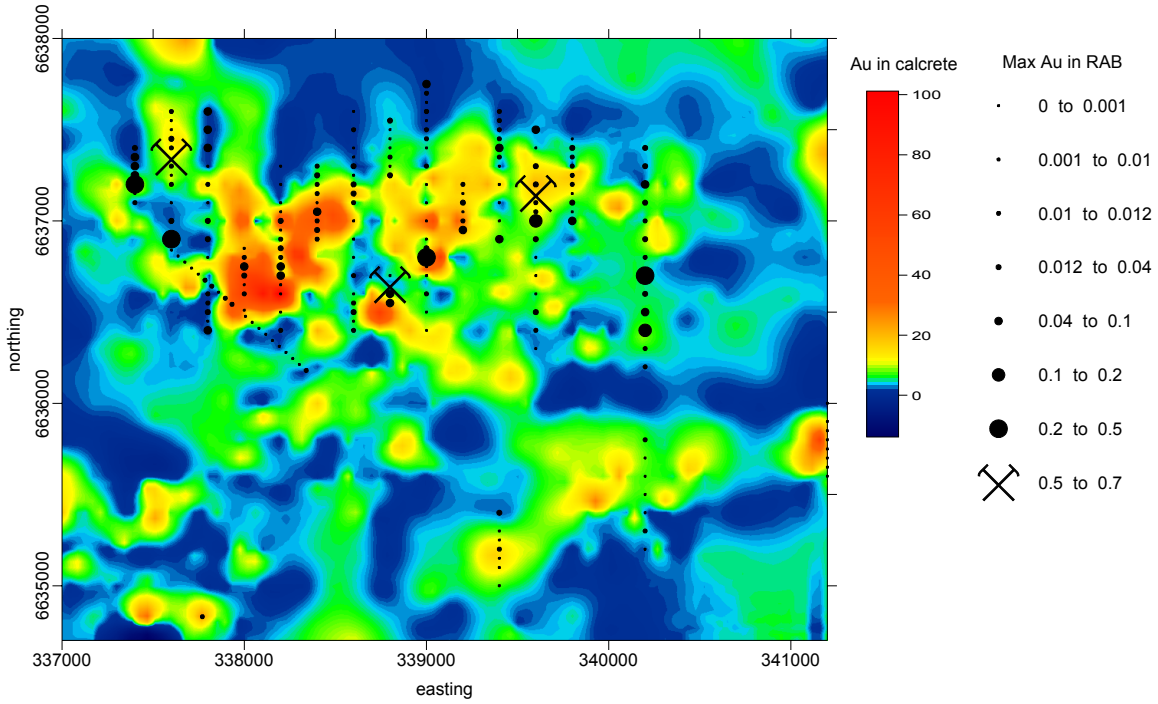

Figure 5-4 Comparison between Au in calcrete (ppb) and maximum Au in drill cuttings (ppm), (from GJV data).

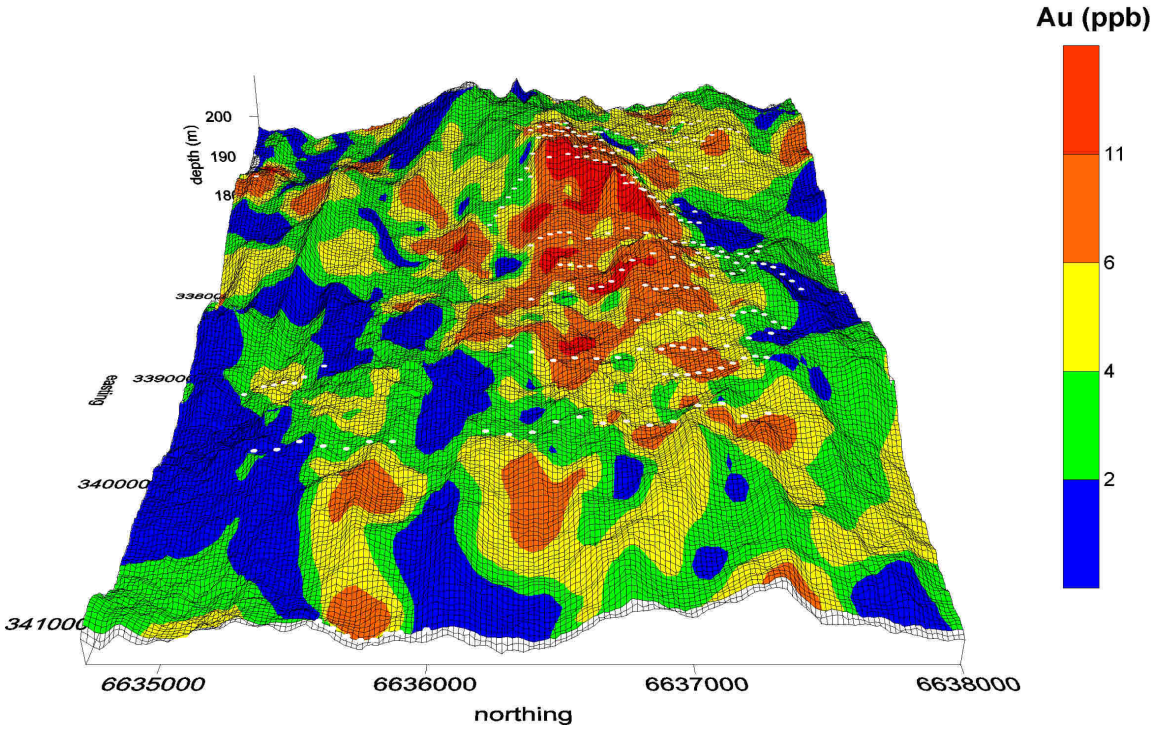

Figure 5-5 Au concentration of calcrete and drill holes overlaid on vertically-exaggerated DEM viewed looking west with tilt of 27 degrees (from GJV data).

The effect of sieving on selected calcrete material was briefly investigated. Element concentrations were determined for three different size fractions for a massive calcrete sample type taken from the base of one of the soil profiles (profile 4). The Ca and Mg concentrations suggest that the calcrete consists mainly of calcite. Gold concentrations for size fractions 2-5, 5-10 and >10 cm were 22, 36 and 32 ppb respectively indicating no systematic concentration with size fraction. No trend between concentration and size fraction was found for other elements (Table 5-5; Appendix DVD).

Table 5-5 Comparison of element concentrations in different calcrete size fractions taken from the base of soil profile 4. All concentrations in ppm.

Calcrete type	id	Ag (cn)	Ag	As	Au	Cu (cn)	Cu	Ca	Mg
fine (2-5 cm)	R435887	0.017	0.4	2.5	0.022	3.2	11	301000	7700
coarse (5-10 cm)	R435888	0.023	0.05	5.5	0.036	2.8	12	297000	7050
v.coarse (>10 cm)	R435889	0.018	0.05	3.5	0.032	3.3	11	299000	7250

The Au concentrations of selected calcareous and non-calcareous sub-samples from RAB drill spoil were compared along 340200E; down hole contamination of samples is possible and sample depth may be inaccurate. Calcrete is generally arenaceous and nodular from the dune sands and massive-laminar from areas where saprolite was close to the surface. Dolomite increases with depth; however, Au concentrations show no systematic variation with carbonate mineral type. Gold is weakly associated with, but not restricted to, the calcrete. The Au content of calcrete samples is compared with finer sized non-calcareous or less calcareous bulk material from the same drill interval in Figure 5-6. The calcrete samples are generally richer in Au and Au concentration increases with depth. Gold is generally anomalous in this section (maximum of 21 ppb) but not particularly anomalous above mineralisation in the transported material *i.e.,* a mixture of false anomalies and false backgrounds; for comparison, 13% of the GJV database calcrete samples had Au concentrations of 15 ppb or greater.

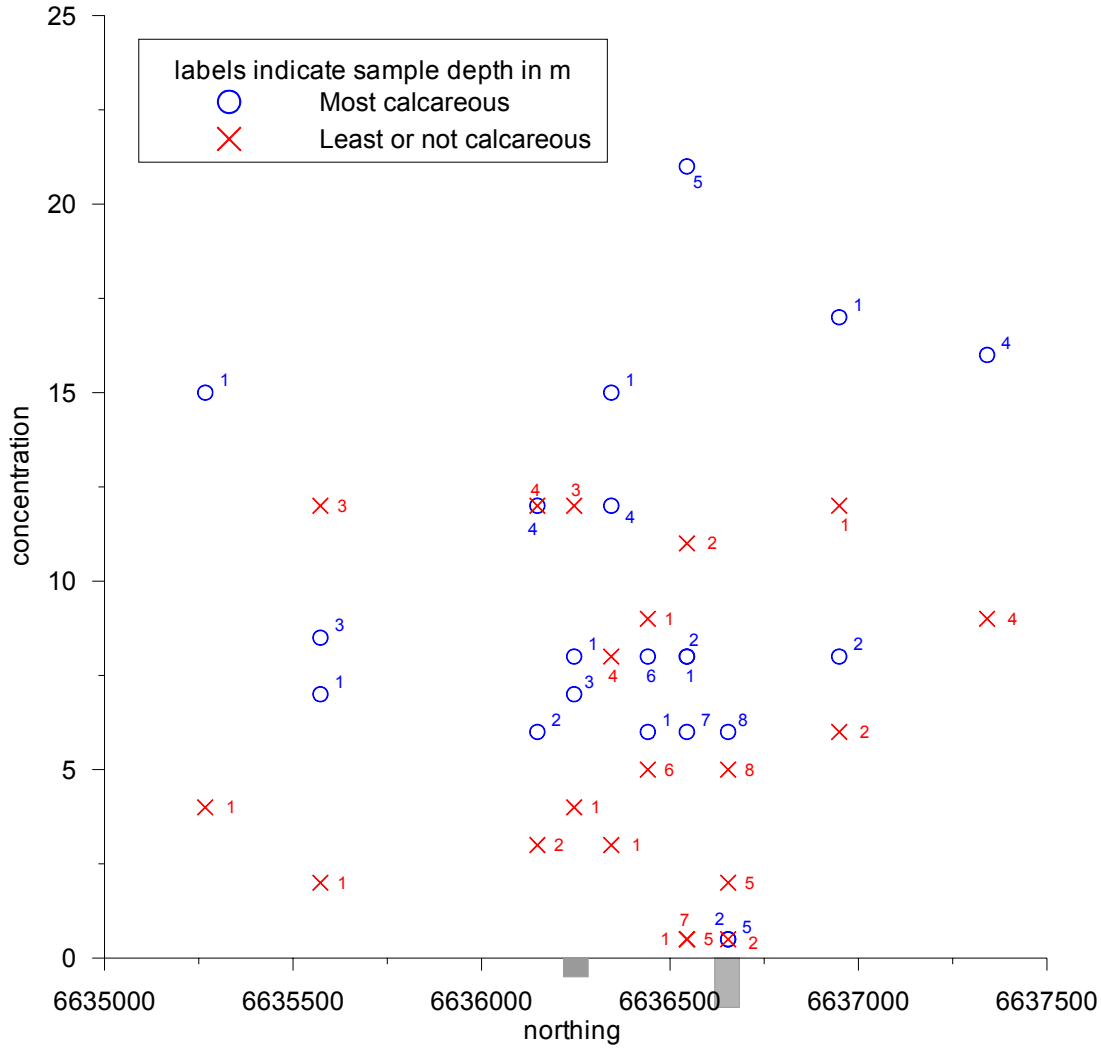

Figure 5-6 Comparison of highly calcareous material with less/not calcareous material from drill cuttings on 340200E. Data labels indicate depth of sample. Grey rectangle size indicates position and tenor of mineralisation.

5.4.3 Lag

Seven lag samples and one saprolite sample were collected opportunistically during 0-10 cm soil sampling (Section 5.4.6). The lag was dominantly silcrete and contained 0.3 to 2.2 ppb Au. A systematic geochemical survey was not conducted of this material.

5.4.4 Overview of Au distribution in the sub-surface regolith

Visualisation of the Au distribution in the sub-surface regolith was undertaken using 2D (SURFER) and 3D (MVS) software. Histograms of the log transformed Au data are shown in Figure 5-7. 2D visualisation was restricted to the top 10 m due to low sampling density below this. For 2D visualisation, the data were not transformed prior to kriging and contour interval classes were fixed at a constant level *for all depths* to aid comparisons; maximum contour interval has been set at a constant 7.3 ppb (for all plots) to remove distortions caused by extreme Au values. Several features are apparent in the images (Figure 5-8):

i) Collectively, the images show that most Au occurs in the 0-1 m interval (average depth 0.5 m) with a decreasing trend to about 4 m. Most upper regolith Au is in the transported overburden (Figure 5-7).
ii) Below 4 m, Au is generally <2.4 ppb, with concentrations above this restricted to isolated samples or areas *e.g.,* spikes due to particulate Au, or over-interpretations of regions outside the drilled area.
iii) There is a trend for higher Au concentrations to occur along the central ridge (Section 3.3.2) as with Au in calcrete, where transported overburden is quite thin *i.e.,* Au appears to be associated with calcareous *in situ* regolith. However, some exceptions do occur where higher Au concentrations are not associated with the ridge (*e.g.,* 339000E 6636600N).
iv) There appears to be a "plume" of Au extending into the SE and SW corners of the prospect (arrowed); the SE feature is coincident with a buried/surficial drainage identified from drill cuttings (see Figure 4-11) The plumes may be due to Au being mobilised away from the ridge (see Figure 2-39). Infill drilling between 339000E and 340200E (south of 6636800N) and in the SW would assist in the interpretation.

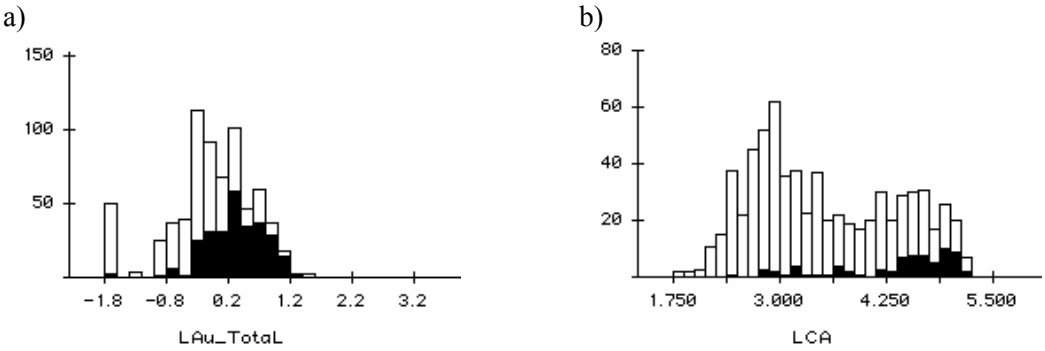

Figure 5-7 Histograms of upper regolith samples from selected sections: a) log Au data with samples from transported regolith unit in black; b) log Ca data with samples containing top 10% Au in black.

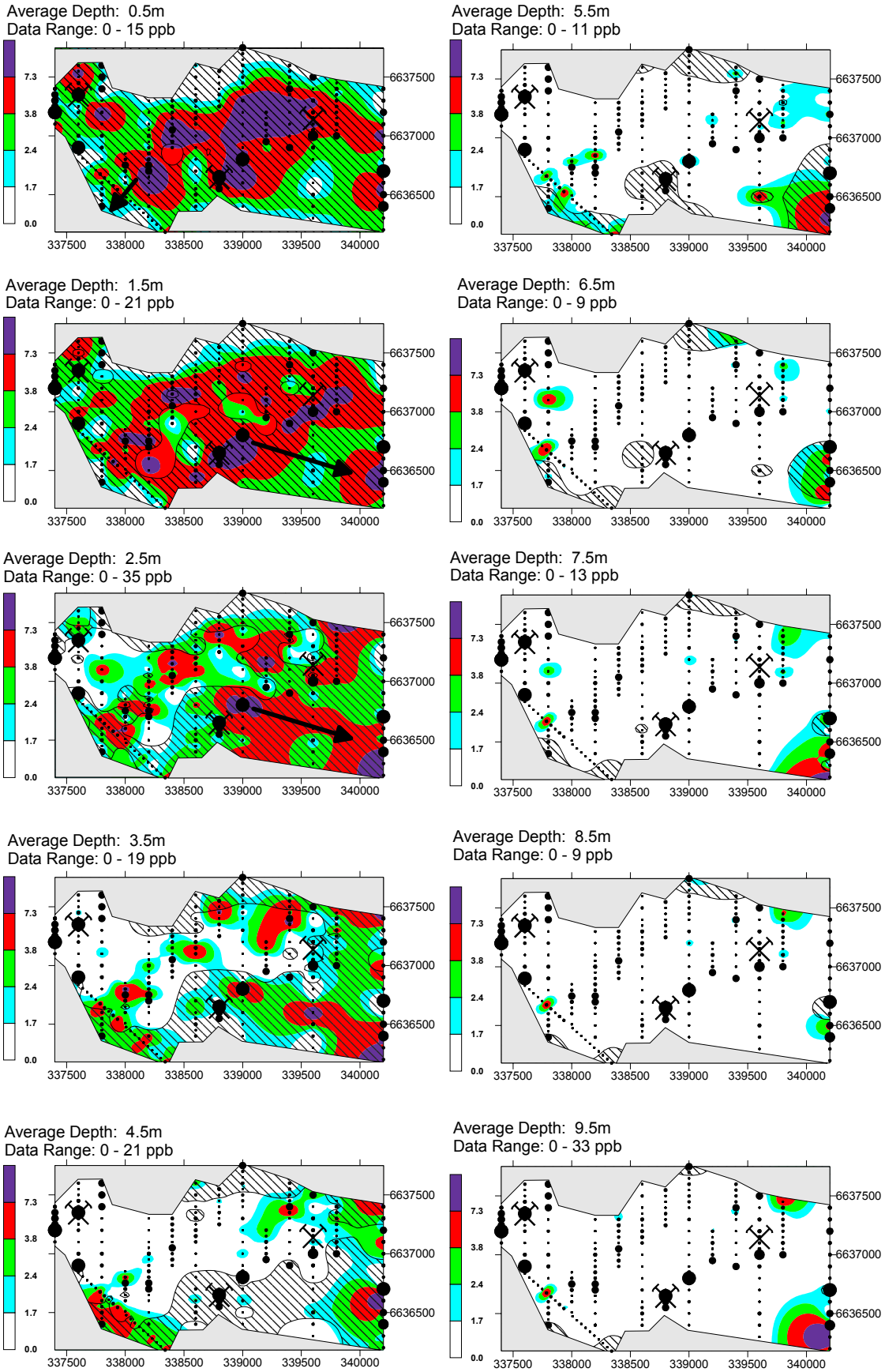

Figure 5-8 Gold concentrations at 1 m intervals to 10 m depth. Mineralisation (black dots) and transported overburden (hatching) are shown. See text for details of data treatment. Crossed hammers indicate positions of the three highest Au concentrations found in the drill cuttings.

For 3D visualisation, the data were clipped to a maximum of 16 ppb Au (to remove distortion due to very high concentrations), logarithmically transformed and gridded using kriging. Data were sourced from GJV and CRC LEME for this purpose. The raw untransformed data are shown in Figure 5-9. Using MVS, a series of "slices" was generated from, and parallel to, the surface down to 54 m depth at 2 m intervals. These can be viewed sequentially as a "movie" or as individual images (Appendix DVD). The Au distribution is shown at 10 m intervals from the surface to 50 m depth in Figure 5-11.

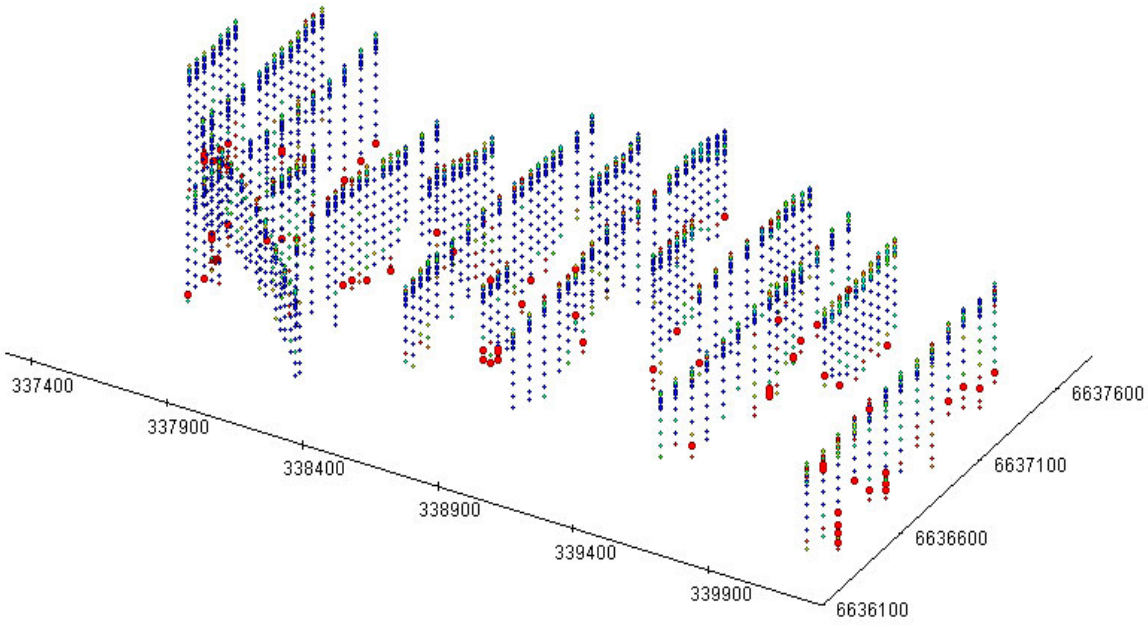

Figure 5-9 Location of drill holes and raw, un-clipped Au data. Data range is from 1-700 ppb with concentrations related to colour and size of circle. View from SE.

Features arrowed in Figure 5-10 (a-f) are discussed below:

i) The Au distribution in drill cuttings taken from near the surface is, not surprisingly, broadly similar to the Au in calcrete distribution; however, Au concentrations in the drill cuttings are generally lower than the corresponding calcrete sample, presumably due to dilution from other Au-poor material in the drill sample (Section 4.5.1.3). Gold appears to be concentrated along the ridge (yellow-orange-red) that runs east-west through the centre of the prospect (Section 3.3.2) with local higher concentrations (red) appearing at two or three locations *e.g.,* 338900E 6637100N.

ii) At the 10 m interval, Au concentrations, indicated by green colours, are much lower than at the surface. Some surface anomalies persist with depth but concentrations are only approximately 3 ppb (green). Most Au anomalies at this level are found in the eastern part of the prospect.

iii) At 20 m, Au concentrations decrease further. The broad Au anomaly at the surface is now poorly represented by narrow zones and is almost indistinguishable from background concentrations. The highest concentrations (~3 ppb) are still mostly confined to the eastern end of the prospect.

iv) By 30 m, mineralisation (red, arrowed,) becomes a feature at 339000E 6636300N (*e.g.*, ~250 ppb at 25-26 m in hole ETAR070). It appears, therefore, that beneath the calcrete, there is a ~25 m thick zone depleted in Au.

v) By 40 m depth, relatively high (>10 ppb) Au concentrations (red and yellow) are evident at various locations within the prospect *e.g.,* 338900E 6636300N, 339700E 6637400N and, in particular, the eastern-most traverse, indicating zones of weakly mineralised saprolite. Mineralisation is still evident at 50 m depth, but patchy, which is partly a reflection of gridding and partly due to relatively higher Au concentrations near the base of the drill holes indicating saprock.

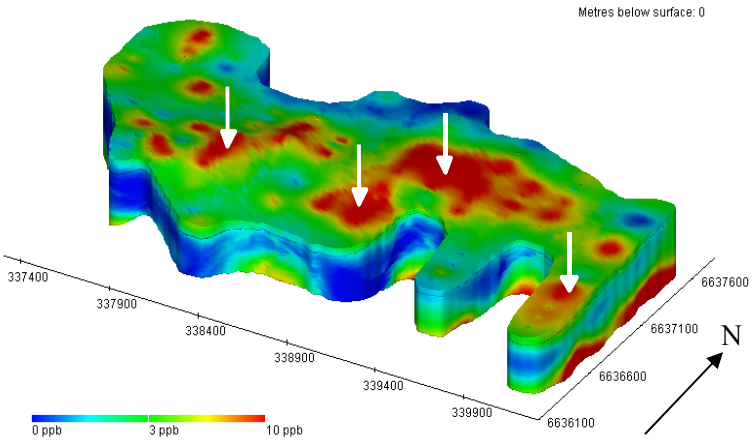

a) surface

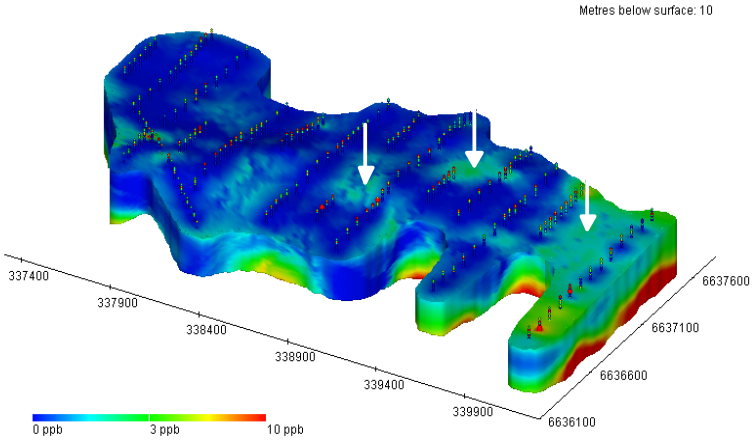

b) 10 m

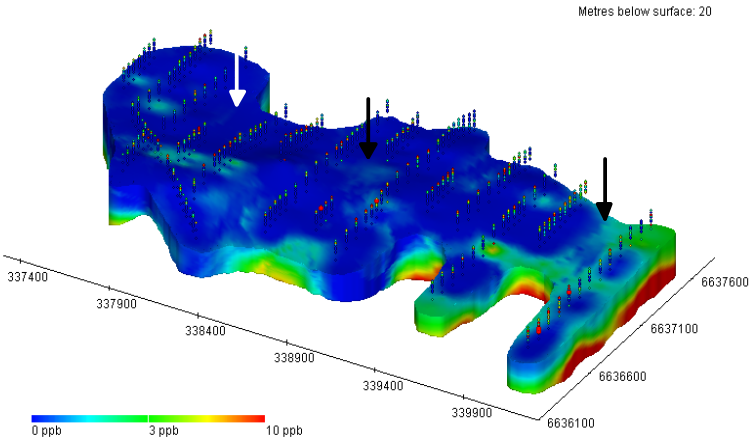

c) 20 m

Figure 5-10 (a-c) A series of diagrams showing the change in Au distribution at 10 m intervals from the surface to 50 m depth, overlaid on the DEM. Drill hole samples are coloured according to Au content. Gold data have been Box-Cox transformed before gridding by kriging and reconverting to ppb. Features are arrowed and discussed in text.

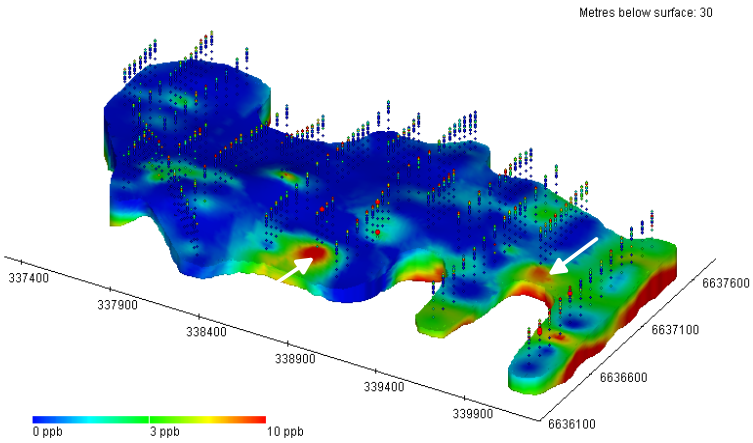

d) 30 m

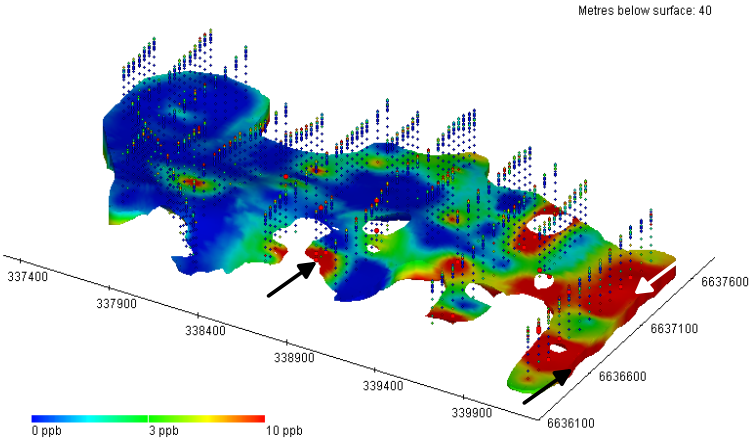

e) 40 m

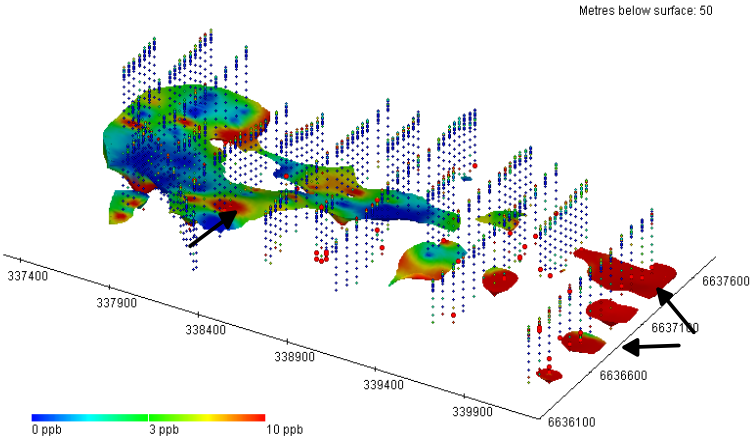

f) 50 m

Figure 5-10 continued (d-f).

MVS was used to calculate the mean concentration of Au at 1 m slices in the regolith using the methods of Sergeev and Gray (2001). The slices were made parallel to (i) the surface, and (ii) the *in situ*/transported boundary (unconformity). Box-Cox transformed data were used. Density data were not available so uniform density was assumed. As the element concentration data are mass/mass rather than mass/volume, the use of uniform density has only a minor influence on most calculations. Unfortunately, this method can lead to over- or under-estimations as the slices get further from the boundary in question. This is because the further from the boundary then the greater the probability that slice being analysed is incomplete *e.g.*, due to the presence of a dipping unconformity or undulating surface. This can be

expressed as a reliability factor, which is the mass of the slice divided by the mass of an untruncated slice and is illustrated in Figure 5-11. A reliability index of 85% indicates that the slice is 15% truncated (Sergeev and Gray, 2001).

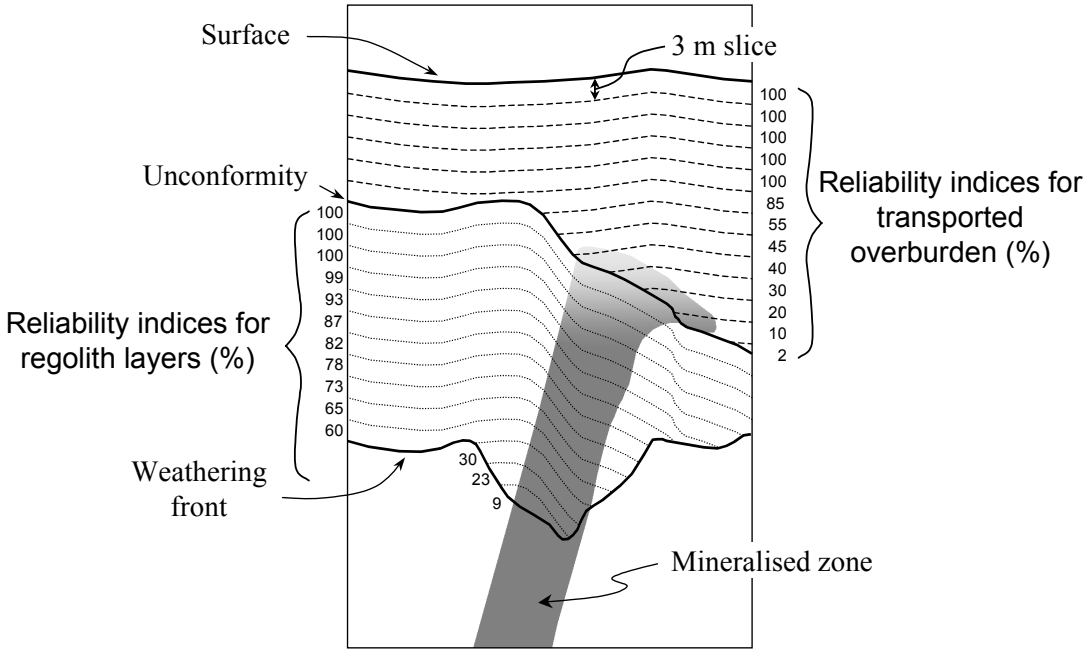

Figure 5-11 Diagrammatic representation of method for calculating Au concentration from slices defined for the upper surface and for the unconformity. The shaded area represents mineralisation, with depletion near the top of the *in situ* regolith (Sergeev and Gray, 2001).

Calculations on the distribution of Au in the regolith (Figure 5-12 and Figure 5-13) indicate the following:

1. Mean Au concentrations in transported overburden decrease downwards to the unconformity (Figure 5-12) then increase with increasing depth away from the unconformity (Figure 5-13). Thus, Au concentrations average 3.6 ppb at the unconformity, and then decrease to a minimum of 3.2 ppb at about 10 m before gradually increasing to reach a mean maximum of over 5 ppb at 32 m from the unconformity (Figure 5-13).
2. Mean Au concentrations decrease with depth from 3.8 ppb near the surface to 3.3 ppb at 10 m depth. The concentration of Au in the transported overburden and top 2 m (*in situ* and transported) is almost identical since most hole locations have a veneer of transported material. Gold concentrations are greatest in the transported material from 0-1 m, and slightly lower at the unconformity (Figure 5-12).

Gold concentrations are therefore generally weaker but show a "fish hook" distribution curve (Figure 5-12) consistent with regolith evolution models of Au depletion and concentration found for many Au deposits in the Yilgarn Craton (Butt *et al*., 1991, Butt *et al*., 1993, and Butt *et al*., 1997).

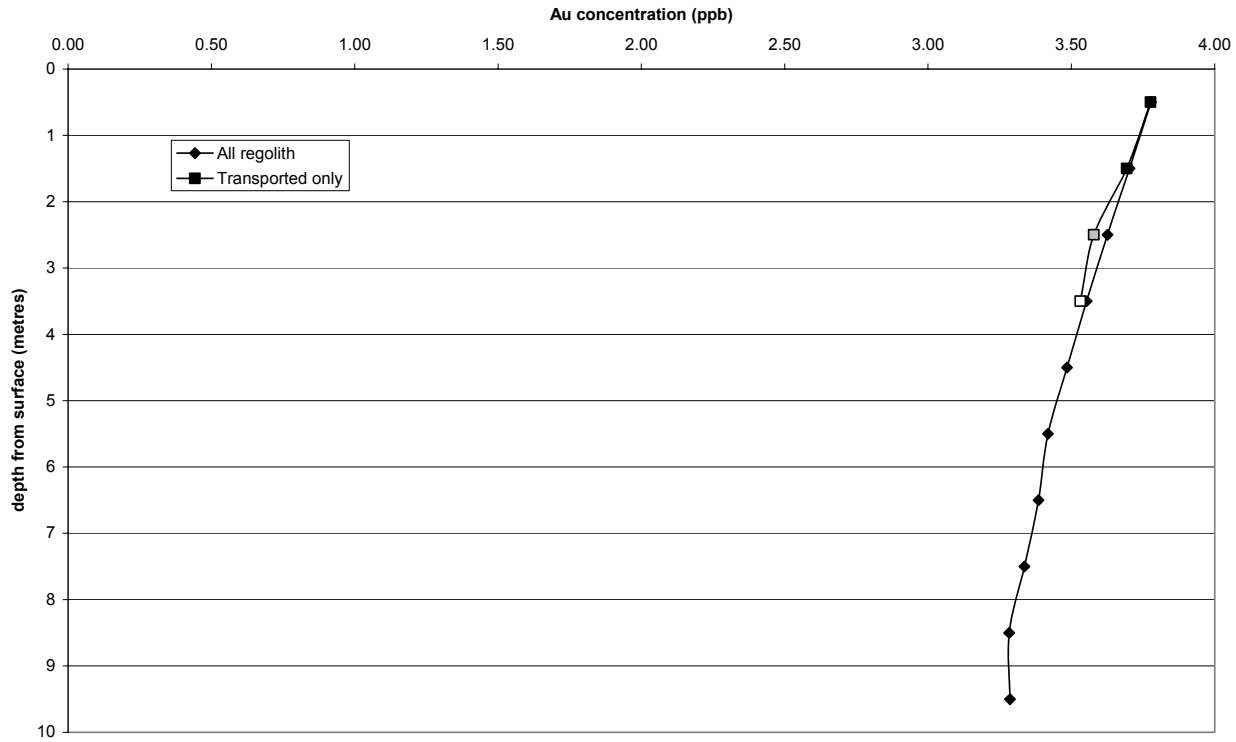

Figure 5-12 Average concentration of Au with depth from the surface. The concentrations are calculated using a series of slices at 1m intervals from, and parallel to, the surface. Calculations were performed using MVS and drill cutting data. Grey and white symbols illustrate decreasing confidence with data due to incomplete slices (see text).

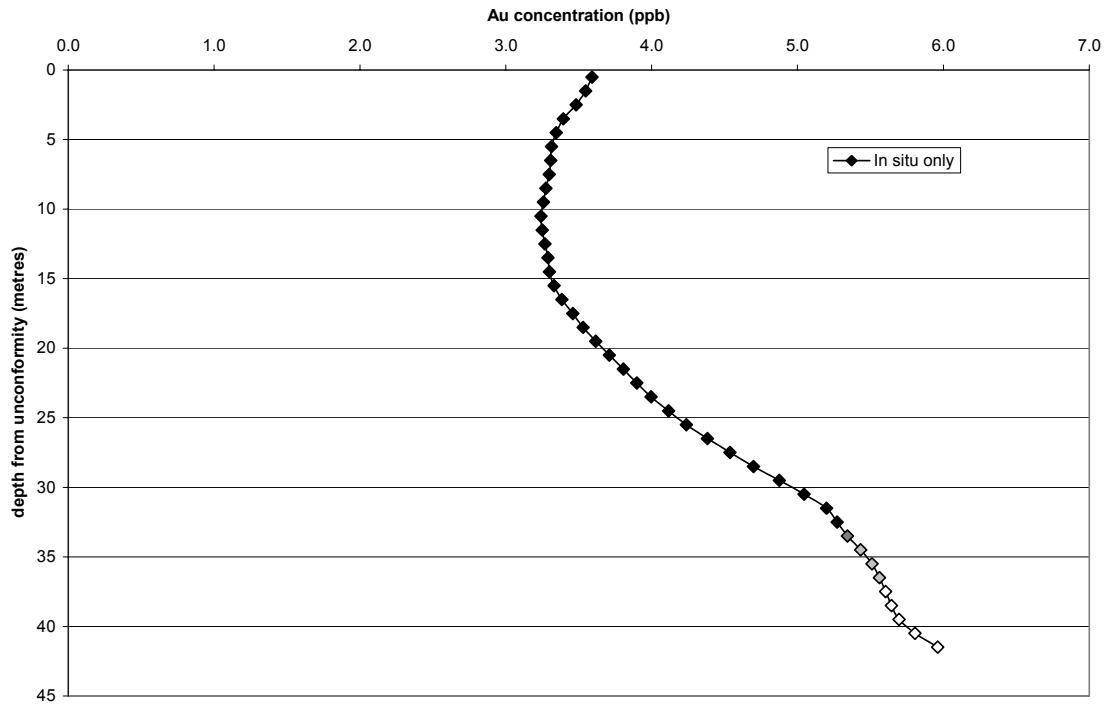

Figure 5-13 Average concentration of Au versus depth from the unconformity. The concentrations are calculated using a series of slices at 1m intervals below, and parallel to, the unconformity. Calculations were performed using MVS and drill cutting data. Grey and white symbols illustrate decreasing confidence with data due to insufficient drilling and therefore incomplete slices (see text).

5.4.5 Gold distribution in drill cuttings, section by section

5.4.5.1 Section 337400

Section 337400 is located on the western boundary at ET (Figure 5-14). The overburden is generally thin reaching just 3 m thickness in ETAR084 (Figure 5-15). Gold concentrations are highest (maximum of 5 ppb) in the calcareous overburden, whereas those for the *in situ* upper regolith are generally close to detection with a maximum of about 2 ppb in ETAR080. Mineralisation is found in the lower regolith reaching a concentration of 460 ppb at 52-53 m in ETAR082 (Figure 5-16) with corresponding surficial Au concentrations reaching 4 ppb at 0-1 m indicating poor correlation with mineralisation *i.e.,* false background or only a weak anomaly.

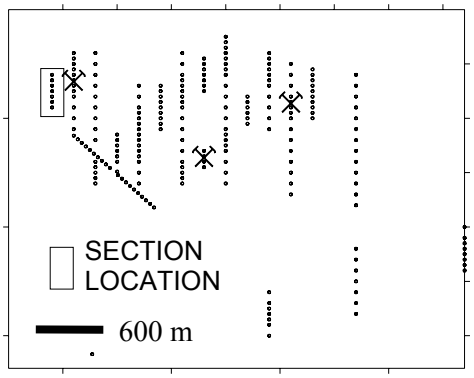

Figure 5-14 Plan showing location of drill holes, the three most mineralised holes and section 337400E.

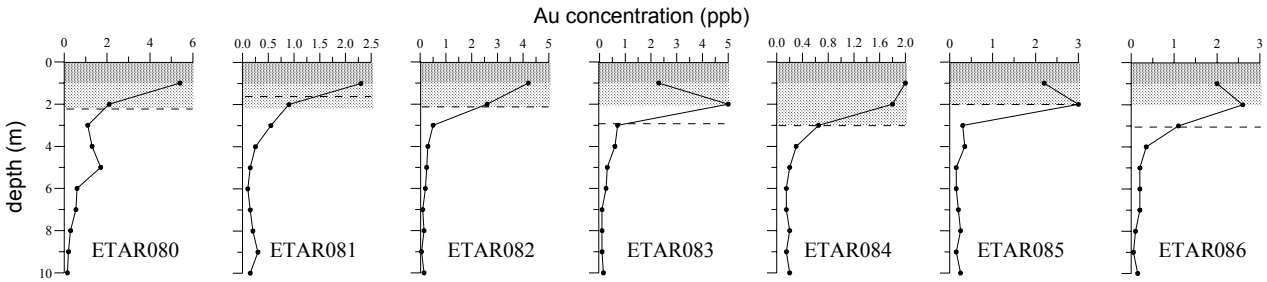

Figure 5-15 Gold distribution in 0-10 m drill hole samples on 337400E. Dashed line indicates approximate position of the unconformity. Shaded area indicates semi-quantitative estimate of carbonate concentration. Holes are displayed sequentially south (top left) to north (bottom right).

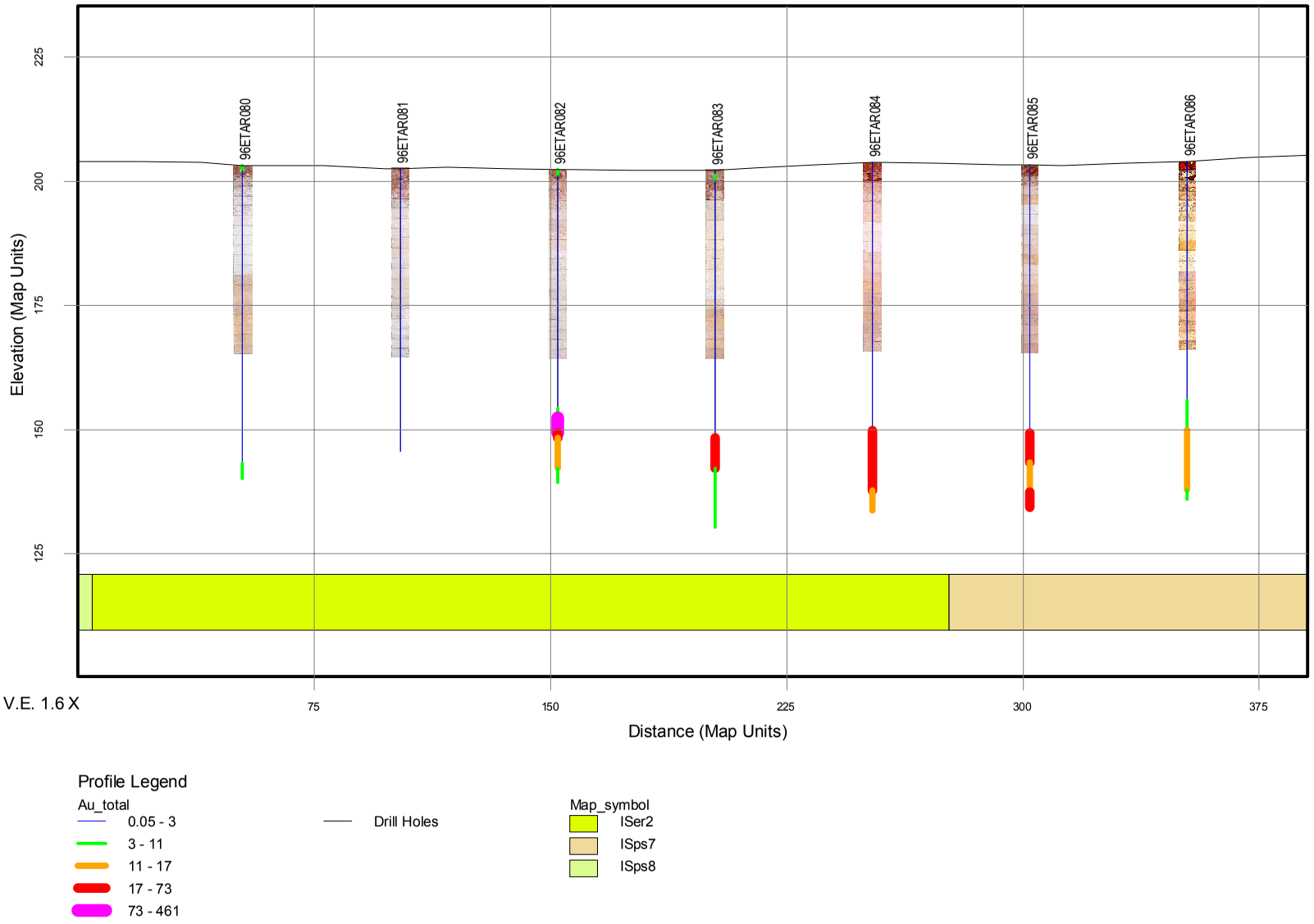

Figure 5-16 Drill section 337400E showing drill holes, Au concentration, regolith geology, chip tray photographs (0-38 m) and land surface. For detailed description of regolith-landform map symbols see text or map. All map units in metres.

5.4.5.2 Section 337600

Section 337600E is located in the far western part of the study area (Figure 5-17). The overburden is generally thin reaching a maximum of about 3 m thickness (Figure 5-18). The maximum Au concentration is 120 ppb in 0-1 m (ETAR 121) although this sample result is suspect since duplicate re-analysis gave a concentration of 1.2 ppb suggesting the presence of particulate Au or an analytical problem with the original sample. ETAR119 has one of the three highest Au concentrations in the lower regolith (Figure 5-19, 670 ppb at 50-51 m), but the maximum Au concentration in the upper regolith is a mere 4 ppb; similarly in ETAR125 where mineralisation reaches 310 ppb at 63-64 m the maximum in the upper regolith is only 2.4 ppb *i.e.,* these are both false negative anomalies. Gold concentrations reach 9 and 10 ppb in ETAR116 and 115, respectively, but no mineralisation was recorded in the lower regolith *i.e.,* a false or displaced anomaly. The Au data for this section do not suggest a correlation between lower and upper regolith concentrations.

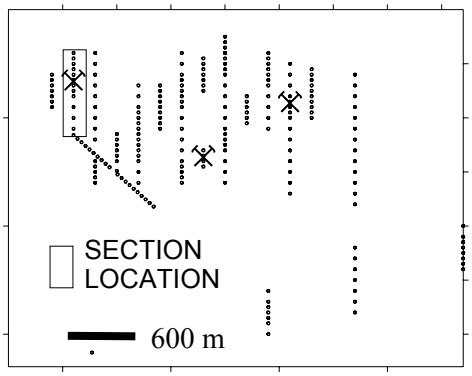

Figure 5-17 Plan showing location of drill holes, the three most mineralised holes and section 337600E.

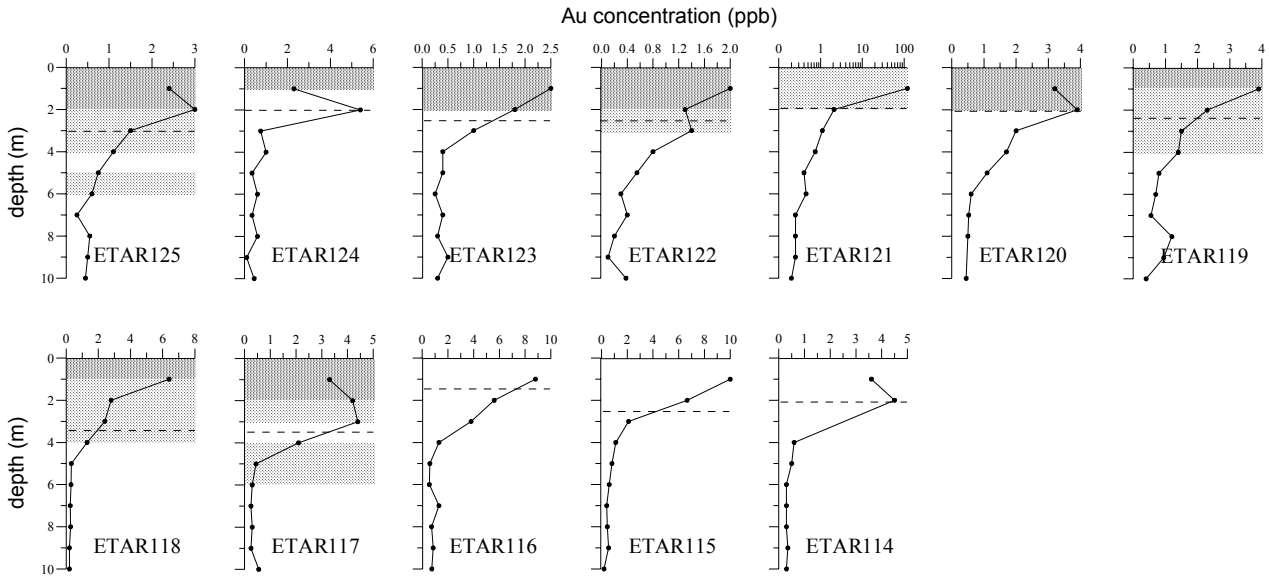

Figure 5-18 Gold distribution in 0-10 m drill hole samples on 337600E. Dashed line indicates approximate position of the unconformity. Shaded area indicates semi-quantitative estimate of carbonate concentration. Holes are displayed sequentially south (top left) to north (bottom right).

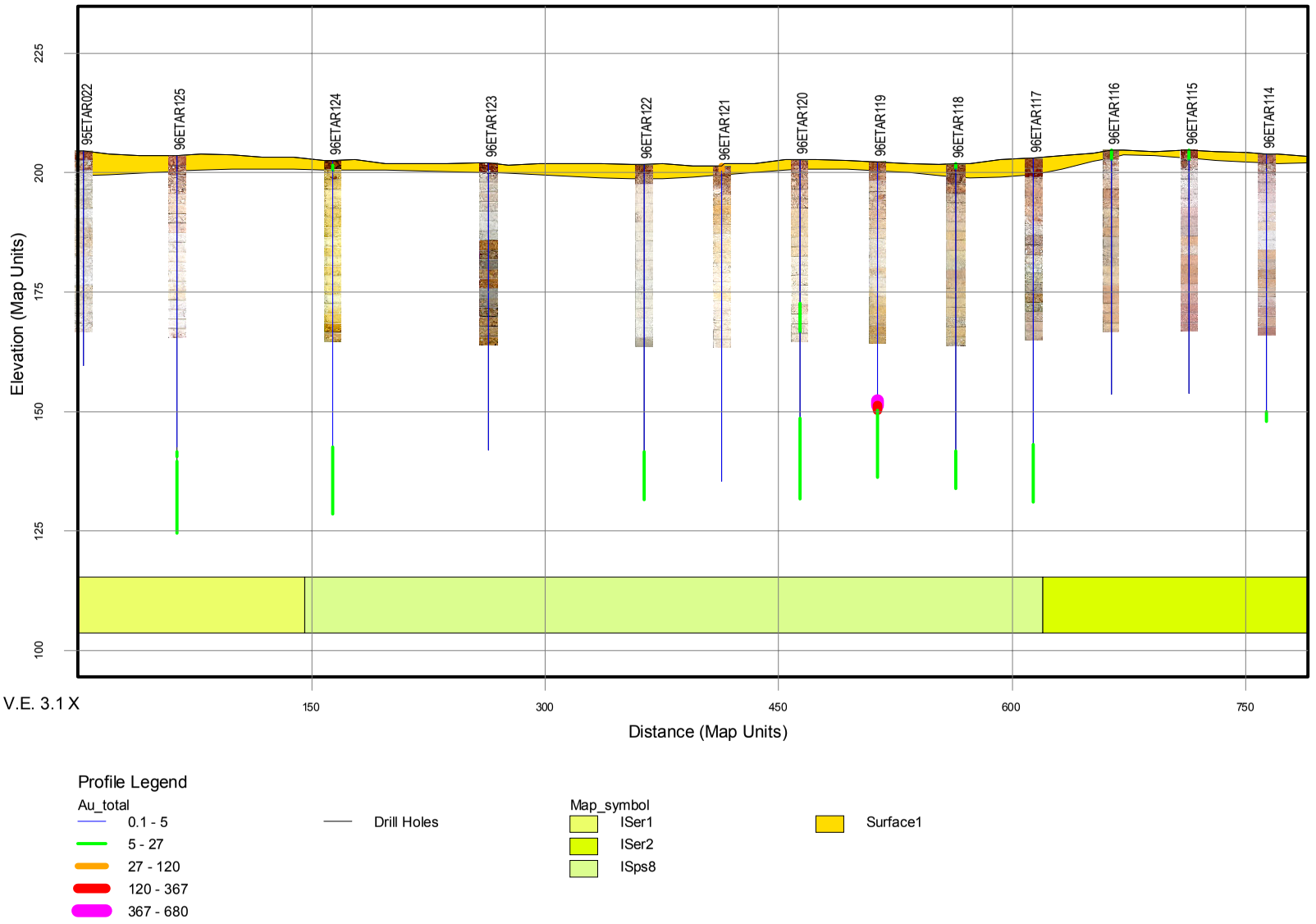

Figure 5-19 Drill section 337600E showing drill holes, Au concentration, regolith geology, chip tray photographs (0-38 m) and depth of overburden ("surface"). For detailed description of regolith-landform map symbols see text or map. All map units in metres.

5.4.5.3 Diagonal section

The NW-SE orientated "Diagonal section" is located in the western part of ET Gold Prospect (Figure 5-20). The section straddles a topographic high with thicker overburden at either end (Figure 5-21). Only minor mineralisation (maximum of 12 ppb) was recorded in the lower regolith (Figure 5-22). Overburden is thickest in the SE (maximum 10 m) for ETAR 004. Gold concentrations reach 9 ppb in calcareous samples of the SE overburden but are highest (11 ppb) in the thinner overburden (3 m) of ETAR014 coincident with a topographic palaeohigh. A "tongue" of carbonate (partly dolomitic), anomalous in Au, extends from the palaeohigh into the deep overburden of the SE, indicating mobilisation of Au downslope (see Figure 5-8). Many of the 0-1 m drill cuttings in the field were absent and had either been washed or blown away or were never recovered from the drill hole, presumably due to their sandy nature.

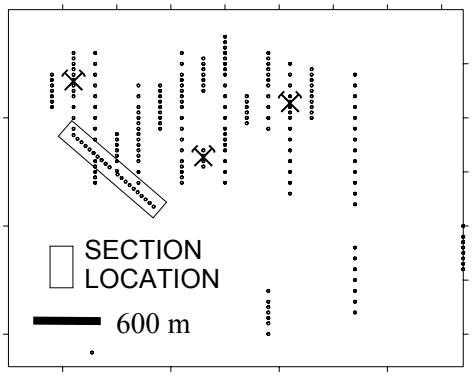

Figure 5-20 Plan showing location of drill holes, the three most mineralised holes and Diagonal section.

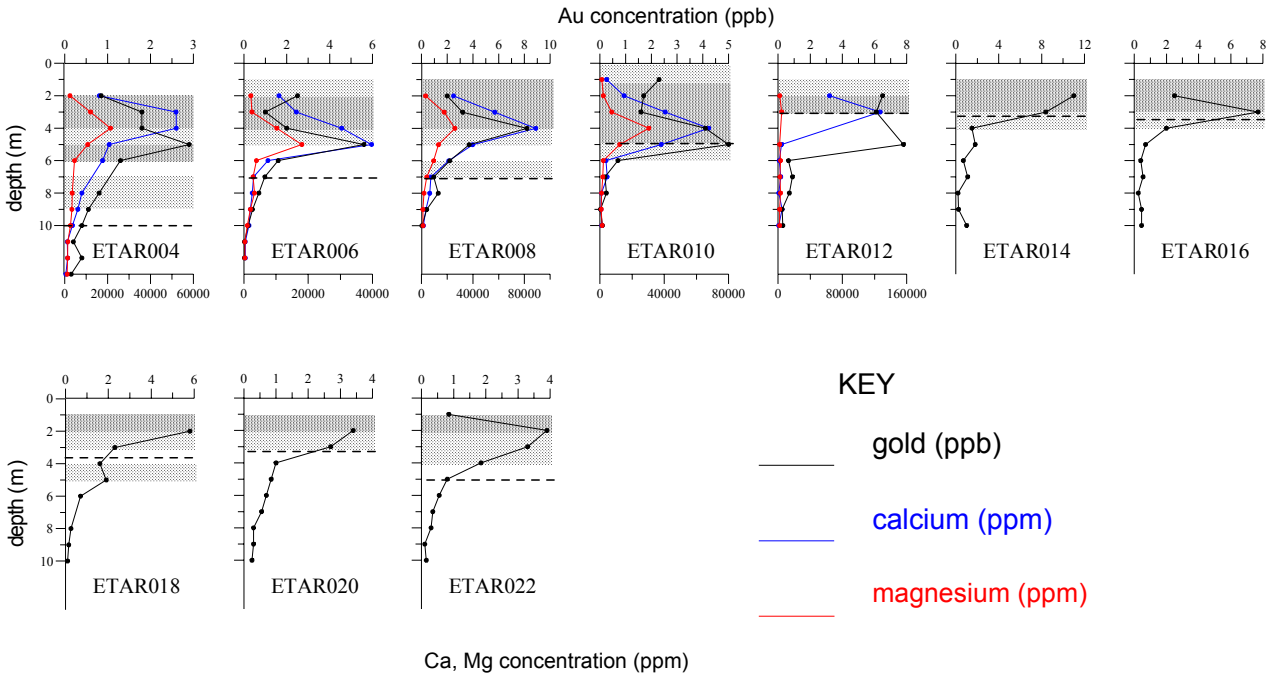

Figure 5-21 Gold, Ca and Mg distributions in 0-13 m drill hole samples on Diagonal section. Dashed line indicates approximate position of the unconformity. Shaded area indicates semi-quantitative estimate of carbonate concentration. Holes are displayed sequentially NW to SE (top left to bottom right).

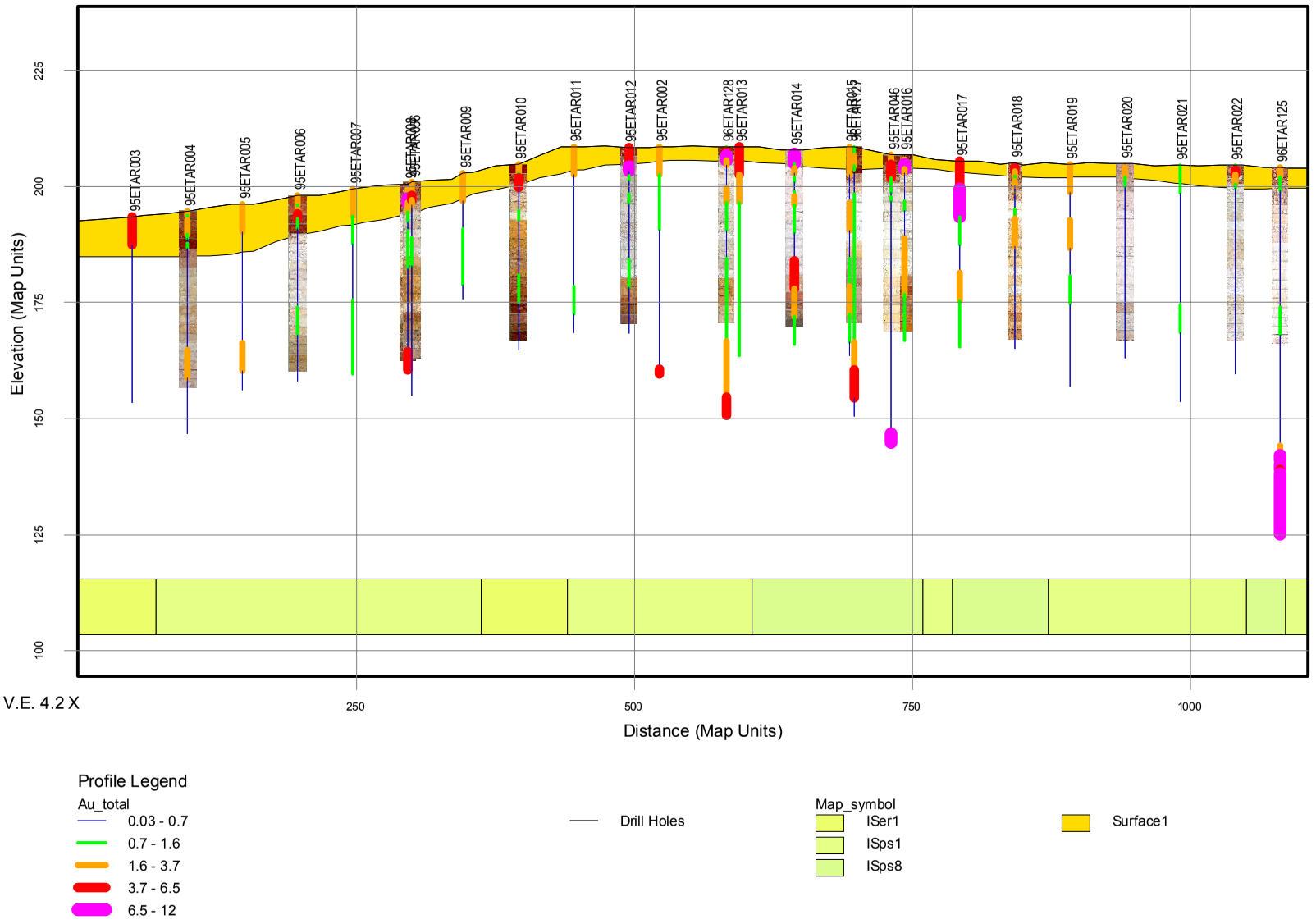

Figure 5-22 Diagonal drill section showing drill holes, Au concentration, regolith geology, chip tray photographs (0-38 m) and depth of overburden ("surface"). For detailed description of regolith-landform map symbols see text or map. All map units in metres.

5.4.5.4 Section 337800E

Section 337800E is located in the western part of the study area (Figure 5-23). Overburden is thickest (maximum of 10 m) in the south and is thin (~2-3 m) in the centre and northern part of the section (Figure 5-24). A "tongue" of Au (maximum of 8 ppb), also evident in the Diagonal section, is present in the south and, with the Diagonal section data, suggests a widespread dispersal of Au extending from the *in situ* regolith into the transported overburden towards the SW (see Figure 5-8 and Figure 5-24). The highest Au concentrations (up to 7 ppb) in the *in situ* upper regolith were recorded in ETAR 046 and 050. Weak mineralisation (40-60 ppb for BOH samples for ETAR053-055) was recorded in the northern part of the section (Figure 5-25).

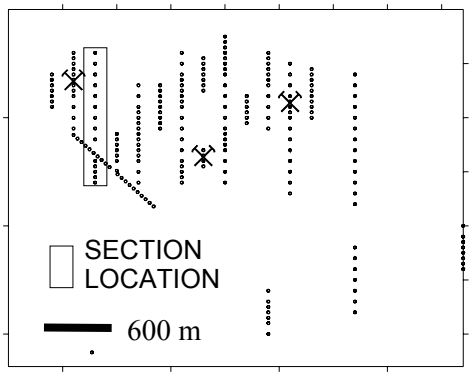

Figure 5-23 Plan showing location of drill holes, the three most mineralised holes and section 337800E.

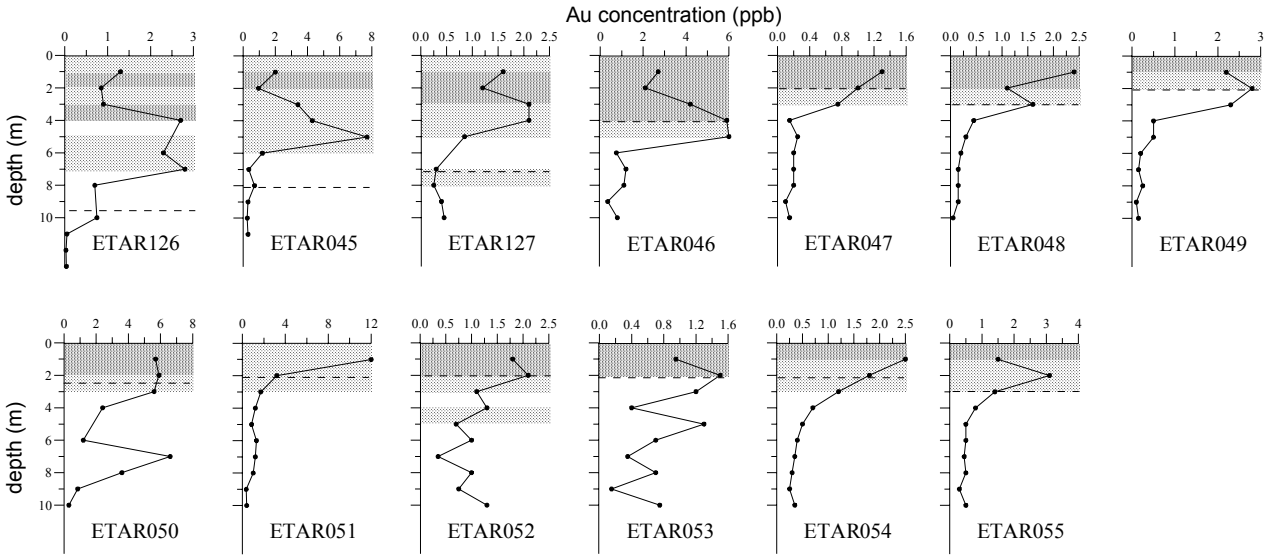

Figure 5-24 Gold distribution in 0-13 m drill hole samples on 337800E. Dashed line indicates approximate position of the unconformity. Shaded area indicates semi-quantitative estimate of carbonate concentration. Holes are displayed sequentially (left to right) with the southern most hole located left and northern most hole right.

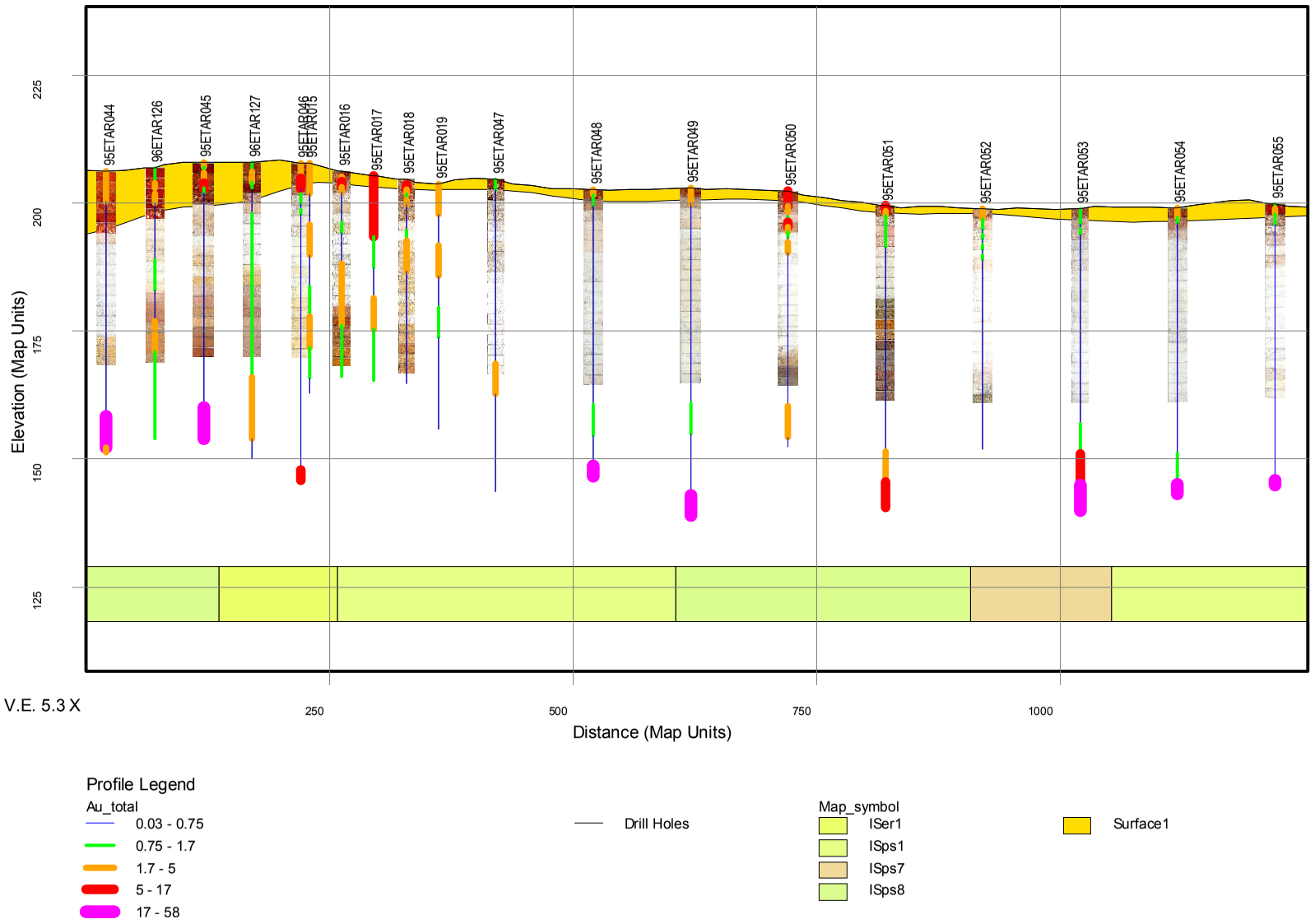

Figure 5-25 Drill section 337800E showing drill holes, Au concentration, regolith geology, chip tray photographs (0-38 m) and depth of overburden ("surface"). For detailed description of regolith-landform map symbols see text or map. All map units in metres.

5.4.5.5 Section 338000E

The thickness of transported overburden is variable (2-5 m) on section 338000E, located in the western part of ET (Figure 5-26, Figure 5-27). Weak mineralisation is present in ETAR131 (35 ppb) and, to a lesser extent, in adjacent locations (Figure 5-28). However, most Au is in the upper *in situ* and transported regolith. ETAR132 is particularly anomalous in Au with concentrations over 5 ppb (maximum of 12 ppb) in the top 6 m (false or displaced anomaly). Similarly, ETAR128 and 131 also have Au maxima in excess of 9 ppb with no immediate source of Au to cause the anomaly. The alkaline earth metal data indicate peak concentrations correspond with anomalous Au. This section is located through the centre of the strongest Au in calcrete anomaly at ET though there is poor vertical agreement between calcrete and drill cutting data.

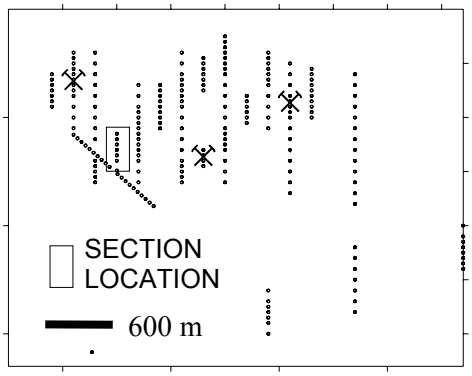

Figure 5-26 Plan showing location of drill holes, the three most mineralised holes and section 338000E.

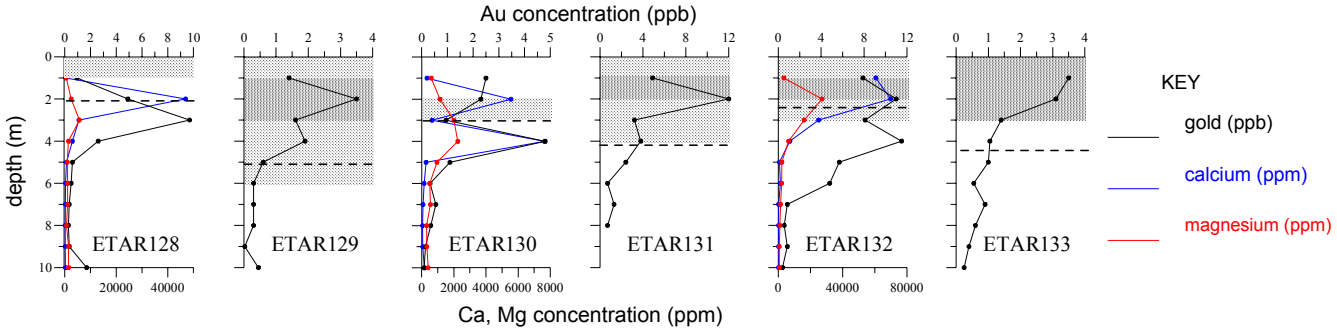

Figure 5-27 Gold, Ca and Mg distributions in 0-10 m drill hole samples on 338000E. Dashed line indicates approximate position of the unconformity. Shaded area indicates semi-quantitative estimate of carbonate concentration. Holes are displayed sequentially (left to right) with the southern most hole located left and northern most hole right.

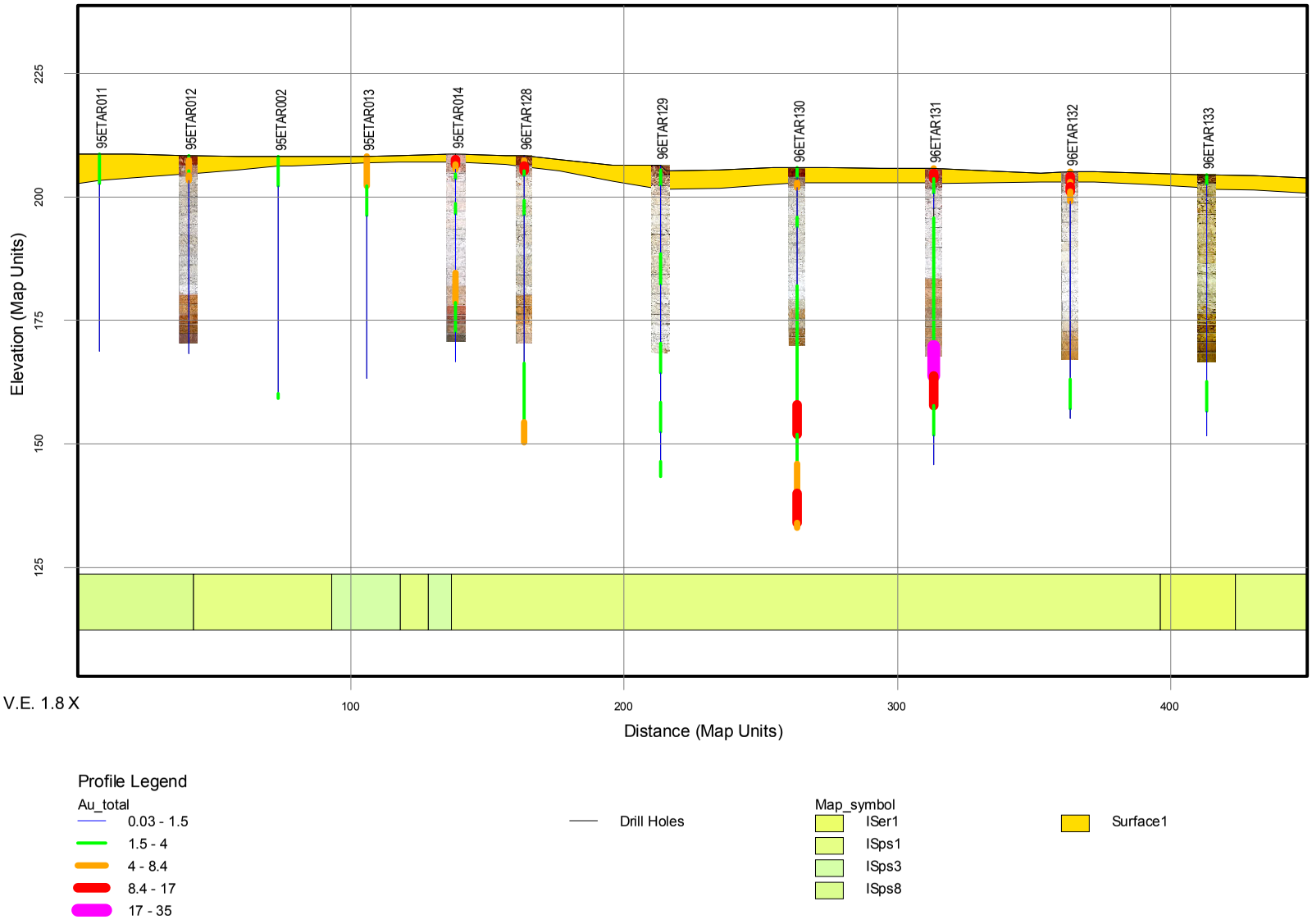

Figure 5-28 Drill section 338000E showing drill holes, Au concentration, regolith geology, chip tray photographs (0-38 m) and depth of overburden ("surface"). For detailed description of regolith-landform map symbols see text or map. All map units in metres.

5.4.5.6 Section 338200E

Section 338200E is located in the western half of ET (Figure 5-29). Weak mineralisation occurs in the centre of the section around ETAR059 and 088 (Figure 5-30). Transported overburden is generally thin (<3 m) but reaches 5 m at the extreme southern hole (ETAR056). Gold concentrations in excess of 4 ppb occur in all holes except ETAR063 and 065. Anomalous Au concentrations (>10 ppb) were recorded in the upper regolith in several holes (ETAR058, 059, 088 and 060), corresponding with weak mineralisation (Figure 5-31, up to 74 ppb) in the lower regolith (true anomaly), and the appearance of calcrete at the unconformity. Soil profile 4 is located near hole ETAR 087. The southern part of this section is the approximate eastern boundary of the strongest Au in calcrete anomaly at ET although the Au concentrations are higher than found in the drill cuttings from the area (Figure 5-4).

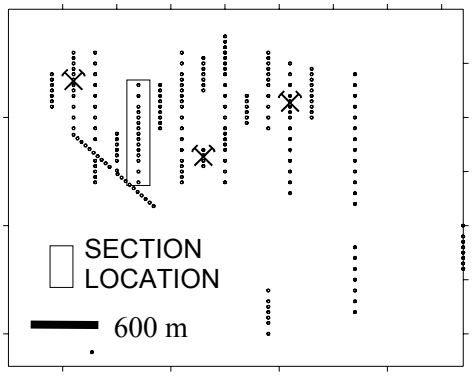

Figure 5-29 Plan showing location of drill holes, the three most mineralised holes and section 338200E.

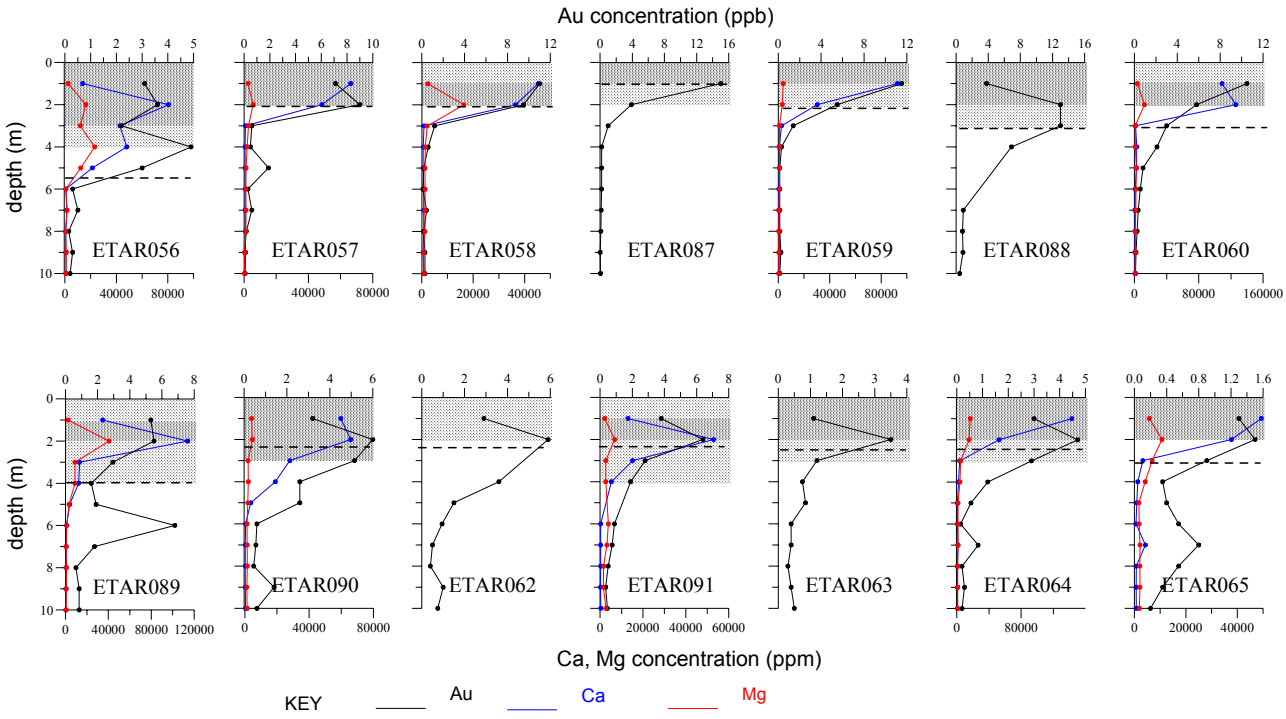

Figure 5-30 Gold, Ca and Mg distributions in 0-10 m drill hole samples on 338200E. Dashed line indicates approximate position of the unconformity. Shaded area indicates semi-quantitative estimate of carbonate concentration. Holes are displayed sequentially (left to right) with the southern most hole located left and northern most hole right.

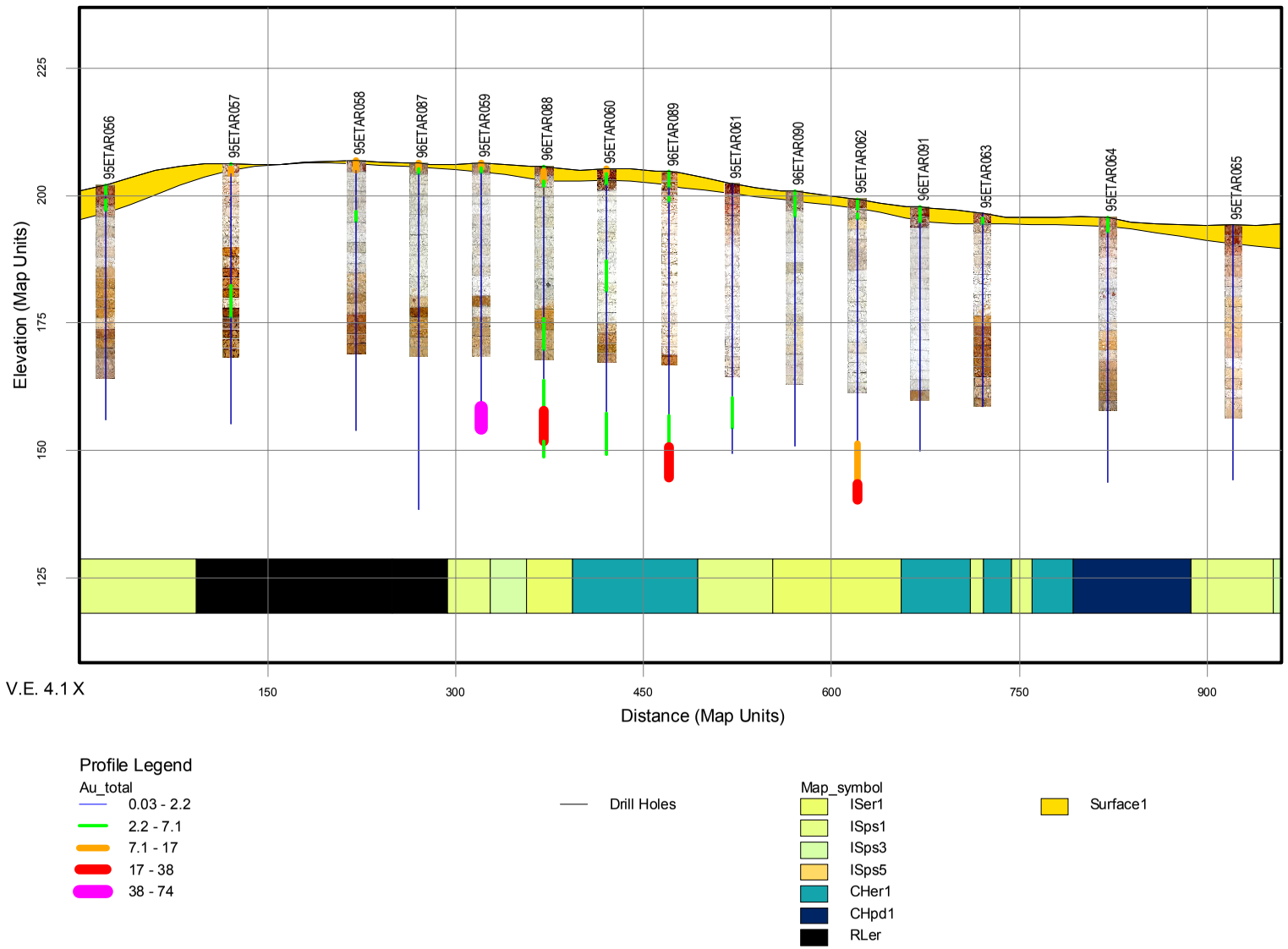

Figure 5-31 Drill section 338200E showing drill holes, Au concentration, regolith geology, chip tray photographs (0-38 m) and depth of overburden ("surface"). For detailed description of regolith-landform map symbols see text or map. All map units in metres.

5.4.5.7 Section 338400E

Section 338400E is located in the western half of ET (Figure 5-32). Transported overburden is generally thin but gradually thickens to the north reaching 4 m in ETAR136. Maximum Au concentrations exceed 4 ppb in all drill cutting samples except ETAR136, and exceed 10 ppb in ETAR135, 142 140 and 139 (Figure 5-33). Weak saprolite mineralisation occurs in ETAR141 (40 ppb at 42-48 m) with similar concentrations of Au in most of the other locations (Figure 5-34). As with 338200E, Au concentrations tend to peak about the unconformity. There is reasonable agreement between Au and calcrete distributions.

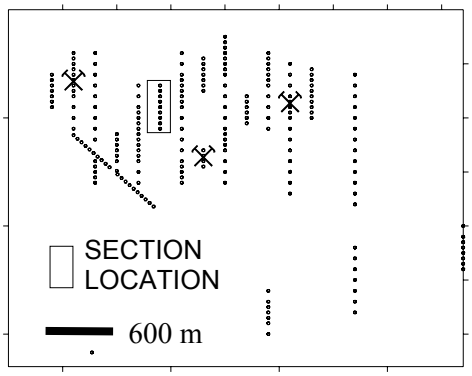

Figure 5-32 Plan showing location of drill holes, the three most mineralised holes and section 338400E.

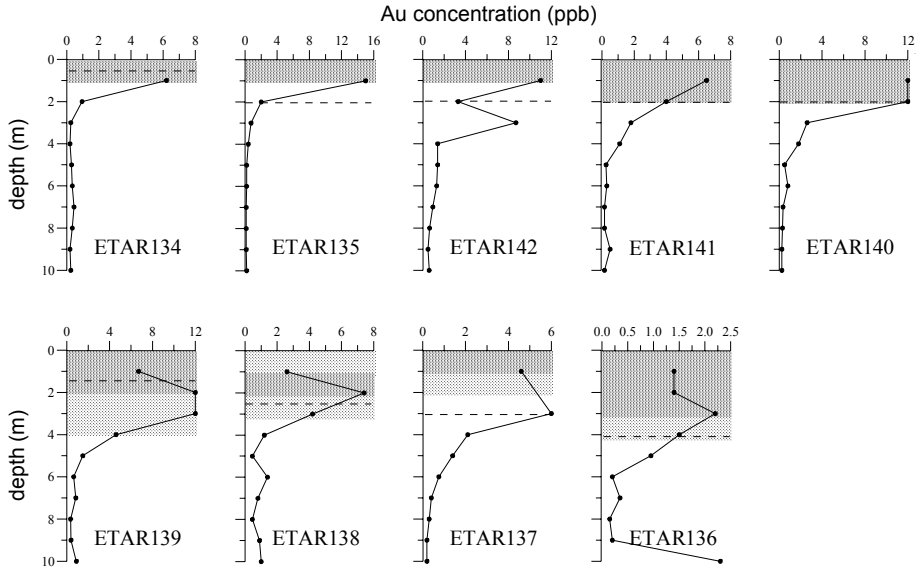

Figure 5-33 Gold distribution in 0-10 m drill hole samples on 338400E. Dashed line indicates approximate position of the unconformity. Shaded area indicates semi-quantitative estimate of carbonate concentration. Holes are displayed sequentially (left to right) with the southern most hole located left and northern most hole right.

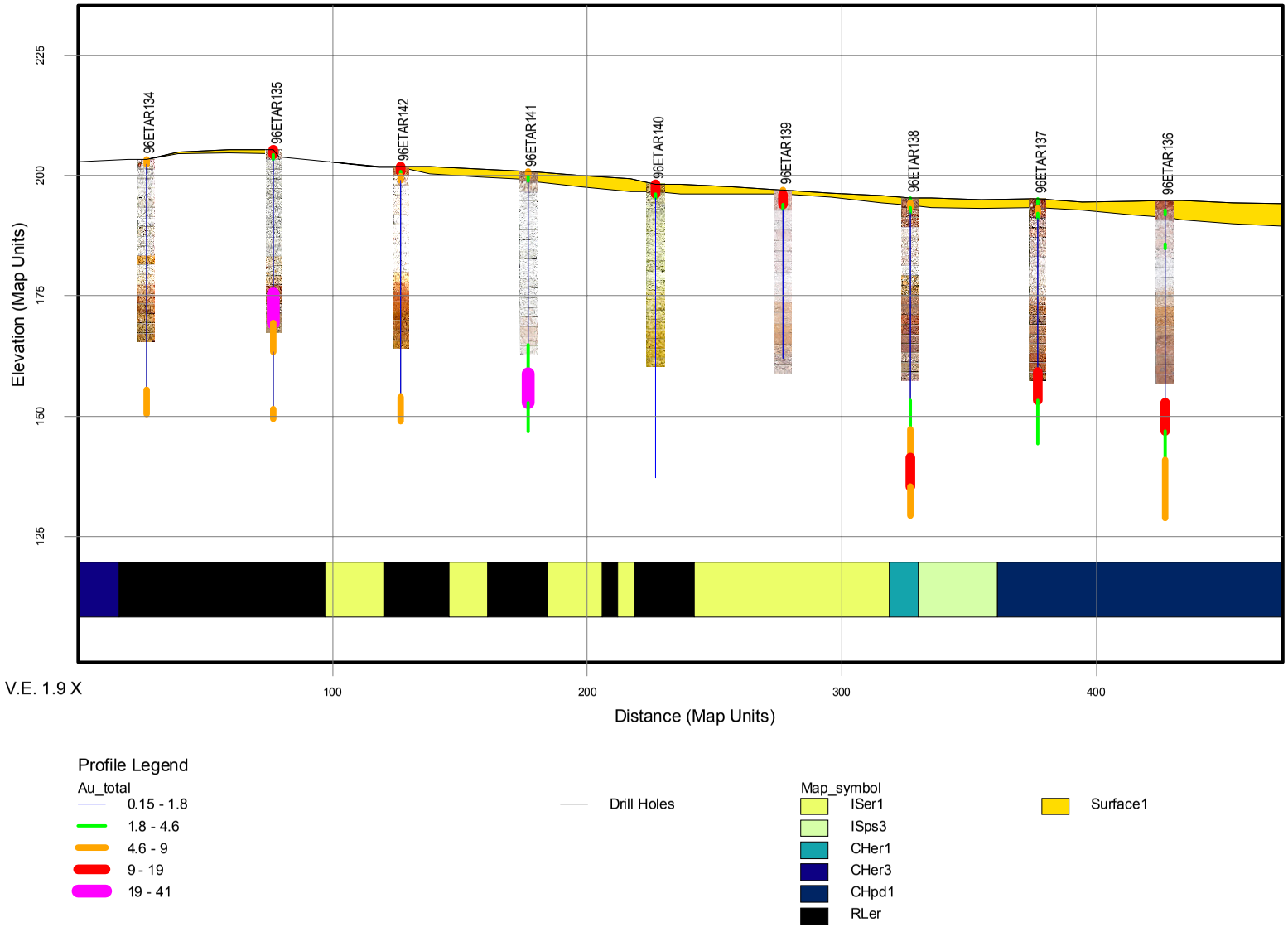

Figure 5-34 Drill section 338400E showing drill holes, Au concentration, regolith geology, chip tray photographs (0-38 m) and depth of overburden ("surface"). For detailed description of regolith-landform map symbols see text or map. All map units in metres.

5.4.5.8 Section 338600E

Section 338600E is located west of the centre of the prospect (Figure 5-35). Some Au was detected in the deeper regolith but concentrations are very low (maximum of 30 ppb, Figure 5-36). The section straddles a ridge and paleoridge with thicker transported overburden occurring at either end of the section, including a shallow channel (9 m deep) in the south. Gold concentration is highest (13 ppb) and transported overburden is thinnest (< 1 m) in ETAR037 (false or displaced anomaly); adjacent near surface samples are also relatively high in Au and have minor mineralisation located beneath them (Figure 5-37). An anomalous horizon of Au, 2-5 m below the surface, occurs in the transported overburden either side of the palaeoridge. Gold and calcrete distributions are similar.

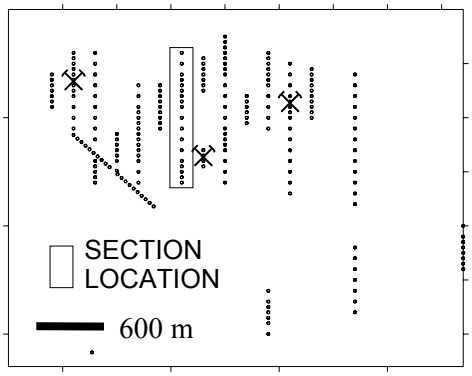

Figure 5-35 Plan showing location of drill holes, the three most mineralised holes and section 338600E.

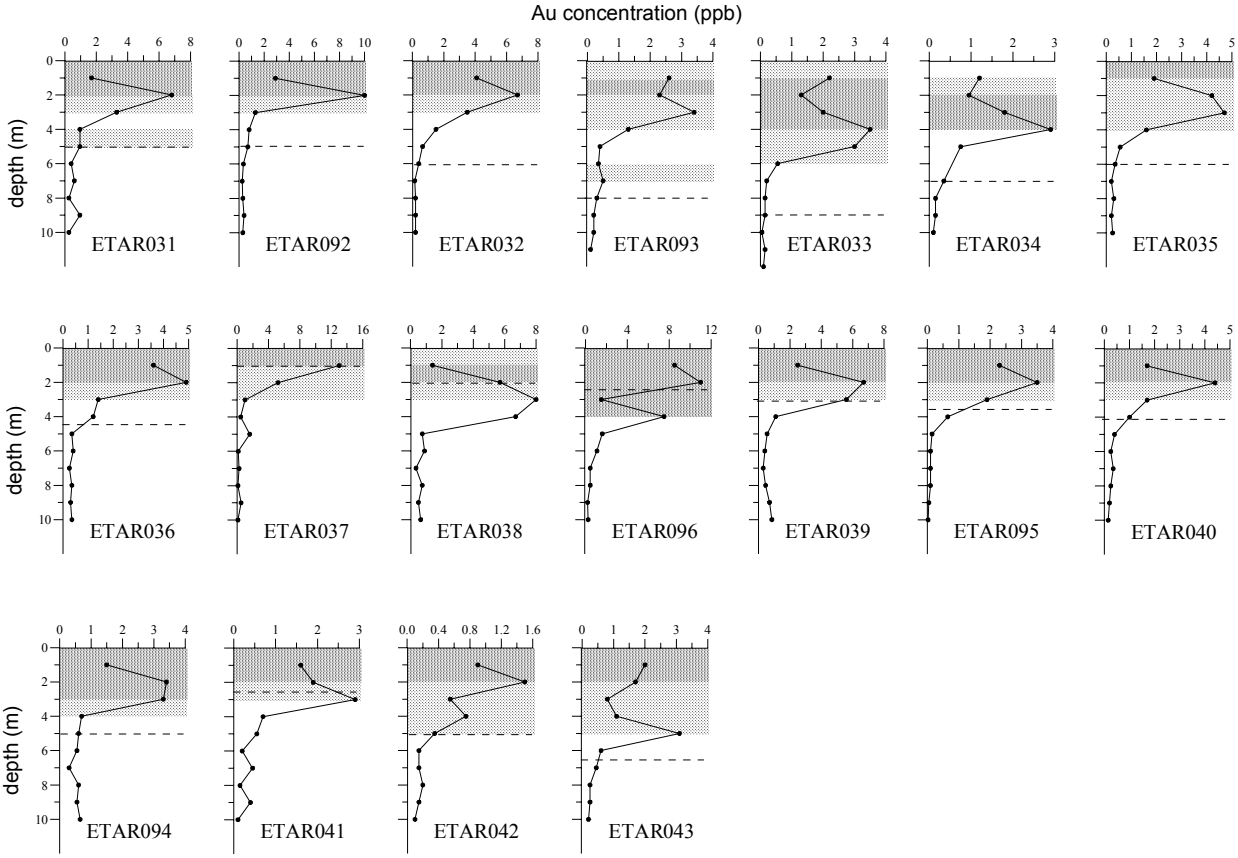

Figure 5-36 Gold distribution in 0-10 m drill hole samples on 338600E. Dashed line indicates approximate position of the unconformity. Shaded area indicates semi-quantitative estimate of carbonate concentration. Holes are displayed sequentially (left to right) with the southern most hole located left and northern most hole right.

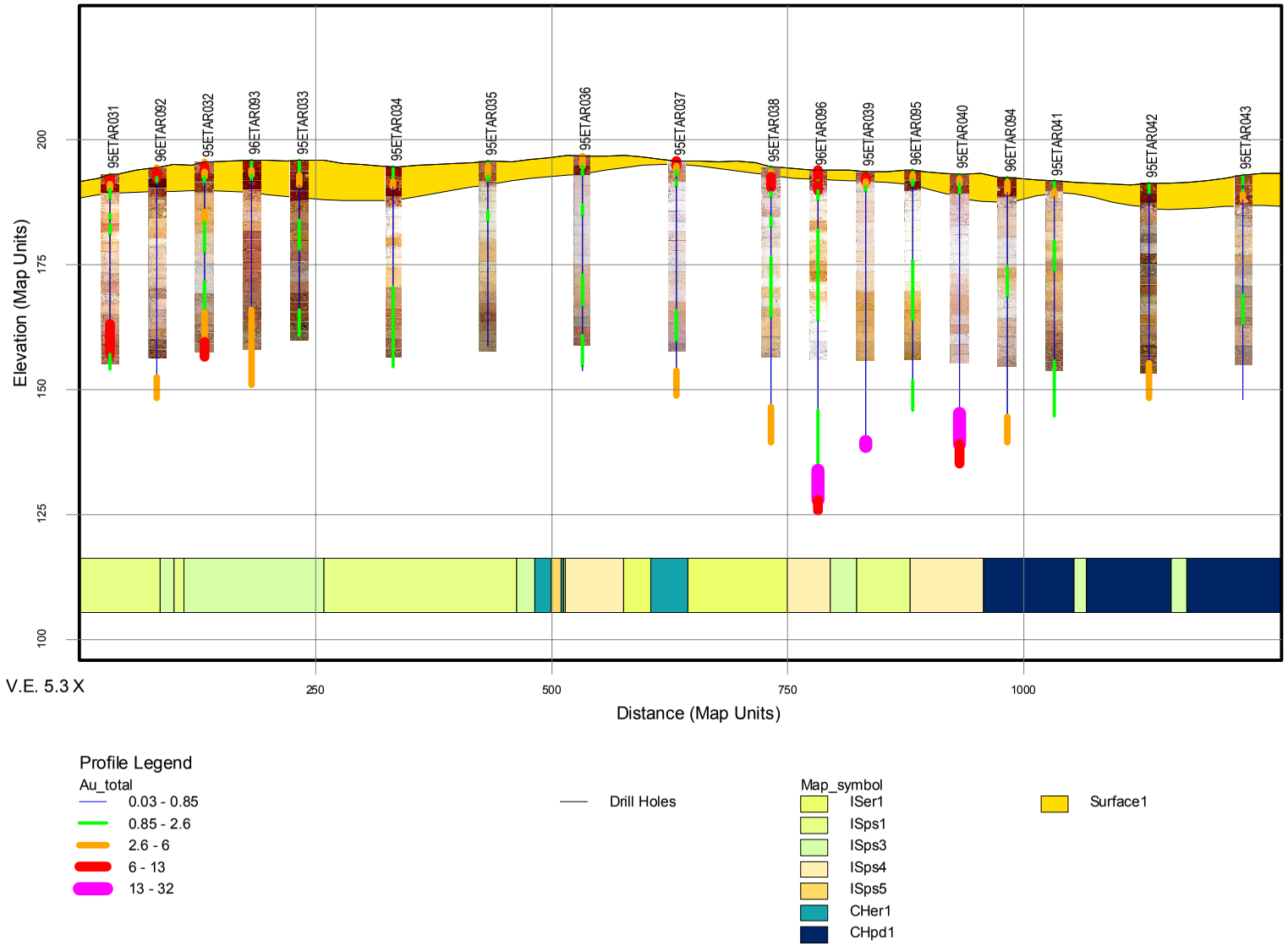

Figure 5-37 Drill section 338600E showing drill holes, Au concentration, regolith geology, chip tray photographs (0-38 m) and depth of overburden ("surface"). For detailed description of regolith-landform map symbols see text or map. All map units in metres.

5.4.5.9 Section 338800E

Section 338800E is located in the centre of the prospect (Figure 5-38). In the southern part of the section, one of the three highest Au concentrations from the lower regolith was recorded together with a strong association between Au and the alkaline earth metals (Figure 5-39). In the southern part of the section, the transported overburden is 4-6 m thick with an anomalous concentration of 20 ppb Au (1-2 m, ETAR152). with moderate mineralisation at depth (Figure 5-41, 80 ppb at 42-44 m). Fifty metres to the north, ETAR151 is strongly mineralised (0.69 ppm Au at 40-41 m) but peak Au concentrations are similar (7-8 ppb) to less mineralised ETAR150 and 153 *i.e.,* a false background. Thus, there is little evidence for a direct association between mineralisation and Au within the overlying transported overburden and the calcrete c.f. section 339000E.

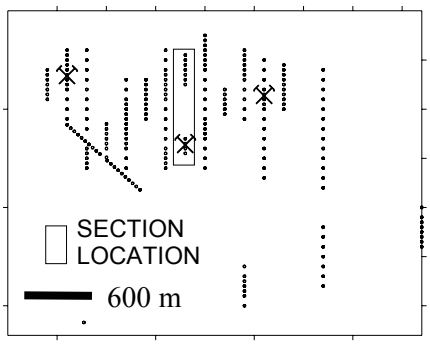

Figure 5-38 Plan showing location of drill holes, the three most mineralised holes and section 338800E.

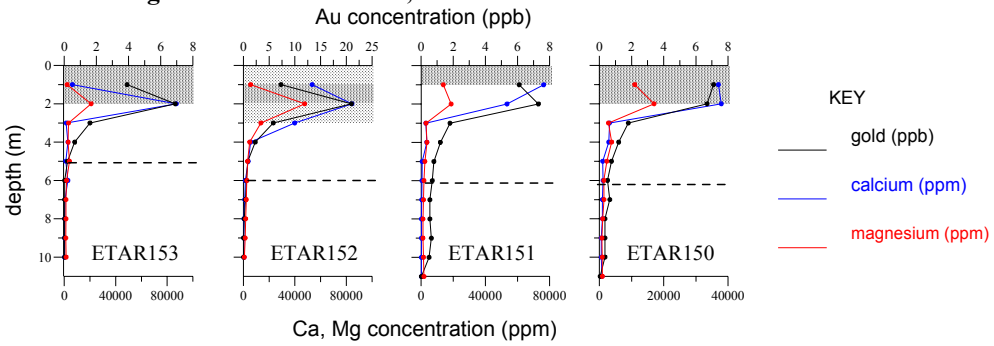

Figure 5-39 Gold, Ca and Mg distributions in 0-10 m drill hole samples on regolith section 338800E southern part. Dashed line indicates approximate position of the unconformity. Shaded area indicates semi-quantitative estimate of calcrete concentration. Holes are displayed sequentially (left to right) with the southern most hole located left and northern most hole right.

In the northern part of the section, the transported overburden is thinner but thickens northwards to 3-4 m (Figure 5-40). The highest Au concentration (12 ppb) occurs close to, but below, the unconformity.

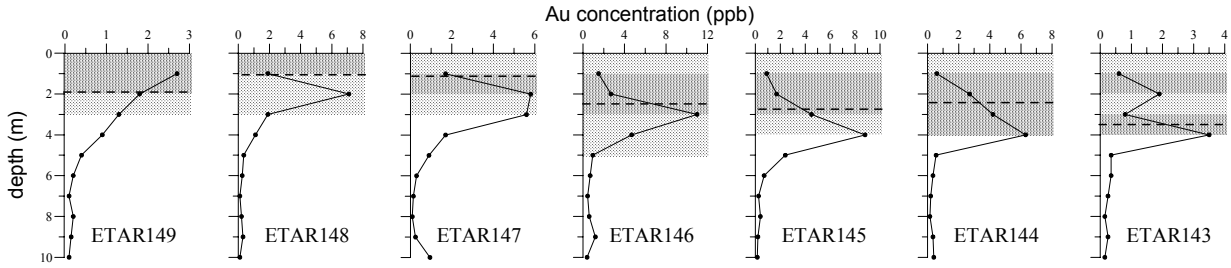

Figure 5-40 Gold distribution in 0-10 m drill hole samples on regolith section 338800E northern part. Dashed line indicates approximate position of the transported-*in situ* boundary. Shaded area indicates semi-quantitative estimate of carbonate concentration. Holes are displayed sequentially (left to right) with the southern most hole located left and northern most hole right.

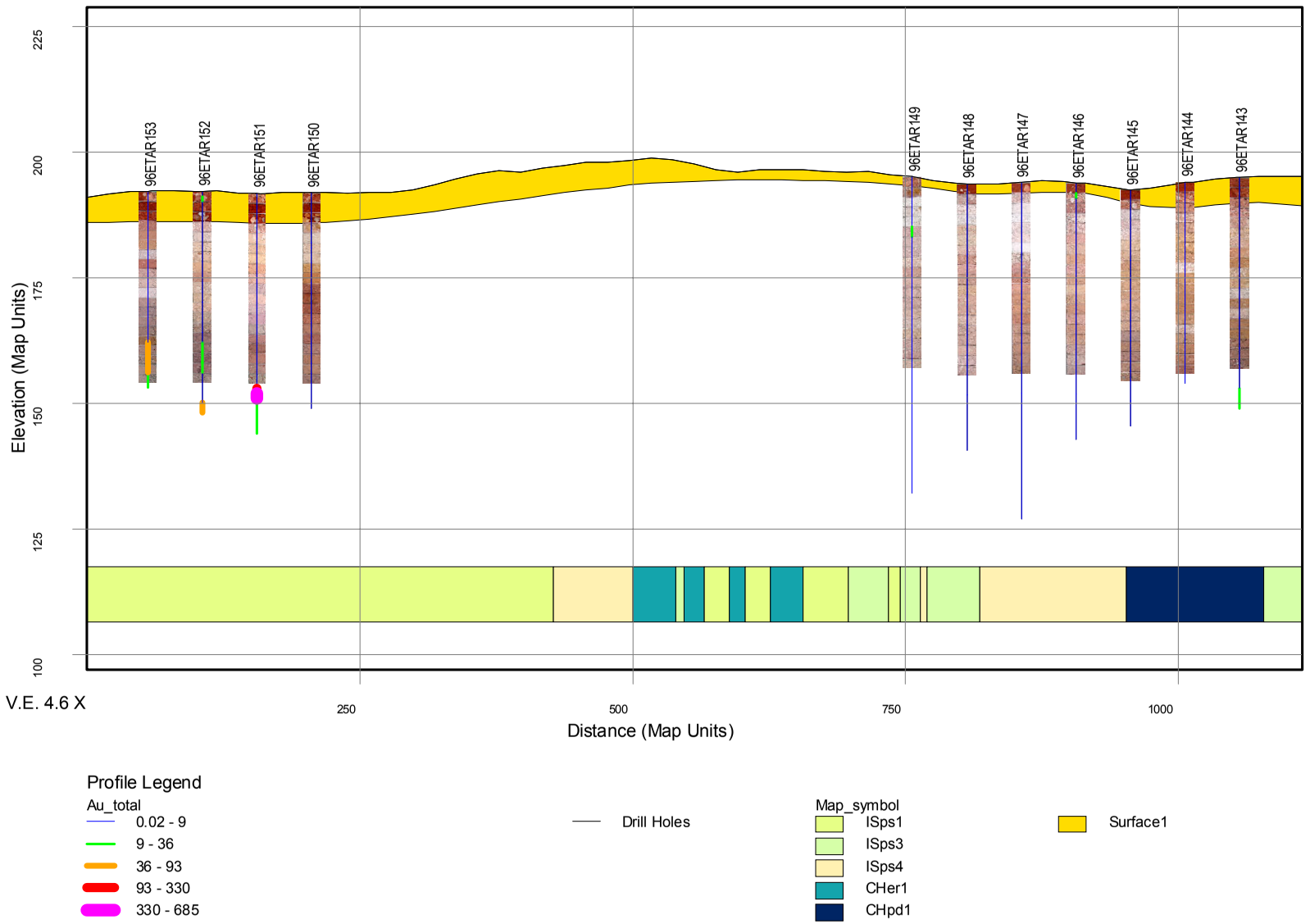

Figure 5-41 Drill section 338800E showing drill holes, Au concentration, regolith geology, chip tray photographs (0-38 m) and depth of overburden ("surface"). For detailed description of regolith-landform map symbols see text or map. All map units in metres.

5.4.5.10 Section 339000E

Section 339000E is in the centre of the prospect (Figure 5-42). Transported overburden is thicker (maximum of 6 m) in the south than the north (1-2 m) (Figure 5-43). ETAR070, in the southern part of the section, is mineralised (250 ppb at 25-26 m) and there are also holes in the northern part that contain some weaker mineralisation (Figure 5-44). Surficial Au is anomalous in all holes reaching a maximum of 35 ppb in clayey calcareous sand at 2-3 m over mineralised ETAR070 *i.e.,* a true anomaly within transported overburden c.f. section 338800E or, possibly, a chance anomaly derived from upslope. This is one of a few holes where anomalous Au persists in the upper saprolite to at least 6 m depth. It is located on the southern flanks of the central ridge. Calcrete and Au are strongly associated and occur near the surface. Soil profiles 1a and 1b are located ~20 m east of ETAR070 and also have highly anomalous Au (maximum of 50 ppb).

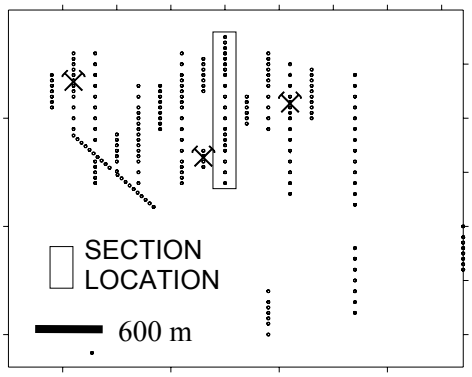

Figure 5-42 Plan showing location of drill holes, the three most mineralised holes and section 339000E.

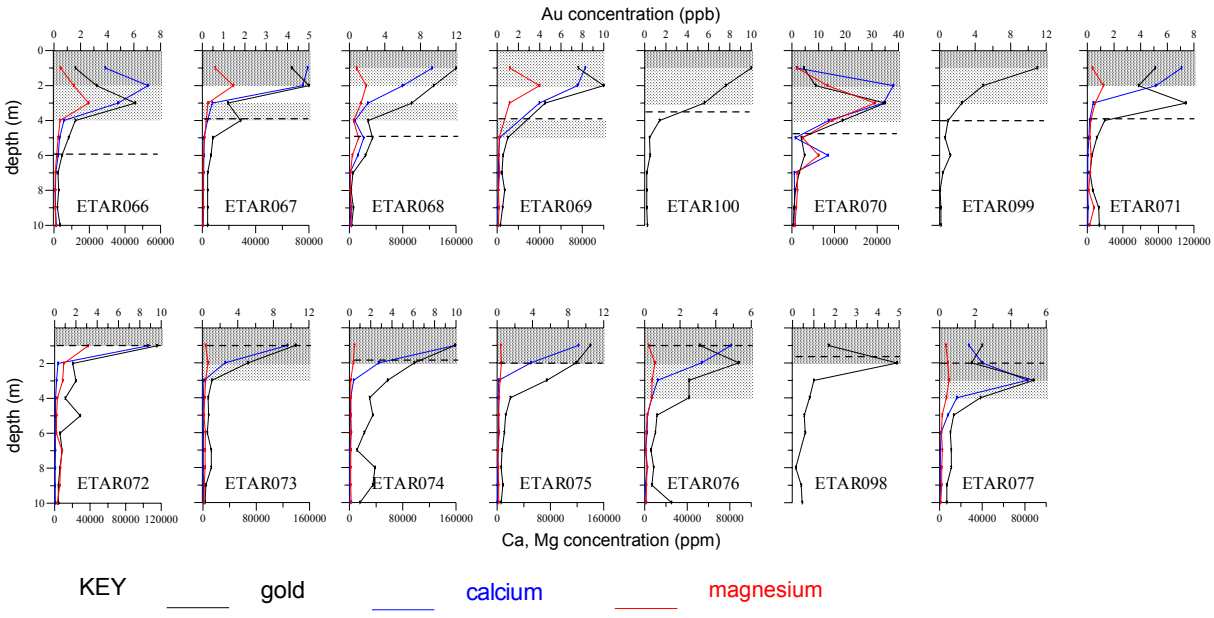

Figure 5-43 Gold, Ca and Mg distributions in 0-10 m drill hole samples on 339000E. Dashed line indicates approximate position of the unconformity. Shaded area indicates semi-quantitative estimate of carbonate concentration. Holes are displayed sequentially (left to right) with the southern most hole located left and northern most hole right.

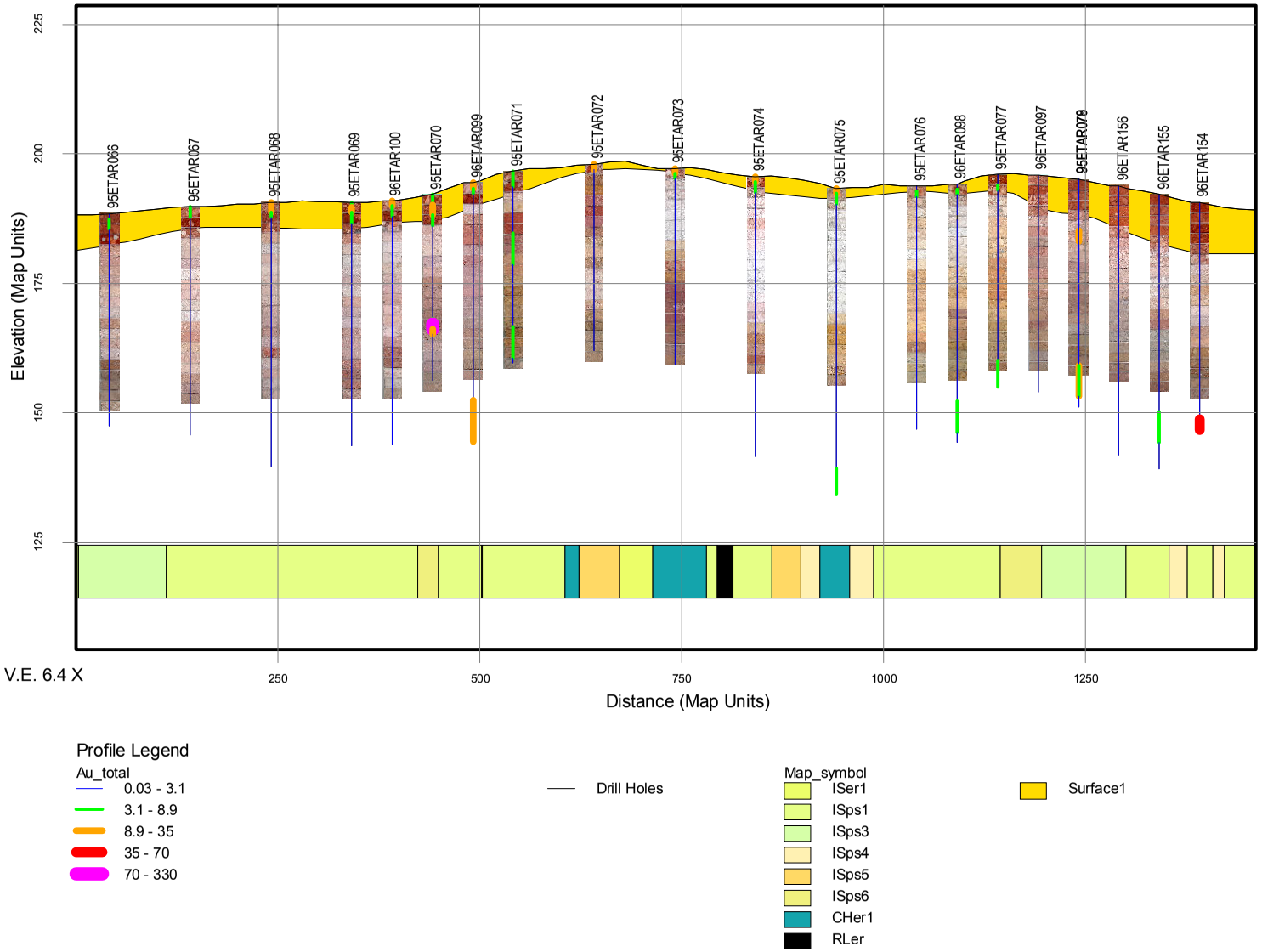

Figure 5-44 Drill section 339000E showing drill holes, Au concentration, regolith geology, chip tray photographs (0-38 m) and depth of overburden ("surface"). For detailed description of regolith-landform map symbols see text or map. All map units in metres.

5.4.5.11 Section 339200E

Section 339200E is east of centre of the prospect (Figure 5-45). Gold concentrations in the lower regolith are low in contrast to the surficial material. Transported overburden is generally thin but thickens northwards to 3 m (Figure 5-46). Gold in the upper transported regolith unit is anomalous in drill cuttings except those from ETAR162 where overburden is thinnest. Maximum Au (16 ppb) occurs in ETAR159. Gold and calcrete are strongly associated. The high Au contents in the upper regolith is part of a broad east-west anomaly occurring along the ridge (see Figure 5-8). The data suggests that this part of the anomaly is false or displaced since there is no mineralisation; the DEM suggests a gentle upslope gradient to the west, where the source of the anomaly may be located.

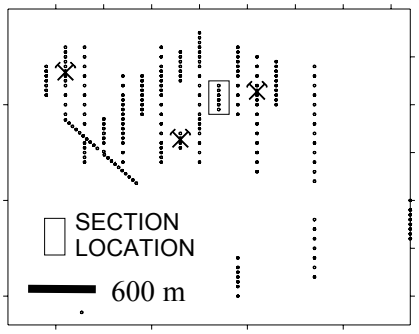

Figure 5-45 Plan showing location of drill holes, the three most mineralised holes and section 339200E.

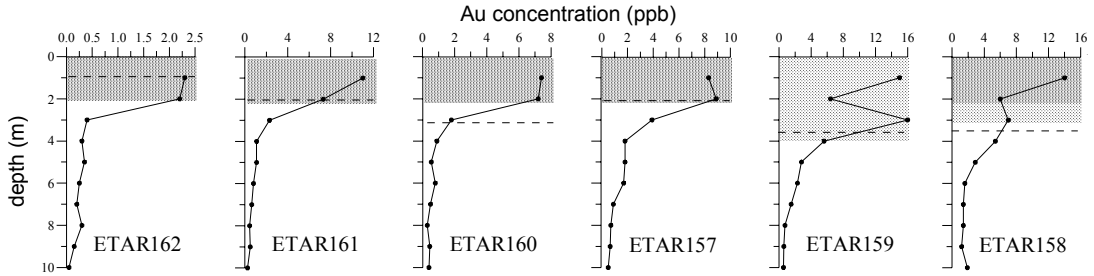

Figure 5-46 Gold distribution in 0-10 m drill hole samples on 339200E. Dashed line indicates approximate position of the unconformity. Shaded area indicates semi-quantitative estimate of carbonate concentration. Holes are displayed sequentially (left to right) with the southern most hole located left and northern most hole right.

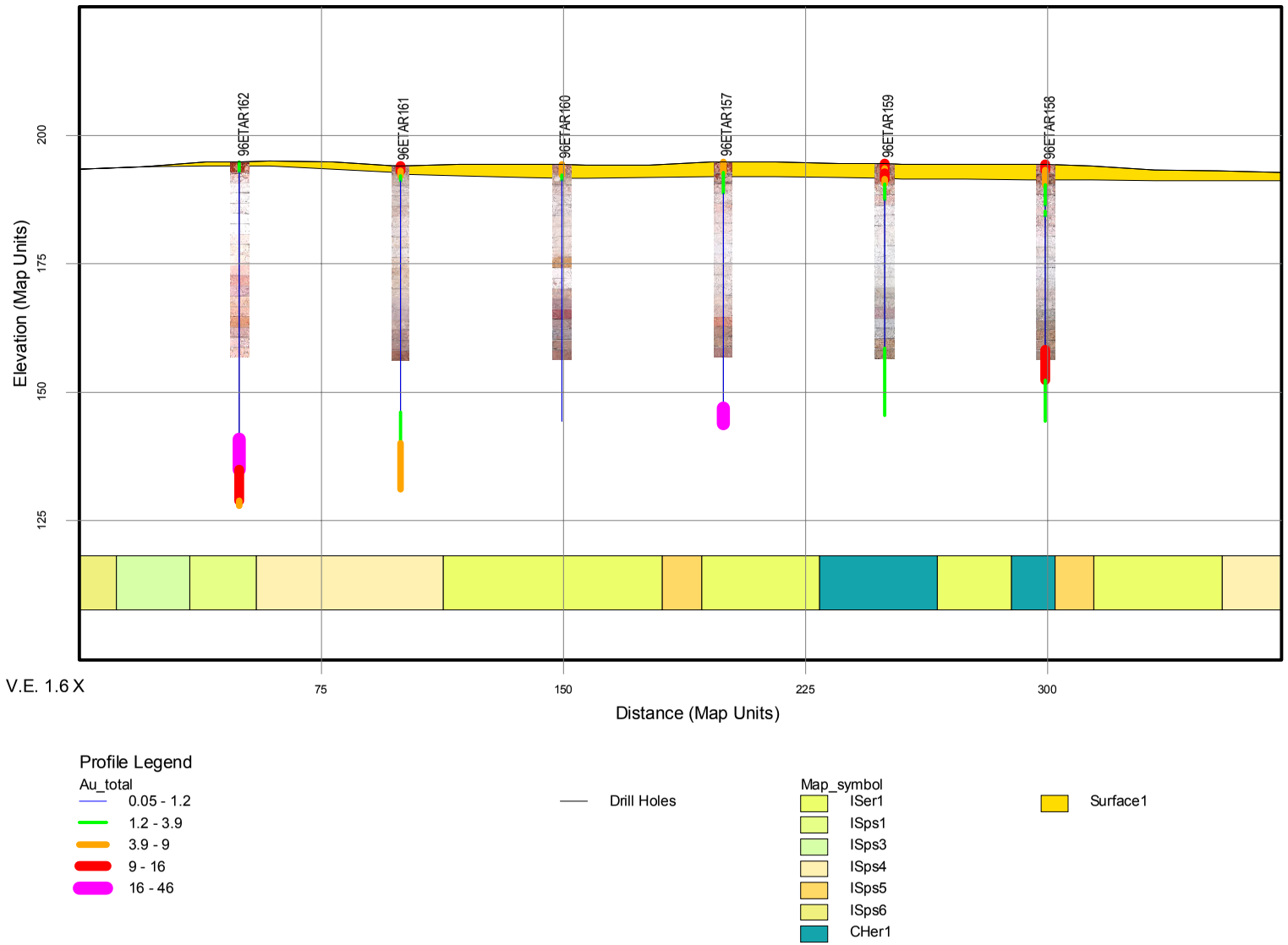

Figure 5-47 Drill section 339200E showing drill holes, Au concentration, regolith geology, chip tray photographs (0-38 m) and depth of overburden ("surface"). For detailed description of regolith-landform map symbols see text or map. All map units in metres.

5.4.5.12 Section 339400E

Section 339400E occurs east of centre and is divided into two sets, 1500 m apart (Figure 5-48). The southern set is a background area with little Au mineralisation. Overburden thickness varies from 2 m in the south (Figure 5-49) becoming gradually deeper (5 m) to the north (Figure 5-50). Gold concentrations reach 5 ppb (8-9 m, ETAR319), but are generally below 2 ppb, and associated with calcrete.

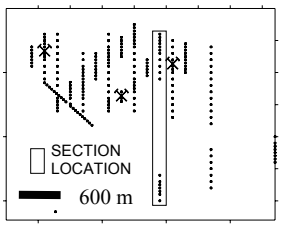

Figure 5-48 Plan showing location of drill holes, the three most mineralised holes and section 339400E. Drill fences are 200 m apart.

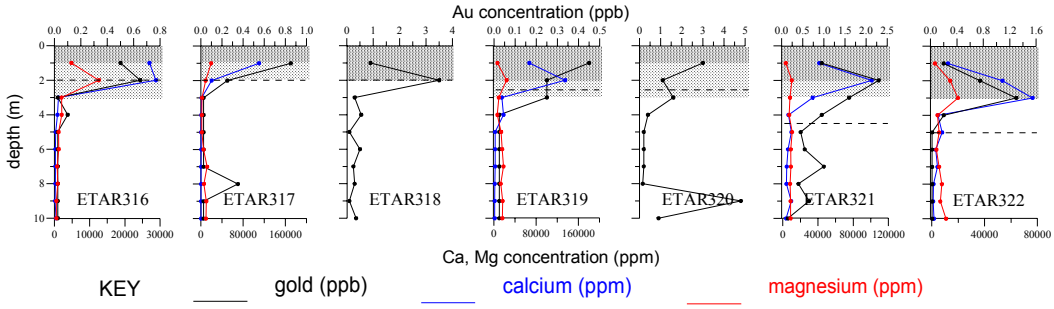

Figure 5-49 Gold, Ca and Mg distributions in 0-10 m drill hole samples on 339400E, southern part. Dashed line indicates approximate position of the unconformity. Shaded area indicates semi-quantitative estimate of calcrete concentration. Holes are displayed sequentially (left to right) with the southern most hole located left and northern most hole right.

Very weak mineralisation occurs in the northern set (Figure 5-51, maximum of 40 ppb). Most upper regolith samples have Au >4 ppb with a maximum of 13 ppb in ETAR025 (false anomaly). The 0-5 m samples of ETAR103 and some samples from adjacent ETAR028, which includes samples from the *in situ* regolith, are anomalous in Au (maximum of 10 ppb) and provide an area for further investigation. Gold and calcrete are strongly associated. High carbonate (and Au) concentrations persist deeper into the sandy transported regolith than the (commonly) silicified upper *in situ* regolith.

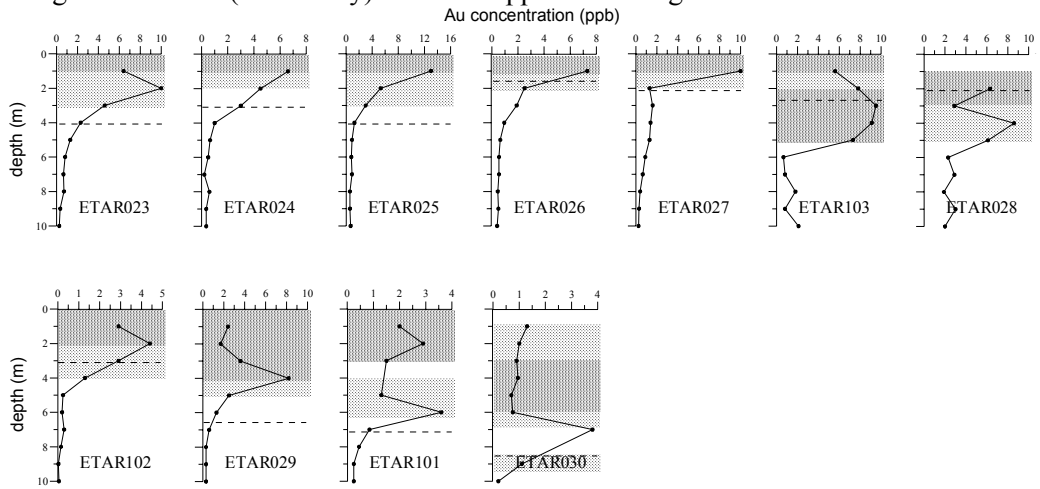

Figure 5-50 Gold distribution in drill hole samples on 339400E, northern part. Dashed line indicates approximate position of the unconformity. Shaded area indicates semi-quantitative estimate of carbonate concentration. Holes are displayed sequentially (left to right) with the southern most hole located left and northern most hole right.

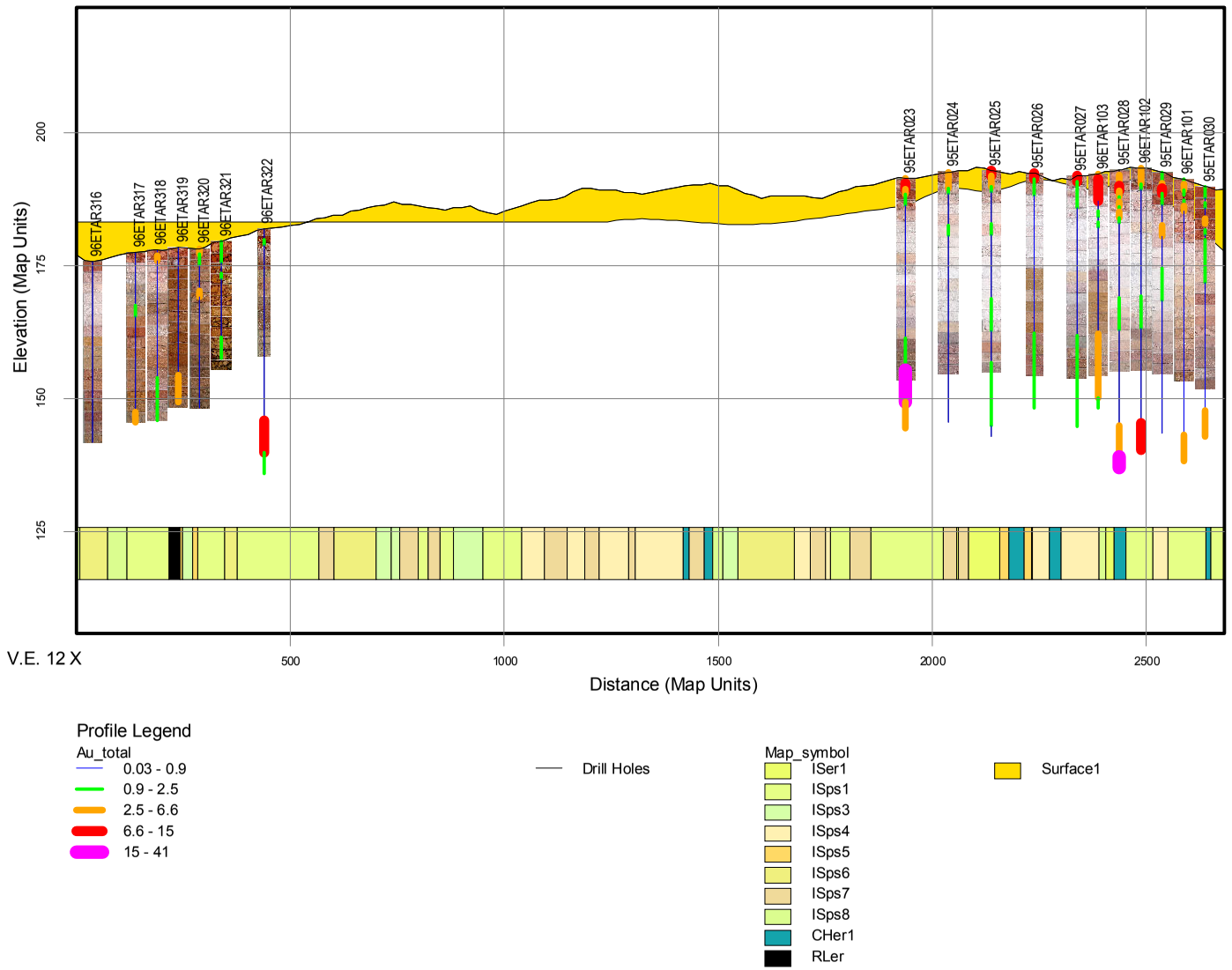

Figure 5-51 Drill section 339400E showing drill holes, Au concentration, regolith geology, chip tray photographs (0-38 m) and depth of overburden ("surface"). The indicated depth of overburden for holes ETAR316-ETAR322 is incorrect due to data limitations. For detailed description of regolith-landform map symbols see text or map. All map units in metres.

5.4.5.13 Section 339600E

Section 339600E is located in the eastern part of the prospect (Figure 5-52) and has one of the three most mineralised locations (ETAR167, 0.68 ppm at 43-44 m); other drill cuttings show small concentrations of Au in the same area. The thickness of transported overburden is moderate (maximum of 6 m) but variable, indicating the presence of small dunes (Figure 5-53). Gold concentrations are variable with a highly anomalous maximum of 20 ppb in transported overburden from ETAR170, the second highest Au concentration in the upper regolith drill cuttings; mineralisation (Figure 5-54, maximum of 140 ppb at 50-51 m) occurs in the lower saprolite indicating that the surficial Au is reflecting the mineralisation beneath i.e. a true anomaly. In contrast, however, concentrations reach only 4 ppb above the more strongly mineralised ETAR167.

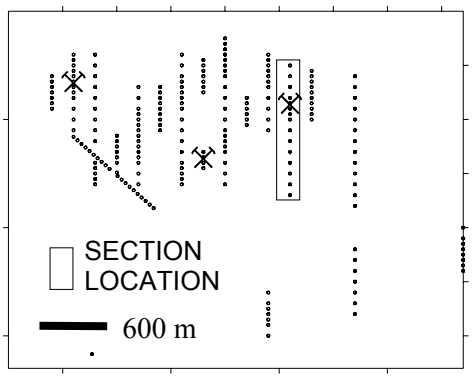

Figure 5-52 Plan showing location of drill holes, the three most mineralised holes and section 339600E.

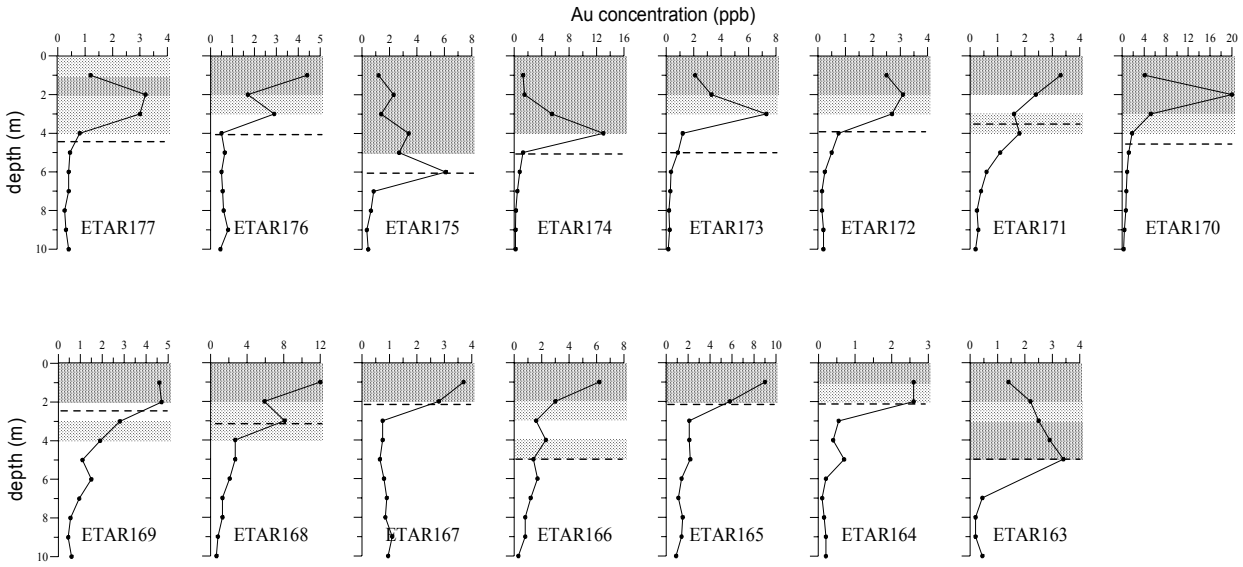

Figure 5-53 Gold distribution in 0-10 m drill hole samples on 339600E. Dashed line indicates approximate position of the unconformity. Shaded area indicates semi-quantitative estimate of carbonate concentration. Holes are displayed sequentially (left to right) with the southern most hole located left and northern most hole right.

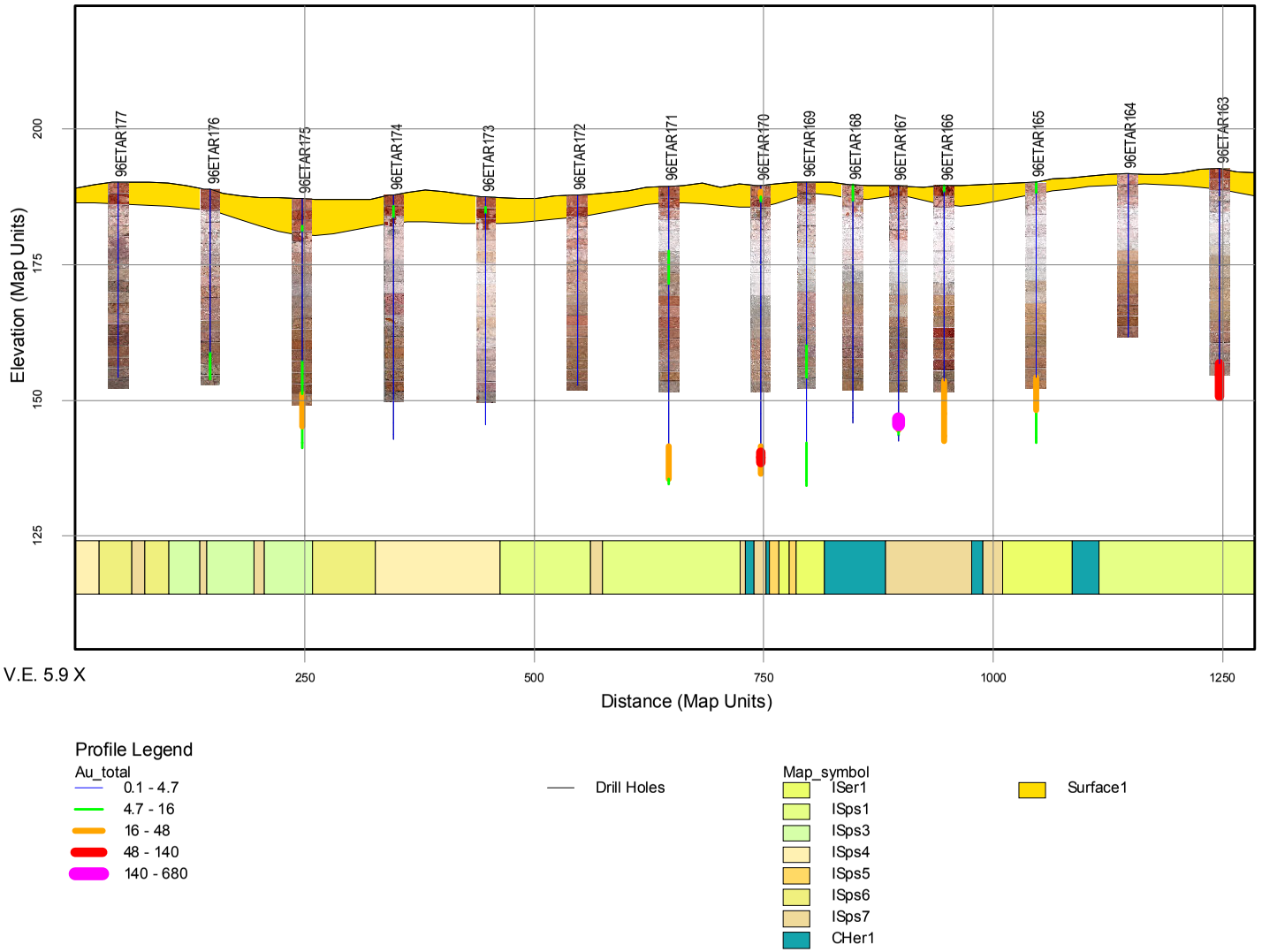

Figure 5-54 Drill section 339600E showing drill holes, Au concentration, regolith geology, chip tray photographs (0-38 m) and depth of overburden ("surface"). For detailed description of regolith-landform map symbols see text or map. All map units in metres.

5.4.5.14 Section 339800E

Section 339800E is located in the eastern part of the prospect (Figure 5-55). Transported overburden thickness varies from 3 to 6 m (Figure 5-56). Gold concentrations in the lower regolith are generally below 30 ppb (Figure 5-57). Gold concentrations are anomalous in the transported overburden (maximum of 17 ppb in ETAR110), exceeding 10 ppb in samples from ETAR104, 110 and 111 (false or displaced anomalies).

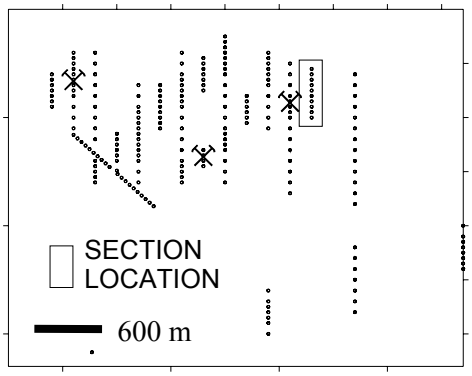

Figure 5-55 Plan showing location of drill holes, the three most mineralised holes and section 339800E.

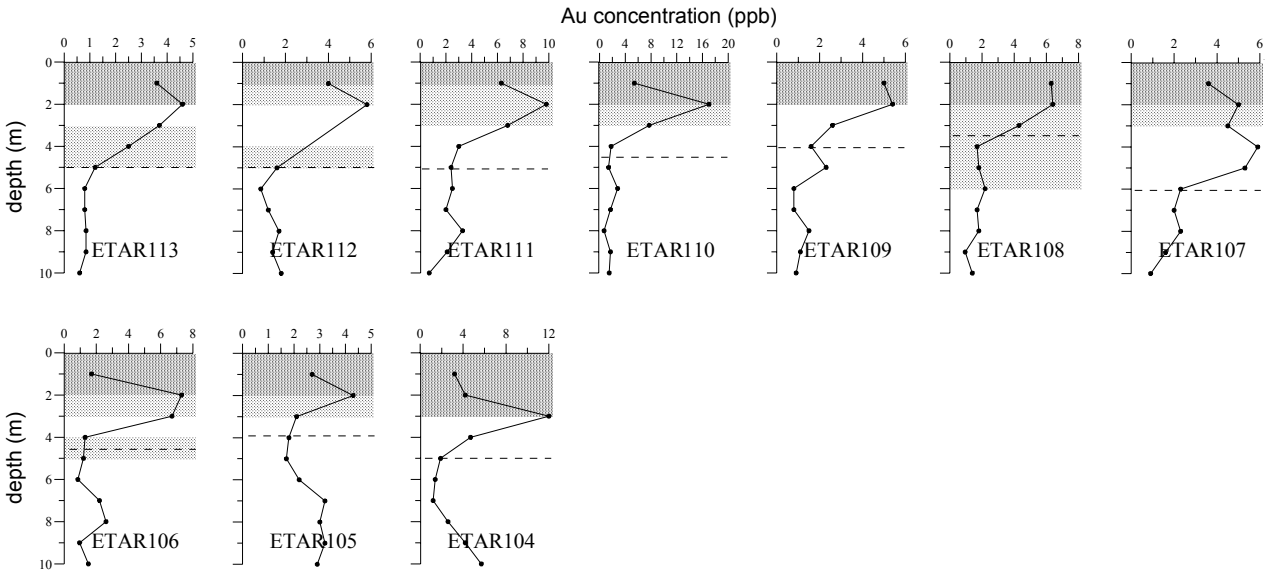

Figure 5-56 Gold distribution in 0-10 m drill hole samples on 339800E. Dashed line indicates approximate position of the unconformity. Shaded area indicates semi-quantitative estimate of carbonate concentration. Holes are displayed sequentially (left to right) with the southern most hole located left and northern most hole right.

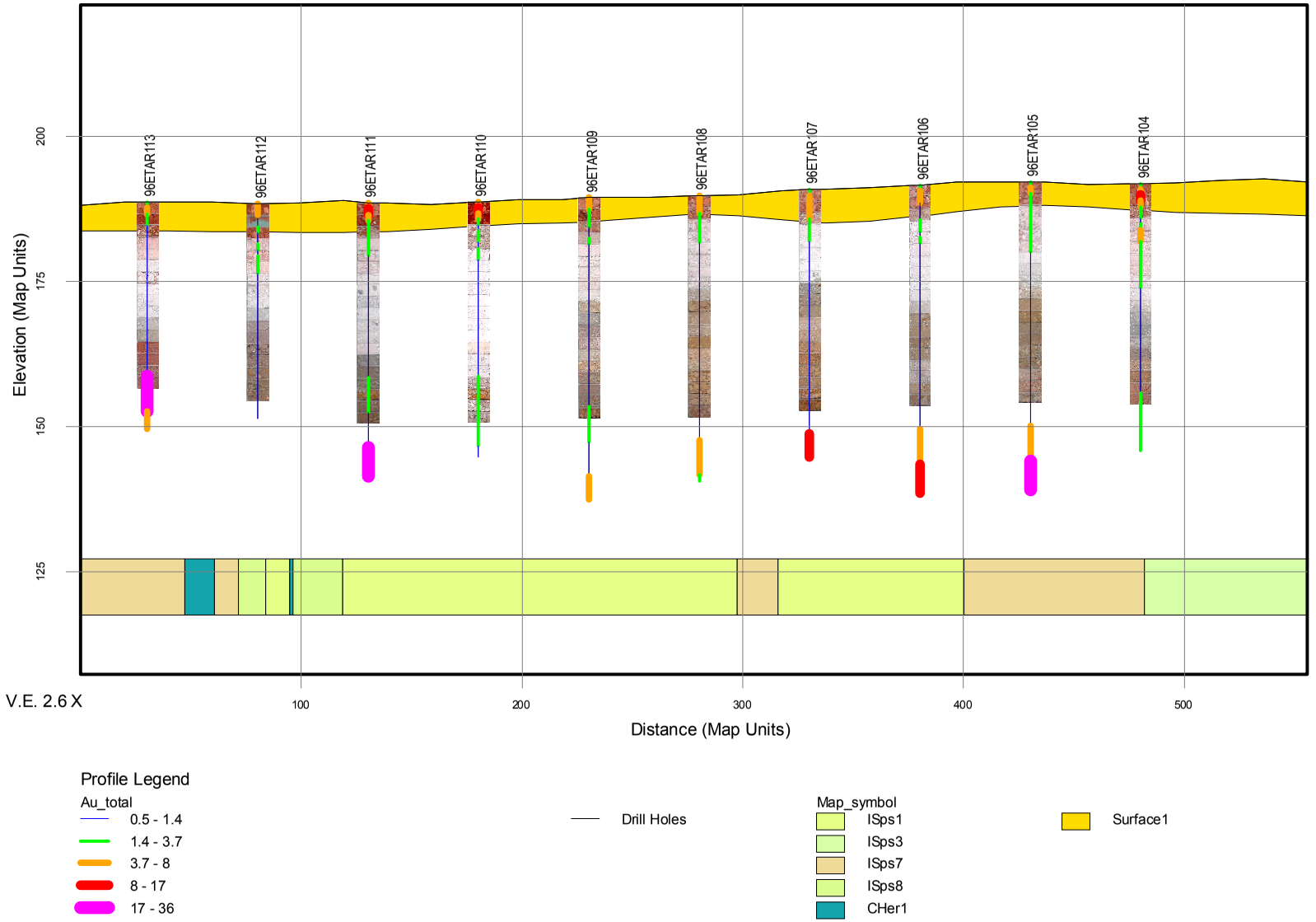

Figure 5-57 Drill section 339800E showing drill holes, Au concentration, regolith geology, chip tray photographs (0-38 m) and depth of overburden ("surface"). For detailed description of regolith-landform map symbols see text or map. All map units in metres.

5.4.5.15 Section 340200E

Section 340200E is located in the eastern part of ET and where transported overburden is thickest (Figure 5-58, Figure 5-59). For drill cuttings, Mg:Ca ratios and selected XRD indicate that the calcrete is partly dolomitic and increasingly so with depth. The transported overburden is 11 m thick towards the centre of the section and has filled in an E trending palaeovalley that gets deepens towards the east (Figure 4-11).

A Au concentration of 755 ppb was recorded for a non-calcareous sample from the unconformity (Figure 5-60, ETAR189). This sample is not over mineralisation and although it is over upper saprolite with 33 ppb Au, the Au is considered to be detrital, originating from the palaeo-upslope (false anomaly); this hypothesis is supported by analysis of a new sub-sample which contained <1 ppb Au. Elevated Au contents in the transported overburden (maximum 21 ppb) on 340200E may also be partly or wholly detrital in origin because hydromorphically re-located Au from underlying saprolite would be expected to give a less erratic Au distribution. In addition, Au concentrations only reach a maximum of 4 ppb in mineralised ETAR185 (false background) whereas they reach an anomalous 20 ppb in the adjacent ETAR186, which is not mineralised (false anomaly). In ETAR188, lower regolith Au concentrations peak at 100 ppb between 36-42 m and at 15 ppb in the upper regolith indicating a true anomaly. Thus, Au concentrations in the transported overburden, do not relate mineralisation directly below.

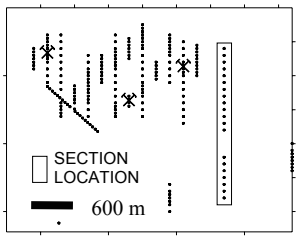

Figure 5-58 Plan showing location of drill holes, the three most mineralised holes and section 340200E.

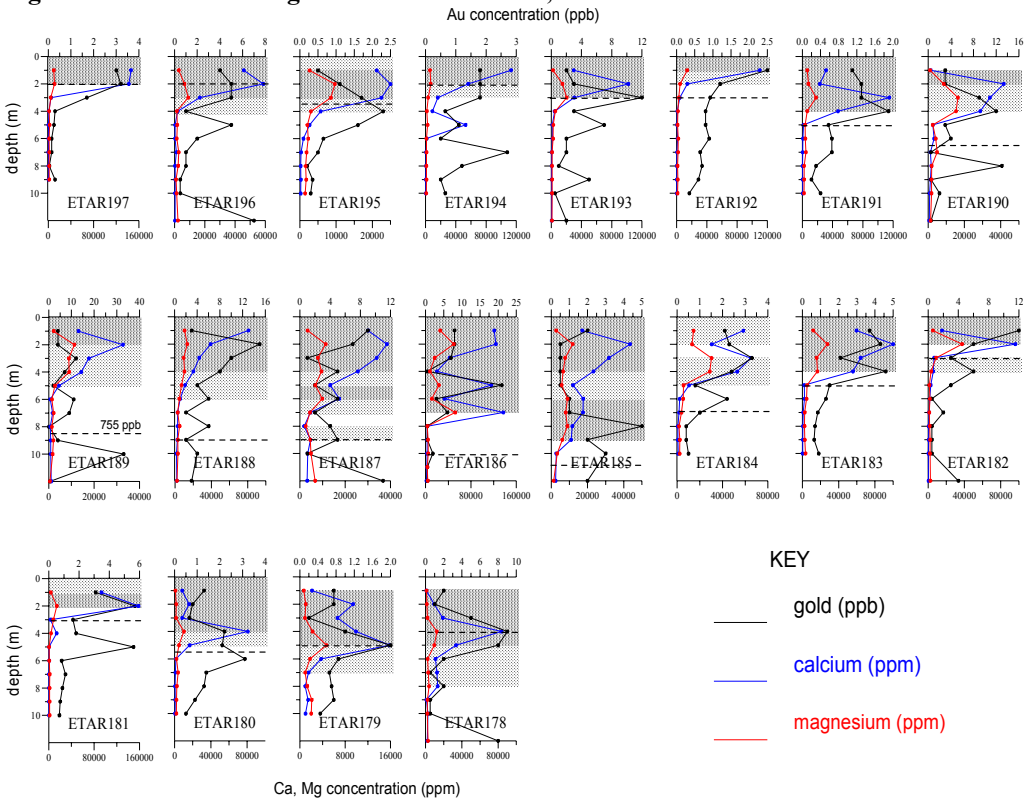

Figure 5-59 Gold, Ca and Mg distributions in 0-12 m drill hole samples on 340200E. Dashed line indicates approximate position of the unconformity. Shaded area indicates semi-quantitative estimate of carbonate concentration. Holes are displayed sequentially (left to right) with the southern most hole located left and northern most hole right.

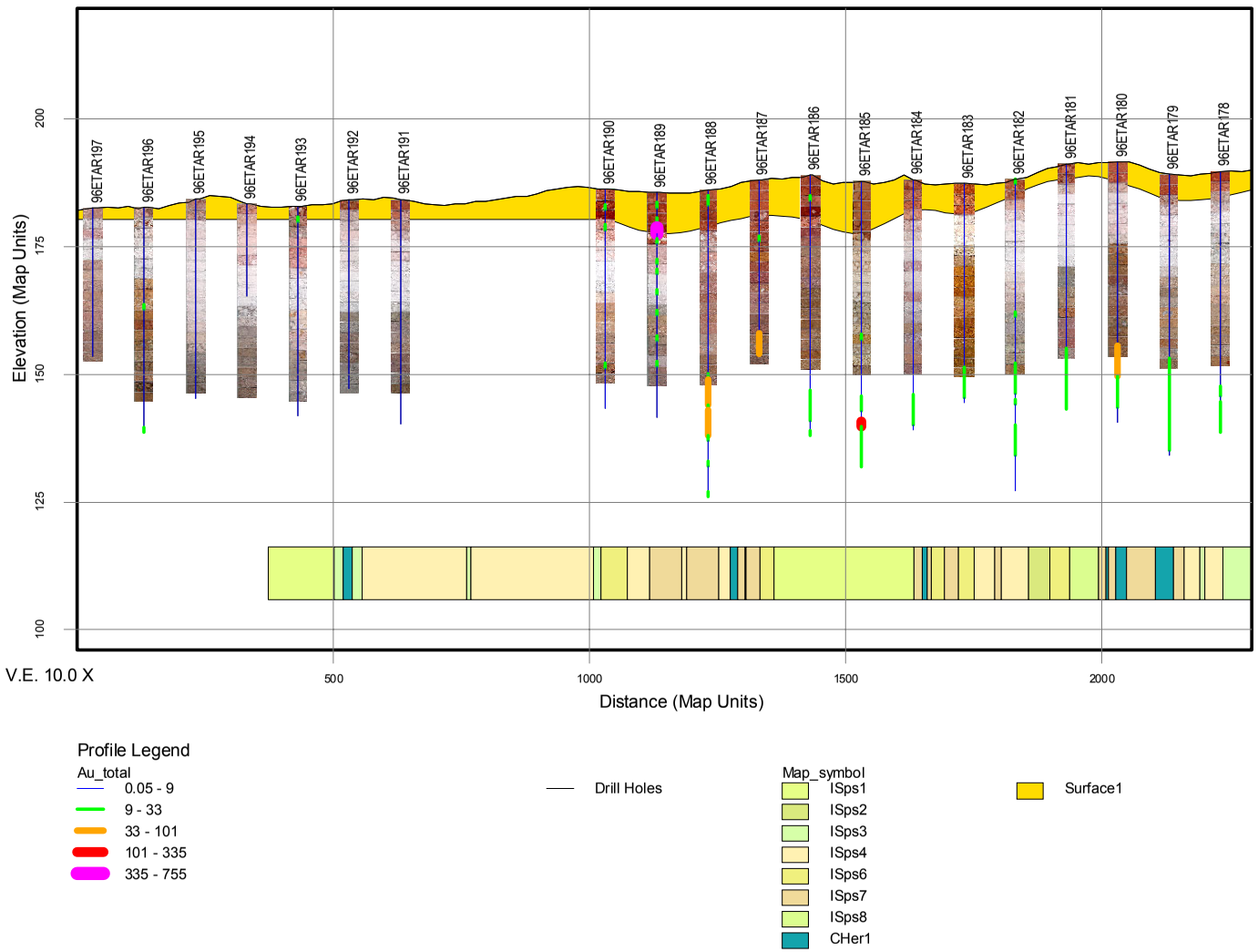

Figure 5-60 Drill section 340200E showing drill holes, Au concentration, regolith geology, chip tray photographs (0-38 m) and depth of overburden ("surface"). The indicated depth of overburden for holes ETAR191-ETAR197 is incorrect due to data limitations. For detailed description of regolith-landform map symbols see text or map. All map units in metres.

5.4.5.16 Section 341200E

Section 341200E is an isolated line of drill holes at the eastern-most section of the prospect. Mineralisation is absent but drilling is sparse (Figure 5-61). Lower regolith Au concentrations are near or below the limit of detection (<1 ppb). Transported overburden thickness increases towards the north reaching a maximum depth of 6 m (Figure 5-62). Gold concentrations are generally low (2-4 ppb) and commonly greatest in the carbonate horizon.

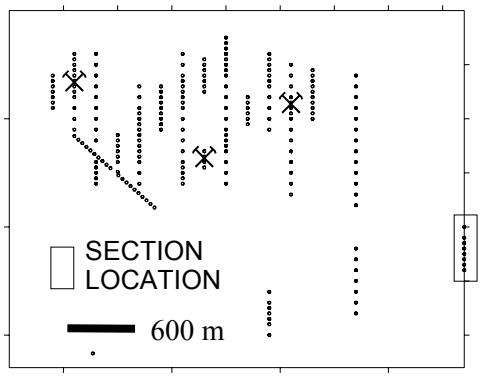

Figure 5-61 Plan showing location of drill holes, the three most mineralised holes and section 341200E.

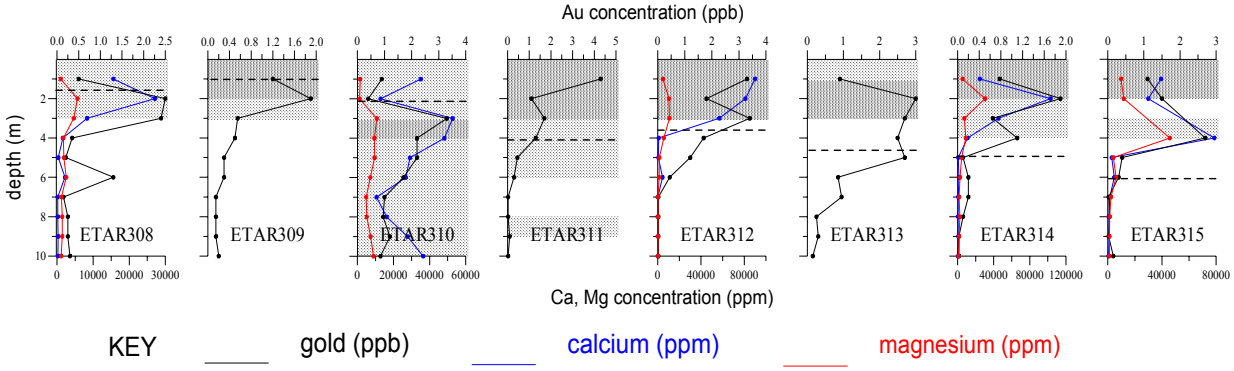

Figure 5-62 Gold, Ca and Mg distributions in 0-10 m drill hole samples on 341200E. Dashed line indicates approximate position of the unconformity. Shaded area indicates semi-quantitative estimate of carbonate concentration. Holes are displayed sequentially (left to right) with the southern most hole located left and northern most hole right.

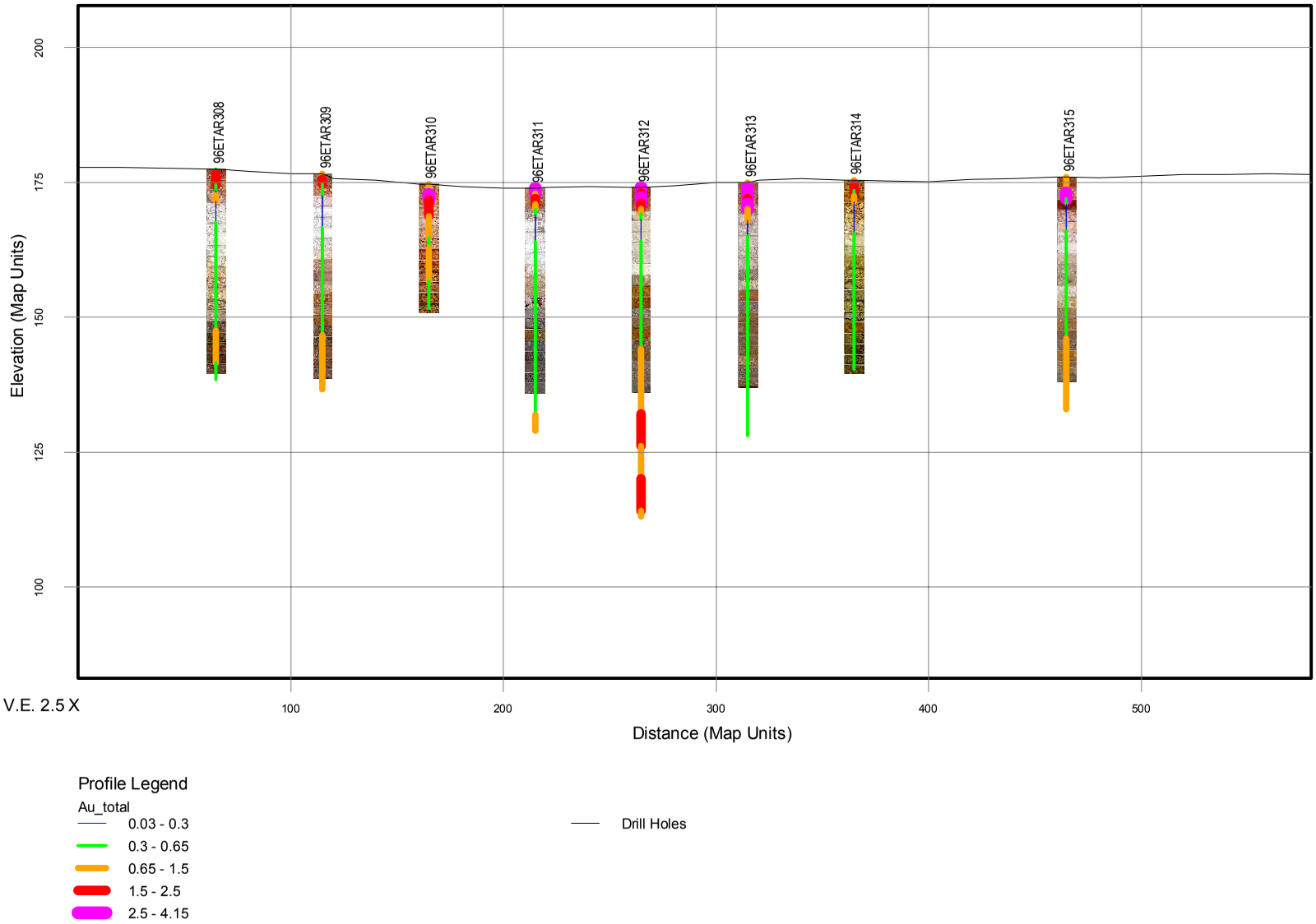

Figure 5-63 Drill section 341200E showing drill holes, Au concentration and chip tray photographs (0-38 m) and surface. For detailed description of regolith-landform map symbols see text or map. All map units in metres.

5.4.6 Soil and soil profiles

The distribution of Au in soils (10-20 cm depth) is shown in Figure 5-64. The maximum (8.9 ppb Au) was recorded in the only calcareous sample with other samples being comprised of sand to clayey sand. This sample was located in thin soils to the west of centre of the study area and correspond with the central ridge (Figure 5-64). A nearby sample with 5.4 ppb Au was located within the major calcrete anomaly. There is a weakly anomalous area (4 samples) in the SW corner but not in corresponding calcrete; its significance is unknown since there is no drilling in that region.

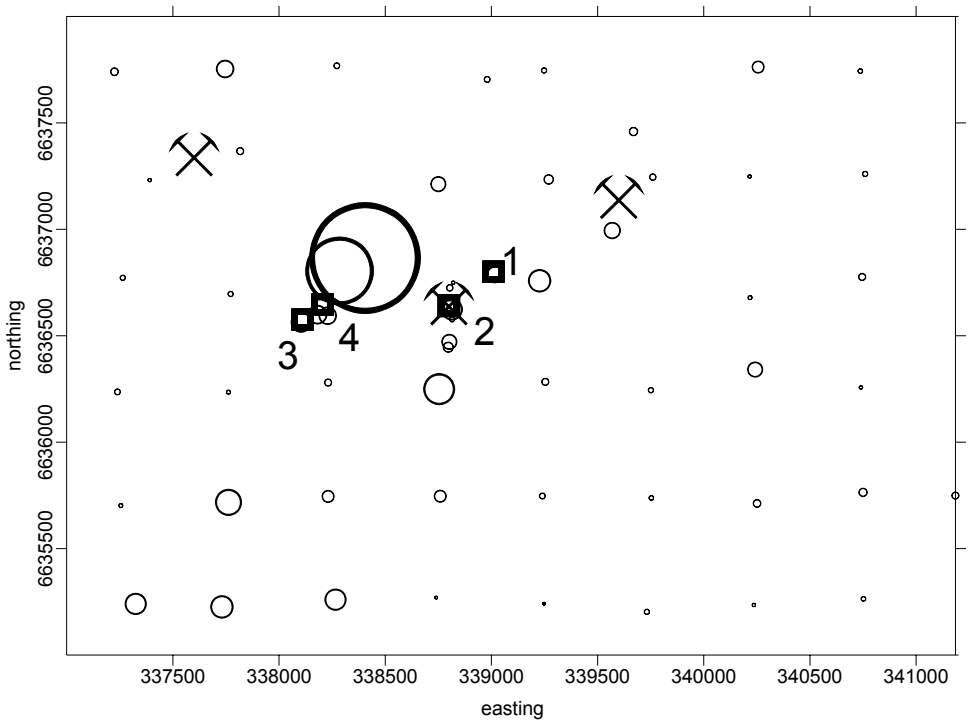

Figure 5-64 Distribution of Au in soil (10-20 cm) at ET. Concentrations range from 0.1 to 8.9 ppb. Boxes indicate positions of soil profiles.

The soil profile data indicates that Au concentrations markedly increase with the appearance of calcrete (Figure 5-65); Co, REE, Ho, Na, Nd, Ni, P, S, Sr, Tl and, possibly, Cd and Se, also increase (Appendix 8). Concentrations reach 75 ppb and 22 ppb Au at the base of profiles 3 and 4 respectively, located within the major calcrete in ~2 m of transported material on top of the ridge. Concentrations reach 50 ppb at the base of profile 1 located above minor mineralisation near ETAR070 and where transported material is ~5 m thick. Profile 2, with a maximum of 8 ppb Au at its base, has the lowest Au concentration for any profile despite its location over one of the three RAB holes with the highest maximum Au concentration and where transported material is ~5 m thick (as for profile 1). Calcrete here is nodular rather than massive as in the other soil profiles.

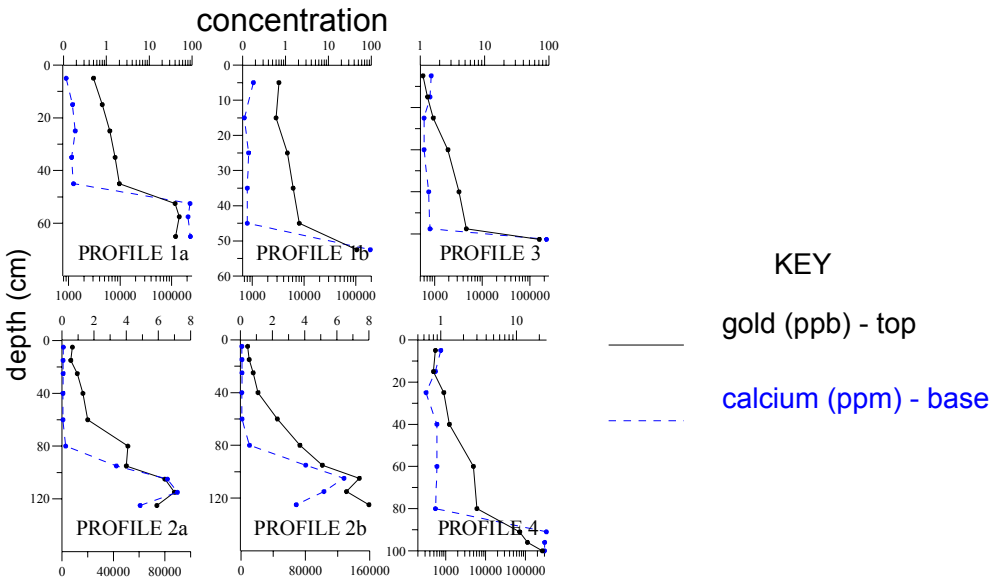

Figure 5-65 Gold and Ca (calcrete) concentrations in soil profiles at ET. Note that certain axis scales are logarithmic to highlight the gradational increase in Au concentration from the surface to the calcrete horizon where concentrations usually sharply increase. Top axis is Au; base axis is Ca.

Gold concentrations near the surface (0-0.1 m or 0.1-0.2 m samples) of the soil profiles are low (mostly <1 ppb) and do not reflect Au concentrations at the top of the underlying calcrete nor any underlying mineralisation. This suggests that bulk surface soil is a poor substitute for buried calcrete. This may be a reflection on the age of the materials concerned.

The origins of Au in the calcrete at ET require more detailed study. Clearly from an exploration point of view, it is important to establish whether:

(i) the Au is sourced from upslope and has been mobilised under gravity from an *in situ* source such as downwards and lateral percolating meteoric waters or fluvial-lateral movement of sediment; or

(ii) the Au is sourced from mineralisation beneath and has moved to the surface by a mechanism such as bioturbation or capillarity.

Proof of the former would allow greater spacing of calcrete sampling and alert explorers to the possibility of displaced anomalies. Proof of the latter would provide a means of seeing through transported overburden in certain circumstances.\

5.4.7 Vegetation

Vegetation (mostly *Acacia* phyllodes and small branches) was collected at the same sites as the soils. High Au concentrations (>0.4 ppb equivalent dry weight) occur in the western part of the study area and correspond with an erosional area identified from mapping (Section 3.3.2) and particularly the NW (1.4 ppb, Figure 5-66). Some weak mineralisation has been detected in this part of the prospect. Other anomalous concentrations were recorded above one of the three Au-rich RAB holes (0.6 ppb, close to soil profile 3) and above weak mineralisation on 340200E (0.7 ppb). These concentrations, however, are lower than anomalous concentrations found in different vegetation types associated with Au mineralisation in WA (~2 ppb, summarised in Butt *et al*., 1997,). There appears to be no consistent association at ET between Au in vegetation and Au in calcrete, soil, upper regolith or mineralisation.

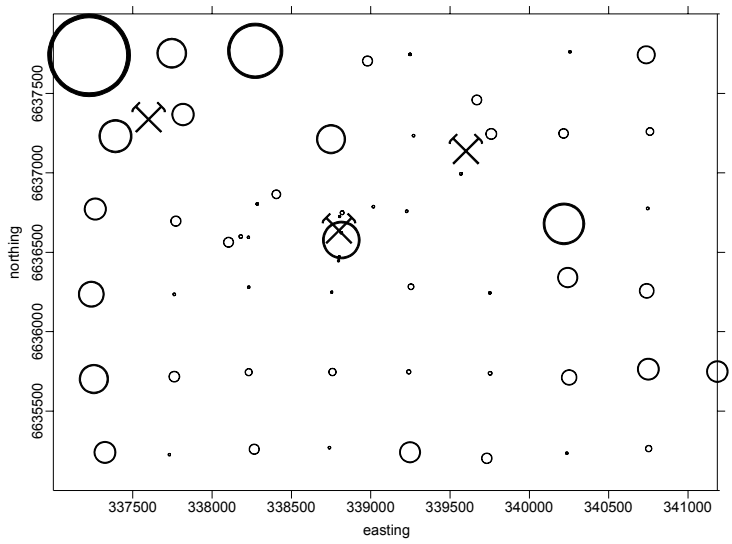

Figure 5-66 Gold in vegetation (mostly *Acacia* phyllodes and small branches) at ET. Concentration ranges from <0.02 to 1.43 ppb Au in dry weight or <0.5 to 26 ppb ash weight.

5.5 Silver geochemistry

Silver was analysed by two methods: i) a multi-acid digest (see Section 5.3.1) which provided a "total" Ag analysis (referred to herein as Ag_{tot}) and ii) a cyanide "partial" leach which determined the labile portion of Ag (Ag_{cn}). The detection limit for Ag_{cn} (0.5 ppb) is 200 times lower than the Ag_{tot} (100 ppb) method. Most samples were analysed by the two methods although only half the drill cuttings were analysed from 340200E for Ag_{cn}. Summary data are recorded in Table 5-6. Most Ag_{tot} concentrations are close to the detection limit and therefore considered less reliable that the Ag_{cn} concentrations (Figure 5-67); consequently, correlations between Ag_{tot} and Ag_{cn} and between Ag_{tot} and other elements are poor (Figure 5-68).

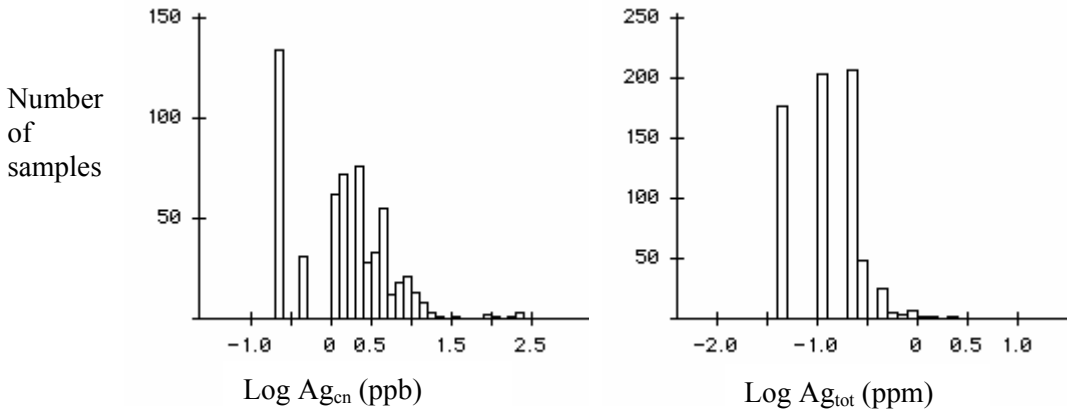

Figure 5-67 Histogram data (ppm, logarithmic) for Ag by the cyanide digest (left) and mixed acid digest (right). Data are normally distributed but skewed (particularly Ag_{tot}) after the transformation.

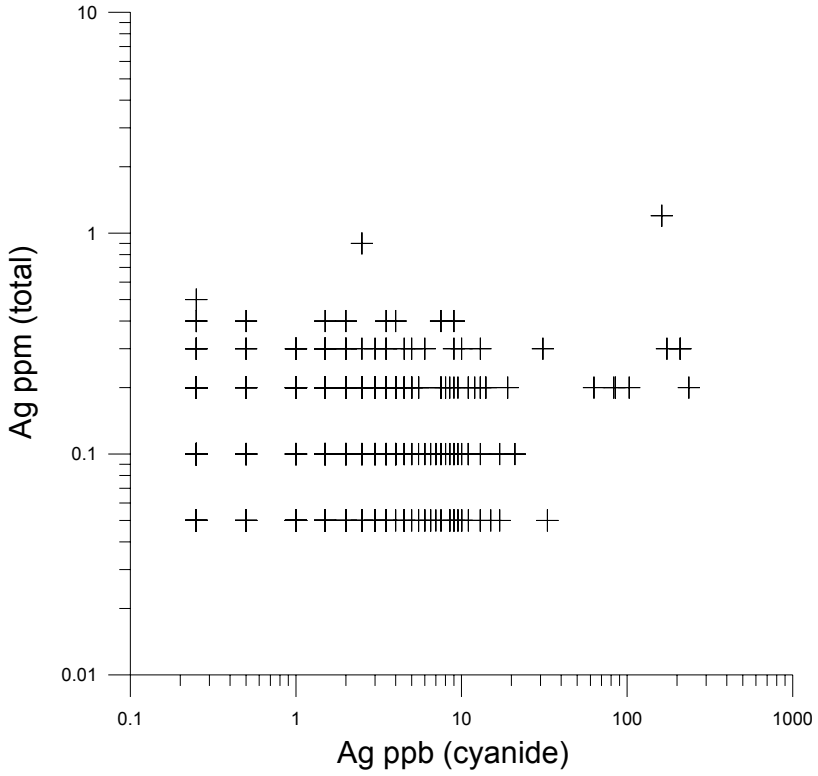

Figure 5-68: Scatter plot of cyanide digest Ag vs triple added digest (total) Ag.

Table 5-6 Summary statistics for Ag data.

Sample medium	Detection limit (ppm)	Range (ppm)	Mean (ppm)	Standard deviation (ppm)	number
0-~10 m drill cuttings (cyanide)	0.0005	0.0005-0.236	0.005	0.018	575
0-~10 m drill cuttings (total)	0.1	0.1-5.5	0.18	0.29	686
Calcrete (total)	0.001	0.001-0.0139	0.005	0.0028	0.103
Soil (cyanide)	0.0005	0.002-0.020	0.007	0.004	57
Soil (total)	0.1	0.1-0.3	0.06	0.04	57
Soil profile (cyanide)	0.0005	0.0005-0.065	0.011	0.018	55
Soil profile (total)	0.1	0.1-0.4	0.06	0.05	55
Vegetation (total, dry)	~0.003	<0.003-0.031	0.013	0.007	58

The distribution of Ag_{tot} in the upper regolith appears to be unrelated to mineralisation (Figure 5-69). For example, the highest concentrations of Ag_{tot} are in the centre (5.5 ppm) and the northern part (2.4 ppm) of drill section 340200E, in drill cuttings, where there is no mineralisation; corresponding Ag_{cn} analyses were not performed on these particular samples. In contrast, Ag_{tot} concentrations were close to detection limits over mineralisation on 338800E. Away from mineralisation, (sections 339400E and 341200E) concentrations appear to be no different from mineralised areas. A maximum of 236 ppb Ag_{cn} appears in transported clayey sand and underlying saprolite at the base of the slope in section 338000E (Figure 5-20). The significance of this is not known but only minor Au was recorded in the drill cuttings. Other high Ag_{cn} concentrations appear in 338800E (maximum of 21 ppb) and are associated with mineralisation and/or indicate Ag has been mobilised downslope.

Visualisation of the Ag_{cn} distribution in the regolith was undertaken using 2D (SURFER) and 3D (MVS) software (Figure 5-70 and Figure 5-71, respectively). Visualisation was restricted to the top 10 m due to

data limitations. For 2D visualisation, the data were untransformed prior to kriging and contour intervals classes have been fixed at a constant level *for all depths*; maximum contour interval has been set at a constant 9 ppb (for all plots) to remove distortions caused by extreme Ag_{cn} values. Several features are apparent from the images:

1. Ag_{cn} concentrations are higher in the 0-1 m samples.
2. There are a number of coincident anomalies with Au at 0-1 m (c.f Figure 5-8).
3. Strong anomalies persist to 3 m with Au, but with Ag_{cn} they are only apparent in the top 0-1 m, with one exception (see 4 below).
4. On the southern part of the Diagonal section, a Ag_{cn} anomaly persists to various depths in the transported material.
5. A Ag_{cn} anomaly occurs in *in situ* regolith centred on 338800E 6636600N.
6. A strong Ag_{tot} anomaly in the *in situ* and lower transported regolith occurs on 340200E with a possible surface expression.

The data suggest that Ag_{cn} is not as effective as Au at locating mineralisation but 0-1 m data may be useful when used in conjunction with Au to provide areas worthy of follow-up investigations.

Soil Ag_{tot} concentrations are generally too close to detection limit to be considered further; distribution is erratic and not spatially related to the three drill holes with the highest maximum Au concentration. Soil Ag_{cn} forms a coherent anomalous zone towards the SW, but drill holes are absent in this area to test its economic significance. Ag_{cn} also sharply increases towards the base of some of the soil profiles; this occurs for many elements as noted earlier (Section 5.4.6) and corresponds with the appearance of calcrete.

Silver in vegetation is more erratic in its distribution with only one mineralised hole showing elevated Ag.

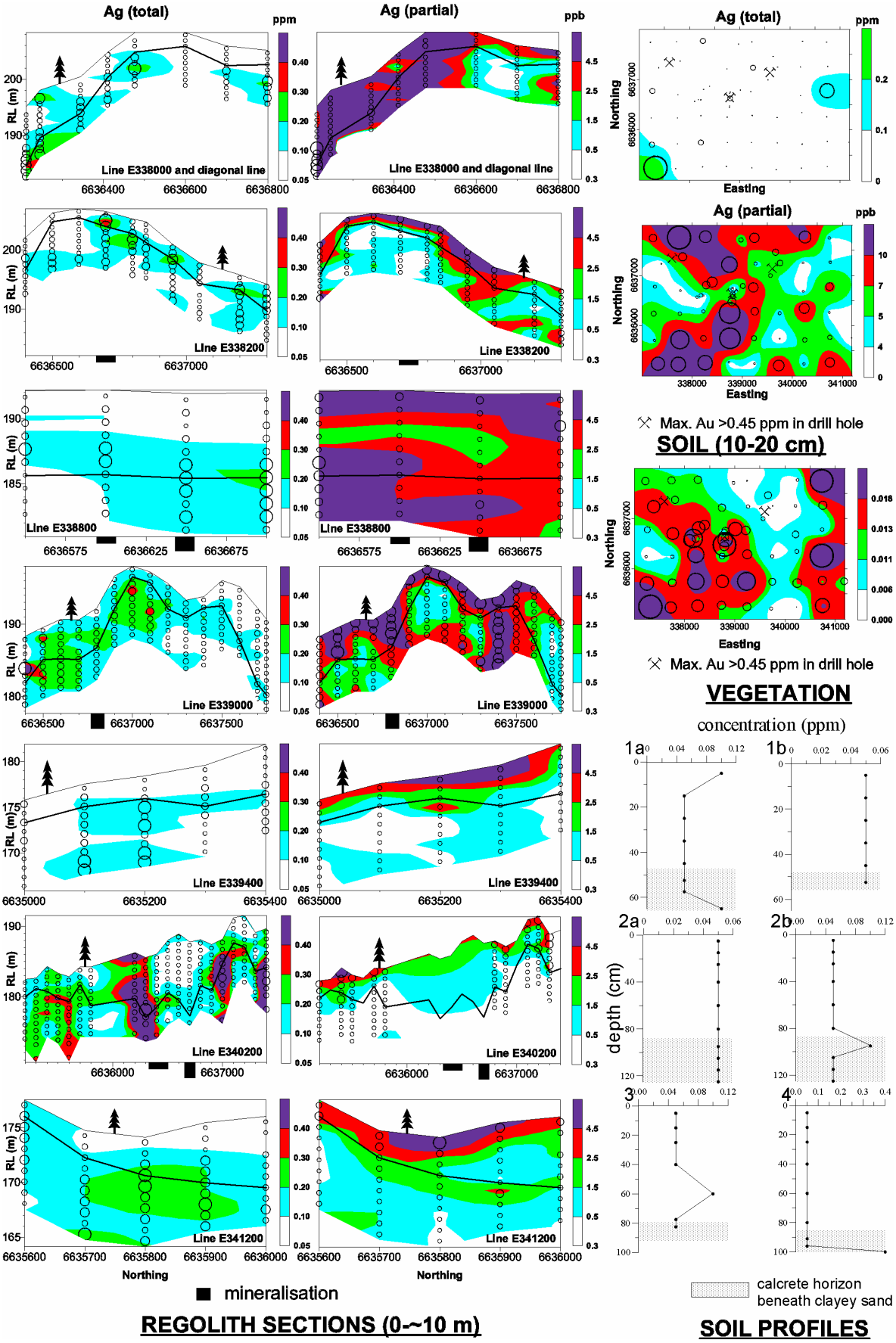

Figure 5-69 Distribution of Ag in the regolith at ET. Circles indicate sample location. Minimum and maximum Ag_{tot} (ppm) and Ag_{cn} (ppb) drill cutting concentrations are 0.05, 5.5, 0.025 and 236, respectively.

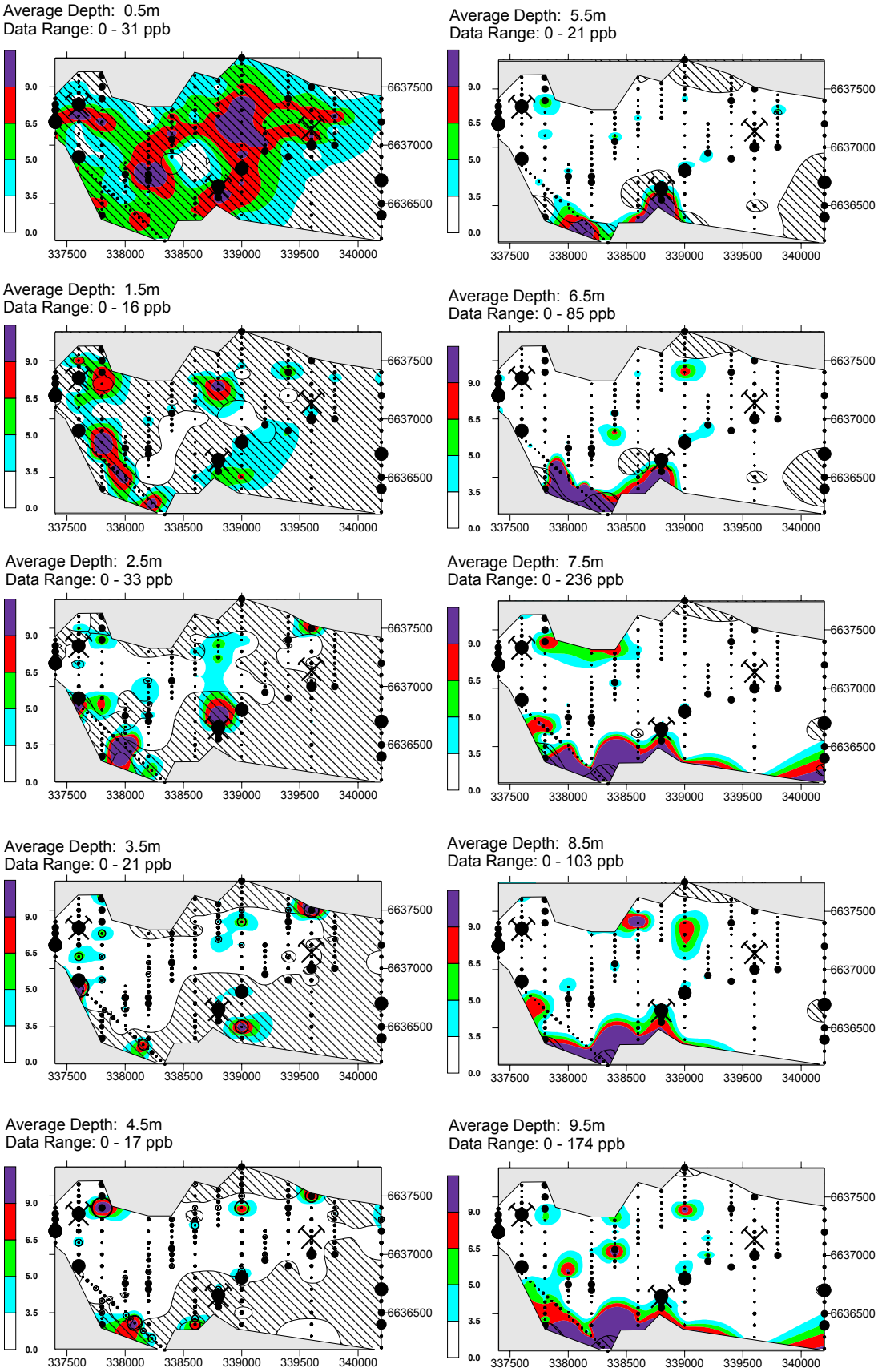

Figure 5-70 Ag_{cn} concentrations at 1 m intervals to 10 m. Mineralisation (black dots and hammer-pick symbols) as maximum Au concentration per hole, and transported overburden (hatching) are shown. See text for details of data treatment.

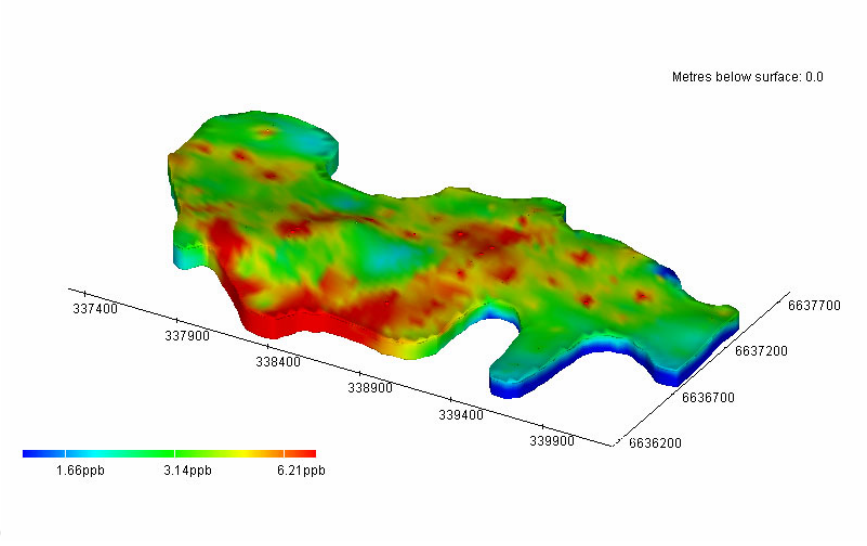

a)

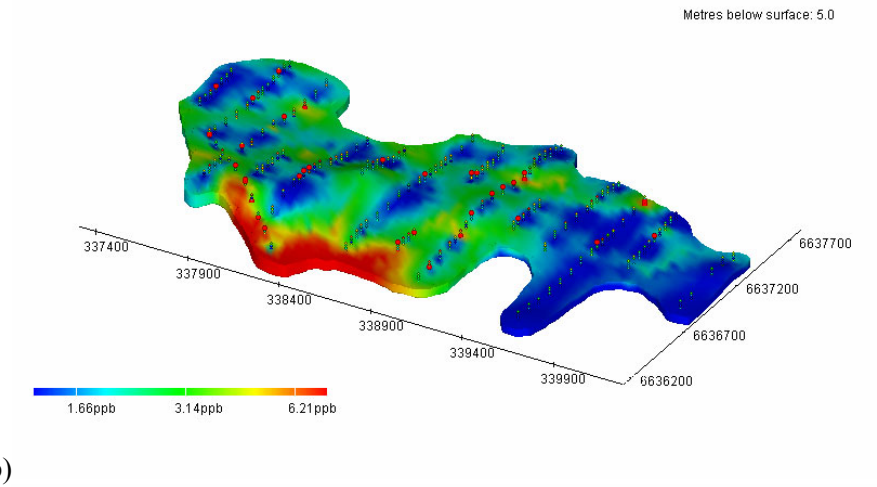

b)

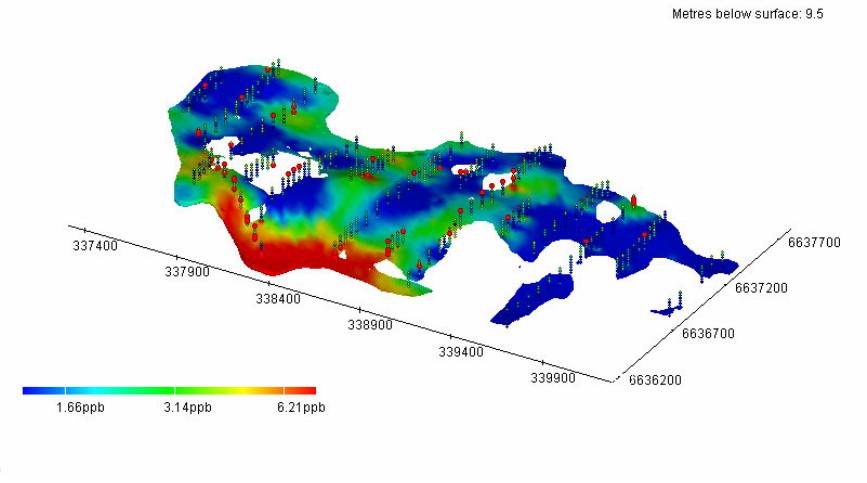

c)

Figure 5-71 A series of diagrams showing the change in Ag_{cn} distribution at intervals from the surface to 9.5 m depth, overlaid on the DEM. Drill hole samples are coloured according to Ag_{cn} content.

5.6 Copper geochemistry

Copper was analysed by two methods, mixed acid (see Section 5.3.1) and cyanide digests (designated Cu_{tot} and Cu_{cn}, respectively). The detection limit for Cu_{cn} is 10 times lower than Cu_{tot} but, unlike Ag, most data were well above detection for both methods. There is little published information available on the use of Cu_{cn} in exploration but Cu_{cn} would intuitively indicate more soluble or mobile forms of Cu in the regolith. Histograms of Cu data appear to indicate that the transported regolith unit has a higher proportion of soluble Cu (Figure 5-72).

The scatter plots (Figure 5-73) show two populations of data. In one population, a close correlation between Cu_{tot} and Cu_{cn} consists predominantly of Cu_{cn}-rich/Cu_{tot}-poor samples from the transported regolith. The second population contains Cu_{tot}–richer samples of *in situ* regolith, which appear to be lithologically controlled and related to higher Fe and Mg concentrations (mafic rocks). Selected scatter plots between Cu and other elements reflect the homogenous nature of the samples from the transported regolith unit (Figure 5-73). Absolute abundances of elements in the transported unit are determined by the intensity of dilution due to the aeolian sand. Copper concentrations are related to those of Fe, present as oxides and oxyhydroxides, with the highest concentrations forming a small separate population associated with the mafic rock on 339000E (Figure 5-75). The Ga *vs* Cu scatter plot shows two populations with a strong correlation for samples in the transported unit population. Gallium is associated with clays and Fe oxides-oxyhydroxides.

Summary statistics for Cu are listed in Table 5-7.

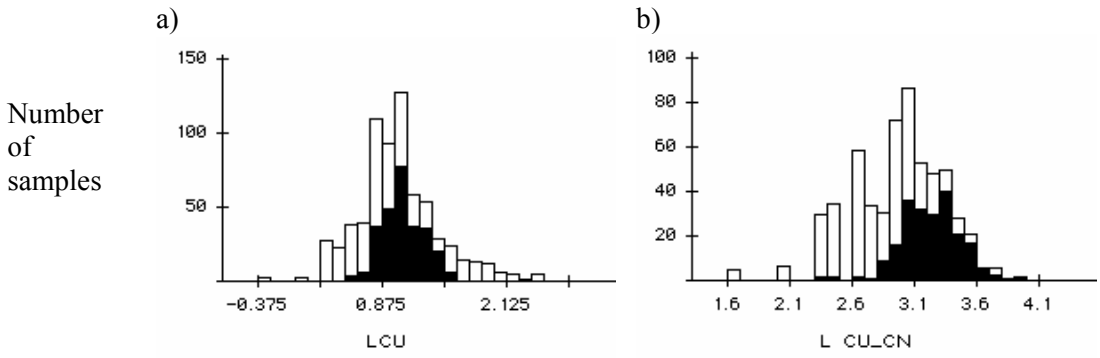

Figure 5-72 Histograms of Cu distribution in upper regolith: a) Cu_{tot} (ppm); b) Cu_{cn}.(ppb). Transported regolith unit data shown in black.

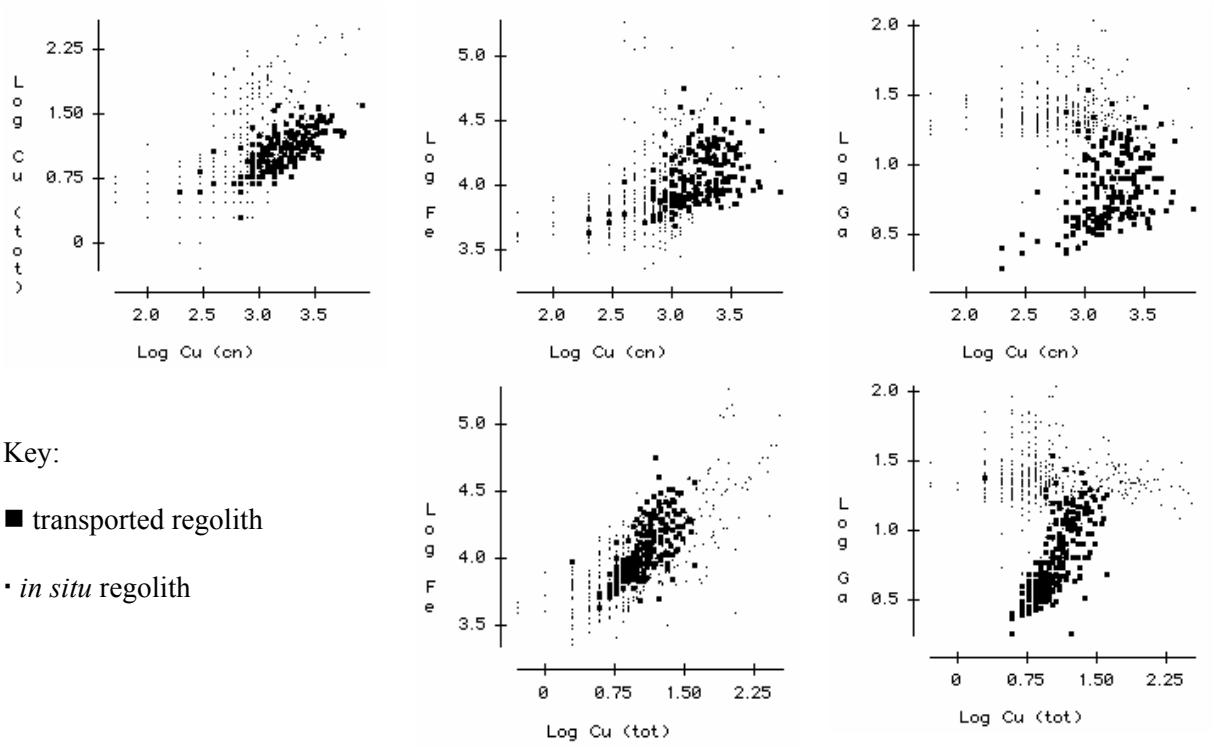

Figure 5-73 Selected scatter plots for Cu_{tot} (ppm) and Cu_{cn}.(ppb). Other elements in ppm. Large and small symbols are for samples located in transported and *in situ* regolith, respectively.

Table 5-7 Summary statistics for Cu data.

Sample medium	Detection limit (ppm)	Range (ppm)	Mean (ppm)	Standard deviation (ppm)	number
0-~10 m (cyanide)	0.1	<0.1-8.4	1.3	1.1	575
0-~10 m (total)	1	<1-340	19.3	34.6	686
Calcrete (total)	1	4-51	13.5	5.6	791
Soil (cyanide)	0.1	0.7-5.8	1.8	0.88	57
Soil (total)	1	4-17	6.9	2.3	57
Soil profile (cyanide)	0.1	0.5-15	2.5	2.96	55
Soil profile (total)	1	4-51	11	10	55
Vegetation (total, dry)	~0.1	1.7-42	6.4	5.1	58

Copper is associated with mineralisation at ET (Table 5-3). The distribution of Cu_{tot} in the upper regolith, however, appears not to be always related to mineralisation (see sections in Figure 5-74). The highest concentrations (max. of 340 ppm) occurs along 339000E, about 200 m N of mineralisation and is coincident with more mafic lithologies (Section 4.5.1). High concentrations of Cu_{cn} also occur here and, interestingly, in transported regolith to the south suggesting Cu is being mobilised from the mafic rocks although an adjacent east-west source cannot be discounted. Some elevated Cu_{tot} occurs in the upper saprolite above mineralisation along 338800E (max. of 155 ppm) and Cu_{cn} is generally anomalous for this area in the transported unit. Copper concentrations along 338200E or340200E do not suggest mineralisation.

Visualisation of the Cu_{cn} distribution in the regolith was by 2D (SURFER) and 3D (MVS) software. Visualisation was restricted to the top 10 m due to data limitations. For 2D visualisation, the data were untransformed prior to kriging and contour intervals classes are identical *for all depth* so that comparisons

can be made; the maximum contour interval has been set at a constant 3500 ppb (for all plots) to remove distortions caused by extreme Cu_{cn} values.. Several features are apparent from the images (Figure 5-75 and Figure 5-76):

1. Cu_{cn} concentrations are highest in the 0-1 m samples;
2. there are few coincident anomalies with Au at 0-1 m;
3. the main anomaly (section 339000E) persists to 4 m and is not related to mineralisation but to lithology and/or weathering of mafic rocks (as discussed above); and
4. Cu in calcrete is strongly related to Cu in the surficial drill cuttings.

The data suggest that Cu_{cn} is not as effective as Au at locating mineralisation and imply that Cu_{cn} distribution is principally related to lithology.

The distribution of Cu_{tot} in calcrete (Figure 5-77) partly reflects the Cu distribution in the upper regolith (Figure 5-74). In alkaline environments, Cu is relatively immobile and will precipitate as a carbonate complex such as malachite or azurite. Concentrations in calcrete are, as expected, low, particularly at ET where many samples have been collected from the top of the calcrete horizon. Anomalous Cu_{tot} in calcrete (up to 44 ppm) is located in the northern and central part of the study area that coincides with the higher concentrations of Cu_{tot} (up to 340 ppm) found in the upper saprolite (339000E) and with high concentrations of Ni (600 ppm) in calcrete and in the upper saprolite. As with Au, calcrete Cu_{tot} is richest in areas that are topographically high and have little cover (Section 3.3.2). This is not surprising since the saprolite, although highly weathered, still retains relatively high concentrations of trace elements such as Cu, albeit patchily distributed, near the surface. Very little Cu is found in calcrete or drill cuttings along 340200E.

Soil Cu_{tot} and Cu_{cn} are anomalous in the SW corner of the study area, showing the two highest Cu_{tot} concentrations (17 and 13 ppm, Figure 5-74). Concentrations of Cu_{cn} or Cu_{tot} are not anomalous in the vicinity of the 3 holes with the highest Au. Generally, there is no interpretable pattern to the Cu data for the soils. The soil profile data show a sharp increase in Cu (both forms) with depth, attributable to the appearance of calcrete. There is a strong correlation between Cu_{tot} and Cu_{cn}. for soils and soil profile samples suggesting a constant percentage of Cu (~0.3 %) exists in soil in a soluble form.

Copper concentrations in vegetation vary from 2-42 ppm (mean of 6 ppm) dry weight. The maximum concentration (42 ppm) is located in the NE corner of the prospect and appears unrelated to concentrations of Cu or Au in other sample media. There is little variation in the Cu abundance and no association with Cu concentrations in soil or drill cuttings.

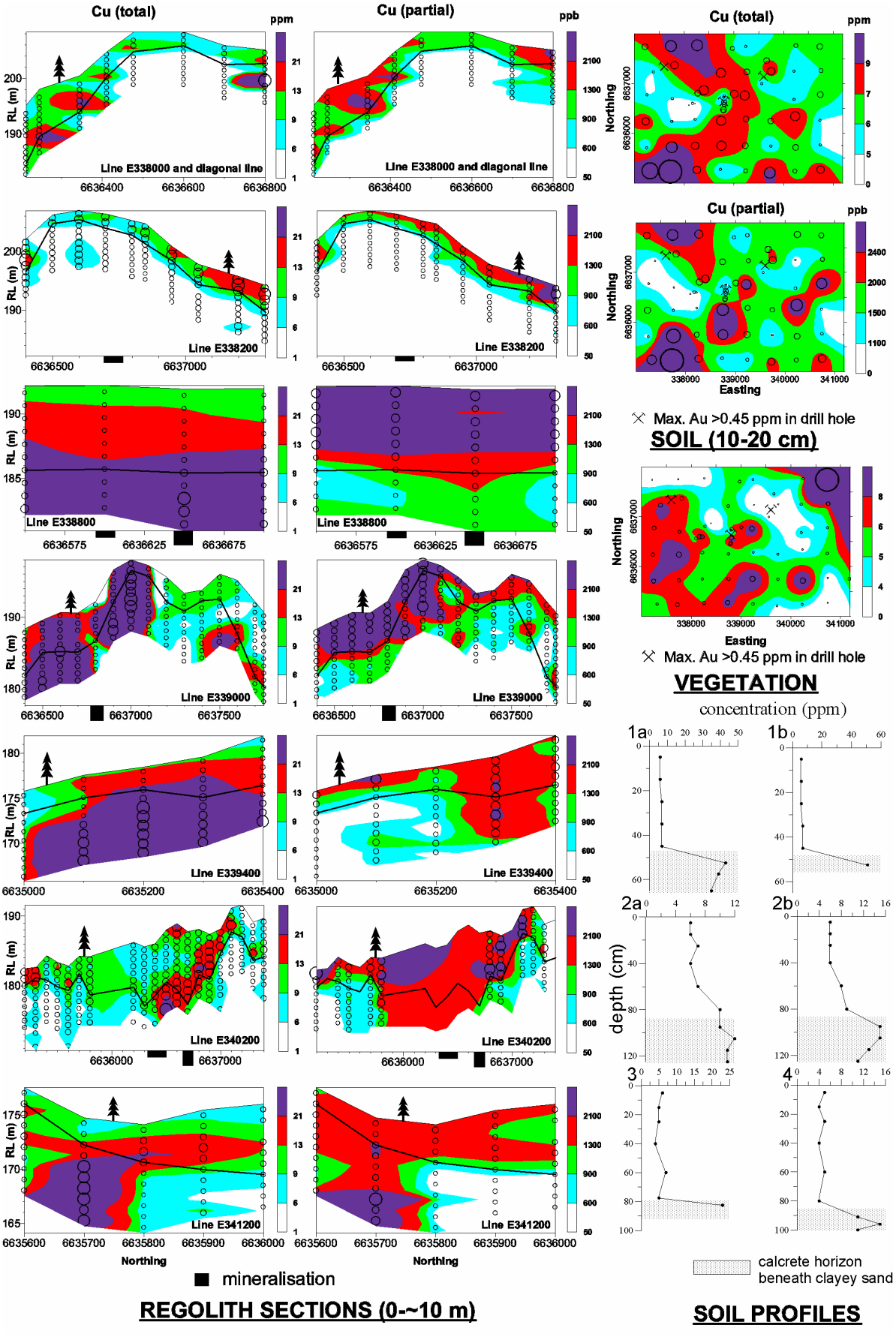

Figure 5-74 Distribution of Cu in the regolith at ET. Circles indicate sample location. Minimum and maximum Cu_{tot} (ppm) and Cu_{cn} (ppb) drill cutting concentrations are 0.05, 340, 50 and 15000, respectively.

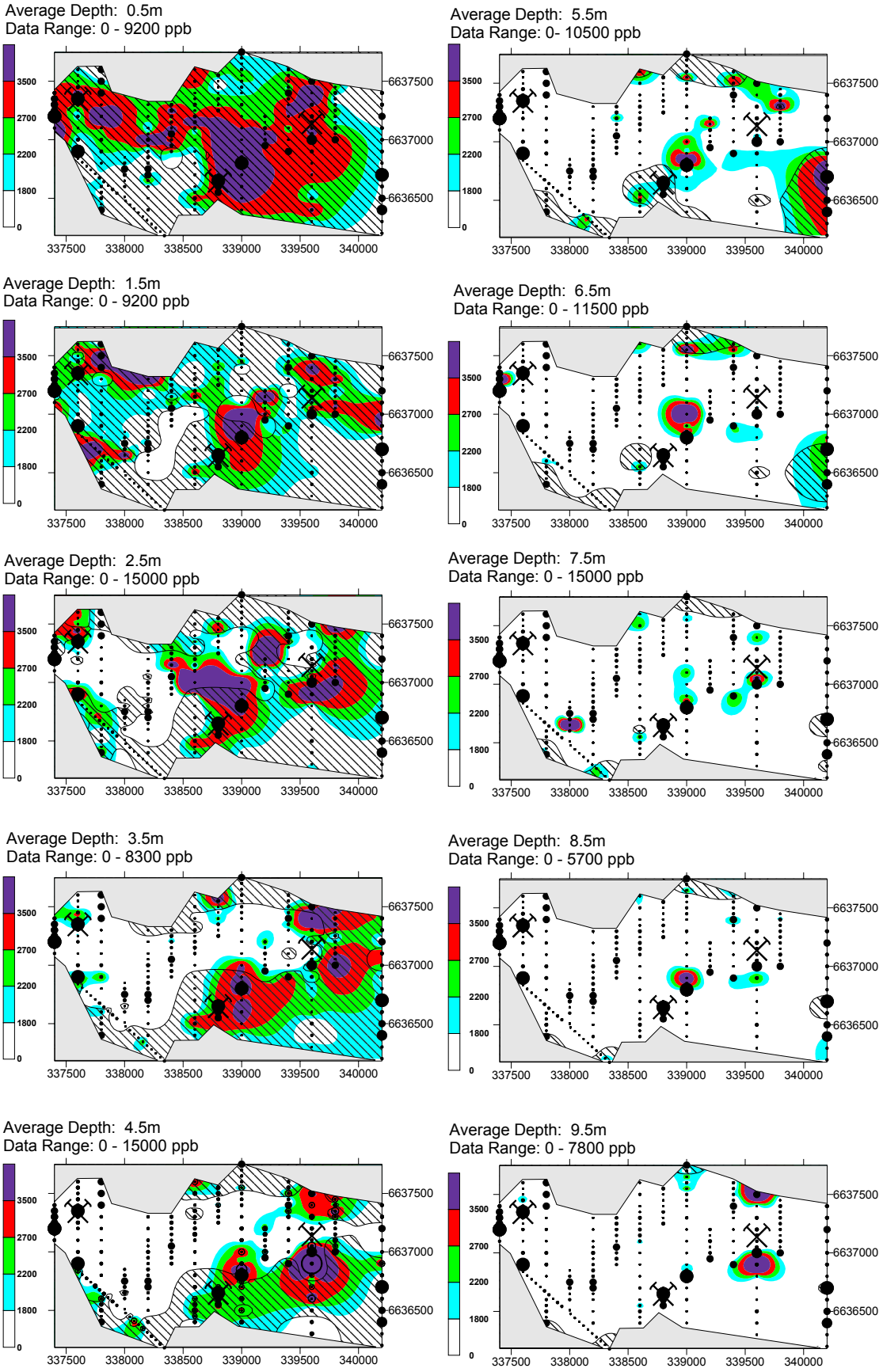

Figure 5-75 Cu_{cn} concentrations at 1 m intervals to 10 m. Mineralisation (black dots and hammer-pick symbols) as maximum Au concentration per hole, and transported overburden (hatching) are shown. See text for details of data treatment.

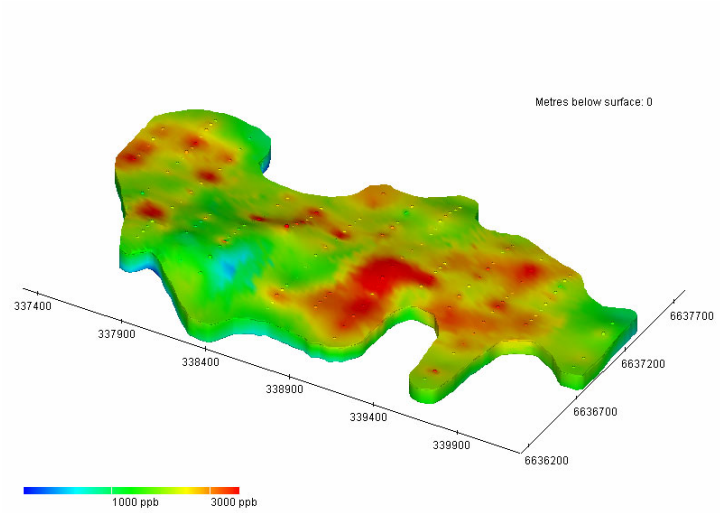

a)

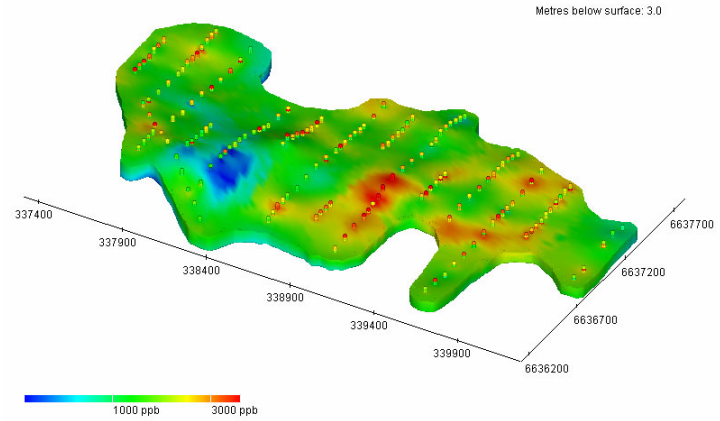

b)

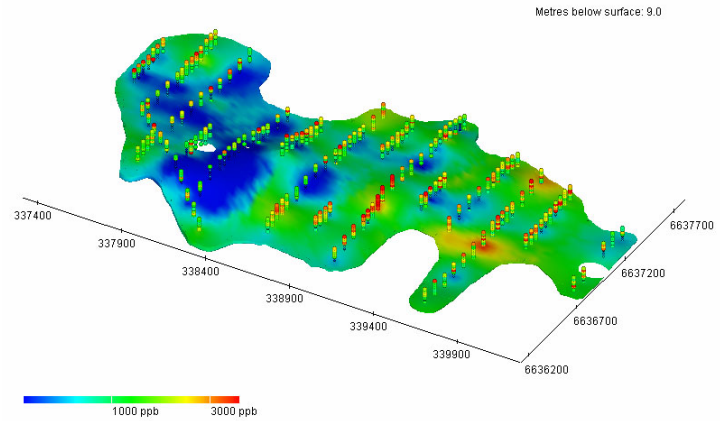

c)

Figure 5-76 A series of diagrams showing the change in Cu_{cn} distribution at intervals from the surface to 9 m depth, overlaid on the DEM. Drill hole samples are coloured according to Cu_{cn} content.

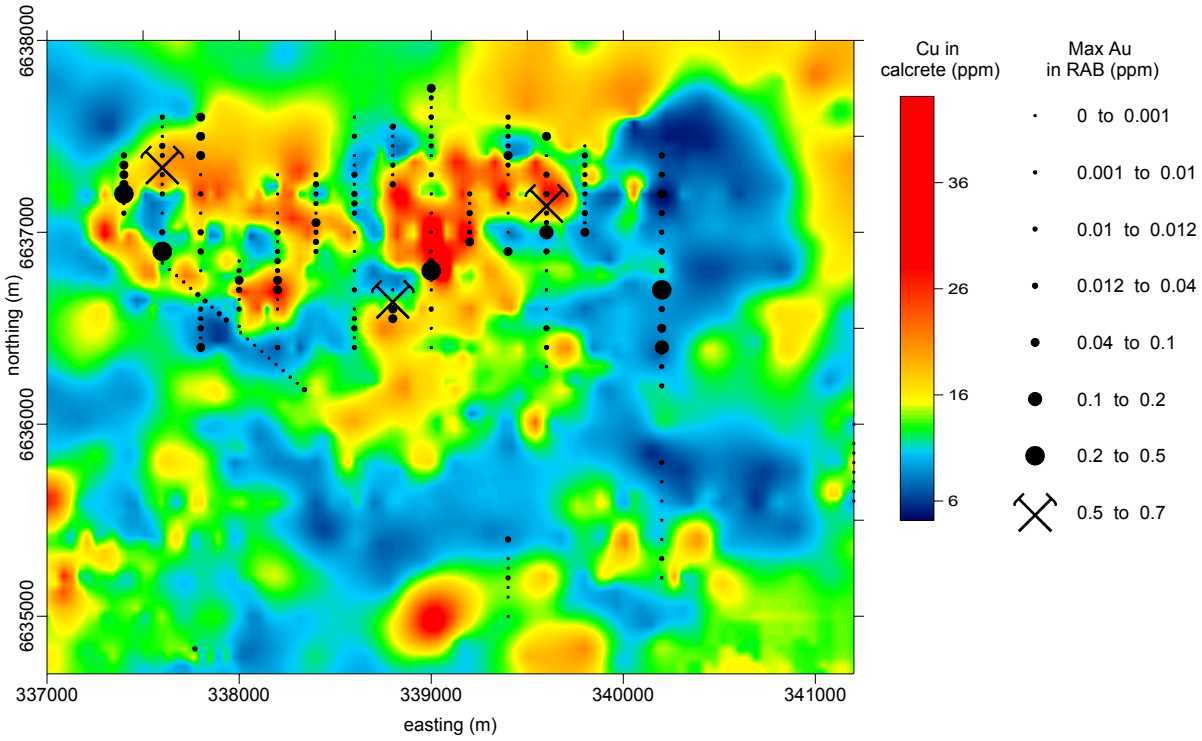

Figure 5-77 Copper concentrations in calcrete. Concentration range is from 4 ppm to 44 ppm. Also shown is maximum Au concentration in drill cuttings (ppm, black circles). (GJV data).

5.7 Arsenic geochemistry

Arsenic was analysed by ICP-MS after mixed acid digest. Unlike Au and Cu, many of the calcrete samples (GJV data) were not analysed for As. Nearly all of the soils (including those from the profiles) and half of the upper regolith samples had very low concentrations of 5 ppm or less, and means were also close to detection (0.5 ppm, Table 5-8). Arsenic is commonly associated elsewhere with hydrothermal-style Au mineralisation. Arsenic concentrations here and at other prospects *e.g.,* Challenger, Monsoon, Golf Bore, Jumbuck and South Hilga are generally below 500 ppm (Lintern and Sheard, 1998; Lintern *et al*, 2002). The mean As concentration of mineralised samples at ET is 79 ppm (ranging from 10-350 ppm), which is significantly lower than the mean of 202 ppm at Challenger. The most probable reason for lower concentrations at ET is the poorer mineralisation and lower sulphide content in the saprock (and, presumably, fresh rock), and limited secondary Fe accumulations found in the regolith.

Table 5-8 Summary statistics for As data.

Sample medium	Detection limit (ppm)	Range (ppm)	Mean (ppm)	Standard deviation (ppm)	Number
RAB drill cuttings	**5**	**<5-460**	**18**	**32**	**1345**
0-~10 m	**0.5**	**<0.5-135**	**7.5**	**13**	**686**
Calcrete	**5**	**<5-39**	**8**	**6.4**	**617**
Soil	**0.5**	**1-5.5**	**1.6**	**0.7**	**57**
Soil profile	**0.5**	**<0.5-5.5**	**2.4**	**1.1**	**55**
Vegetation (dry)	**~0.02**	**<0.02-1.4**	**0.05**	**0.04**	**58**

Despite their low concentrations, As and Fe are associated in the upper regolith (Figure 5-78). A scatter plot of As *vs* Fe indicates two populations, representing *in situ* and transported regolith units with Fe concentrations and Fe:As ratios generally higher in the transported unit. The highest concentrations of As (and Cu) on 339000E are related to mafic lithologies and occur to the north of mineralisation

(Figure 5-79). Samples from the upper saprolite close to mineralisation on the southern part of 339000E are also generally anomalous in As and have higher As:Fe ratios. However, there is little expression of this As anomalism in calcrete samples or from the transported unit above. Other mineralised hole data on 338200E, 338800E and 340200E also lack anomalism in the upper regolith.

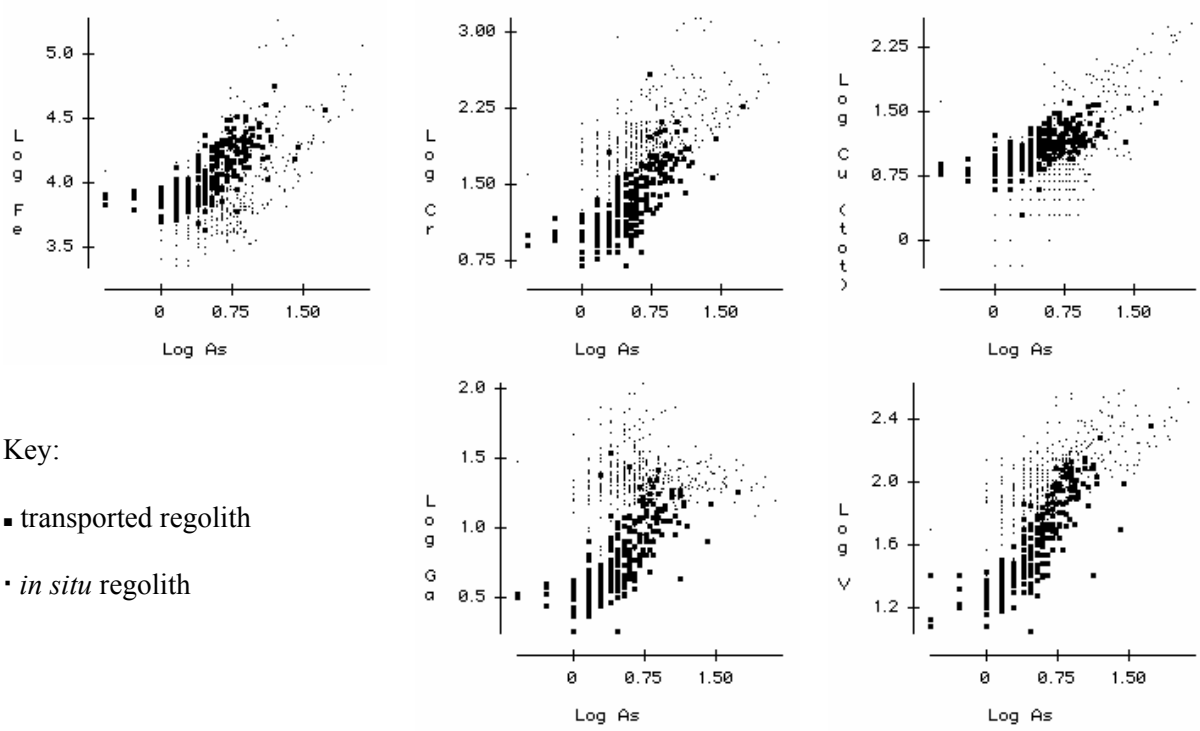

Figure 5-78 Selected scatter plots for As.

Company data indicates that As in calcrete is anomalous in the central and eastern part of the study area. The data do not grid satisfactorily (unlike Au and Ag) since there is considerable, unexplained variation in As concentrations in adjacent and duplicate samples (Figure 5-80); raw data plots (with symbols proportional to concentration) indicate a large coherent anomaly in the eastern part of the ridge (Figure 5-81). The source of the As anomaly is unclear but may be related to higher Fe concentrations in the calcrete; however, there are no Fe data for the calcrete to corroborate this.

Visualisation of the As distribution in the regolith was by 3D (MVS) software (Figure 5-82). The data set is slightly smaller in area coverage compared with Au, Ag and Cu data. Several features are apparent from the images:

1. Arsenic concentrations are relatively low in the near surface regolith.
2. There are no surface anomalies coincident with Au.
3. Strong anomalies appear at 20 m depth, persist and strengthen with depth, and some are related to Au mineralisation.
4. The principal As anomaly at depth trends NE.
5. Arsenic anomalies in calcrete are not associated with As anomalies at depth.

In summary, two observations suggest that As is not very effective at targeting Au mineralisation in the calcrete:

1. Arsenic concentrations in calcrete do not reflect the known locations of underlying mineralisation; and
2. peak As concentrations in the upper saprolite of 339000E are not reflected in the calcrete, even though there is only 1-2 m of transported material, suggesting that As is not as mobile as Au in this environment.

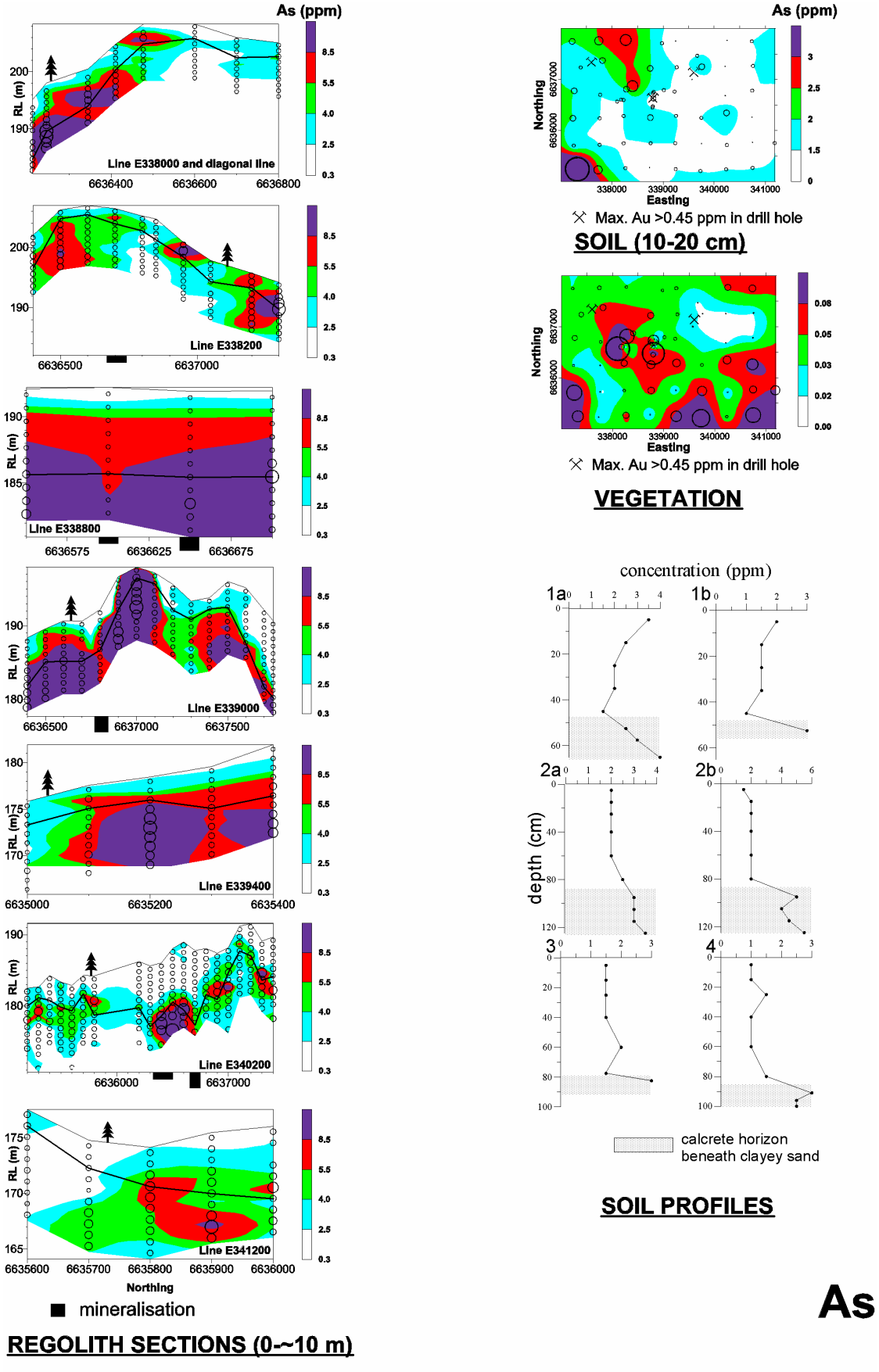

Figure 5-79 Distribution of As in the regolith at ET. Circles indicate sample location. Minimum and maximum As drill cutting concentrations are 0.025 and135 ppm, respectively.

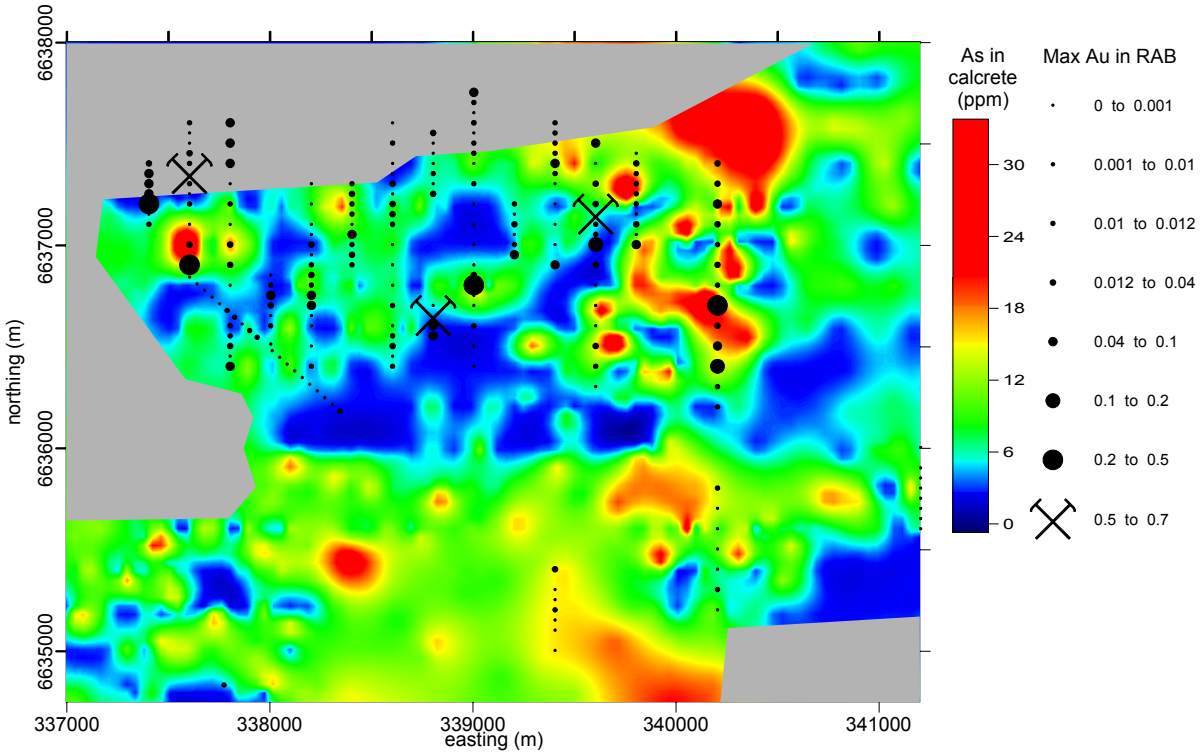

Figure 5-80 Arsenic concentration in imaged kriged calcrete data. Greyed area is where data are not available. Concentration range is from <5 ppm to 39 ppm. Also shown are maximum Au in drill cuttings (ppm). (GJV data).

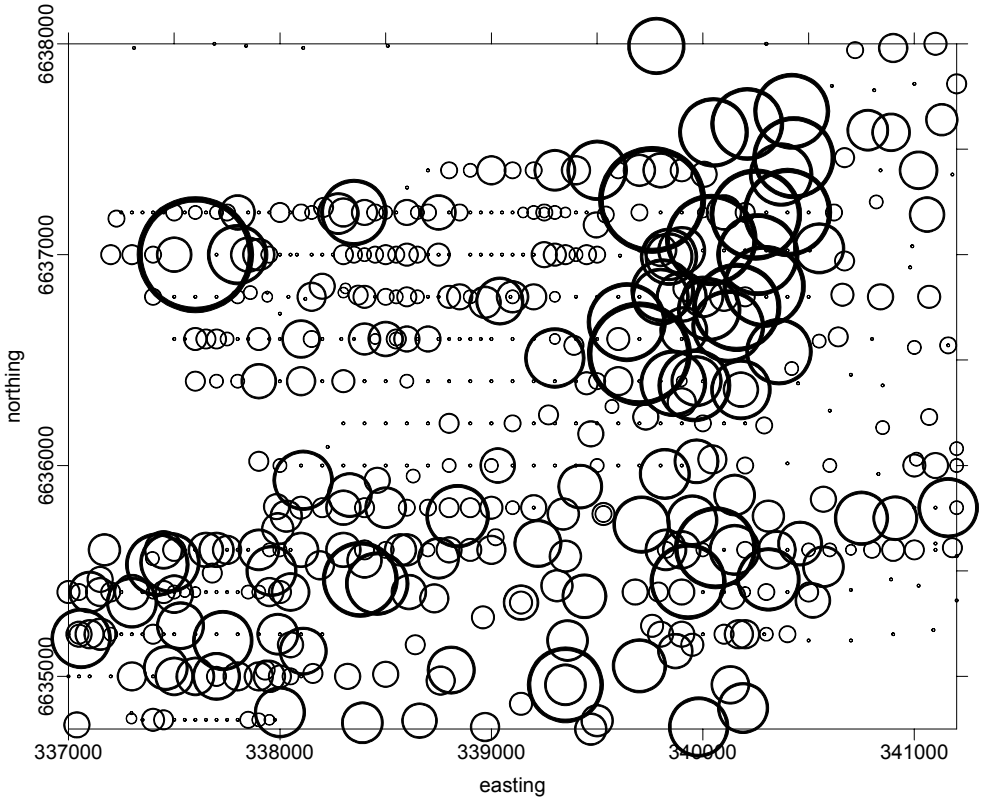

Figure 5-81 Arsenic concentration for raw data imaged in Figure 5-80. Circle diameter represents As from <5 ppm to 39 ppm. Note how the anomaly at centre-east is accentuated compared with the imaged plot.

Soils have very low As concentrations (mean 1.6 ppm), close to detection (0.5 ppm), reflecting their sandy and transported nature and presumably their low Fe contents (Figure 5-79). There is an anomalous sample (5.5 ppm) in the far SW corner of the study area but adjacent samples are background. A group of anomalous samples (2-3 ppm) occurs along the NW boundary of the study area. Soil profile samples are low in As concentration and show little variation with depth. There is a marginal increase in concentrations with the appearance of calcrete at the base of the profiles.

The As concentration in vegetation is very low (maximum of 1.4 ppm). Elevated As concentrations occur close to only one of the three drill holes intersecting mineralisation. The concentrations of As in vegetation associated with the As anomaly in calcrete are low. Arsenic in vegetation at ET is not a reliable indicator of mineralisation.

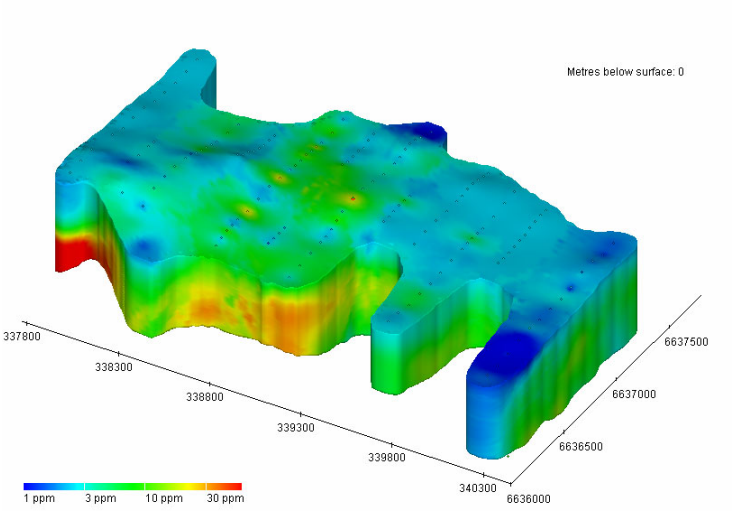

a) surface

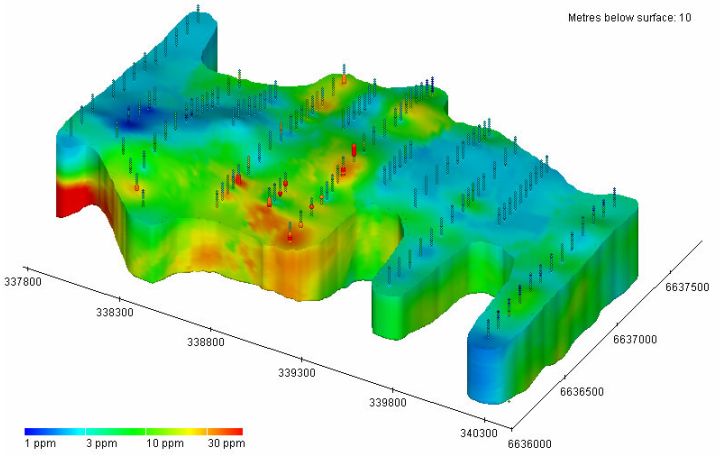

b) 10 m

Figure 5-82 A series of diagrams showing the change in As distribution at intervals from the surface to 40 m depth; the surface diagram is overlaid on the DEM. Drill hole samples are coloured according to As content.

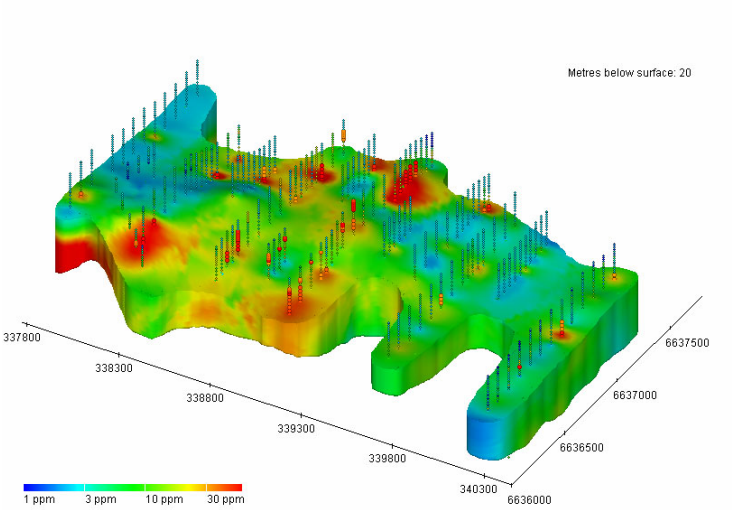

c) 20 m depth

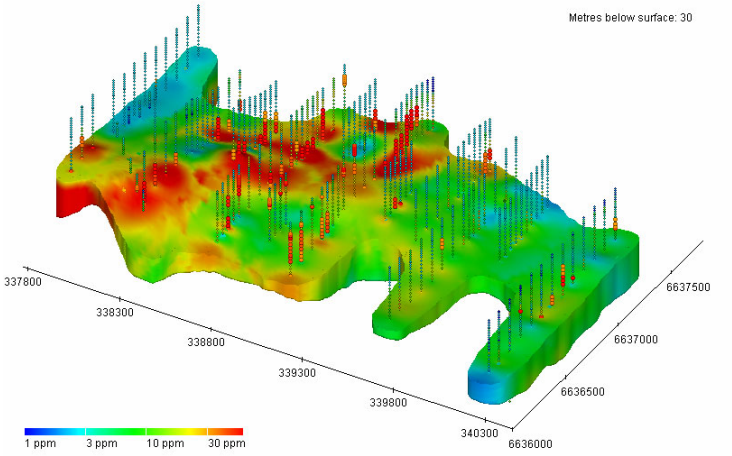

d) 30 m depth

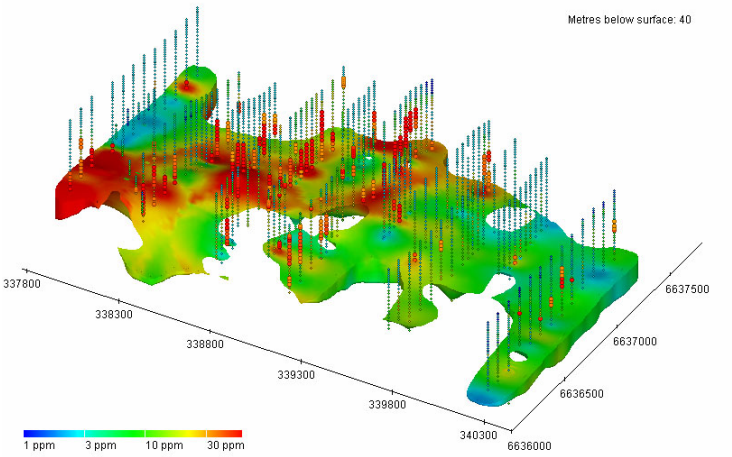

e) 40 m depth

Figure 5-64 (continued)

At Challenger, the As:Fe ratio in drill cuttings was found to delineate mineralisation better than As data alone (Lintern and Sheard, 1998). The latter also produced spurious anomalies related either to lithology or to accumulation of Fe oxide-oxyhydroxides during weathering processes. The plotted As/Fe ratio

produces two new anomalies (in addition to As anomalies), one at the western most end of the Diagonal section, the other over and adjacent to mineralisation on 339000E (Figure 5-83). The anomalism is not present in the overlying transported overburden. The strongest anomaly for As (centre of 339000E) is eliminated by the As:Fe ratio, suggesting that it is not indicating mineralisation but probably reflecting lithology or regolith processes. The maximum upper saprolite As:Fe anomaly at ET is weaker at As/Fe=30 compared with Challenger at As/Fe>80.

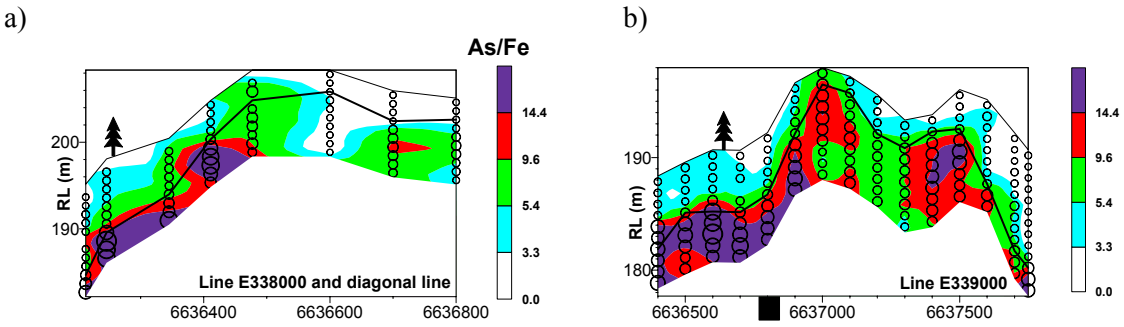

Figure 5-83 Upper regolith sections 338000E (a) and 339000E (b) showing As/Fe anomaly. Circle size is proportional to concentration. Black rectangle locates known mineralisation. .

5.8 Elements related to lithology – Co, Cr, (Cu), Ni, V and Fe

Nickel and Cr concentrations are elevated in some mineralised samples at ET (Table 5-3). The distributions of Ni and Cr were examined in the upper regolith and associated transported overburden in order to examine their potential role as pathfinders to mineralisation. Anomalous Ni is not found at the surface above mineralisation. However, anomalous surficial concentrations of Cr and Ni (with Fe, Co, and V) do occur over non-mineralised mafic rocks. The distribution of Ni was investigated in two settings:

(i) saprolite beneath thin residual soil. On section 339000E, saprolite containing up to 360 ppm Ni, subcrops at the top of a small rise (Hole ETAR072, Figure 5-84). The land surface gently slopes to the south (average gradient of 1:65). Nickel concentrations in calcrete (GJV analysis) are anomalous (600 ppm) immediately above the saprolite. The results suggest that Ni has dispersed into the transported overburden and has specifically concentrated in the calcrete. Furthermore, the anomaly extends more than 600 m downslope (to the edge of the sampling line) where concentrations are still anomalous (175 ppm). Further investigation of this material is warranted since corresponding calcareous drill cuttings are not anomalous in Ni;
(ii) saprolite beneath several metres of transported material. In the southern part of 339400E at hole ETAR319, saprolite containing 900 ppm Ni is buried beneath 3 m of transported material and a further 2-5 m of Ni-poor saprolite (Figure 5-85a). Calcrete was not specifically sampled here but calcareous drill cuttings were not anomalous in Ni (or other elements associated with mafic rock) in the transported overburden above the saprolite (Figure 5-85b).

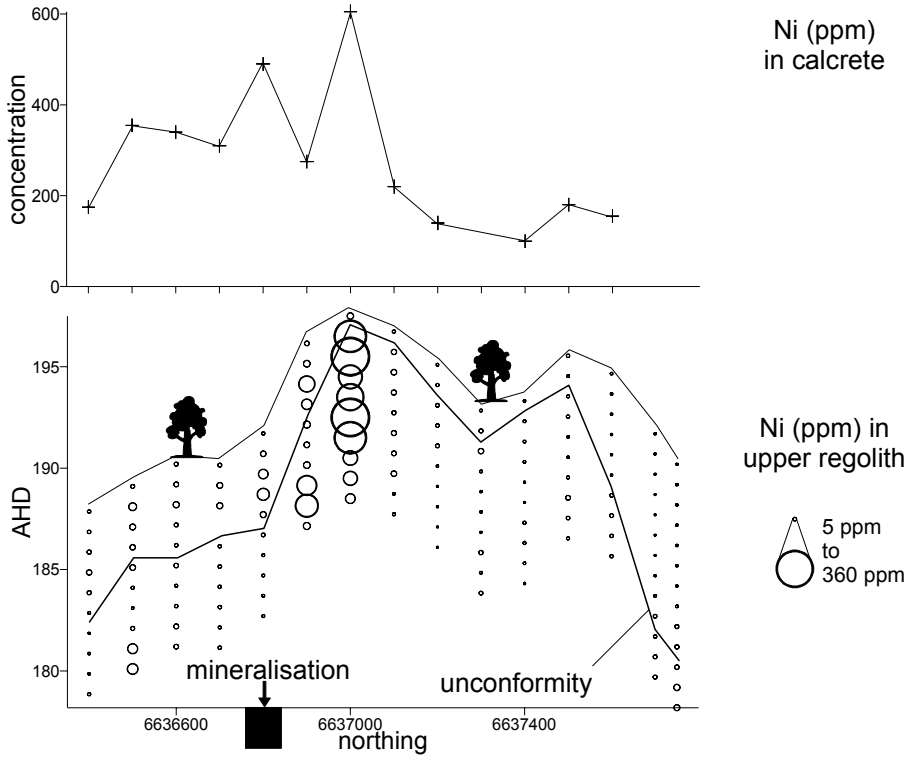

Figure 5-84 Nickel concentrations in calcrete compared with Ni distribution in the upper regolith drill cuttings on 339000E. Land surface height (AHD) has been calculated from the DEM. Note curiously low Ni concentrations in the calcareous drill cuttings downslope of 6637000N.

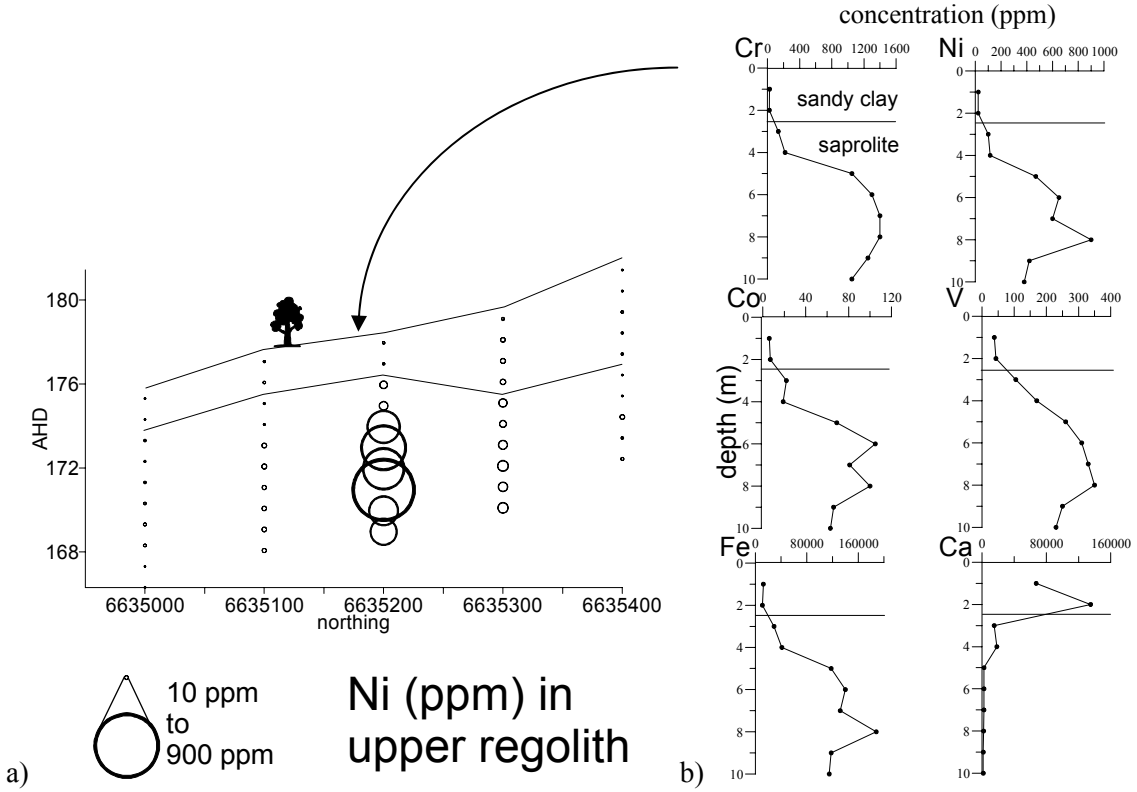

Figure 5-85 a) Upper regolith geology and Ni concentrations for 339400E south and showing location of profiles for b); b) selected element concentrations down hole for ETAR 319. Land surface height (AHD) has been calculated from the DEM.

The results suggest that Ni is being laterally dispersed, physically and/or chemically, but only where the saprolite breaches the surface. Nickel appears to be best concentrated in the calcrete horizon. If the saprolite is buried, then Ni dispersal is limited to the immediate vicinity. More data are required to confirm whether the observations are repeated elsewhere.

5.9 Elements related to phyllic alteration – K, Cs, Rb and Tl

Concentrations of K, Cs, Rb (alkalis) and Tl (ionic radii similar to alkalis) in the regolith at ET are correlated (Appendix 2). High concentrations of theses elements are commonly associated with mica, especially muscovite. At ET, mica is generally common in the lower regolith and is visible in the drill cuttings. Muscovite, biotite and phlogopite have been identified by selected XRD spectroscopy (56 samples) and their presence in 163, 63 and 17 drill hole samples, respectively, (Figure 5-86), has been interpreted from PIMA spectroscopy of the top 38 m of each hole. Micas from the main ridge appear to be dominated by muscovite, whereas biotite appears to be the main type in the south east of the prospect (foreground in Figure 5-86). There appears to be an association between As and muscovite with the ridge marking the southern boundary; this may indicate the presence of a structure such as a fault. At Challenger, alteration was associated with mineralisation and related K was anomalous in a zone several hundred metres wide (Lintern and Sheard, 1998). At ET, alteration associated with mineralisation is poorly defined, and so the distribution of mica (and K) is not confined to a particular part of the prospect. The plans and sections showing the distribution of K suggest that it is more concentrated in the *in situ* regolith or where transported materials are thin (Section 3.3.2; Figure 5-87). High concentrations of K (muscovite) in the *in situ* regolith are not reflected in the overlying transported overburden making K, here, a poor indicator of "buried" alteration i.e. no vertical movement of muscovite particles.

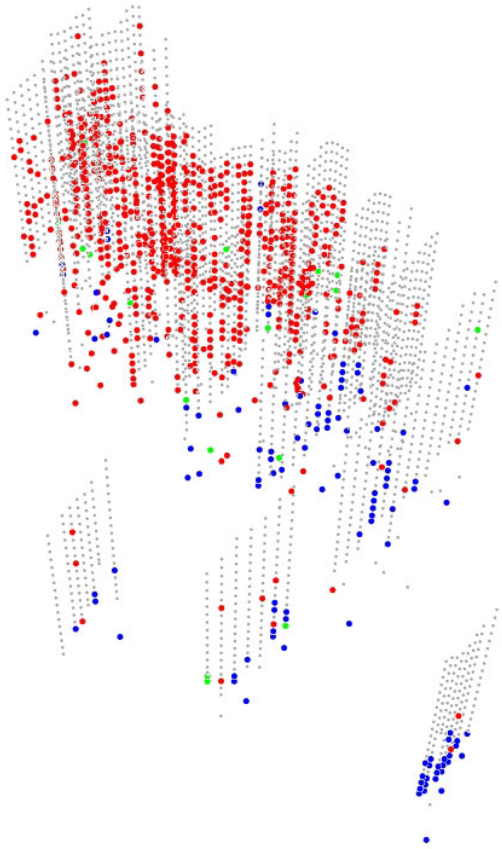

Figure 5-86 Three-dimensional image of the distribution and type of micas in drill hole cuttings as determined by PIMA. Red is muscovite, blue is biotite, green is phlogopite. Viewed from above and south east.

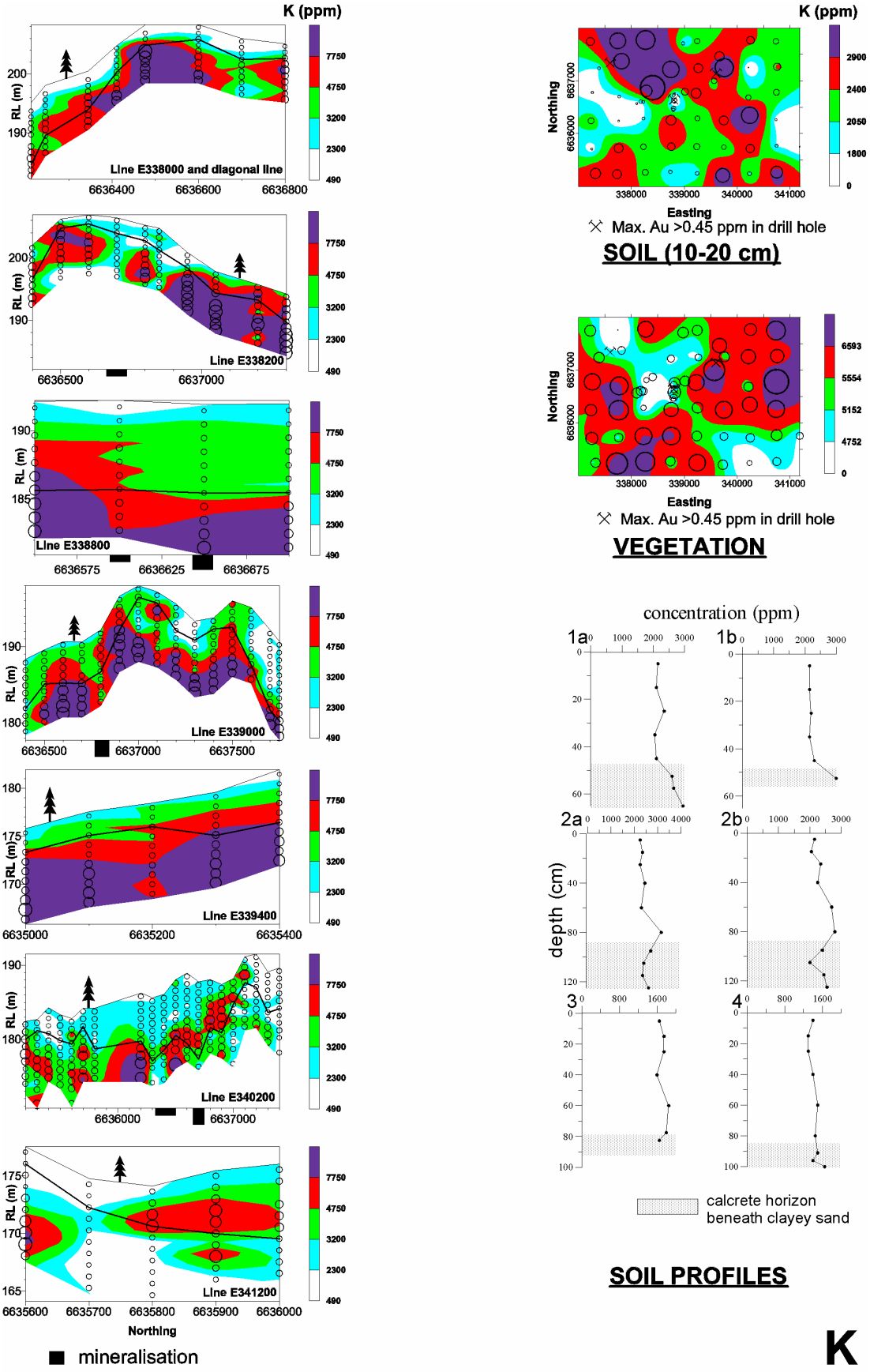

Figure 5-87 Distribution of K at ET. Circles indicate sample location. Minimum and maximum K drill cutting concentrations are 490 and 25400 ppm, respectively.

5.10 Conclusions

1. The main Au anomaly in calcrete (Figure 5-5) is associated with a thinly covered, topographic high of *in situ* regolith flanked by lower lying deeper sand. It is not directly coincident with the main Au anomaly found in the upper regolith, which is further east along the ridge (Figure 5-8). The reasons for this are unclear since there is a strong association with Au and carbonate in the drill cuttings.
2. The drilling data suggest that neither the main anomaly in the upper regolith nor that in calcrete is fully explained by the current understanding of the extent of mineralisation. Further drilling in both areas is recommended.
3. Multi-element geochemistry has limited value in delineating new anomalies but can support Au data. For example, Ag (cyanide-soluble) is anomalous over the Au anomalies occurring in calcrete and the 0-1 m drill cuttings. However, Cu (cyanide-soluble) is much more related to lithology than mineralisation. Arsenic from lower saprolite appears to be following a structural trend and may be related to mineralisation.
4. Most of the surficial Au is associated with calcrete in the transported regolith, which suggests at least some mobilisation of Au in chemical form through the sand.
5. Whereas many anomalies in *in situ* regolith are directly related to mineralisation, there are several examples where the surficial data are not easily explained by the drilling data. The Au has either been dispersed from its source and seemingly concentrated, or the drilling has been inadequate.
6. The best evidence for an anomaly occurring in transported overburden is hole ETAR 070 (Figure 5-43). On easting 340200E, there is also an anomaly in the transported overburden over mineralisation (ETAR 188) at 2-5 m depth in 9 m of overburden. However, downslope mobilisation of Au to form a chance anomaly cannot be categorically ruled out (see next paragraph).
7. In some locations there are no surficial Au anomalies over concealed mineralisation. For example, no anomaly exists within *in situ* regolith unit over mineralisation on 337600E or within transported regolith unit on 340200E (ETAR 185). This suggests surficial regolith materials may not be always entirely relied on to detect all mineralisation at the prospect scale. Alternatively the mineralisation may be so weak that it does not form an anomaly or be discontinuous, in which case the lack of anomaly is reflecting the real situation.
8. Vegetation Au data (0.5 km x 0.5 km grid) can potentially provide additional exploration targets, but their failure to substantiate existing anomalies reduces the confidence in their use. The highest Au concentrations appear to be more related to transported overburden, suggesting that vegetation may be responding more to run-off from the ridge.
9. Soil Au data (0.5 km x 0.5 km grid) appear to be useful in delineating the main Au in calcrete anomaly but they probably respond more to the co-presence of thin overburden and proximity to the underlying anomalous calcrete. Size fraction analysis was not undertaken but may provide some support to pre-concentrate the low concentrations found in the bulk soil.
10. The use of partial extraction procedures using bulk surficial soils is unlikely to bring additional benefits over more conventional analyses at ET. Concentrations of Au and many other elements are very weak in the bulk sand and do not appear to directly reflect the underlying Au concentrations either in the sub-surface calcrete or mineralisation itself.
11. The use of MVS and SURFER software enables 2D and 3D visualisation of data, in particular, the spatial distribution of Au, As, Ag and Cu in the regolith.
12. The design and use of an ARCVIEW add-in software program (on the DVD) allows the user to simultaneously view and interrogate in plan, section and block models a range of data sets, these include: photographic images of drill cuttings, element concentrations, PIMA spectra/data, DEM, mineralogy and lithological boundaries. The software permits investigation of the roles and links of diverse variables in a GIS environment. This program can be used with other data sets.
13. With further development, the GIS and data sets will be useful as teaching aids for industry and students. There is more information yet to be mined from the data set that is beyond the scope of the current project such as the relationship between other trace elements and mineralogy.

6 IMPLICATIONS FOR EXPLORATION

6.1 Remote sensing technologies

1. DEM was especially useful in low-relief sandridge terrains where sand dunes disguised local undulations in basement topography and the presence of basement highs. The use of the DEM was invaluable in interpreting the Au in calcrete anomalies.
2. Of the technologies examined, SPOT-PAN, Airborne gamma-ray spectrometry, HyMap^{TM}, Polarimetric AIRSAR radar and Landsat TM, the latter is the only cost-effective, operational multispectral dataset of adequate spatial resolution available for routine regolith-landform mapping in the ET area.
3. Near-surface (0-25 cm depth) descriptions of radioelement concentrations of K, Th and U are available from airborne gamma-ray spectrometry signals but the usefulness of these data for mapping the regolith is controlled by the line spacing, gridding and calibration of the data. This is particularly important in areas of minimal definition such as ET where the majority of bedrock and indurated materials are masked by aeolian sands.

6.2 Regolith landform mapping

1. At 1:5000 scale, identification and detailed representation of the distribution of potential geochemical sampling media and the broader surface regolith units was not possible based only on datasets commonly used in regolith map construction alone *e.g.*, Landsat, DEM and aerial photography. This is especially the case at ET where the broader regolith units belong to only one of three major classes (aeolian, colluvial or residual).
2. The usual ranges of broad landform surrogates were not available at ET. Landform classes belonged to two major classes *i.e.,* depositional and erosional. Regolith materials were of three broad types: lag, aeolian sand or sheetflow deposit.
3. Subdivision of landform classes did not markedly improve the surrogate relationships observed between regolith and landforms, yet the regolith patterns and distribution was not fully resolved by remotely-sensed imagery alone.
4. Patterns generated by field observation were modified by those derived from Landsat TM and HyMap^{TM} datasets and to a lesser extent by the DEM.
5. Field observations were essential to (i) assess the gross patterns generated by remote sensed imagery, (ii) determine subtleties within the ET regolith framework and (iii) determine the final regolith-landform relationships.
6. The 1:5000 scale mapping was insufficient to examine discrete anomalies in the calcrete, but was beneficial in providing a broad understanding of the distribution of the main regolith units and in understanding the geochemical distributions.

6.3 Regolith Stratigraphy

1. RAB and RC drill cuttings were essential to determine the extent of transported overburden and the regolith stratigraphy. Down hole contamination, particularly from RAB, was a problem for determining accurately the stratigraphic boundaries of regolith materials. Determining the exact location of the unconformity in the siliceous regolith was especially difficult.
2. Prospect scale drilling should include at least 1 or 2 fully cored holes (diamond) per surface anomaly area to augment RAB and RC drilling cuttings for key regolith zone and geochemical interpretation.
3. PIMA spectral analysis is recommended at ET as a tool for determining sample provenance.

6.4 Geochemistry

1. The main Au anomaly in calcrete is associated with a thinly covered, topographic high of *in situ* regolith flanked by lower lying deeper sand. It is not directly coincident with the main Au anomaly found in the upper regolith, which is further east along the ridge. The reasons for this are unclear since there is a strong association with Au and carbonate in the drill cuttings. This is clearly an area worthy of further investigation including drilling.

2. The drilling data suggest that neither the main anomaly in the upper regolith nor the anomaly in calcrete is fully explained by the current understanding of the extent of mineralisation. Further drilling (in-fill and possibly deeper) in both areas is recommended.
3. Higher As concentrations (as observed in 3D) coincident with a change in white mica distribution (PIMA data) obliquely through the prospect suggest a structural input to the geochemistry and possibly provide an additional target for drilling.
4. Most multi-element geochemical data (including Ba, Bi, Ca, Cd, Cs, Ce, Cr, Cu, Fe, Ga, In, K, Mg, Mn, Mo, Na, Nb, Ni, P, Pb, Rb, S, Sb, Se, Sr, Te, Th, Ti, Tl, U, V, W, Y, Zn and the REE) have limited extra value in delineating new anomalies but may support Au data. Determining Ag and As appear to offer some advantage in providing new anomalies that should be followed up.
5. Anomalies were classified according to varying types at ET. These include true anomalies in transported overburden, false or displaced anomalies and potential chance anomalies. False backgrounds may also occur at ET indicating surficial materials may not be entirely reliable as indicators of mineralisation.
6. Vegetation Au data can provide additional targets for further exploration but their failure to substantiate existing anomalies reduces confidence in their use.
7. Soil Au data appear to be useful in delineating the main Au calcrete anomaly but they probably respond more to the co-presence of thin overburden and proximity to the underlying anomalous calcrete.

7 CONCLUSIONS

One of the principal objectives of this project was to examine the geochemical implications for exploration in transported overburden. As the ET Gold Prospect is located on the edge of the Great Victoria Desert dunefield, broader implications for exploring in sand covered terrain are obvious. The multi-disciplinary approach at ET proved to be especially useful in interpreting geochemical anomalies and establishing regolith controls. Regolith stratigraphy and mapping of regolith materials is important for any exploration programme since the geochemistry of sampling media respond differently to different materials *e.g.*, silcrete *vs* saprolite *vs* calcrete. Determining regolith stratigraphy for an area like ET, with relatively subdued topography and sand cover, is usually only possible with the use of careful drilling practices.

Regional calcrete sampling by the GJV followed by in-fill calcrete sampling discovered the ET Gold Prospect. The geochemical anomaly is typical of many in the Gawler Craton:

1. Gold is concentrated in calcrete near the surface for *in situ* regolith.
2. Beneath the surficial enrichment of Au in calcrete and upper regolith, very low Au concentrations may occur for several tens of metres depth.
3. Spatially large anomalies commonly extend hundreds of metres.
4. Drilling the bullseye of the anomaly is commonly unsuccessful.
5. High Au concentrations in the surface anomaly do not always equate to strong mineralisation in bedrock.
6. Usually, Au is the best target element.

Some of these characteristics have led to a degree of pessimism amongst exploration companies as to the real value of Au in calcrete anomalies in finding economic targets. Of many hundreds of such anomalies, few have been thoroughly investigated and developed into prospects. It has been proposed that because there are so many anomalies, a ranking procedure is required so that limited funds can best be used on drilling those anomalies more likely to yield mineralisation. As yet, the criteria used to rank anomalies have not been successfully designed, developed and rigorously tested. However, each anomaly that is investigated provides additional information to assist in the establishment of these criteria. Notwithstanding this, at ET, careful examination of the Au-in calcrete anomalies and the company data indicate that more drilling is required for full assessment of the prospect because additional targets have been identified using this detailed approach.

Calcrete still appears to be the best sample medium for regional and prospect scale Au exploration in the western Gawler Craton despite our limited understanding of the material. This is based on the following observations:

1. It is cheaper to collect calcrete than upper regolith samples. The silicified upper regolith is a severe hindrance for collecting 0-1 m or deeper upper regolith samples using a power auger.
2. Calcrete appears to be better than the sandy soil as the former appears to be "seeing through" at least limited thicknesses of sandy transported overburden in some cases (<5 m). However, calcrete does not detect all mineralisation and further work needs to be undertaken in this area.
3. In residual regolith, calcrete gives broader anomalies than other sample media, especially saprolite. There is evidence for lateral (down slope) movement of Au into transported overburden and that this Au is primarily located in calcrete. Calcrete can potentially provide larger anomalies for broad-based sampling programmes.

8 REFERENCES

Anand, R.R., Smith, R.E., Innes, J. and Churchward, H.M., 1989. Exploration geochemistry about the Mt Gibson gold deposits, Western Australia. CSIRO Divion of Exploration Geoscience. Restricted Report 20R (re-issued as Open File Report 35, CRC LEME, Perth, 1998).

Benbow, M.C., 1982. COOBER PEDY South Australia 1:250 000 Geological series - Explanatory Notes map sheet and explanatory notes, Sheet SH/53-6. South Australia. Geological Survey. 1:250,000 Series Explanatory Notes.

Benbow, M.C., Crooks, A.F., Rankin, L.R., Martin, A.R. and Fairclough, M.C., 1995. BARTON map sheet. South Australia. Geological Survey. Geological Atlas 1:250,000 Series, sheet SH/53-9.

Butt, C.R.M., Gray, D.J., Lintern, M.J., Robertson, I.D.M., Taylor, G.F., and Scott, K.M., 1991. Gold and associated elements in the Regolith - Dispersion processes and implications for exploration. CSIRO Australia, Division of Exploration Geoscience Report No. 167R. 114 pp.

Butt, C.R.M., Gray, D.J., Lintern, M.J. and Robertson, I.D.M., 1993. Gold and associated elements in the regolith - dispersion processes and implications for exploration - Final Report, Project 241A. CSIRO Australia, Division of Exploration Geoscience Report No. 396R. 64 pp.

Butt, C.R.M., Gray, D.J., Robertson, I.D.M., Lintern, M.J., Anand, R.R., Britt, A.F., Bristow, A.P.J., Munday, T.J., Phang, C., Smith, R.E. and Wildman, J.E., 1997. Geochemical exploration in areas of transported overburden, Yilgarn Craton and environs, Western Australia. CRC LEME 36R/Exploration and Mining Report 333R. 153 pp.

Callen, R.A. and Benbow, M.C., 1995. Chapter 11, Quaternary. The Deserts – Playas, Dunefields and Watercourses. In: Drexel, J.F. and Preiss, W.V. (Editors) 1995. The Geology of South Australia. Volume 2. The Phanerozoic. South Australia. Geological Survey. Bulletin, 54, 244-251.

Craig, M.A., 2001 Regolith Mapping for geochemical exploration in the Yilgarn Craton, Western Australia. Geochemistry: Exploration, Environment, Analysis, Vol 1 2001, pp383-390

Craig, M.A., (coordinator), Anand, R.R., Churchward, H.M., Gozzard, J.R., Smith, R.E., & K. Smith, 1992 Regolith-Landform Mapping in the Yilgarn Craton, Western Australia: Towards a standardised approach. AMIRA Project P240A Yilgarn Lateritic Environments, CSIRO Exploration Geoscience, Wembley, WA, Australia.

CSES, 1999. Atmosphere REMoval program (ATREM) Users Guide, Version 3.1, Centre for the Study of Earth from Space, Boulder, Colorado, 31 pages.

Cudahy, T.J., Lintern, M.J. and Gabell, A.R., 1992. Spectral properties of soil overlying the sites of the Bounty and North Bounty gold mines, Forrestania region, Western Australia. CSIRO IMEC Division of Exploration Geoscience Restricted Investigation Report No. 169R, 80 pages.

Cudahy, T.J. and Ramanaidou, E.R., 1992. Relationships between spectral properties and ferric oxides. CSIRO IMEC Division of Exploration Geoscience Restricted Investigation Report No. 244R, 68 pages.

Cudahy, T.J., 1992. A model for the development of the regolith of the Yilgarn Craton incorporating selected spectral information. CSIRO IMEC Division of Exploration Geoscience Restricted Investigation Report No. 243R, 26 pages.

Cudahy, T.J., 1998. PIMA-II spectral characteristics of natural kaolins. CSIRO Exploration and Mining Restricted Investigation Report No. 420R, 57 pages.

Gray, D.J., Sergeev, N.B., Britt, A.F., and Porto, C.G., 2001. Supergene mobilization of gold and other elements in the Yilgarn Craton - Final Report. CSIRO Exploration and Mining Restricted Report EM757R. 79 pp.

Daly, S.J. and Fanning, C.M., 1993. Chapter 3, Archaean. In: Drexel, J.F., Preiss, W.V. and Parker, A.J. (Editors) 1993. The Geology of South Australia. Volume 1. The Precambrian. South Australia. Geological Survey. Bulletin, 54, 33-48.

Daly, S.J., Webb, A.W. and Whitehead, S.G., 1978. Archaean to early Proterozoic banded Fe formations in the Tarcoola Region, South Australia. Royal Society of South Australia. Transactions, 102:141-149.

Eggleton, T., 1999. Glossary of regolith and related terms. Cooperative Research Centre for Landscape Evolution and Mineral Exploration. Open File Report.

Gozzard, J.R. and Tapley, I.J., 1992. Regolith-Landform Mapping in the Lawlers District. Report 2: Terrain Classification mapping (Volumes 1 and 2). CSIRO IMEC Division of Exploration Geoscience Restricted Report 240R.

Huntley, D.J., Prescott, J., Sheard, M.J. and Lintern, M.J., 1999. Optical luminescence dating of Quaternary Dunes and its implications for mineral exploration: Great Victoria Desert, South Australia. In: Rowett, A. (Complier) 1999. Exploring Ancient Landscapes, Workshop Abstracts. South Australia. Department of Primary Industries and Resources. Minerals Group. 12th December 1999, Adelaide. 8th paper.

Kelly, K.L. and Judd, D.R., 1976. Color - Universal Language and Dictionary of Names. National Bureau of Standards, United States Commerce Department, Washington, D.C.

Kruse, F.A., Lefkoff, A. B., Boardman, J.B., Heidebrecht, K.B., Shapiro, A.T., Barloon, P.J., and Goetz, A.F.H., 1993. The Spectral Image Processing System (SIPS) – interactive visualization and analysis of imaging spectrometer data. Remote Sensing of Environment, Special Issue on AVIRIS, May-June 1993, v. 44, pp. 145-163.

Lintern, M.J. and Sheard, M.J., 1998. Regolith studies related to the Challenger Gold Deposit, Gawler Craton, South Australia. Geochemistry and stratigraphy of the Challenger Gold Deposit. CRC LEME Restricted Report 78R, 2 Volumes. 95 pp and Appendices (un-paginated). Reissued as CRC LEME Open File Report 78, 1999.

Lintern, M.J. and Sheard, M.J., 1998. Silcrete – a potential new exploration sample medium. South Australia. Department of Primary Industries and Resources. MESA Journal, 11:16-20.

Lintern, M.J. and Sheard, M.J., 1999a. Regolith studies related to the Challenger Gold Deposit, Gawler Craton, South Australia. Cooperative Research Centre for Landscape Evolution and Mineral Exploration. Open File Report, 78 (Second Impression) and South Australia. Department of Primary Industries and Resources. Minerals Group. Report Book, RB 98/10.

Lintern, M.J. and Sheard, M.J., 1999b. Regolith geochemistry and stratigraphy of the Challenger Gold Deposit. South Australia. Department of Primary Industries and Resources. MESA Journal, 14:9-14.

Lintern, M.J., Sheard, M.J. and Gouthas, G, 2002. Preliminary regolith studies at ET, Monsson, Jumbuck, South Hilga and Golf Bore Gold Prospects, Gawler Craton, South Australia. CRC Open File Report 115, 2 Volumes. 305 pp.

Lintern, M.J., Sheard, M.J. and Gouthas, G., 2000. Regolith Studies related to the Birthday Gold Prospect, Gawler Craton, South Australia. Cooperative Research Centre for Landscape Evolution and Mineral Exploration. Open File Report, 79 and South Australia. Department of Primary Industries and Resources. Minerals Group. Report Book, RB 2000/00003.

Lintern, M.J., Sheard, M.J. and Gouthas, G., 2002. Preliminary Regolith studies at ET, Monsoon, Jumbuck, South Hilga and Golf Bore gold prospects, Gawler Craton, South Australia. CSIRO Exploration and Mining. Report, 864R. Cooperative Research Centre for Landscape Evolution and Mineral Exploration. Open File Report, 115 and South Australia. Department of Primary Industries and Resources. Minerals Group. Report Book, RB 2002_004.

Mason, D.R. and Mason, J.E., 1998. A petrographic study of regolith samples from the Challenger Project (Gawler Craton, South Australia). Mason Geoscience Pty. Ltd., Report, 2413 (Clients: Mines and Energy South Australia and CRC LEME) 235p. (unpublished).

Merembeck, B., Boyden, F. Y., Podwysocki, M. H. and Applegate, D. N., 1977. Application of canonical analysis to multispectral scanner data. Proceedings 14th Annual Symposium Application of Computer Methods in the Mineral Industries. University Park, Pennsylvania, pp. 867-879.

Munsell Color, 1975. Munsell Soil Color Charts. Munsell Color, Baltimore, Maryland, United States of America.

Northcote, K.H. and Skene, J.K.M., 1972. Australian soils with saline and sodic properties. CSIRO Soil Publication Number 27.

Northcote, K.H., 1979. A Factual Key for the recognition of Australian soils. Rellim Technical Publications, Adelaide.

Pain, C., Chan, R., Craig, M. A., Hazell, M., Kamprad, J., and Wilford, J., 2001. RTMAP BMR Database Field Book and Users' Guide. CRCLEME, Perth, Open File Report 138.

Povey, D.A., 2000. An investigation into the distribution and geochemistry of surficial regolith materials at the Challenger Gold Deposit, South Australia. University of South Australia. School of Geoscience, Minerals and Civil Engineering. Honours thesis (unpublished).

Rankin, L.R., Benbow, M.C., Fairclough, M.C. and Daly, S.J., 1996. BARTON, South Australia, sheet SH/53-9. South Australia. Geological Survey. 1:250,000 Series – Explanatory Notes.

Robertson, I.D.M. and Butt, C.R.M., 1997. Atlas of weathered Rocks. CSIRO Division of Exploration Geoscience. Report, 390 (1st Revision) / Cooperative Research Centre for Landscape Evolution and Mineral Exploration. Open File Report, 1.

Sergeev, N.B. and Gray D.J., 2001. Gold mass balance in the regolith, Mystery Zone, Mt Percy, Kalgoorlie, Western Australia. Geochemistry: Exploration, Environment, and Analysis (in press).

Sheard, M.J. and Bowman, G.M., 1996. Soils, stratigraphy and engineering geology of near surface materials of the Adelaide Plains. South Australia. Department of Mines and Energy. Report Book, 94/9. (3 Volumes, 492 p).

Tapley, I.J. and Craig, M.A., 1995. An evaluation of AIRborne Synthetic Aperture Radar (AIRSAR) for mapping surface and sub-surface structures in the Telfer region, Paterson Province, Western Australia (Volumes 1 and 2). CSIRO/AMIRA Project 392, CSIRO Exploration and Mining Report 146R. pp.110.

Tapley, I.J. and Gozzard, J. R., 1992. . Regolith-landform mapping in the Lawlers District. Report 1: Aerial photographic interpretation and Landsat Thematic Mapper processing for mapping regolith-landforms (Volumes 1 and 2). CSIRO IMEC Division of Exploration Geoscience Restricted Investigation Report No. 239R, 165 pages.

Tapley, I.J., Okada, K. and Tsukada, M., 1999. Mapping regolith gelogy in Australia with radar polarimetry and interferometry. Proceedings of 13th ERIM Geological Remote Sensing conference, Vancouver. pp. I100-I108

Tapley, I.J., 1998. Landform, Regolith and Geological Mapping in the North-Eastern Goldfields Region, Western Australia, and North Drummond Basin, Queensland, using AIRSAR Polarimetric Radar Data (Volumes 1 and 2). CRC LEME/AMIRA Project 392, CRC LEME Report 55, CSIRO Exploration and Mining Report 147R. pp.136

Whitten, G.F., 1965. The investigation of Fe formations in the Mulgathing District (Tarcoola 4 mile sheet). South Australia. Department of Mines. Report Book, 60/42.

Wilford, J.R. and Craig, M.A., 1998a. Regolith-Landforms Map of Half Moon Lake, South Australia, 1:50,000 scale, Australian Geological Survey Organisation/CRC LEME.

Wilford, J.R. and Craig, M.A., 1998b. Regolith-Landforms Map of the Jumbuck Region South Australia, 1:50,000 scale, Australian Geological Survey Organisation/CRC LEME.

Wilford, J.R., Craig, M.A., Tapley, I.J. and Mauger, A, 1998. Regolith-landform mapping and its implications for exploration over the Half Moon Lake region, Gawler Craton, South Australia. CRC LEME Restricted Report 92R / CSIRO Exploration and Mining Report 542C.